Investigating the role of enhancer–promoter proximity in regulating gene expression

Dissertation der Fakultät für Biologie
der Ludwig-Maximilians-Universität München

Gabriela Stumberger

München, 2025

Diese Dissertation wurde angefertigt
unter der Leitung von Prof. Dr. Heinrich Leonhardt
am Lehrstuhl für Humanbiologie und BioImaging
an der Ludwig-Maximilians-Universität München

Erstgutachter: Prof. Dr. Heinrich Leonhardt
Zweitgutachter: Prof. Dr. Philipp Korber
Tag der Abgabe: 24. 11. 2025
Tag der mündlichen Prüfung: 7. 1. 2026

Eidesstattliche Versicherung

Ich versichere hiermit an Eides statt, dass die vorgelegte Dissertation von mir selbstständig und ohne unerlaubte Hilfe angefertigt wurde.

München, den 19. 11. 2025

Gabriela Stumberger

Erklärung

Hiermit erkläre ich, dass die vorliegende Dissertation weder ganz noch teilweise bei einer anderen Prüfungskommission vorgelegt wurde. Ich habe mich nicht anderweitig einer Doktorprüfung ohne Erfolg unterzogen. Ich habe noch zu keinem früheren Zeitpunkt versucht, eine Dissertation einzureichen oder an einer Doktorprüfung teilzunehmen.

München, den 19. 11. 2025

Gabriela Stumberger

Contents

List of publications

Parts of this work have been published elsewhere:

Steinek, C., Guirao-Ortiz, M., **Stumberger, G.**, Tölke, A. J., Hörl, D., Carell, T., Harz, H. and Leonhardt, H. (2024) Generation of densely labeled oligonucleotides for the detection of small genomic elements. *Cell Reports Methods*, 4, 100840.
DOI: 10.1016/j.crmeth.2024.100840

Stumberger, G., Hörl, D., Tsouraki, D., Steinek, C., Oudelaar, A. M., Leonhardt, H. and Harz, H. (2025) Nanoscale Dynamics of Enhancer-Promoter Interactions during Exit from Pluripotency. *Nucleic Acids Research*, 53, gkaf1255.
DOI: 10.1093/nar/gkaf1255

Declaration of contributions

Generation of densely labeled oligonucleotides for the detection of small genomic elements

I analyzed some of the imaging data, contributing to figures 1, 3 and 4. Additionally, I designed the overhang sequences for xNOVA.

Nanoscale Dynamics of Enhancer-Promoter Interactions during Exit from Pluripotency

I identified target enhancers in naive and primed states. I performed all FISH experiments and analyzed the imaging data. Together with David Hörl, I wrote the scripts for analysis of the imaging data. With help from Dimitra Tsouraki, I analyzed the Tri-C data. I interpreted the data together with Dimitra Tsouraki, A. Marieke Oudelaar and Hartmann Harz. I prepared the figures with input from all co-authors. We wrote the manuscript together with all co-authors, mainly Hartmann Harz and me.

München, den 19. 11. 2025

Gabriela Stumberger

Prof. Dr. Heinrich Leonhardt

Abbreviations

3C	chromosome conformation capture
AML	acute myeloid leukemia
ATAC-seq	assay for transposase-accessible chromatin using sequencing
BAC	bacterial artificial chromosome
BILD	bayesian inference of looping dynamics
BMP4	bone morphogenetic protein 4
BRD4	bromodomain-containing protein 4
BrdU	bromodeoxyuridine
BRG1	Brahma-related gene 1
CAGE-seq	cap analysis of gene expression sequencing
CDK	cyclin-dependent kinase
ChIA-PET	chromatin interaction analysis by paired-end tag sequencing
ChIP-seq	chromatin immunoprecipitation followed by high-throughput sequencing
COMBO-FISH	combinatorial oligonucleotide FISH
CTCF	CCCTC-binding factor
CTD	carboxy-terminal domain
DABCO	1,4-diazabicyclo[2.2.2]octane
DamID	DNA adenine methyltransferase identification
DNA	deoxyribonucleic acid
DNase-seq	DNase I hypersensitive sites sequencing
DSIF	DRB sensitivity-inducing factor
DyMIN	dynamic intensity minimum
E-P	enhancer - promoter
ENCODE	encyclopedia of DNA elements
EpiLC	epiblast-like cell
EpiSC	epiblast stem cell
ERK	extracellular signal-regulated kinase
eRNA	enhancer RNA

ESC	embryonic stem cell
FANTOM	functional annotation of the mouse/mammalian genome
FCS	fetal calf serum
FGF2	fibroblast growth factor 2
FISH	fluorescence in situ hybridization
FRAP	fluorescence recovery after photobleaching
FRET	Förster resonance energy transfer
GAM	genome architecture mapping
GOLD-FISH	genome oligopaint via local denaturation FISH
GRO-seq	global run on sequencing
GSK3β	glycogen synthase kinase 3β
GTF	general transcription factor
H3K4me3	trimethylation of histone H3 on lysine 4
HAWK	HEAT associated with Kleisin
HCl	hydrochloric acid
HCR-FISH	hybridization chain reaction FISH
HeLa	Henrietta Lacks
Hi-C	high-throughput chromosome conformation capture
HP1	heterochromatin protein 1
ICM	inner cell mass
KLF4	Krüppel-like factor 4
LCR	locus control region
LIF	leukemia inhibitory factor
MAPK	mitogen-activated protein kinase
MEF	mouse embryonic fibroblast
MEK	MAPK/ERK kinase
mESC	mouse embryonic stem cell
MINFLUX	minimal (fluorescence) photon flux
MNase	Micrococcal nuclease
mRNA	messenger RNA
NELF	negative elongation factor
NIPBL	nipped-B-like protein
NOVA-FISH	nanoscopy-compatible oligonucleotides with dyes in variable arrays FISH
OCT4	octamer-binding transcription factor 4
P-TEFb	positive transcription elongation factor b
PALM	photoactivated localization microscopy
PCR	polymerase chain reaction

PGCs	primordial germ cells
PIC	pre-initiation complex
PTM	post-translational modification
RASER-FISH	resolution after single-strand exonuclease resection FISH
RESCue	reduction of state transition cycles
RESI	resolution enhancement by sequential imaging
RNA	ribonucleic acid
RNA-seq	RNA sequencing
RNAPII	RNA polymerase II
SABER-FISH	signal amplification by exchange reaction FISH
scaRNA-seq	short capped RNA sequencing
SCR	Sox2 control region
SDS	sodium dodecyl sulfate
SMC	structural maintenance of chromosomes protein
SMLM	single-molecule localization microscopy
SOX2	SRY-box transcription factor 2
SPRITE	split-pool recognition of interactions by tag extension
SRY	sex-determining region Y
STED	stimulated emission depletion
STORM	stochastic optical reconstruction microscopy
SV40	simian virus 40
TAD	topologically associating domain
TAG	transcription factor activity gradient
TE	trophectoderm
TSA	tyramide signal amplification
TSS	transcription start site
YAC	yeast artificial chromosome
ZGA	zygotic genome activation

Abstract

The development of an organism requires the expression of each gene to be precisely orchestrated in space and time. This spatiotemporal control is partly achieved through enhancers: *cis*-regulatory sequences that can modulate transcription at their cognate promoters, even from millions of base pairs away. Despite the important regulatory role of enhancers, the mechanisms by which enhancers and promoters interact to exchange regulatory information is still debated. Specifically, it is unclear whether close spatial proximity between regulatory elements is required for transcription. Adding another layer of complexity, recent studies have revealed multiway enhancer-promoter (E-P) interactions that appear to drive cell type-specific gene expression. However, the frequency of these multiway interactions in single cells remains under-explored.

To address these questions, we combined DNA and RNA fluorescence in situ hybridization (FISH), super-resolution microscopy, and Tri-C to investigate changes in E-P distances during the transition from naive to primed pluripotency in mouse. To this end, we developed NOVA-FISH - a method capable of visualizing small regulatory elements in close genomic proximity. We then used NOVA-FISH, together with Oligopaint, to examine pairwise and multiway E-P interactions for five genes that are differentially expressed during the naive-to-primed transition: *Nanog, Dppa3, Sox2, Dnmt3a* and *Prdm14*. For *Nanog* and *Dppa3*, we additionally correlated E-P distance with nascent transcription.

Despite transcriptional changes of several orders of magnitude, we found that changes in pairwise E-P distances during the naive-to-primed transition are highly locus-dependent. Tri-C data at the *Nanog* locus revealed a weak enrichment of multiway contacts when *Nanog* was highly expressed in the naive state, but not in the primed state, when *Nanog* was downregulated. As transcription often occurs in transient bursts within a subset of cells, we combined RNA and DNA FISH to identify active alleles. We observed a positive correlation between shorter E-P distances and transcription at the *Nanog* and *Dppa3* loci. Together, our data support models of dynamic contact, in which shorter E–P distances are transiently stabilized during transcriptional initiation, and multiway hubs may contribute to regulating cell type–specific gene expression.

Introduction

1.1 Hierarchical view of 3D genome organization

The human interphase nucleus contains ∼6.2 billion base pairs of DNA, divided into 23 pairs of chromosomes, together spanning 2 m in length. Therefore, the DNA must be extensively packaged to fit in the nucleus, which measures only a few micrometers in size. This packaging is not random, but rather follows a hierarchical structure known as "chromatin architecture" (Figure 1), ranging from chromosome territories at the largest scale, over compartments, topologically associating domains (TADs) and loops to the arrangement of nucleosomes at the basepair level [1–3].

Chromosome territories

At the largest scale, chromatin in the mammalian nucleus is organized into chromosome territories. Throughout interphase, individual chromosomes occupy spatially distinct areas of the nucleus, typically around 2-3 µm in diameter [4, 5]. Chromosomal regions rich in active genes generally localize in the center of the nucleus, while regions rich in inactive genes more frequently reside closer to the periphery [6–8]. Although chromosomes preferentially interact with themselves, different chromosomes have also been shown to intermingle, especially at their boundaries [4, 5].

Compartments and subcompartments

At a megabase scale, genomic regions with similar chromatin characteristics tend to interact with each other [3, 9]. Transcriptionally active regions, for example, tend to interact with other active regions. These active regions are characterized by higher gene density, higher levels of chromatin accessibility, and histone modifications associated with active (H3K36me3) and poised chromatin (H3K27me3). On the other hand, transcriptionally inactive regions, characterized by lower gene density, higher chro-

matin compaction, and high levels of repressing histone marks (eg. H3K9me3), tend to interact with other inactive regions. Based on high-throughput chromosome conformation capture (Hi-C) data, these two types of regions are often referred to as the "A compartment" (active) and "B compartment" (inactive) and roughly correspond to euchromatin and heterochromatin in microscopy studies, respectively [1, 9, 10].

Based on interaction patterns observed in Hi-C maps, Rao et al. [11] further divided compartments into five subcompartments: A1, A2, B1, B2 and B3. Subcompartments show even more specificity with respect to active and inactive histone marks, gene density, DNA replication timing, and association with proteins and nuclear structures. Active subcompartments A1 and A2, for example, are bound by RNA polymerase II (RNAPII) and binding factors such as Bromodomain containing proteins, the inactive B1 is bound by the Polyxomb complex, while inactive B2 and B3 contain heterochromatin protein 1 (HP1) [12]. Subcompartment A1 is located in close proximity to nuclear speckles, while A2 is more distant [13]. B2 is enriched at the nuclear lamina and nucleolus, while B3 is enriched at the lamina, but depleted at the nucleolus [11, 13].

Topologically associating domains (TADs) and loops

At a megabase to sub-megabase level, the genome is organized into so-called TADs. These can be identified as "triangles" or "squares" in Hi-C maps, where regions within the same TAD interact ∼2-fold more frequently with each other than with adjacent regions outside the TAD [2, 14–16]. Initial studies estimated the size of TADs to be ∼800kb [15], however, later analysis of higher resolution Hi-C data suggested sizes ranging between 40kb - 3Mb, with a median domain size of ∼185kb [2, 11]. It should be noted that TADs and their size can vary significantly, depending on the algorithm and parameters used to call them [17]. Different TADs are demarcated by TAD boundaries. In mammals, TAD boundaries are usually enriched for binding of insulator proteins such as CCCTC-binding factor (CTCF) (detected at ∼76% of boundaries), cohesin, active transcription marks such as H3K4me3 and H3K36me3, presence of housekeeping genes (∼34% of TAD boundaries) and repetitive elements [2, 11]. A relatively high degree of conservation of TADs and TAD boundaries was observed between celltypes [11, 15], during differentiation [18] and even across species [19, 20]. A domain organization similar to mammals was found in non-mammalian species like *Drosophila* [14], zebrafish [21], *C. elegans* [22] and yeast [23, 24], suggesting the importance of TADs.

TADs are though to play a role in regulating gene expression through different mechanisms. Firstly, TAD boundaries can act as barriers, insulating a promoter from the

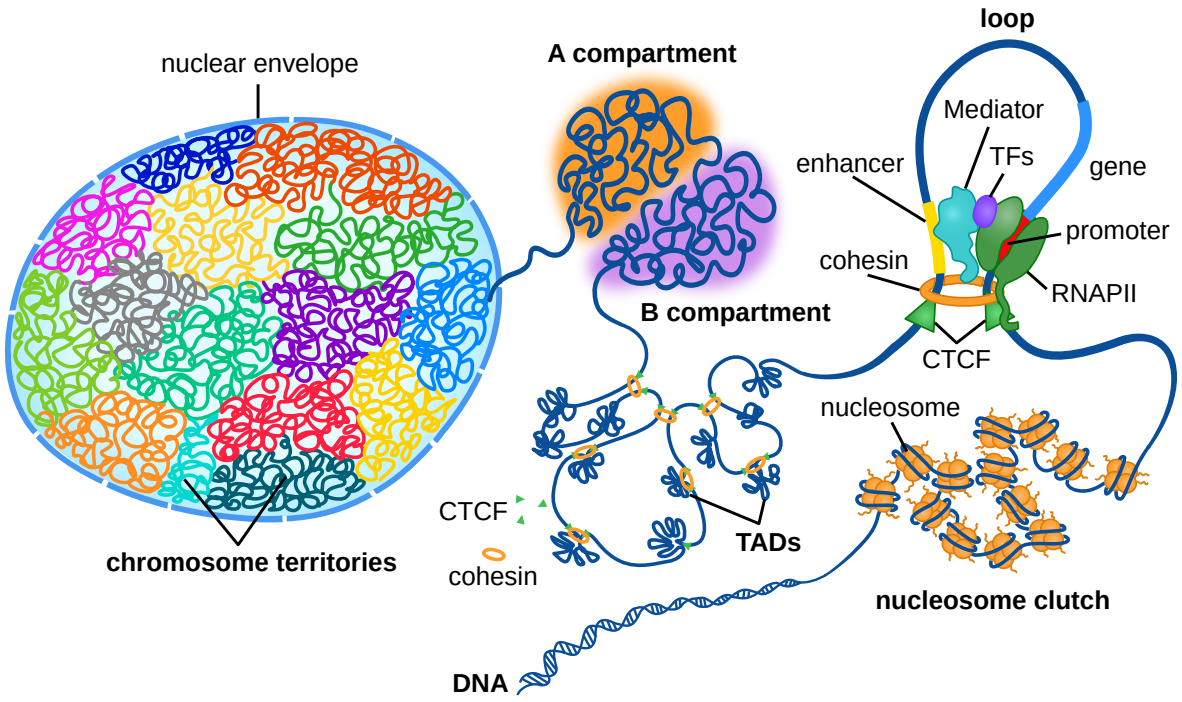

Figure 1: Hierarchical view of 3D genome organization. Chromosomes occupy distinct territories within the mammalian interphase nucleus. At the megabase scale, transcriptionally active and inactive chromatin segregate into A/B compartments and topologically associating domains (TADs). Within these domains, CTCF- and cohesin-mediated loop extrusion organizes chromatin into loops that facilitate enhancer–promoter communication. At the smallest scale, DNA is wrapped around histone octamers to form nucleosomes, which assemble into heterogeneous clusters known as nucleosome clutches.

action of enhancers in neighboring TADs [25]. Studies in mice that deleted TAD boundaries [26] or inverted CTCF binding sites at boundaries [27] have demonstrated that the loss of TAD boundaries can lead to aberrant gene expression, caused by ectopic E-P interactions. Similarly, creating chromosomal inversions or duplications that fuse adjacent TADs also leads to misregulated gene expression [28]. Highlighting their critical role *in vivo*, a recent study has shown that targeted deletion of TAD boundaries near developmentally important genes *Smad3/Smad6* causes complete embryonic lethality, while a deletion near *Tbx5/Lhx5* results in a severe lung malformation in mice [29]. Secondly, TADs could also increase the contact probability of enhancers and promoters within the same TAD by restricting their movement in 3D space. The *Shh* gene promoter, for example, displayed much more frequent interactions with its enhancers when they were contained within the same TAD, compared to when those enhancers were genomically equidistant or closer, but located outside the TAD [30]. Finally, TAD boundaries can also function as insulating elements which restrict the spreading of euchromatin into heterochromatin and vice versa [25]. This was exemplified by a study

showing that the deletion of CTCF binding sites within *Hox* clusters resulted in the expansion of active chromatin into a previously repressed region [31]. While additional experimental evidence is required to validate these mechanistic models, it is reasonable to assume that TADs are able to influence gene expression [25, 32, 33].

At the kilobase level, long-distance genomic contacts are facilitated by the formation of chromatin loops. Some of these loops are formed via loop extrusion, which is mediated by cohesin and boundary factors such as CTCF [34–40]. CTCF is an 11-zinc finger DNA binding protein with an insulator function [41]. Cohesin is a ring-shaped multi-protein complex, consisting of two structural maintenance of chromosomes (SMC) subunits, linked by a kleisin and additionally interacting with HEAT repeat proteins associated with kleisins (HAWK proteins) [42]. It was initially discovered for its ability to hold sister chromatids together after DNA replication until mitosis [43–45]. According to the "loop extrusion model" NIPBL first loads cohesin onto the DNA [46], then cohesin begins extruding a loop, which grows larger until cohesin spontaneously falls of, or encounters a DNA-bound CTCF molecule in a convergent orientation. CTCF then halts the loop extrusion process [34, 35, 42, 47, 48]. Additionally, the length of loops is limited by WAPL, which competes with CTCF and is able to release loop-extruding cohesin from DNA [38, 49–51]. Loops preferentially form when two CTCF molecules at the boundaries of a TAD are arranged in a convergent orientation. Loops are thought to facilitate E-P interactions by bringing distal regulatory elements at loop anchors closer together. Different models of E-P interaction will be discussed in more detail in section 1.2.3. Furthermore, loops are the basis for the formation of TADs [34–40] and depletion of both CTCF [36, 38] and cohesin largely leads to loss of TADs [37, 38, 50, 52].

Since TADs were originally identified from Hi-C, which averages interaction frequencies across millions of cells, TADs were long considered to be properties of a population [53]. Indeed, single cell Hi-C [54, 55] and super-resolution imaging studies [56, 57] have later revealed that loops and TADs are highly variable between cells. Although individual cells still contain compartments and domains, even strong loop anchors observed in bulk Hi-C matrices are only present in a small subset of cells. These observations have raised the idea that TADs are statistical properties of chromatin [58, 59]. Here, TADs from population averages are explained by chromosomal configurations, where loops can form anywhere between two TAD boundaries, whereas loops that cross boundaries are rare [60]. Live cell imaging experiments have shown that pairs of CTCF binding sites at nearby TAD boundaries are in contact for prolonged periods of time, approximately between 10-30 min [40, 61]. Furthermore, biophysical modeling of looping kinetics has

suggested that most of the time TADs are in a partially extruded state and the fully looped state is rare, supporting the idea that TADs are transient [40, 60, 61].

Nucleosome - nucleosome interactions

At the smallest scale of 3D genome organization nucleosomes form the basic unit of DNA packaging. The nucleosome core consists of a 147 bp segment of DNA, wrapped around two copies of each of the four core histones: H2A, H2B, H3 and H4. The cores are connected by sections of linker DNA and linker histone H1 [62]. Based on *in vitro* electron microscopy and x-ray crystallography studies, nucleosomes were long believed to neatly organize into arrays of solenoid or zigzag shapes termed the 30 nm fiber [63, 64]. We know today that the 30 nm fiber is an artifact of sample preparation for electron microscopy and, as such, does not exist *in vivo* [23, 34, 65–67]. Instead, chromatin appears to be a lot more flexible than initially thought [34, 66, 67]. A pioneer electron microscopy study revealed that chromatin in human interphase and mitotic nuclei organizes into disordered chains ranging from 5 to 24 nm in thickness [67]. These chains exhibit considerable variability in their arrangement, packing density, and structural conformations, depending on nuclear region and chromatin activity state. In line with these findings, a super-resolution microscopy study [66] demonstrated that nucleosomes are arranged in clusters of heterogeneous sizes, so-called "nucleosome clutches", which are interspersed by nucleosome depleted regions. Smaller, less compact clutches tend to contain active chromatin and RNAPII, whereas larger, high-density clutches are associated with a higher content of linker histone H1 and the more tightly compacted heterochromatin.

1.2 Enhancers in regulating gene expression

The development of an organism requires the expression of each gene to be precisely orchestrated in space and time [68, 69]. While gene expression can be regulated at numerous points, the very first step of gene expression, the transcription of DNA into mRNA, is one of the key regulatory events. To initiate transcription, RNAPII is recruited to the promoter, together with the general transcription machinery and core transcription factors (TFs) [70]. However, promoters by themselves can often only drive a basal level of transcription. For many genes, other *cis*-regulatory elements, such as enhancers, are required to achieve the target level of gene expression [68–71].

1.2.1 A brief history of transcriptional enhancers

Enhancers were originally defined as *cis*-regulatory sequences, capable of stimulating transcription of their target gene in a distance- and orientation-independent manner [72–74]. The first described enhancer was a 72 bp sequence of the SV40 virus, which could enhance the transcription of a reporter β-globin gene in HeLa cells by several 100-fold, even when its sequence was flipped or inserted several kilobases form the promoter [72]. Later studies in various cell types identified several other endogenous mammalian enhancers which could control transcription in specific tissues [73–76]. The development of DNA footprinting and electrophoretic mobility shift assay revealed that tissue-specific TFs bind at enhancers, thereby explaining why activation is restricted to particular cell types [77–79]. Subsequent studies centered around enhancers in the context of *Drosophila* development [80–82]. Despite emerging evidence on the role of tissue-specific enhancers controlling gene expression in mammals, gene regulation research was still primary focused on promoters [79, 83, 84].

However, this changed dramatically with the Human Genome Project. To the surprise of the scientific community, the human genome was found to contain only ∼25000 protein-coding genes, covering only ∼1.5% of the genome - far less than previously estimated [85]. This sparked a significant interest in the role of the noncoding genome in biology and disease. Early estimates already indicated that the number of enhancers could be vastly higher than the number of active genes in a given cell type, suggesting a role of enhancers in regulating genome-wide transcription programs [79]. More than 4 decades later from the original discovery, the development of high-throughput genomic methods, microscopy and computational biology has shifted the definition of an enhancer. Today, enhancers are associated with binding by particular transcription factors or co-activators (eg. p300 acetyltransferase and Mediator complex), presence of certain histone modifications (H3K27ac, H3K4me1/2), depletion of nucleosomes or transcription of enhancer RNAs (eRNAs) [86]. Additionally, the distinction between promoter and enhancer is becoming increasingly unclear, as their chromatin architectures are surprisingly similar [87–92], several promoters have been shown to exhibit enhancer activity [93–96], and active enhancers are able to drive local transcription initiation at their boundaries, thereby functioning as promoters [71, 97–99]. The variety of these characteristics makes is difficult to unambiguously define an enhancer.

1.2.2 An overview of eukaryotic transcription

Chromatin accessibility

In order to understand how enhancers may regulate transcription, it is first necessary to consider the process of transcription itself. For transcription to take place, the promoter, a regulatory sequence at the 5' end of the gene, first has to become accessible. The accessibility of regulatory elements is highly regulated by the presence of nucleosomes and larger chromatin structures which hinder binding of TFs at the genomic regions they occupy. A subset of TFs, known as pioneer TFs, can nonetheless bind to the nucleosome-occupied DNA and recruit chromatin remodellers that make the regulatory element more accessible. Other TFs can then bind at these loci, further increasing chromatin accessibility, making it permissive for transcription [100, 101].

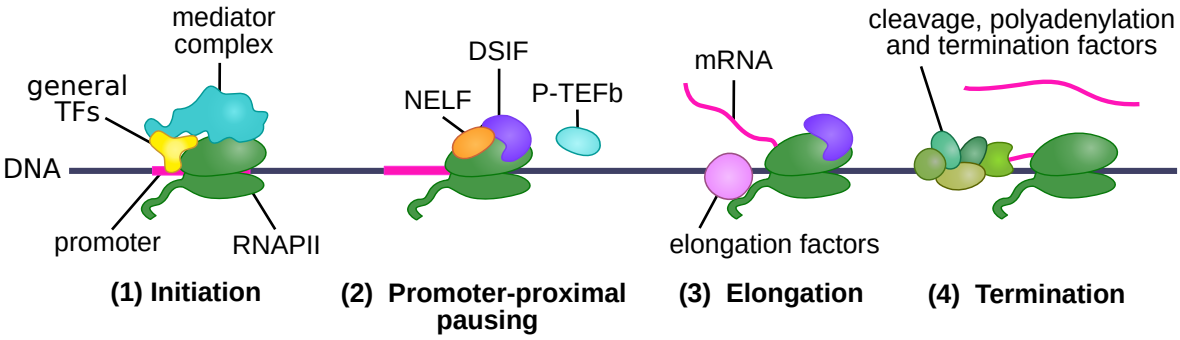

Figure 2: Steps of transcription. (1) Pioneer transcription factors (TFs) recruit general TFs and RNA polymerase II (RNAPII) to the promoter, forming the preinitiation complex. The complex unwinds the DNA and the unphosphorylated carboxy-terminal domain (CTD) of RNAPII recruits the Mediator complex. Phosphorylation of the CTD by cyclin-dependent kinase 7 (CDK7) triggers promoter escape. (2) Binding by negative elongation factor (NELF) and DRB sensitivity-inducing factor (DSIF) causes RNAPII to pause 20 - 100 bps downstream of the promoter. Phosphorylation of NELF by positive transcription elongation factor b (P-TEFb) causes its dissociation, permitting RNAPII to resume transcription. (3) During productive elongation, several factors associate with RNAPII to maintain processivity and proper post-transcriptional modification of mRNA. (4) Upon encountering a termination signal, RNAPII pauses and is released from the DNA, together with the nascent transcript. Redrawn and adapted from [102] with permission.

Initiation

Subsequently, multiple regulatory elements cooperatively recruit a set of general transcription factors (GTFs). Through the interaction with these GTFs, the RNAPII complex is recruited to the promoter, forming the preinitiation complex (PIC) (Figure 2). With the help of additional factors, the PIC opens the DNA helix in a series

of enzymatic reactions [100]. In the preinitiation state, RNAPII carries an unmodified carboxy-terminal domain (CTD), which exhibits high affinity for the Mediator complex. The Mediator acts as a transcriptional co-activator by bridging transcriptional activators bound at enhancers with the core transcription machinery at promoters [102, 103]. Upon phosphorylation of the Ser5 and Ser7 of the CTD by cyclin-dependent kinase 7 (CDK7), this affinity is lost and RNAPII can escape the promoter [102, 104].

Elongation

Prior to entering productive elongation, RNAPII is typically paused 20 - 100 bp downstream of the promoter (Figure 2) [105]. Promoter-proximal pausing can cause RNAPII to backtrack, stall, or terminate, thereby regulating gene expression by restricting the frequency of productive elongation. Pausing is induced when RNAPII is bound by negative elongation factor (NELF) and DRB sensitivity-inducing factor (DSIF). To release RNAPII from its pause state, positive transcription elongation factor b (P-TEFb) phosphorylates NELF, causing it to dissociate, and phosphorylates DSIF, causing it to turn into a positive elongation factor [102, 106]. During productive elongation, several other factors bind to the CTD of RNAPII, ensuring processive elongation and proper post-transcriptional modification of mRNA, such as capping and splicing [100].

Termination

The elongation complex extends the mRNA chain until it encounters a termination signal, upon which it dissociates from both the DNA template and the newly synthesized transcript. For most protein-coding eukaryotic genes termination is poly (A)-dependent. RNAPII recognizes a highly conserved poly(A) signal (5'-AAUAAA-3'), followed by a G/U-rich sequence near the 3' end of the gene. Transcribing the poly(A) signal causes a marked reduction in RNAPII processivity, leading to pausing further downstream. Concurrently, Ser2P levels at the CTD peak towards the end of elongation, promoting the recruitment of cleavage, polyadenylation and termination factors. The binding of these factors at the transcribed poly (A) site induces RNAPII pausing, followed by cleavage and release of the nascent transcript and RNAPII from the DNA. Once released, RNAPII can be dephosphorylated and recycled for a new round of transcription [107].

Where do the enhancers come in?

Current literature suggests that enhancers can influence transcriptional regulation during both the initiation and promoter-proximal pausing stages of the transcription cycle.

Studies employing ChIP-seq and nascent RNA methods, including GRO-seq and Start-seq, have revealed that RNAPII accumulates across the promoter-proximal region and the transcription start site (TSS). This led to the conclusion that promoter-proximal pausing is the key regulatory step in the transcription cycle, potentially controlled by enhancers [105, 108, 109]. Consistent with this view, β-globin enhancers were previously reported to facilitate the release of paused RNAPII [110–112]. Conversely, a recent genome-wide analyses employing short capped RNA sequencing (scaRNA-seq) and nascent gene expression measurements in differentiating primary cells indicates that gene expression is mainly regulated through transcription initiation, possibly driven by enhancer-mediated recruitment of RNAPII to promoters [113]. The exact stage at which enhancers exert their regulatory influence remains subject of current studies.

1.2.3 Models of enhancer - promoter interaction

For an enhancer to activate transcription of a cognate promoter, the two elements have to exchange information and/or material. This is referred to as an interaction [114]. The precise proximity required for enhancers and promoters to interact [115–117], as well as the frequency and duration of these interactions needed for a transcription event to occur [118, 119] remain a topic of ongoing debate. Yang and Hansen (2024) [114] have classified models of E-P interactions based on two factors: (i) spatial proximity where no contact, direct contact or action at a distance models are compared; and (ii) duration of interaction, where stable interactions are compared to dynamic ones (Figure 3B). Notably, the "contact" in contact models does not necessarily imply physical contact, but rather an estimation of whether the regulatory elements are in spatial proximity to each other. In these models, the distance between elements must be below a certain threshold for the elements to functionally interact [120]. Importantly, different models of E-P interaction are not mutually exclusive [114].

Linear models: tracking and linking

Early models, often referred to as linear or 1D models, propose that interactions between enhancer and promoter, which are several kilobases apart on the linear genome, can occur without the enhancer and promoter being brought into spatial proximity to each other [121]. One such model, the "tracking" model (Figure 3A), proposes that RNAPII together with other transcriptional machinery is loaded at the enhancer and tracks along the DNA, until they reach their cognate promoter [75, 122]. A version of this model suggests that chromatin remodellers can track along the DNA to spread

histone PTMs from the enhancer toward the promoter [123]. Another model is the "linking" model, where TFs bound to the enhancer oligomerize along the DNA to form a bridge to the promoter [124]. However, these models cannot explain how enhancers can often skip nearby promoters to activate more distal ones [125, 126]. This observation, together with recent studies showing increased 3D spatial proximity between enhancers and their cognate promoters compared to other genomic regions [117, 118, 127–131], have supported 3D models of E-P interaction [114].

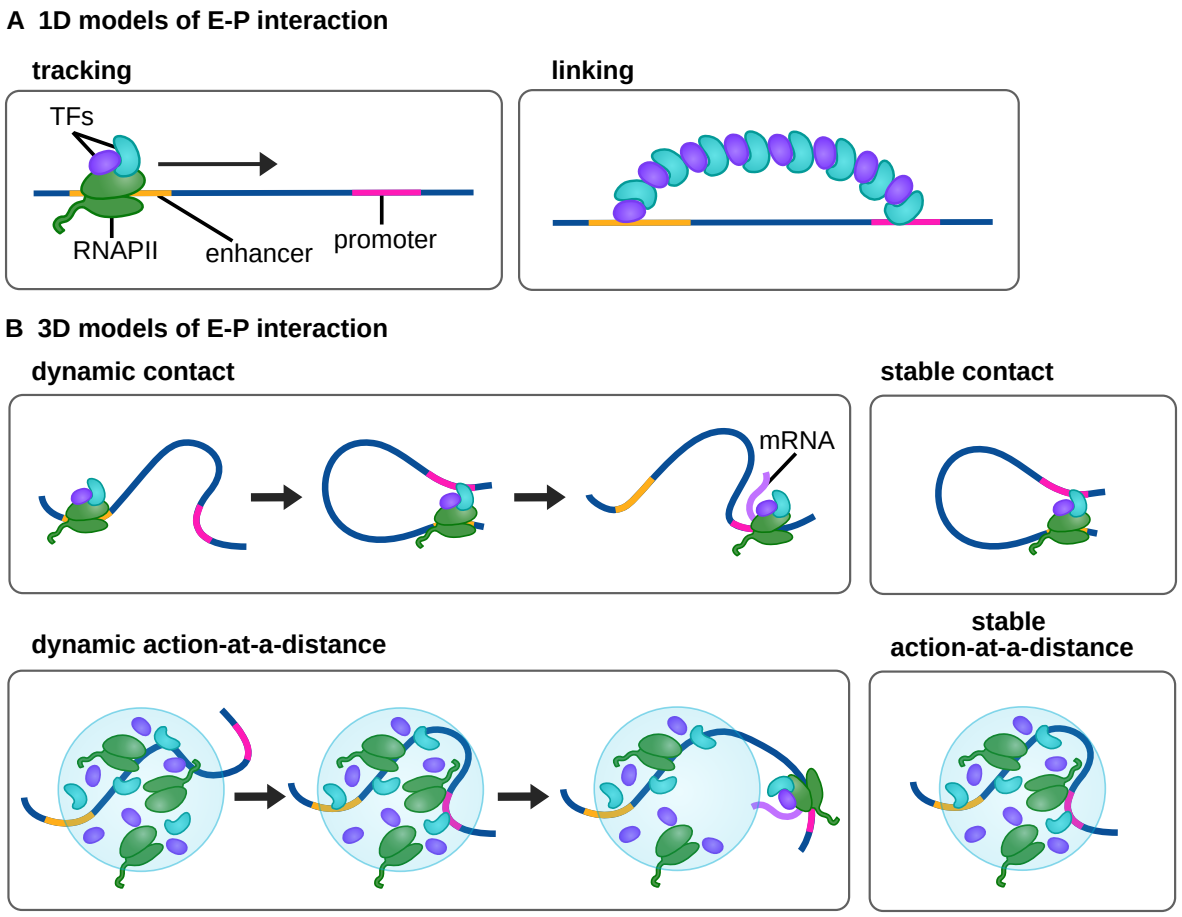

Figure 3: Models of enhancer - promoter (E-P) interaction. (A) 1D models of E-P interaction. The tracking model proposes that RNA polymerase II (RNAPII) and transcription factors (TFs) are loaded at the enhancer and track toward the promoter. The linking models suggests that TFs bound at the enhancer and oligomerize along the DNA to form a bridge to the promoter. (B) 3D models of E-P interaction. The direct contact model posits than enhancers and promoters come into close physical proximity (e.g., via chromatin looping) to initiate transcription. The action-at-a-distance model proposes that enhancers can regulate promoters hundreds of nanometers away (eg. mediated via transcriptional condenses). Both of these models can be either dynamic or static. Redrawn and adapted from [114] with permission.

Direct contact models: looping

The textbook 3D model is the stable contact model, where genomically distant enhancer and promoter are brought into close spatial proximity to each other via chromatin looping and the contact is then stabilized (Figure 3B) [114]. Early functional evidence for looping stems from studies in *Escherichia coli* [132] and the SV40 enhancer [133], where proteins had to be bound on the correct side of the DNA helix for highest transcriptional output. First *in vivo* evidence for the looping model was presented in studies of the β-globin locus [134]. In humans, the expression of β-globin genes is developmentally regulated. Fetal β-globin genes are active before birth and switch to adult β-globin genes shortly after [135]. The expression of these β-globin genes is controlled by a LCR located ∼50 kb upstream of the genes [136, 137]. Forced chromatin looping between developmentally silenced fetal β-globin genes and the LCR has been shown to activate the expression of these genes in adult cells [130, 138, 139], demonstrating that bringing enhancer and promoter in close spatial proximity via chromatin looping can be causal for gene activation.

Several microscopy studies in fixed and live cells have also demonstrated a correlation between increased E-P proximity and gene expression. Williamson et al. [140] have shown using FISH that the *Shh* promoter is significantly closer to its ZRS enhancer in expressing mouse limb buds than in tissues not expressing *Shh*. Chen et al [125] demonstrated using 3D FISH, that for 3 genes activated during development of the mouse forebrain, midbrain and face and forelimb cells, E-P distances decrease significantly in tissues where genes are active. A FISH study in mouse embryonic stem cells (mESCs) by Ohishi et al. [141] reported that several genes exhibited increased enhancer–promoter (E–P) proximity frequency in their transcriptionally active state compared to the inactive state. A live cell imaging study in *Drosophila* embryos by Chen et al. [117] has shown that that sustained proximity of the *eve* enhancers to their target is required for gene activation. Imaging distant enhancer clusters of *Nanog*, *Sox2* and *Pou5f1* in live cells, together with an MS2-based transcriptional readout, Li et al [142] reported a correlation between E-P proximity and nascent transcription. All of these studies support the notion of E-P proximity driven transcription. Interestingly, however, other studies [115, 116, 128, 143] have observed transcription in the absence of close E-P proximity, challenging the validity of the contact model.

Action-at-a-distance models: condensates and TAG

Action-at-a-distance models propose that direct physical contact between enhancers and promoters is not required for a functional interaction. Some variants of action-

at-a-distance models posit that the interaction is mediated by liquid-like condensates, several hundred nm in size [116, 144–149], which act as reservoirs of Pol II, coactivators and transcription factors (Figure 3B) [114, 144, 146, 150–152]. The formation of these condensates is driven by dynamic multivalent interactions between DNA, protein and RNA. While proteins provide the source of multivalent interactions, DNA regulatory elements, together with associated chromatin and RNA, act as a multivalent scaffold to regulate the formation of condensates at specific loci [100]. Regulatory elements are enriched in TF binding sites, to which TFs can bind and recruit cofactors and other TFs. Through a cascade of co-activator-mediated interactions, this ultimately leads to an increased local concentration of different components of the transcriptional machinery [100]. Additionally, specific histone PTMs [153, 154] and transcription of nascent RNAs at enhancers also favor the formation of condensates [155–157].

The reported E-P distances at active genomic loci range between 200 - 350 nm [115, 142–144, 158], which corresponds strikingly well to the observed sizes of condensates in live cells [144, 157]. The condensate model is further supported by live-cell imaging studies observing the formation of condensates around so-called super-enhancers. Super-enhancers are genomic regions containing multiple enhancers which can drive high levels of transcription at cognate promoters and were originally defined based on Mediator enrichment [114]. Sabari et al. [147] have shown that transcriptional co-activators BRD4 and Mediator form liquid-like condensates at such multi-enhancer regions. The IDRs of BRD4 and Mediator are able to form phase-seperated droplets which can compartmentalize and concentrate transcriptional machinery from nuclear extracts. Similarly, Cho et al. [159] found that RNAPII and Mediator form small (∼100 nm) transient and large (∼300 nm) stable clusters, which co-localize with each other, associate with super-enhancers, and exhibit properties of phase-separated condensates. Du et al. [144] have observed that the transcription of the *Sox2* promoter strongly correlates with the proximity of RNAPII condensates, but not with the proximity of the SCR enhancers. These studies offer an explanation for the weak correlation between E–P distance and transcription [115, 116, 128, 143]. However, condensates are not the only explanation for the lack of close E-P proximity.

Another variant of action-at-a-distance models is the transcription factor activity gradient (TAG) model. The TAG model proposes that co-activators bound at enhancers are able to modify nearby TFs, thereby creating a gradient of active TFs centered at the enhancer [160]. This model is grounded in the observation that histone-modifying enzymes are also capable of modifying TFs [161, 162]. Therefore, enhancers which are enriched in a number of histone modifications could bring together enzymes with

specific substrates, acting as platforms for TF modification. In one such example, the lysine acetyltransferase p300, which has been indicated necessary for enhancer function [163], is recruited to an enhancer by a sequence-specific DNA-binding TF. p300 is then activated by an allosteric regulator and acetylates nearby substrates, including histones and enhancer-bound TFs. The now activated, acetylated TFs (with typical residence times of a few seconds) disengage and diffuse outward from the enhancer. Histone deacetylases rapidly deacetylate the diffusing TFs, creating a concentration gradient of acetylated TFs and limiting the signal's spatial range. When acetylated TFs reach a promoter, they increase its transcriptional output [160]. Both the TAG and the condensate model would explain how enhancers and promoters can interact without the need for direct contact.

Interactions between multiple regulatory elements

While E-P interactions are typically viewed in a pairwise manner, both contact and action-at-a-distance models do not exclude interactions between multiple regulatory elements. In fact, most eukaryotic genes are regulated by multiple enhancers, especially during development, with the average human gene estimated to have at least 10 to 20 enhancers [120, 164–166]. Mounting evidence suggests that multiway E-P hubs play important roles in regulating cell type-specific gene transcription. Using GAM, Beargie et al. [167] observed an abundance of three-way contacts genome-wide, particularly linking super-enhancer regions with highly transcribed loci. A Tri-C study by Oudelaar and Davies et al. [168] revealed erythroid-specific interactions connecting multiple enhancers and promoters at the α- and β-globin loci. Similarly, single-cell Hi-C analysis by Lando et al. [169] has shown that hundreds of cell type-specific multiway hubs form during the transition from naive to primed pluripotency, potentially providing a structural framework for reconfiguring long-range E-P interactions during differentiation in mouse embryonic stemm cells (mESCs). Supporting a functional role for these hubs, gene expression levels correlate positively with enhancer number [170–172], suggesting an additive effect of enhancer action on transcription levels [173]. More recently, a region capture Micro-C study by Goel et al. [127] revealed that enhancers and promoters often reside within highly nested chromatin microcompartments, suggesting that multiway regulatory interactions form through condensates rather than loop extrusion. However, future imaging studies will be needed to understand the frequency and nature of multiway interactions in single and live cells.

The fourth dimension: time

In general, E-P interactions can either be stable, expected to last several hours, or dynamic, with durations in the scale of minutes to seconds. Evidence for stable E-P interaction models primarily comes from early studies in prokaryotes where stable E–P loops were observed [114, 174, 175]. In contrast, live cell imaging studies in animals have mainly found dynamic chromatin interactions [40, 61, 115, 117]. For example, both Gabriele et al. 2022 [40] and Mach et al. 2024 [61] have estimated CTCF-cohesin looping times in mESCs to be in the range of minutes. Comparing the contact frequencies between cohesin loops and E-P interactions in Hi-C maps, one can expect E-P contacts to be even more transient [114]. These interaction times are in agreement with the "hit-and-run" model, where enhancer and promoter briefly come into contact, exchange regulatory information, and then diffuse apart again [176]. Similarly to contact models, action-at-a-distance models can also be dynamic or stable. This likely depends on the lifetime of the condensates or TAG [114, 144, 159, 160]. Moving forward, additional work will be necessary to fully understand the temporal and spatial dynamics of E-P interactions and the mechanisms behind them.

1.3 Phases of pluripotency

Pluripotency describes the capacity of a cell to differentiate into all cell types of the body. Rather than existing as a single, fixed state, pluripotency unfolds as a developmental continuum through which embryonic cells progressively transition. This progression is typically divided into three consecutive phases: naive, formative, and primed pluripotency. Each transition involves coordinated, genome-wide reorganization of gene expression programs, DNA methylation landscapes and E-P interaction patterns [177, 178]. This dynamic molecular landscape makes pluripotency an ideal model for studying the fundamental principles of gene regulation.

1.3.1 From fertilization to pluripotency

Embryonic development begins when the maternal and paternal gametes fuse to produce a zygote. At fertilization, the zygote inherits not only the parental genomes but also their epigenetic information, including DNA methylation patterns, histone modifications, and non-coding RNAs. These epigenetic marks must be reprogrammed to establish a permissive environment for zygotic genome activation (ZGA) [179, 180]. While reprogramming takes place, the zygote remains transcriptionally silent and depends on maternally deposited RNAs and proteins. During the maternal-to-zygotic

transition (MZT), these maternal components are degraded and regulatory control of development is passed to the newly synthesized components of the embryonic genome [179, 181, 182]. In mouse, the zygotic genome is activated in two distinct waves. The minor ZGA wave coincides with the S phase of the first cell division and is characterized by the transcription of a limited set of unspliced transcripts and intergenic regions. The major ZGA wave follows during the S phase of the 2-cell stage, when thousands of stage-specific genes are transcribed. In other mammals, the distinction between those two waves is less pronounced and major ZGA occurs much later [180].

In subsequent cell divisions, the embryo polarizes and compacts at the 8-cell stage, leading to the formation of the morula at the 16-cell stage (Figure 4A). Cells then undergo specification depending on their position in the embryo: cells on the inside of the embryo will give rise to the inner cell mass (ICM), while cells on the outside will become the trophectoderm (TE). The ICM further segregates into the primitive endoderm, which will give rise to extraembryonic tissues; and the epiblast, which contains the pluripotent stem cells (PSC) [183, 184]. Pluripotency is defined as the ability to form germ cells and all three germ layers of the developing embryo - endoderm, ectoderm and mesoderm - which will eventually give rise to all cells of the body. PSCs can, however, not contribute to the trophectoderm or extraembryonic cell types [185, 186]. The timing and duration of pluripotency differs between mammals. In mice, for example, pluripotency usually arises at embryonic day (E) 3.5 and persists until about E7.5, while in humans, pluripotency begins at E6 and lasts approximately until E12. During this period, the blastocyst implants into the uterus as the epiblast undergoes further cell divisions and expansion [186]. This process is accompanied by global changes in transcriptional activity, epigenetic modifications, genome organization, metabolism, and signaling pathways [177, 178, 184, 186, 187]. Pluripotency ends with gastrulation, when the epiblast differentiates into the three embryonic germ layers, marking the first step of organogenesis [177, 186].

1.3.2 Pluripotency *in vitro*: the naive-to-primed transition

Embryonic pluripotency has been successfully captured *in vitro* [186, 188–190]. Mouse embryonic stem cells (mESCs) were the first PSCs to be isolated from mammals [186, 188, 189]. However, PSCs are not one uniform cell type. Depending on the culture conditions, different states of a continuous developmental process can be maintained. *In vitro*, PSCs are most commonly classified into three states: naive (ESC), formative (EpiLC - epiblast-like cells), and primed (EpiSC - epiblast stem cells), which correspond to the pre-implantation epiblast, early post-implantation epiblast and late

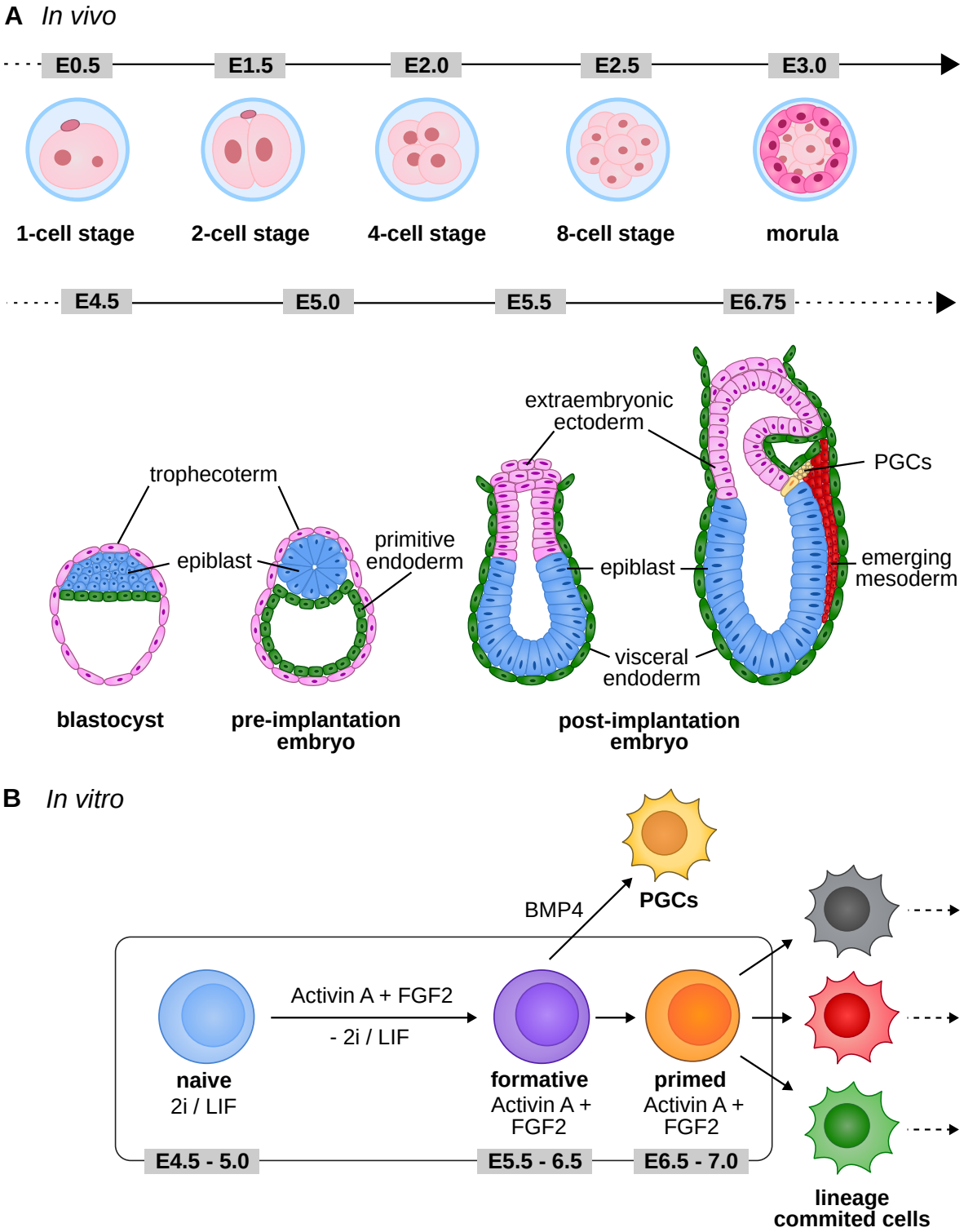

Figure 4: Phases of pluripotency. (A) *In vivo* early embryonic development in mouse, from totipotent zygote to pluripotent pre- and post- implantation embryo. (B) *In vitro* model of pluripotency. Cells can be maintained in a naive state with medium containing 2i/LIF. Upon 2i/LIF withdrawal and addition of Activin A + FGF2, cells transition to a formative state after 48 h, and to a primed state after 72 h. Naive, formative, and primed states correspond to the pre-, early post-, and late post-implantation epiblast, respectively. Redrawn and adapted from [178].

post-implantation epiblast *in vivo*, respectively [177].

Initially, mESCs were cultured in medium containing fetal calf serum (FCS) on feeder layers of mouse embryonic fibroblasts (MEFs), which serve to maintain pluripotency and facilitate growth of the stem cells [188, 189]. The later discovery of leukemia inhibitory factor (LIF) enabled a feeder-free culture [191, 192]. Yet, ESCs cultured with FCS and LIF alone were found to produce a heterogeneous population with characteristics of both naive and primed states which are able to convert between each other [193–195]. The addition of 2i, small molecule inhibitors targeting MAPK/ERK (MEK; PD0325901) and glycogen synthase kinase 3β (GSK3β; CHIR99021), produces a better-defined culture condition by suppressing differentiation and stimulating ESC proliferation [196]. ESCs cultured in a medium containing 2i and LIF homogeneously express naive factors and are thought to be almost equivalent to the pre-implantation epiblast [178, 195, 196].

In the presence of Activin A and fibroblast growth factor 2 (FGF2), ESCs convert into EpiSCs over the course of at least three days (Figure 4B). This transition is largely irreversible, reflecting diminishing developmental potential and progressive specification of pluripotent states during development [197–199]. EpiSCs are, for example, unable to form primordial germ cells (PGCs) upon the addition of inductive cytokines such as bone morphogenetic protein 4 (BMP4) [200]. Culturing ESCs with Activin A and FGF2 for just two days results in a transient, intermediate population of EpiLCs, termed the formative state. EpiLCs mimic the early post-implantation epiblast and, unlike EpiSCs, retain the ability to form PGCs [178, 201, 202].

Beyond isolation from embryos and differentiation from ESCs, PSCs can be generated from already differentiated somatic cells through reprogramming [186]. The most commonly used approach relies on forced expression of four TFs, the so called "Yamanaka factors" (Krüppel-like factor 4 (KLF4), SRY-box transcription factor 2 (SOX2), octamer-binding transcription factor 4 (OCT4) and c-MYC), in somatic cells [203–207]. Under appropriate culture conditions, fibroblasts can be reprogrammed not only into ESCs but also directly into EpiSCs [208]. Methods employing different combinations of transcription factors or microRNAs have also proven successful [209]. However, reprogramming efficiency is generally low, and the precise mechanisms underlying this process remain poorly understood [186]. Alternatively, a somatic cell can be fused with a pluripotent cell, resulting in the formation of a pluripotent cell hybrid [210, 211]. Another approach involves transplanting a somatic cell nucleus into an enucleated oocyte. The somatic nucleus is then reprogrammed by the maternal factors

present in the oocyte, leading to the generation of a blastocyst from which ES cell lines can be derived [212]. Most recently, chemical reprogramming has also been achieved using small molecules alone, eliminating the need for transgenes [186, 213].

1.3.3 Transcriptional changes during phases of pluripotency

Pluripotency is maintained by a core network of master transcription factors, comprising of OCT4, SOX2 and NANOG. These factors are co-recruited to regulatory elements of their target genes, where they activate the expression of pluripotency-associated genes and actively suppress the expression of genes associated with lineage commitment [182, 184]. OCT4 is a POU family transcription factor which is uniformly expressed across all PSCs and acts as a gatekeeper preventing differentiation [214–216]. Expression of OCT4 must be precisely regulated, as overexpression promotes mesoderm differentiation, while downregulation leads to differentiation along the trophectodermal lineage [216, 217]. Similarly, knockdown of SOX2 in mESCs induces differentiation into multiple lineages, including trophectoderm [218]. NANOG is a homeobox transcription factor which is expressed throughout PSCs of the ICM. It maintains pluripotency by blocking the differentiation towards primitive endoderm, neuronal and mesodermal lineages [184, 219, 220]. When overexpressed in cultured ESCs, NANOG can maintain pluripotency even in the absence of LIF [221, 222].

Both OCT4 and SOX2 act as pioneer TFs, remodeling tightly packaged chromatin to make it accessible to other TFs [223, 224]. OCT4 is capable of changing the nucleosome structure by stabilizing the otherwise flexible linker DNA and repositioning the nucleosomal DNA by recruiting chromatin remodellers like Brahma-related gene 1 (BRG1) [223]. Furthermore, OCT4 also enhances the pioneering activity of SOX2. It has been shown that SOX2 can bind more effectively to nucleosomes bound by OCT4, than to nucleosomes alone. Working synergistically, while SOX2 induces DNA bending and unwraps the nucleosomal DNA, OCT4 stabilizes the created structure, deforming the chromatin to facilitate its opening [223, 224]. OCT4, SOX2 and NANOG co-occupy regulatory sequences of their target genes, particularly at large clusters of enhancers known as "super-enhancers". The three master regulators are thought to recruit the Mediator complex to these sites, which facilitates the subsequent recruitment of GTFs to the promoter, thereby helping initiate transcription of select genes [182, 225]. Through mutual regulation of their own and each other's expression, OCT4, SOX2 and NANOG form an autoregulatory network that maintains pluripotency [182, 184, 226, 227]. To maintain the naive state, the activity of the master regulators is supported by additional key TFs, including ESRRB, KLF2, KLF4, KLF5, PRDM14,

REX1, TBX3 and TFCP2L1 [195, 228, 229].

The exit from naive pluripotency towards the formative state reflects the shift from the pre- (E4.0–5.0) to the post-implantation epiblast (E5.5-E6.5) [178, 228, 229]. This transition is triggered by the MEK/ERK and GSK3β signaling pathways [230–232]. While FGF helps stimulate the ERK signaling, Nodal (replaced by Activin *in vitro*) serves to suppress the differentiation towards neural lineages [233, 234]. The naive-to-formative transition is accompanied by substantial reorganization of enhancer landscapes and OCT4 binding patterns. OCT4 is lost from enhancers of naive pluripotency genes, leading to their downregulation. Notably, master TF NANOG is also downregulated, but not completely extinguished. Simultaneously, OCT4 engages with enhancers associated with post-implantation epiblast development, such as those of FGF5, OCT6 and WNT8A, driving their upregulation. This reorganization is mediated, at least in part, by the cooperation between OCT4 and OTX2 [235, 236]. Additional upregulated factors include SOX3, SALL2 [228, 229], and the *de novo* methyltransferases DNMT3A and DNMT3B. The increased expression of DNMT3A and DNMT3B drives a substantial, genome-wide increase in CpG methylation [237–239]. Compared to naive cells, the formative phase also exhibits an increased number of bivalent promoters, marked by both activating (H3K4me1) and repressive (H3K27me3) histone marks, which is crucial for enabling differentiation into multiple lineages in subsequent stages [177, 240].

The formative-to-primed transition mirrors the *in vivo* transition from the early (E5.5-E6.5) to the late (E6.5-E7) post-implantation epiblast [178, 228, 229]. In contrast to the abrupt transcriptional changes observed during the transition from naive into formative pluripotency, the shift from formative to primed pluripotency proceeds more gradually [177]. While OCT4 and SOX2 remain central to the pluripotency network, formative-specific factors such as OTX2, OCT6 or SOX3 become spatially restricted to regions corresponding to prospective tissue fates. Concurrently, lineage specific markers including T, FOXA2, and SOX1 are upregulated, and previously poised bivalent promoters resolve according to their future lineage commitment [177, 228, 237, 241–243].

1.4 Methods for studying enhancer - promoter interactions

The first challenge in studying E-P interactions lies in accurately identifying the enhancers themselves. Although large epigenomic consortia like FANTOM and ENCODE

have identified millions of regulatory elements, enhancers exhibit a high cell type specificity, which makes it challenging to create a comprehensive reference list of enhancers. While high-throughput gene reporter assays in cultured cells are commonly used to identify whether a selected sequence can function as an enhancer, *in vivo* reporter assays or *in vivo* genome editing of the sequence are considered definitive proof [244, 245]. However, these methods are not suitable for *de novo* genome-wide identification of enhancers. To identify putative enhancers genome-wide, combinations of co-factor binding, histone modifications and chromatin accessibility can be used [244].

Once identified, the next challenge is pairing enhancers with their target genes. Matching E-P pairs is not straightforward, as enhancers can be located millions of basepairs upstream or downstream from the genes they regulate [58, 246, 247]. Moreover, regulatory relationships are often complex: one gene can be regulated by multiple enhancers, while individual enhancers can regulate multiple genes [168, 170–172]. Based on models where enhancer and promoter come into close spatial proximity to exchange information, chromosome conformation capture (3C) methods such as 4C [248, 249], Hi-C [9] or capture Hi-C [171] can be used to match putative enhancers to their target promoters.

Chromatin interaction data has enabled the genome-wide identification of E-P loops [11, 250–252], mapping of regulatory networks [249, 253, 254], and tracking of E-P rewiring during differentiation [235, 252, 255]. Microscopy-based approaches provide complementary insights that address key limitations of sequencing-based methods. While 3C-based methods are only able to detect interactions within their capture radius, methods like fluorescence in situ hybridization (FISH) enable measurement of 3D distances between regulatory elements at single-cell resolution, regardless of proximity. FISH also offers information about the nuclear localization of selected loci. Furthermore, live-cell imaging captures the highly dynamic nature of E-P interactions in real time, providing temporal information that is lost in population-averaged snapshots from chromatin interaction data.

1.4.1 Sequencing-based approaches

Epigenomic data for identifying enhancers

Chromatin immunoprecipitation followed by high-throughput sequencing (ChIP-seq) [256, 257] has been widely used to identify TFs, co-activators, and histone modifications associated with active enhancers. For ChIP-seq, chromatin is first crosslinked with formaldehyde, which creates covalent bonds between DNA and associated proteins

(Figure 5A). The chromatin is then fragmented, either by sonication or enzymatic digestion, and immunoprecipitated using an antibody against the protein of interest (such as a TF or a histone with a specific modification). Subsequently, the crosslinking is reversed, the DNA is purified, the library is prepared (indexing and adapter ligation) and sequenced. Regions enriched for the protein of interest are identified computationally. ChIP-seq studies have revealed that active enhancers are frequently bound by the transcriptional co-activator p300 [163], which has previously been used to annotate enhancers [244, 258, 259]. However, not all enhancers are p300-dependent, prompting the use of histone modifications as a more universal marker. Active enhancers typically display both H3K27ac and H3K4me1, whereas active promoters are marked by H3K27ac and H3K4me3 [260–263]. Poised enhancers, characteristic of developmental transitions, exhibit H3K4me1 together with the repressive mark H3K27me3 [262, 264–266]. Consequently, H3K27ac commonly serves as the primary marker for identifying active enhancers, sometimes combined with H3K4me1 for increased specificity [261, 262, 267–269].

Another characteristic of active enhancers is the depletion of nucleosomes, which results in higher chromatin accessibility. Methods for probing chromatin accessibility, like DNase I hypersensitive sites sequencing (DNase-seq) [270] and assay for transposase-accessible chromatin using sequencing (ATAC-seq) [271], are therefore also widely used to identify putative enhancers. DNase-seq relies on nucleases like DNase I to cleave accessible chromatin at DNase hypersensitive sites, while regions bound by proteins such as histones or TFs are protected from digestion (Figure 5B). After digestion, linkers are added to the cut DNA fragments to enable sequencing [270, 272]. ATAC-seq modified the DNase-seq protocol by employing a Tn5 transposase carrying sequencing adapters. Tn5 simultaneously fragments and tags accessible DNA, eliminating the need for separate digestion and adapter ligation steps, which greatly shortens the protocol [271, 272]. While both methods can achieve basepair resolution, DNase-seq generally performs better, as footprinting efficiency of the Tn5 transposase is significantly lower than that of DNase I for most TFs. However, ATAC-seq is still usually preferred, as the protocol is faster and requires less input material [273]. Chromatin accessibility is a less biased predictor of *cis*-regulatory sequences than ChIP-seq-based methods, as it does not rely on specific TFs, co-factors, or histone modifications. It is less specific though, as it cannot distinguish between different types of regulatory elements, and open chromatin is not necessarily active. Therefore, chromatin accessibility is particularly powerful in predicting active enhancers when integrated with ChIP-seq data [260, 272].

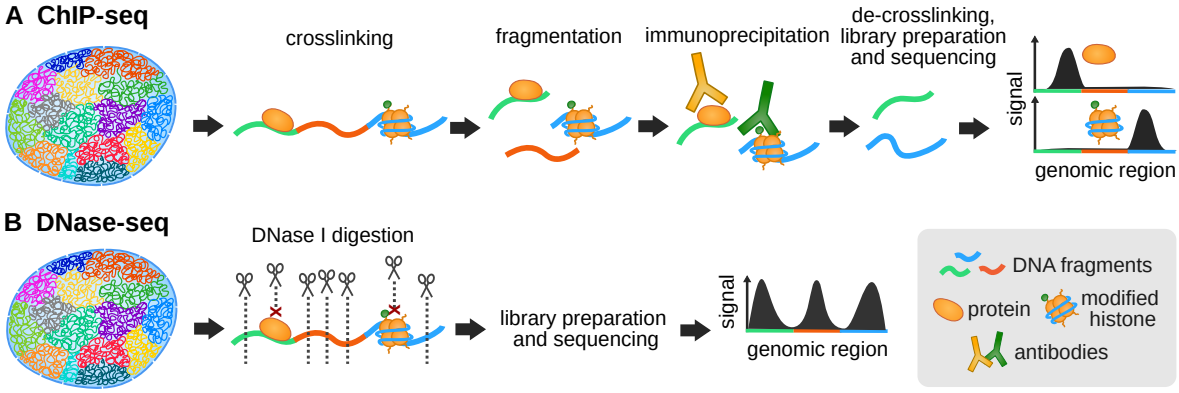

Figure 5: ChIP-seq and DNase-seq workflow. (A) In ChIP-seq, chromatin is fixed with formaldehyde, crosslinking DNA with associated proteins. Chromatin is then fragmented, immunoprecipitated for the protein of interest, de-crosslinked, and the purified DNA is sequenced. (B) DNase-seq relies on DNase I to cleave accessible chromatin at DNase hypersensitive sites, while regions bound by proteins are protected. After purification of cut DNA fragments, a library is prepared and sequenced.

It is important to note, however, that enhancer predictions using these methods are based on correlative data. The presence of particular histone modifications or chromatin features is not necessarily indicative of functional enhancers. Moreover, no currently known histone modification, or even combination of modifications, correlates perfectly with active enhancers [260, 261, 272] and some active enhancers even lack characteristic modifications like H3K27ac and H3K4me1 [261, 272]. Therefore, despite being much lower throughput, functional validation using *in vitro* reporter assays or transgenic animal models is still needed to identify functional enhancers [272]. Nonetheless, ChIP-seq and chromatin accessibility-based predictions provide valuable tools to identify putative enhancers genome-wide. To determine which genes the putative enhancers regulate, such predictions can be integrated with chromatin interaction data.

Contact data for identifying E-P interactions

Contact models of E-P interactions posit that enhancers and promoters are brought into close spatial proximity to interact. Therefore, methods used to study chromosome interactions have been widely used to both identify and investigate E-P interactions [272]. A variety of these methods will be discussed below.

The first method capable of mapping the spatial proximity of all genome sequences relative to each other was spearheaded by the establishment of chromosome conformation capture (3C) by Dekker et al. in 2002 [250]. In 3C, a population of cells is chemically

fixed with formaldehyde to capture protein-mediated DNA-DNA contacts (Figure 6). Subsequently, the chromatin is fragmented with a restriction enzyme, and restriction fragments that were spatially close are ligated, creating a 3C library. The contact frequency between two loci of interest is then quantified by polymerase chain reaction (PCR) using a pair of corresponding primers [274]. In one of its first applications, 3C was used to explain that distal enhancers regulate the β-globin cluster during erythroid differentiation through chromatin looping [275, 276]. However, since 3C focuses on interaction between only two loci ("one-to-one"), throughput is relatively low and prior knowledge of the regions of interest is required. To assay frequencies between multiple genomic loci, a series of derivative methods was developed [274].

Chromosome conformation capture-on-chip [248] and circular chromosome conformation capture [249] (4C) were the first methods to improve the throughput and resolution of 3C. 4C enables mapping of interactions between a locus of interest (the "viewpoint"), such as a promoter, and all loci in the genome ("one-vs-all"). Generally, 4C methods use viewpoint-specific primers to amplify ligation products between the viewpoint and the rest of the genome, which are then quantified using either sequencing or microarrays [1, 274]. Some initial applications of 4C included identifying HoxB1-associated loci in mESCs [277], investigating control of imprinting via a distal IGF2 enhancer [249], and formation of active and inactive domains at the globin loci [248]. Since then, 4C has been widely used to investigate regulatory interactions [278–285]. However, 4C is still restricted to predefined viewpoints.

This limitation has been overcome with the development of Hi-C [9], a high-throughput sequencing method which can capture interactions across the entire genome ("all-vs-all"). Following chemical fixation with formaldehyde and digestion with a restriction enzyme, the fragment ends are biotinylated before ligation. The exonuclease activity of T4 DNA polymerase then removes biotin from unligated ends, ensuring that only successful ligation products retain the biotin label. After DNA purification and sonication, biotinylated junctions are enriched via streptavidin pulldown, eliminating uninformative, unligated fragments from the library. Finally, ligation junctions corresponding to chromatin interactions are identified using paired-end sequencing.

Hi-C is the most commonly used approach to capture chromatin interactions genome-wide [274]. Early versions with a resolution between 40 kb to 1 Mb [1] enabled the discovery of chromatin compartments [9] and TADs [15]. Subsequent technical refinements dramatically improved the resolution of Hi-C, enabling the mapping of chromatin loops and regulatory interactions. For example, the original Hi-C protocol uses sodium

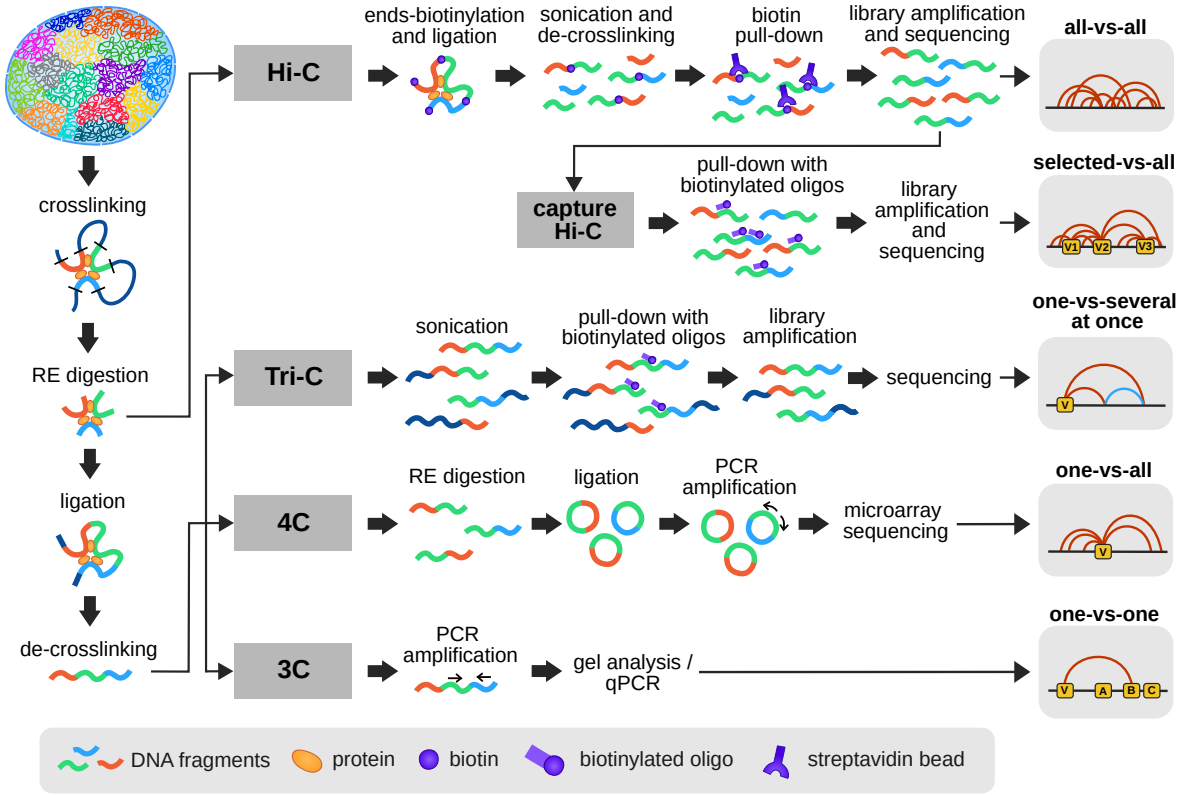

Figure 6: Common chromosome conformation capture workflows and resulting contact information. 3C captures pairwise contacts between individual loci (one-vs-one), while 4C detects contacts between one region of interest (viewpoint) and the rest of the genome (one-vs-all). Tri-C captures contacts between the viewpoint and exactly two other regions of interest (sometimes more) simultaneously. Hi-C captures pairwise contacts between all regions of interest (all-vs-all), while capture Hi-C enriches for specific viewpoints, like all promoters in the genome (selected-vs-all).

dodecyl sulfate (SDS) to permeabilize the nuclear membrane, which causes ligation to occur partially in solution rather than *in situ*. By omitting SDS treatment to reduce background signal and using a restriction enzyme that cuts more frequently, Rao et al. 2014 [11] achieved kilobase resolution. The generated interaction maps enabled systematic identification of approximately 10000 chromatin loops across the genome, revealing that 86% of loop anchors are bound by CTCF. Using the same *in situ* Hi-C approach with ultra-deep sequencing, Bonev et al. 2017 [252] observed global reorganization of A/B compartments and TADs, as well as rewiring of E-P interactions during mouse neural differentiation. Micro-C [23, 253, 286] further improves resolution by replacing restriction enzyme digestion with Micrococcal Nuclease (MNase) fragmentation. This achieves nucleosome-level resolution, which is ideal for capturing local chromatin folding and E-P interactions in even more detail.

Despite these improvements, high-resolution chromatin interaction maps still require

deep sequencing, which is prohibitively expensive at a genome-wide scale [274]. To address this, targeted enrichment methods such as Capture-C [287] and Capture Hi-C [171] have been developed in parallel. These approaches use biotinylated oligonucleotides (oligos) to capture ligation products involving specific regions of interest, which are then sequenced more deeply. For example, Promoter Capture Hi-C has been used to map genome-wide, long-range promoter interactions across different human and mouse cell types [255, 288]. Combining high resolution with targeted enrichment, a recent study using Region Capture Micro-C generated the deepest 3D genome maps to date [127]. These maps revealed previously unresolvable patterns of highly nested and focal 3D interactions, predominantly between active regulatory elements, suggesting that enhancers and promoters form highly connected, multiway interaction hubs. Notably, many of these interactions are CTCF- and cohesin-independent.

While Region Capture Micro-C offers excellent resolution for detecting multiple E-P interactions, it can, like other conformation capture methods, primarily only capture pairwise contacts. Therefore, whether these multiway interactions occur simultaneously in single cells can only be inferred. Tri-C was developed to directly identify such simultaneous interactions between exactly three regions. Following crosslinking, chromatin is digested with a restriction enzyme, typically *NlaIII*, to generate small fragments (∼150-250 bp) centered on the viewpoint of interest. The fragments are then proximity-ligated. Compared to other capture methods, gentler sonication is used to generate longer fragments which have a higher probability to contain multiple ligation junctions. Subsequently, biotinylated oligonucleotides are used to enrich for the viewpoint of interest and the ligation junctions are identified with long-read sequencing [168, 289]. Using Tri-C, Oudelaar et al.[168] directly demonstrated the existence of higher-order regulatory hubs in which multiple enhancers and promoters interact simultaneously. Multiway hubs at the -globin loci were highly enriched in erythroid cells compared to ESCs, revealing their role in cell type specific gene regulation.

Chromatin contacts can be mediated by different proteins, including architectural proteins, chromatin remodellers and TFs. To map chromatin interactions associated with specific proteins, different methods have combined ChIP-seq with Hi-C. Chromatin interaction analysis by paired-end tag sequencing (ChIA-PET) [251] starts with fixing a population of cells, followed by sonication, ChIP-seq against the protein of interest and subsequent proximity-ligation. While sonication before proximity ligation ensures efficient protein pull-down, it is unclear whether the chromatin structure remains preserved [1, 274]. Alternative approaches like Hi-ChIP [290] and proximity ligation-assisted chromatin immunoprecipitation sequencing (PLAC-seq) [291] perform

proximity-ligation first, followed by sonication and subsequent ChIP-seq. These methods have been used to map networks associated with RNAPII, CTCF and TFs [1, 290, 292, 293].

Standard conformation capture methods provide population-averaged contact data. While these measurements are highly reproducible across cell types, they do not always accurately represent the complex, heterogeneous chromatin organization in individual cells [56, 294–296]. Large-scale structures, such as chromatin compartments, appear consistent across cells [297]. In contrast, single-cell Hi-C [54, 55] and super-resolution imaging studies [56, 57] have revealed that smaller structures, such as TADs and loops, are highly variable. This is especially true for E-P interactions, which are transient and occur only in a small fraction of cells at a time [40, 114, 117, 118, 298]. Single-cell Hi-C methods [54, 299] therefore provide a powerful approach for studying chromatin organization in contexts where cell-to-cell variation is important. Applications include characterizing rare cell types [55], tracking dynamic changes in chromosome contacts throughout the cell cycle [274, 300], and resolving cell-type-specific regulatory interactions during differentiation [169]. It is worth noting that chromatin organization in single cells can also be studied using imaging-based methods, which will be discussed in Section 1.4.2.

Ligation-based methods are inherently limited to detecting pairwise interactions, or at most three-way interactions (Tri-C), because each DNA fragment can only ligate with one or two partners. Ligation-free methods overcome this limitation by capturing the entire crosslinked complex [274]. Like conformation capture, split-pool recognition of interactions by tag extension (SPRITE) still relies on fixation and fragmentation of chromatin. Instead of proximity ligation, the crosslinked chromatin is split into a 96 well plate, each marked with a unique barcode. The indexed chromatin is then pooled and the process of splitting, barcoding and pooling is repeated several times. Only the fragments within the same crosslinked complex will acquire the same combination of barcodes [301]. Genome architecture mapping (GAM) takes a different approach [167]. In GAM, fixed nuclei are embedded in sucrose and frozen, before slicing them in $\sim$220 nm slices using ultra-thin cryosectioning. Individual slices are then isolated using laser microdissection. DNA from each slice is amplified and indexed before sequencing. Chromatin contacts between pairs of DNA loci can be inferred by counting how often two loci occur in the same section [274]. Although SPRITE and GAM are orthogonal methods, their findings are remarkably consistent. Both methods not only recapitulate the TADs and loops observed in Hi-C data, but also uncover multi-enhancer hubs associated with highly transcribed regions and reveal previously undetected long-range

E-P interactions [167, 274, 301].

Computational prediction of enhancer - promoter pairs

A variety of computational approaches have been developed to predict E-P pairs from multi-omics datasets, including methods based on correlation, supervised learning, regression, and various other scoring metrics. These approaches rely on integrating different features, such as E-P distance, gene expression, chromatin marks, chromatin accessibility, TF binding, co-activator binding, methylation, sequence, and eRNAs [244]. While reviewing all these methods would be beyond the scope of this chapter (for comprehensive reviews see Gong et al. [302] and Hariprakash et al. [244]), an overview of some of the most common approaches is provided below.

Correlation-based approaches rely on the assumption that the activity of an enhancer and its target gene are correlated across different cell types [244]. Enhancer activity can be estimated from ChIP-seq of active chromatin marks such as H3K4me1 or from chromatin accessibility measured by DNase-seq. Promoter activity can be inferred from RNA-seq or RNAPII ChIP-seq data [268, 303–306]. Correlation-based approaches are able to detect multiple targets of an enhancer and quantify the strength of association for each one. However, they require genomic data of comparable quality and resolution across many different cell types to do so. Furthermore, correlation-based methods face challenges with rare cell types, such as those present only during short developmental transitions. While E-P pairs may show high correlation due to the enhancer's high cell type specificity, the limited number of data points can also lead to spurious correlations and false positives [244].

Supervised learning-based approaches require a known set of true positive and true negative E-P pairs. These sets are used to train a classifier, such as a random forest or a decision tree, based on a variety of features. The features often include measures of gene expression, histone marks, and chromatin accessibility, acquired by the methods described above, as well as a measure of E-P proximity derived from chromatin interaction data [244, 307–311]. Once trained, the classifier can be used to predict E-P pairs in the cell type of interest. The key limitation of supervised learning-based approaches is how to define the true positive and true negative sets. Relying solely on chromatin interaction data can prove problematic, as contact alone does not provide information about enhancer function [312–314]. Conversely, the absence of contact in a Hi-C map does not necessarily define a true negative. This is nicely demonstrated by advancements in chromatin interaction methods: Goel et al. [127] and Quinodoz et al. [301] have both observed E-P interactions that were previously not detectable with

Hi-C.

The approaches described above are only able to examine pairwise E-P interactions. However, a gene is often regulated by multiple enhancers. Regression-based methods can quantify the relative contribution of each enhancer to the overall activity of a gene, based on a selection of features. In an example of a simple regression model, the gene activity (measured by methods like RNA-seq or CAGE-seq) represents the dependent variable, while the activity of each enhancer (consisting of features such as histone marks or chromatin accessibility), serves as the independent / predictor variable. Regression-based methods are often combined with other methods for enhancer prediction [244]. For example, in 2014, the FANTOM consortium combined a regression-based approach with Pearson's correlation to create an atlas of active enhancers across different human cell types and tissues [97]. Notably, the best-performing E-P prediction model to date, featured in the newest ENCODE preprint, combines regression with supervised learning [315]. The created logistic regression classifier compiles 13 molecular features, including DNase-seq signal, Hi-C contact frequency, Activity-by-Contact (ABC) model score, genomic position, promoter class and information about nearby enhancers.

Other recent approaches have implemented their own custom scoring metrics to assign enhancers to their target genes. One of the most widely integrated databases for human enhancers, GeneHancer [316], combines enhancers from different sources such as ENCODE, Ensembl, RefSeq, FANTOM5 and VISTA. It defines a score for enhancer confidence based on agreement between sources, sequence conservation, TF binding, functional validation and eRNAs. It is also worth mentioning the ABC model [165], which was the second best performing model in the ENCODE study [315]. The ABC model first uses chromatin accessibility data to define candidate enhancer regions, then identifies active enhancers based on H3K27ac ChIP-seq peaks within those regions, and finally links enhancers to promoters using Hi-C contact data. Only genes that are actively transcribed in the investigated cell type, as determined by RNA-seq, are considered. An enhancers quantitative effect on the expression of a gene (ABC score) is calculated by weighing enhancer activity A_E with E-P contact frequency $C_{E,G}$, relative to the effect of all other enhancers within 5 Mb, using the following formula:

$$ABC\,\text{score}_{E,G} = \frac{A_E \times C_{E,G}}{\sum_{\text{all elements } e \text{ within } 5\,\text{Mb of } G} A_e \times C_{e,G}}$$

where the activity A of an enhancer E is estimated as the geometric mean of all read

counts of DNase-seq and H3k27ac ChIP-seq, the contact C as the KR-normalized Hi-C contact frequency between E and the promoter of gene G at 5-kb resolution [165].

1.4.2 Microscopy-based approaches

Principles of fluorescence microscopy

Fluorescence is the emission of light by an atom or a molecule, nanoseconds after absorbing light of a shorter wavelength [317]. Fluorescence microscopy exploits this property to visualize cellular components that would otherwise be indistinguishable under conventional light microscopy, by labeling them with fluorescent molecules, known as fluorophores. Fluorophores include fluorescent proteins, small organic fluorescent dyes, and quantum dots, each with differing properties [318]. The process of fluorescence can be depicted in the form of a Jablonski diagram (Figure 7A) [319]. When a fluorophore is not excited by light, it resides in the "ground state" (S_0). Upon absorbing light energy (photons), an electron of the fluorophore's outer shell is sometimes moved to a higher orbital, known as the "excited state" (S_1 / S_2). This happens within the order of femtoseconds. Shortly after, the fluorophore returns to the low-energy ground state by dissipating the absorbed energy, most commonly in the form of vibrational relaxation and fluorescence emission. Since some of the absorbed energy is lost through non-radiative processes such as internal conversion, collisional quenching or vibrational relaxation, the emission wavelength is longer than the excitation wavelength [318]. This difference in wavelengths is known as the Stokes shift (Figure 7B) and is the key property that makes fluorescence microscopy such a powerful tool. It allows selective detection of emitted photons while filtering out the excitation light, visualizing only fluorescent objects [317].

The minimal energy required for fluorescence corresponds to the energy needed to elevate an electron from its ground state S_0 to its lowest excited state S_1. If a fluorophore absorbs more energy than is necessary to reach S_1, the fluorophore will undergo changes in vibration, rotation, and/or move to an even higher electronic orbit (S_2). Therefore, a fluorophore can be excited by a range of wavelengths. However, not every fluorophore absorbs energy equally well. The ability of a fluorophore to absorb energy is measured by the molar extinction coefficient ε. Under otherwise same conditions and molecule properties, molecules with higher ε values appear brighter than those with lower ε when excited by the same light intensity. Higher extinction coefficients are particularly useful when minimizing light exposure is important, for example when imaging live cells [317].

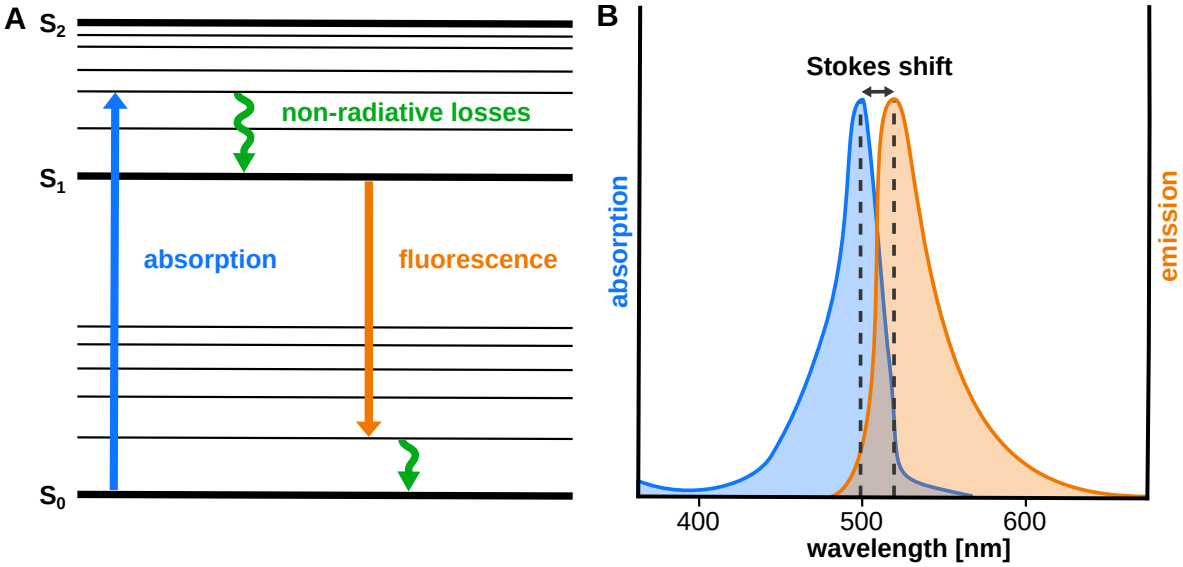

Figure 7: Basic principles of fluorescence microscopy. (A) As simplified Jablonsky diagram showing energy states of a fluorophore. When a ground state (S_0) fluorophore absorbs light, an electron of a fluorophore's outer shell moves to one of the excited states (S_1 / S_2). The flourophore returns to the ground state by dissipating energy between S_2 and S_1 though non-radiative processes, and between S_1 and S_0 by emitting fluorescence. (B) Absorption and emission spectra of ATTO488. The difference between the absorption and emission peak is called the Stokes shift.

Once excited, a fluorophore can dissipate the absorbed energy through different mechanisms. The energy difference between S_2 and S_1 is lost via non-radiative processes. A good fluorophore emits the remaining energy between S_0 and S_1 in the form of a photon. The emission spectrum of a fluorophore corresponds to the different possible wavelengths of this emitted photon. Since the emission starts from the lowest S_1 level, the energy of the emitted photon is usually less than the one of the absorbed photon. The energy difference is lost through non-radiative processes and is responsible for the Stokes shift. Larger Stokes shifts are generally desirable, as they allow the excitation and emission light to be separated more easily [317]. How efficiently a fluorophore can convert the absorbed light into fluorescence is quantified by the quantum yield: a ratio between the number of emitted photons and number of absorbed photons. Quantum yields closer to 1 indicate a more efficient conversion and are generally better. Together with the molar extinction coefficient, quantum yield serves as a useful metric for predicting fluorophore brightness and comparing different fluorophores [318].

When imaging multiple fluorophores within the same sample, it is essential that signals from different fluorophores can be separated reliably. This can prove challenging, as the excitation and emission spectra are very broad (50-150 nm), typically limiting the

number of fluorophores that can be used simultaneously to 4-6. Different strategies address this limitation. Synthetic organic chemistry has produced a wide variety of fluorophores, allowing researchers to select and combine those with minimal spectral overlap [318]. Spectral imaging greatly increases multiplexing capacity (up to ∼10 fluorophores) by recording the complete emission spectrum at each pixel and computationally resolving overlapping signals through linear unmixing [320]. Alternatively, imaging can be performed sequentially through cycles of staining, imaging, fluorophore removal, and re-staining with new labels against different targets, typically for 10, in special cases for up to 130 cycles [56, 321].

Another important attribute of fluorophores is photostability. Although fluorophores can, in principle, be excited and reverted to their ground state indefinitely, environmental factors typically limit their lifespan to 10000-40000 cycles before irreversible loss of fluorescence occurs [317]. This phenomenon, known as photobleaching, results from photochemical destruction due to light exposure and is generally undesirable as it degrades image quality over time. Strategies to mitigate photobleaching primarily focus on chemical redesign of the fluorophore, manipulation of the surrounding environment, and optimization of imaging technique. Structural redesign of the fluorophore can enhance brightness, reduce the generation of reactive oxygen species, or introduce greater rigidity to resist photochemical degradation [318, 322]. The sample medium can also be supplemented with anti-fading agents (such as DABCO) that promote non-destructive decay from the excited state, or with oxygen scavenging systems (such as glucose oxidase and catalase) that deplete oxygen, which catalyzes photodegradation [322, 323]. Finally, the imaging parameters can also be optimized to minimize illumination intensity and exposure time. While most approaches aim to prevent photobleaching, some microscopy techniques, such as fluorescence recovery after photobleaching (FRAP) [324, 325], deliberately exploit this phenomenon to study molecular dynamics. In FRAP, a defined region of the sample is photobleached using the laser of a confocal microscope, and the subsequent recovery of fluorescence is measured as unbleached fluorophores diffuse into the bleached area from the surroundings.

Unlike photobleaching, quenching leads to reversible loss of fluorescence through noncovalent interactions between a fluorophore and its molecular milieu [317]. Quenching can be either static or dynamic. Static quenching occurs when a fluorophore forms a non-fluorescent complex with a quencher molecule. Although static quenching reduces overall fluorescence intensity of the sample, the fluorescence lifetime of the non-complexed molecules remains unchanged. Dynamic quenching involves a collision between the quencher and an excited fluorophore. This collision provides a non-radiative pathway

for energy dissipation that returns the fluorophore to its ground state. In contrast to static quenching, dynamic quenching shortens the fluorophore lifetime and decreases the overall intensity of the sample, as fluorophores are returned to the ground state without emitting a photon. Förster resonance energy transfer (FRET) is a type of dynamic quenching where energy is transferred from an excited state donor to a ground state acceptor molecule. As donor and acceptor molecules have to be within 10 nm of each other, FRET is highly sensitive for measuring distances, which has been leveraged by microscopy [326]. Biological applications include protein-protein interactions, chromatin interactions and Ca^{2+} signaling [327–330].

Super-resolution microscopy

Fluorescence microscopy has played a pivotal role in advancing our understanding of the molecular organization and interactions of biological systems. This is enabled by two key properties: the ability to directly visualize specific cellular structures by labeling them with fluorophores, and the technique's low invasiveness, which allows studying these structures in living cells without significantly disrupting their function. However, the resolution of conventional fluorescence microscopy is limited to ∼200 - 250 nm due to the diffraction of light. Since many cellular structures are separated by distances smaller than this limit, they cannot be resolved using conventional methods [331, 332]. Super-resolution microscopy has overcome this barrier, enabling numerous biological discoveries, including insights into chromatin organization and compaction [66, 295, 333–336], cellular structures [337–342], and biomolecular dynamics [343–348]. Different super-resolution approaches can be broadly divided into two main categories [332].

The first category uses patterned illumination to selectively excite molecules within a sample, thereby separating the detection of these molecules in time [332]. The most common example in this category is stimulated emission depletion (STED) microscopy [349]. In STED, fluorophores are first excited using a focused excitation beam. Excited fluorophores can then return to the ground state through either spontaneous fluorescence emission or stimulated emission induced by a high-power STED laser. The STED laser is shaped like a doughnut with 'zero'-intensity at the center, which selectively depletes fluorescence everywhere except at the center (Figure 8). This allows only molecules at the undepleated core of the beam to emit light, thereby confining fluorescence emission to a region much smaller than the diffraction-limited focal spot of conventional light microscopy. In theory, STED microscopy can achieve resolutions down to the size of a single molecule. In practice, however, the signal-to-noise

ratio limits the resolution in biological samples to 50 - 60 nm. As stimulated emission requires a high light intensity, this high resolution comes at the cost of problems like photobleaching and phototoxicity [332, 350, 351]. Alongside other solutions like creating more stable fluorophores, approaches like reduction of state transition cycles (RESCue) [352] and MINFIELD [353] aim to reduce these problems by minimizing illumination. RESCue restricts STED illumination to regions containing fluorophores through a conditional sampling approach. Each pixel is first probed with a brief illumination pulse, and the STED beam is applied for the remainder of the pixel dwell time only if sufficient fluorescence signal is detected. Similarly, MINFIELD restricts the use of the STED illumination by first acquiring a low-resolution confocal image and then only applying the STED laser to the identified regions of interest. DyMIN combines the RESCue and MINFIELD approaches to reduce illumination in biological samples for up to 20-fold [354].

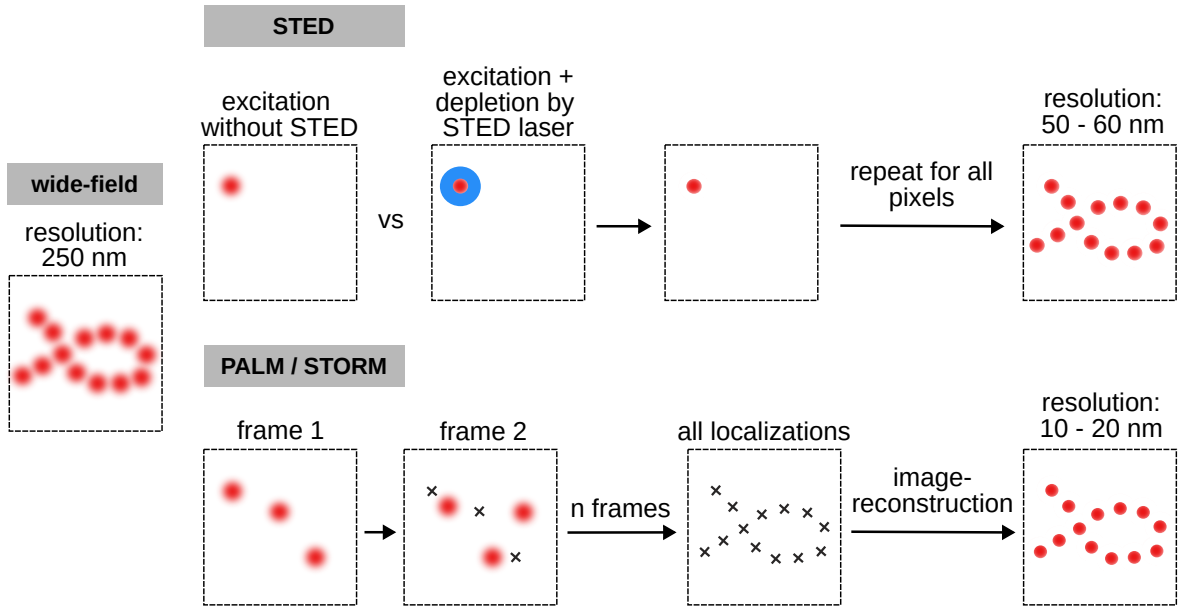

Figure 8: Most common super-resolution microscopy methods. Diffraction-limited fluorescence microscopy provides a spatial resolution of ∼250 nm. Stimulated emission depletion (STED) microscopy overcomes this limitation by using patterned illumination in the form of a doughnut-shaped depletion beam (blue), which selectively depletes fluorophores at the periphery while allowing those at the center to fluoresce. This effectively reduces the point spread function (PSF) and achieves a resolution of about 50–60 nm. Photoactivated localization microscopy (PALM) and stochastic optical reconstruction microscopy (STORM) enhance resolution by stochastically activating sparse subsets of photoswitchable fluorophores over thousands of frames. The localizations obtained from individual frames are then combined to reconstruct a super-resolved image with a resolution of up to 10–20 nm.

The second category of super-resolution approaches, termed single-molecule localiza-

tion microscopy (SMLM), achieves temporal separation of molecules by stochastically activating random subsets of photoswitchable molecules at different time points (Figure 8) [332]. Prominent examples of SMLM include (fluorescence) photoactivated localization microscopy ((f)PALM) [355, 356] and stochastic optical reconstruction microscopy (STORM) [357]. Both methods acquire thousands of images from the same field of view, each capturing a different sparse subset of active fluorophores. A high-resolution image is then reconstructed by combining the molecular localizations across all frames. PALM and STORM differ mainly in their fluorophore switching mechanisms. While PALM uses photoactivation, where fluorophores are switched on and subsequently bleached, STORM uses photoswitching, where fluorophores can be switched between the on and off state. Similarly, point accumulation for imaging in nanoscale topography (PAINT) [358, 359] uses transient binding of fluorescent probes to generate sparse labeling over time. SMLM approaches can usually achieve a resolution of 10 - 20 nm [332, 351]. Minimal (fluorescence) photon flux (MINFLUX) [360] combines the sparse labeling from SMLM with structured illumination to reach single-nanometer localization precision, offering higher temporal resolution while requiring far fewer photons than conventional methods. This is achieved by using a doughnut-shaped excitation beam with a zero-intensity center. When the zero-intensity center is aligned with a fluorophore, the fluorophore does not emit, allowing its exact position to be inferred. Special techniques like resolution enhancement by sequential imaging (RESI) [361] can achieve an even better resolution of a few Ångström.

1.4.3 Fluorescence in situ hybridization

The most widely used method for visualizing chromatin contacts in fixed cells is DNA fluorescence in situ hybridization (DNA FISH). FISH involves hybridizing a collection of fluorescently labeled oligonucleotides (oligos) to a genomic region of interest, followed by fluorescence microscopy. Together with high-throughput super-resolution microscopy and 3C-based methods, FISH has expanded our understanding of 3D genome organization and E-P interactions [58, 274]. For example, chromatin tracing has revealed that loops and TADs clearly visible in Hi-C maps, are highly variable at the single-cell level and present only in a small subset of cells [56, 57]. The spatial dynamics of several E-P pairs during differentiation have also been dissected, showing that cell-type specific enhancers can exhibit either increased or decreased spatial proximity to their cognate promoters, depending on the locus [116, 125, 140, 362]. Furthermore, advances in multiplexed imaging have enabled the simultaneous visualization of E-P contacts, nascent transcripts and / or proteins [8, 128, 141, 321, 363, 364], revealing that E-P proximity only weakly correlates with nascent transcription [128, 141,

363]. The following section outlines the basic principles of FISH and highlights recent technical developments together with current limitations.

Probe design

The first important step in FISH is the choice of probe. Depending on their application, DNA FISH probes can target whole chromosomes, repetitive sequences, or specific genomic loci. Chromosome painting employs a pool of chromosome-specific probes that hybridize to cytological preparations, enabling the visualization of chromosomal aberrations and the spatial organization of chromosome territories [365, 366]. Other probes are designed to bind highly repetitive sequences such as those found in telomeres, centromeres, and satellite DNA, making them particularly useful for detecting aneuploidies [367]. Locus-specific probes, in contrast, allow the detection of structural variations such as translocations, deletions, and inversions [368], and have more recently been applied to studying chromatin contacts. Additionally, RNA FISH probes can be designed to target either nascent RNA or mRNA. Here, I will focus on designing locus-specific DNA FISH probes for studying E-P interactions.

Modern FISH techniques use synthetic pools of oligos as source material for probes [369]. A variety of computational tools, including OligoMiner [370], iFISH4U [371], ProbeDealer [372], Chorus2 [373], and PaintSHOP [369], enable efficient design of customized probes with precisely defined properties. When designing FISH probes, several parameters should be considered. First, probe sequences must exhibit high specificity, binding exclusively to the target region without hybridizing elsewhere in the genome or to other probes in the pool. Off-target binding could lead to false-positives, ambiguous signals and elevated background fluorescence. Probe specificity is usually determined by aligning the probe sequences against the whole genome using Bowtie/Bowtie2 or BLAST. Additional specificity is achieved by screening for abundant short sequences that are part of the probe but may be missed by alignment programs, and by masking repetitive sequences using RepeatMasker [369–372].

Second, probes must efficiently hybridize to their targets under experimental conditions. This requires an appropriate melting temperature (T_m), which is directly influenced by GC content (proportion of guanine and cytosine nucleotides). Higher T_m values are usually better, as they enhance binding specificity. The GC content recommended by most tools lies somewhere between 20% and 80%. Probes must also be screened for secondary structures that can inhibit hybridization [369–372].

Third, probes must provide sufficient sensitivity for target detection. Signal intensity

and detection efficiency increase with probe number and density, as more fluorophores can bind within the same region. Achieving adequate probe coverage can prove challenging when target regions contain abundant or repetitive sequences. In such cases, a tradeoff can be made to increase the number of probes. One approach is to increase the probe length (typically 30–50 bp), which can achieve higher density but may reduce specificity. Alternatively, the targeted genomic region can be extended at the expense of spatial resolution. Probes should be distributed as homogeneously as possible to prevent signal splitting. When probes contain multiple readout sequences for fluorophore binding, these should be sufficiently spaced to avoid fluorescence quenching between adjacent fluorophores [369–372].

Probe synthesis

Locus-specific FISH probes were originally produced by cloning chromosomal fragments of interest into bacterial or yeast artificial chromosomes (BACs or YACs), followed by enzymatic labeling through nick translation or random priming [374]. During nick translation, DNase I introduces random single-strand nicks into double-stranded DNA. DNA polymerase I then binds at these sites, using its 5'→3' exonuclease activity to remove nucleotides ahead of the nick while simultaneously incorporating fluorescently labeled nucleotides at the 3' end [375]. In random priming, double-stranded DNA is first denatured, and a mixture of random hexamer primers is added. These primers anneal to the template and are extended by DNA polymerase, incorporating labeled nucleotides to generate newly synthesized, labeled DNA strands [376]. However, these approaches were time consuming and had limited resolution due to the relatively large size of BACs [371].

A major breakthrough in FISH came with the advent of chemically synthesized oligos. Oligo-based probes can be engineered to have specific thermodynamic properties, avoid repetitive sequences and target any region in the genome. They enable the detection of regions several kb in size, significantly improving upon the resolution of BAC-based probes. Moreover, large-scale oligo pools can be generated by massively parallel array synthesis, enabling simultaneous visualization of multiple genomic regions through methods like Oligopaint [377]. Generation of oligo-based probes from a pool involves selective probe amplification through PCR, production of single-stranded DNA through methods like *in vitro* transcription, and subsequent barcoding by reverse transcription (Figure 9A) [378–380]. The complementary barcodes are designed to be orthogonal to both the genome and the probe pool and can be chemically labeled by conjugation with a fluorophore [381–383].

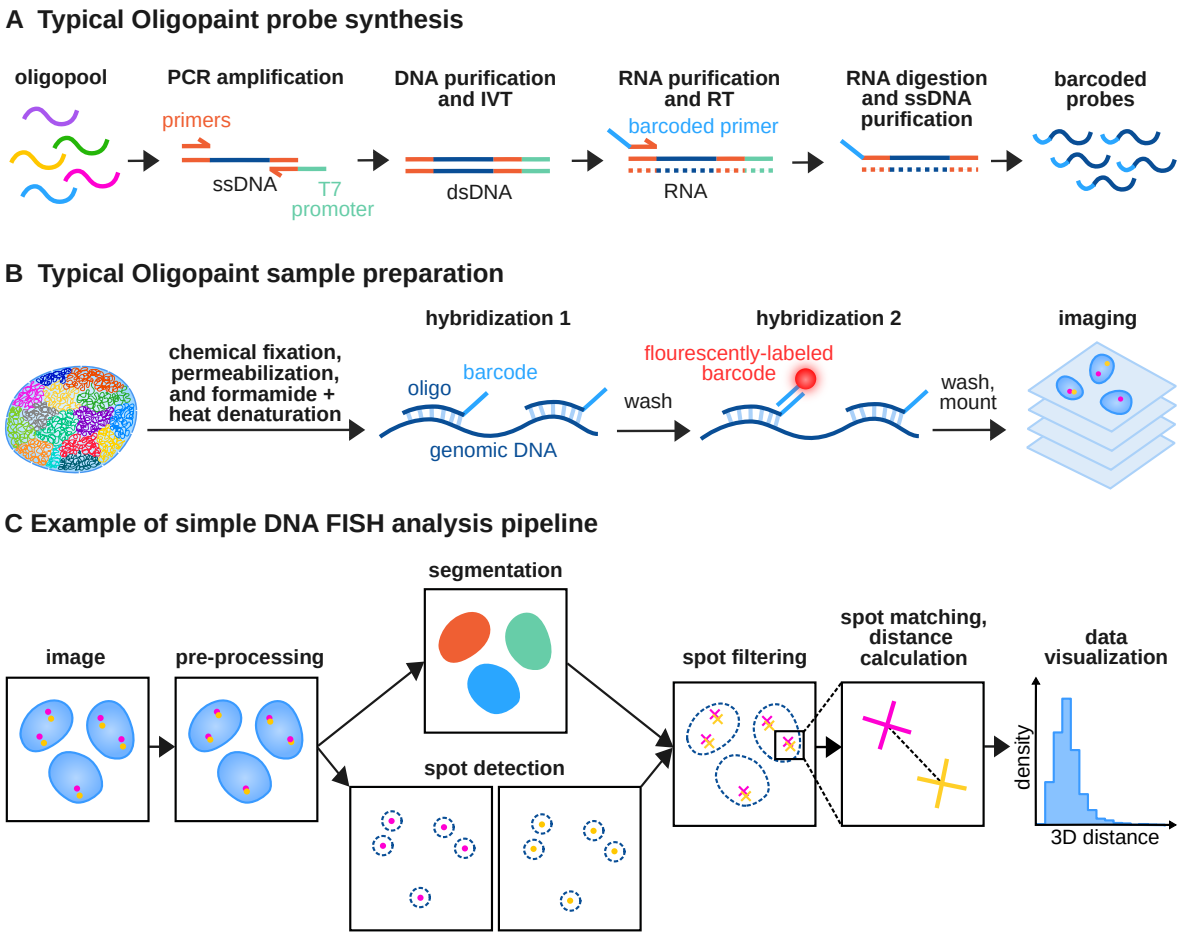

Figure 9: Example of an Oligopaint fluorescence in situ hybridization (FISH) workflow. (A) Oligopaint probe synthesis. Specific probes are amplified from a complex oligonucleotide pool containing thousands of sequences using PCR with probe-specific primers. The resulting double-stranded DNA (dsDNA) is purified and transcribed in vitro (IVT). After RNA purification, reverse transcription (RT) with a barcoded primer produces single-stranded DNA (ssDNA) probes while incorporating a unique readout barcode. Following RNA degradation and ssDNA purification, the barcoded probes are ready for FISH hybridization. (B) Oligopaint sample preparation. Cells are chemically crosslinked, permiabilized and treated with HCl. The DNA is then denatured using formamide and heat, allowing probes to hybridize to genomic DNA overnight. After a series of washes, the probe barcodes are detected by hybridization with complementary fluorescently labeled oligos. Following final washing and mounting, the samples are ready for imaging. (C) Data analysis pipeline. Images are preprocessed, for example by correcting chromatic aberrations and aligning fields from multiple rounds of imaging. Nuclei are segmented, and fluorescent spots are detected. Detected spots are filtered to remove false positives and analyzed quantitatively. For instance, spots from two channels (e.g., enhancer and promoter probes) can be paired and their spatial distances measured. The resulting data are then visualized.

Sample preparation

Despite numerous methodological variations for sample preparation, most DNA FISH protocols share several fundamental steps: chemical fixation to preserve cellular and nuclear structures, permeabilization to allow probes to enter the cell, DNA preparation (eg. heat denaturation) to increase accessibility, followed by a one- or two-step hybridization of fluorescently labeled probes to complementary DNA, and finally, visualization using fluorescence microscopy (Figure 9B). With appropriate modifications, these protocols can also be applied to RNA. Earlier FISH methods employed hypotonic treatment, followed by methanol-acetic acid treatment to fix the cells. As this was shown to flatten the cells and significantly disrupt nuclear architecture, modern FISH protocols typically use formaldehyde-based fixation [384–388], followed by permeabilization. Although permeabilization can be achieved with saponins (such as, saponin and digitonin) or nonionic detergents (such as Triton X-100 or Tween 20), Triton X-100 is preferred for FISH as it effectively permeabilizes the nucleus [389].

Before probes can hybridize to their targets, the double-stranded genomic DNA must be denatured into single strands. This denaturation is facilitated by HCl treatment following permeabilization. Typically, denaturation is achieved through a combination of heat and formamide treatment, where formamide serves to lower the DNA melting temperature. Samples are commonly denatured in 50% formamide at 70 - 80°C for a few minutes [333, 371, 390–393]. These harsh conditions have raised concerns about potential swelling or dispersal of chromatin [391, 393, 394]. Using a FISH protocol optimized for preserving nuclear structure in combination with 3D SIM, Markaki et al [391] showed that larger, characteristic nuclear structures up to the resolution limit of their microscope (∼100 nm) are well preserved. Shim et al. [393], however, found that sub-200 nm chromatin structure is significantly altered during denaturation, predominantly by formamide treatment rather than heat. To enable better preservation of nuclear structure, gentler methods that avoid high heat or formamide, such as combinatorial oligonucleotide (COMBO)-FISH [395], genome oligopaint via local denaturation (GOLD)-FISH [396] and resolution after single-strand exonuclease resection (RASER)-FISH [397] have been developed. One of the first non-denaturing methods, COMBO-FISH, employs bioinformatically designed homopurine/homopyrimidine oligos that bind directly to intact double-stranded DNA via triple helix formation. GOLD-FISH, utilizes a Cas9 nickase to introduce nicks at defined sites on the non-target DNA strand. The superhelicase Rap-X recognizes these nicks and locally unwinds the DNA, exposing single-stranded regions that enable probe hybridization. RASER-FISH, on the other hand, generates single-stranded DNA through global exonuclease III digestion. Be-

fore fixation, cells are treated with BrdU, which is incorporated into replicating DNA. Subsequent UV irradiation induces nicks at BrdU sites, providing entry points for exonuclease III.

After the first round of hybridization, unlabeled oligos require a second hybridization round to generate a fluorescent signal. The primary oligos, complementary to the target genomic region, contain a short barcode that is recognized and bound by a secondary fluorophore-conjugated oligo [58]. Following hybridization, washing to remove unbound probes, and mounting, samples can be imaged using fluorescence microscopy. However, small genomic targets with a low probe abundance, such as enhancers and promoters spanning only a few kb, often suffer from weak fluorescence signals. These signals can be difficult to distinguish from background noise or may fall below the detection threshold of imaging systems. Multiple Oliopaint-based methods have been developed to improve FISH signal and enable imaging at high-resolution. Prominent examples include signal amplification by exchange reaction (SABER)-FISH [364] and hybridization chain reaction (HCR)-FISH [398, 399]. SABER-FISH [364] amplifies signal by extending the primary probe with a long concatemer of barcodes, allowing more fluorescent secondary probes to bind, thereby increasing signal by up to 450-fold. Instead of standard secondary probes, HCR-FISH [398, 399] uses fluorescently labeled hairpins, which self-assemble into long fluorescent polymers at the target site, improving signal by up to 200-fold.

Another major challenge of conventional FISH approaches is the low throughput, which allows only a limited number of targets to be imaged simultaneously [274]. Recent methodological advances have addressed this constraint through the use of sequential hybridization and combinatorial barcoding strategies. Sequential hybridization approaches utilize barcoded primary oligos, each with a unique barcode for a specific target. After labeling all targets with primary oligos in an initial hybridization step, a subset of targets can be detected using barcode-complementary, fluorescently labeled secondary oligos. The sample is then imaged and the secondary oligos are removed, allowing a new subset of targets to be labeled, imaged, and stripped in successive cycles. This process can be repeated multiple times to visualize different targets in the same sample [58]. Methods like ORCA [56] and Hi-M [363] use this approach to trace chromatin in high resolution. Sequential hybridization also enables combinatorial barcoding, where each target is labeled by a unique combination of barcodes. The identity of each locus is decoded from the binary pattern of fluorescence across a series of sequential imaging rounds, allowing the number of hybridization cycles to be reduced by roughly tenfold. Approaches like DNA-MERFISH [8] and DNA-SeqFISH+ [321]

leverage combinatorial barcoding to simultaneously capture information about DNA, RNA, and proteins across thousands of genomic loci.

Data analysis

After the images have been acquired, a quantitative evaluation of the data is necessary. While manually counting individual FISH spots was once common practice, the sheer volume of data generated by modern high-throughput microscopy approaches, particularly those involving multiplexed and sequential hybridization, necessitates automation of the analysis process [400, 401]. A basic FISH analysis workflow might include image preprocessing (such as correcting aberrations or aligning images acquired over multiple rounds of imaging), cell or nucleus segmentation, spot detection, data filtering, quantitative data processing (such as calculating E-P distances), and data visualization (Figure 9C) [8]. Segmentation is commonly performed using tools such as Cellpose [402], CellSeg [403] or CellProfiler [404]. Detection of DNA and RNA FISH spots can be preformed using threshold- and deep-learning-based tools, including RS-FISH [405], FISH-quant v2 [406], deepBlink [407], and U-FISH [408]. Although various Fiji- and Python-based tools are available for different steps of the analysis process, and some FISH analysis pipelines have been developed [401, 409], no universal pipeline exists, as FISH protocols and experimental setups can vary widely [58].

Fixed- vs live-cell approaches

While methodological advances have greatly expanded the capabilities of FISH, fundamental questions about dynamic genomic processes cannot be addressed using fixed-cell approaches alone [410]. Live-cell imaging complements FISH by enabling direct observation of chromatin looping, E-P interactions, and transcriptional activity over time [40, 115, 117, 118, 144]. Critically, live-cell imaging allows quantification of the stability, duration, and kinetics of these transient regulatory interactions [40, 61, 115, 117]. Loci of interest in live cells can be tagged with tandem arrays of DNA-binding sites, enabling visualization through the recruitment of fluorescently labeled cognate DNA-binding proteins [274]. Examples include Lac operator-repressor [411, 412], Tet operator-repressor [413] and ANCHOR systems [414]. More recent approaches use catalytically inactive Cas9 fused to a fluorescent protein, which is recruited to the locus of interest via guide RNAs [415].

1.5 Aim of the thesis

While it is known that enhancers can modulate transcription at their cognate promoters by recruiting RNAPII and TFs, whether physical proximity between enhancers and promoters is required for transcriptional activation remains debated. Furthermore, E-P interactions have traditionally been viewed in a pairwise manner. Although recent sequencing-based studies have highlighted the role of multiple enhancers in regulating gene expression in cell populations, the frequency of multiway interactions between regulatory elements in single cells remains largely unexplored. In this thesis, we combine FISH, STED super-resolution microscopy and Tri-C to investigate changes in E-P distances at two timescales: (i) during the transition from naive to primed pluripotency in mouse and (ii) immediately after transcription. To this end, we develop NOVA FISH - a method capable of visualizing small regulatory elements in close genomic proximity. We then address answer the following questions:

1. How do pairwise E-P distances at *Nanog, Dppa3, Sox2, Dnmt3a,* and *Prdm14* loci change during the naive-to-primed transition?
2. What are the frequencies of multiway E-P contacts at the *Nanog / Dppa3* locus and how do they change during the naive-to-primed transition?
3. Do the E-P distances at the *Nanog / Dppa3* locus correlate with nascent transcription?

Results

2.1 Generation of Densely Labeled Oligonucleotides for the Detection of Small Genomic Elements

Steinek, C., Guirao Ortiz, M., **Stumberger, G.**, Tölke, A. J., Hörl, D., Carell, T., Harz, H. and Leonhardt, H. (2024) *Cell Reports Methods*, 4, 100840.
DOI: 10.1016/j.crmeth.2024.100840

Cell Reports
Methods

Article

Generation of densely labeled oligonucleotides for the detection of small genomic elements

Graphical abstract

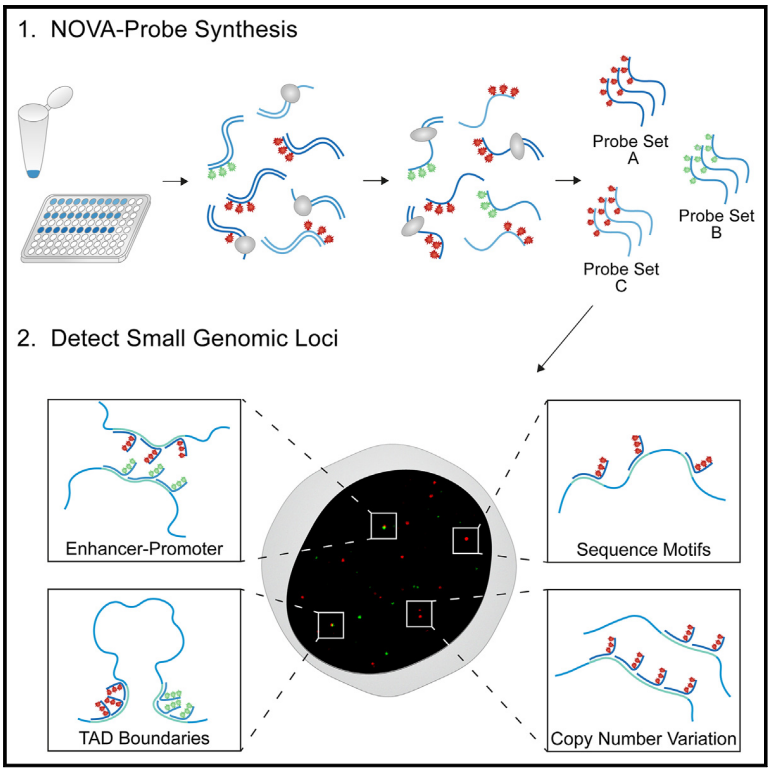

Authors

Clemens Steinek, Miguel Guirao-Ortiz, Gabriela Stumberger, ..., Thomas Carell, Hartmann Harz, Heinrich Leonhardt

Correspondence

steinek@biologie.uni-muenchen.de (C.S.), harz@biologie.uni-muenchen.de (H.H.), h.leonhardt@lmu.de (H.L.)

In brief

Steinek et al. develop a simple workflow for the enzymatic synthesis of densely labeled oligonucleotides. The described approach allows for free choice of fluorophores and flexible adjustment of labeling density to optimize signal detection. NOVA probes enable the detection of sub-kilobase genomic loci using confocal or super-resolution microscopy.

Highlights

- Rapid, flexible, and cost-effective synthesis of densely labeled oligonucleotides
- Systematic analysis of distance-dependent dye-dye interactions
- The NOVA workflow selectively yields labeled probe sets from complex probe pools
- NOVA-FISH enables the visualization of sub-kilobase genomic loci

Steinek et al., 2024, Cell Reports Methods *4*, 100840
August 19, 2024
https://doi.org/10.1016/j.crmeth.2024.100840

CellPress

Cell Reports Methods

CellPress
OPEN ACCESS

Article

Generation of densely labeled oligonucleotides for the detection of small genomic elements

Clemens Steinek,[1,*] Miguel Guirao-Ortiz,[1] Gabriela Stumberger,[1] Annika J. Tölke,[2] David Hörl,[1] Thomas Carell,[2] Hartmann Harz,[1,*] and Heinrich Leonhardt[1,3,*]

[1]Faculty of Biology and Center for Molecular Biosystems (BioSysM), Human Biology and BioImaging, Ludwig-Maximilians-Universität München, 81377 Munich, Germany

[2]Department of Chemistry, Ludwig-Maximilians-Universität München, 81377 Munich, Germany

[3]Lead contact

*Correspondence: steinek@biologie.uni-muenchen.de (C.S.), harz@biologie.uni-muenchen.de (H.H.), h.leonhardt@lmu.de (H.L.)

https://doi.org/10.1016/j.crmeth.2024.100840

MOTIVATION While three-dimensional chromatin conformations can be explored with fluorescence *in situ* hybridization (FISH), the visualization of small genomic loci with high spatial resolution remains challenging. For such applications, programmable oligonucleotides with high brightness are required. To further improve precision and sensitivity, secondary hybridization steps should be omitted. Here, we present a simple, quick, and inexpensive approach to generate labeled FISH probes that carry several fluorophores. Our workflow allows for the free choice of fluorophores, flexible adjustment of labeling density, and selective probe synthesis from large probe pools. With our probes, we reliably detect genomic loci below the kilobase level and examine their topological relationships.

SUMMARY

The genome contains numerous regulatory elements that may undergo complex interactions and contribute to the establishment, maintenance, and change of cellular identity. Three-dimensional genome organization can be explored with fluorescence *in situ* hybridization (FISH) at the single-cell level, but the detection of small genomic loci remains challenging. Here, we provide a rapid and simple protocol for the generation of bright FISH probes suited for the detection of small genomic elements. We systematically optimized probe design and synthesis, screened polymerases for their ability to incorporate dye-labeled nucleotides, and streamlined purification conditions to yield nanoscopy-compatible oligonucleotides with dyes in variable arrays (NOVA probes). With these probes, we detect genomic loci ranging from genome-wide repetitive regions down to non-repetitive loci below the kilobase scale. In conclusion, we introduce a simple workflow to generate densely labeled oligonucleotide pools that facilitate detection and nanoscopic measurements of small genomic elements in single cells.

INTRODUCTION

In recent years, multiple layers of mammalian genome organization ranging from preferential positions of chromosomes in the nucleus to active and inactive compartments and small-scale interactions between individual loci have been uncovered.[1–5] An intricate interplay of chromosome territories, topologically associated domains, and regulatory elements defines cellular identity in development and disease.[6–10] While current methodologies reliably probe pairwise and multi-contact DNA-DNA interactions, deciphering complex 3D chromatin organization in single cells remains challenging, particularly in the kilobase range.[11,12] Thus, there is a growing demand for increased sensitivity to detect and study DNA elements in the 3D context of individual nuclei.

The state of the art for mapping chromatin contacts is chromatin capture assays.[13–17] These methods are especially powerful, as they detect contacts within large-scale genomic regions with a resolution ranging from 1 kb down to the nucleosome level, but typically rely on population averages.[18–20] However, early efforts to probe chromatin contacts in single cells using chromatin capture assays have revealed extensive cell-to-cell variations within the same population.[21–23] Intercell variation of 3D chromatin structures has been observed in multiple imaging studies, which is consistent with the transient nature of chromatin contacts revealed by live-cell imaging.[11,12,24–30] Therefore,

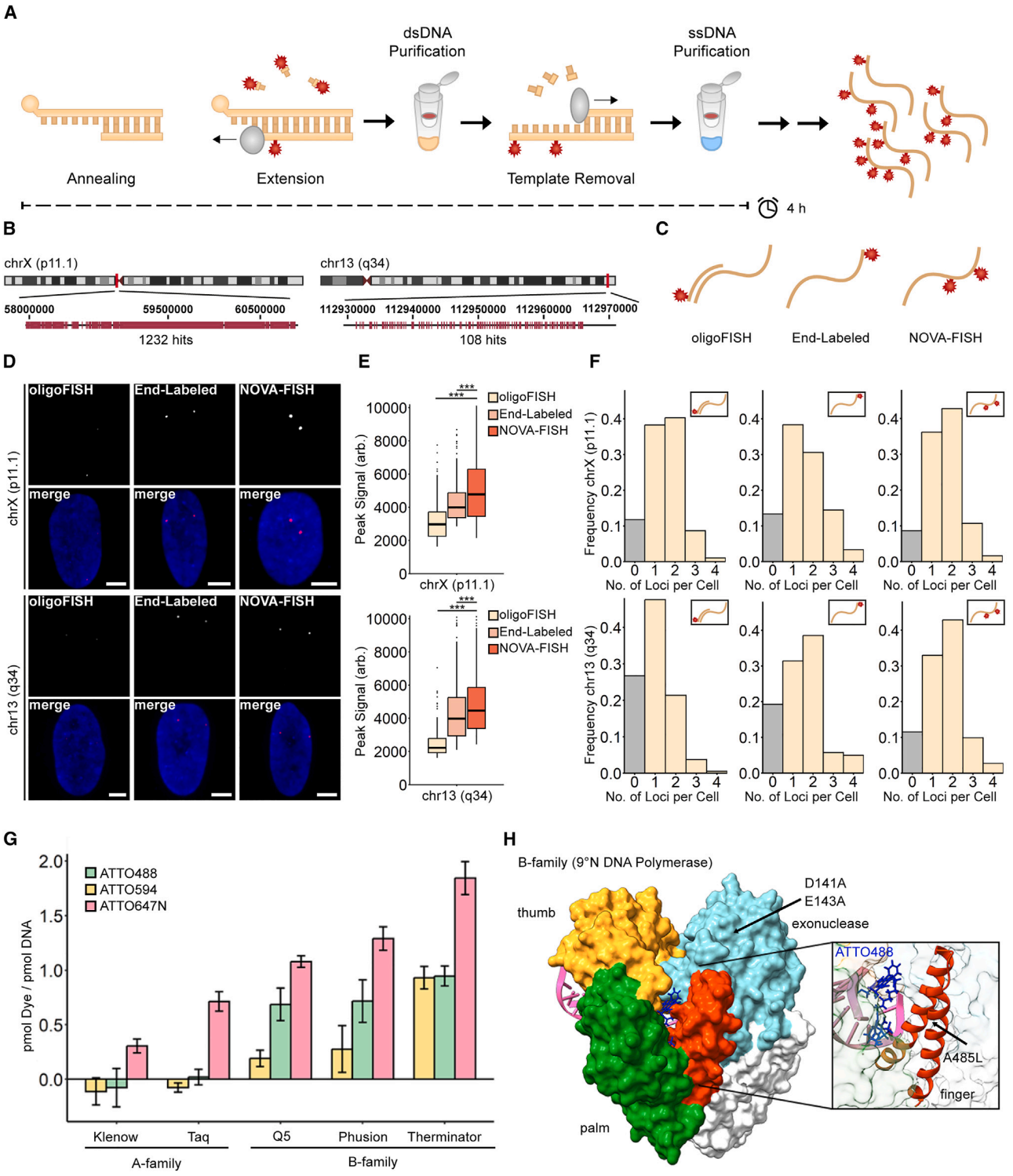

Figure 1. Generating oligonucleotides that carry multiple fluorophores

(A) Schematic workflow of the protocol. Primers are annealed to 5′ phosphorylated template strands, and dye-labeled nucleotides are incorporated in a one-step extension reaction. Template strands are then enzymatically removed, and the product is purified.

(B) Depiction of the target regions. The target regions contain a unique series of repeats (pink) in chrX (p11.1) or chr13 (q34). Human reference GRCh37/hg19 was used to retrieve coordinates.

(legend continued on next page)

chromatin capture assays need to be complemented with sensitive imaging methods to comprehensively address the dynamics and function of chromatin conformations.

Since their advent, microscopy and fluorescence *in situ* hybridization (FISH) have shed light on the spatial distribution of chromatin in single cells and identified chromosomal abnormalities in malignant cells and tissues.[31–35] Although fluorescence microscopy has facilitated studies on large-scale chromatin structures, the detection and resolution of small regulatory elements with traditional FISH methods remains challenging.[24,36] In past works, FISH probes have often been generated from bacterial artificial chromosomes (BACs) or yeast artificial chromosomes (YACs) using polymerases in random priming or nick translation reactions.[37–40] However, the size of BAC or YAC probes limits the genomic resolution and is, therefore, not suitable for the detection of short regulatory DNA sequences.[41] Recent advances in synthetic DNA production and the availability of whole-genome datasets have ushered in a new era of oligonucleotide-based FISH (oligoFISH) methodologies.[28,42–47] Variations of oligoFISH utilize barcoded primary pools and fluorescent secondary readout probes to sequentially detect genomic loci. Although this approach has enabled considerable advancements in understanding chromatin architecture, the usage of single-labeled secondary probes limits the detectable target size and spatial resolution. Signal amplification has been achieved through rolling circle amplification,[48] hybridization chain reaction,[49,50] serial ligation of circular DNA (clamp-FISH[51,52]), branched DNA configurations,[53] or primer exchange reaction (SABER-FISH[54]). These techniques typically involve multiple hybridization rounds and enable detection of multiple targets, but DNA accessibility and an increased risk of non-specific amplification may complicate the visualization of small genomic elements. We hypothesized that the direct coupling of multiple fluorophores to primary oligonucleotides in combination with the elimination of secondary hybridization steps improves the signal-to-noise ratio at DNA loci of interest.

Here, we introduce a protocol to generate nanoscopy-compatible oligonucleotides with dyes in variable arrays (NOVA probes). Multiple fluorophores are attached to oligonucleotides in a one-step biochemical reaction, thereby considerably shortening the time required for probe generation. The protocol has further been optimized to allow precise control of the labeling density and does not require demanding amplification or purification steps. We applied our probes to detect a variety of genomic loci ranging from large-scale repetitive regions to sub-kilobase single loci using FISH (NOVA-FISH). Compared to previous methods, NOVA-FISH probes can efficiently be produced and allow free choice of fluorophores and flexible adjustment of labeling density to optimize signal detection in super-resolution microscopy.

RESULTS

Design and synthesis of NOVA probes

OligoFISH methods have proven valuable in visualizing genomic regions, but the necessity of multiple hybridization steps and/or the use of expensive, end-labeled probes limit their widespread application in nanoscopy. We reasoned that densely labeled oligonucleotide probe sets could be generated with an enzymatic approach in an efficient and cost-effective manner (Figure 1A). To this goal, we hybridized 5′ phosphate-labeled template strands with short primers followed by primer extension and lambda-exonuclease-mediated template degradation. We synthesized two probes that target a series of repeats on chromosome X (chrX; p11.1) or chr13 (q34) (Figure 1B). Compared with barcoded oligonucleotides and end-labeled probes, our densely labeled oligonucleotides (NOVA probes) significantly improve signal strength (Figures 1C–1E). Moreover, NOVA-FISH exhibits a significant improvement in detectability of the smaller target on chr13 (q34) ($p < 0.001$, Wilcoxon rank-sum test) but not chrX (p11.1). Therefore, NOVA probes are well suited for detecting small genomic loci (Figure 1F).

As our approach depends on the enzymatic incorporation of modified nucleotides into short primers, we compared commonly available DNA polymerases. We measured the incorporation of different dye-labeled nucleotides during extension using commonly available family A (Klenow exo-, Taq) and family B (Q5, Phusion, Therminator) DNA polymerases. Photometric measurements of synthetized probes showed that the highest labeling rates were obtained for all tested modified nucleotides with Therminator DNA polymerase (Figures 1G and S1A–S1C).

(C) Comparing three FISH strategies to tag genomic loci. While oligoFISH uses labeled readout strands for detection, end-labeled and NOVA-FISH probes carry fluorophores in their primary sequences.

(D) Representative images of both targets detected with oligoFISH, end-labeled probes, or NOVA-FISH. FISH was conducted in IMR-90 cells. Scale bars, 5 μm.

(E) NOVA-FISH yields bright FISH signals. Number of detected signals: chrX (p11.1): oligoFISH ($n = 430$), end-labeled ($n = 420$), and NOVA-FISH ($n = 548$); chr13 (q34): oligoFISH ($n = 292$), end-labeled ($n = 354$), and NOVA-FISH ($n = 413$). Datasets were tested for significance using the Wilcoxon rank-sum test with Bonferroni's correction for multiple testing (***$p < 0.001$).

(F) NOVA-FISH improves detectability in small genomic loci. Histograms depict the relative number (no.) of chrX (p11.1) or chr13 (q34) foci detected. NOVA-FISH exhibits a significant improvement in the detectability of chr13 (q34) ($p < 0.001$ for NOVA-FISH vs. oligoFISH and NOVA-FISH vs. end labeled, Wilcoxon rank-sum test). Nuclei that have been entirely imaged were included in the analysis. Number of cells analyzed: chrX (p11.1): oligoFISH ($n = 196$), end labeled ($n = 180$), and NOVA-FISH ($n = 243$); chr13 (q34): oligoFISH ($n = 187$), end labeled ($n = 157$), and NOVA-FISH ($n = 182$).

(G) Screening substrate preferences of selected DNA polymerases. Polymerases (Klenow exo-, Taq, Q5, Phusion, Therminator) incorporated dCTP-ATTO488, dCTP-ATTO594, or dCTP-ATTO647N into oligonucleotides using a 1:4 molar ratio of dye-labeled to unlabeled nucleotides. Data are represented as mean ± SD. See also Figure S1A.

(H) Crystal structure of the 9°N DNA polymerase in complex with DNA and dCTP-ATTO488. The protein is shown in white with highlighted palm (green), thumb (yellow), finger (orange), and exonuclease (cyan) domains. dCTP-ATTO488 was superimposed on the incorporated nucleotide in the complex. The magnified image depicts dCTP-ATTO488 in the binding pocket. See also Figure S2. The figure was generated with UCSF Chimera (v.1.17.3, RRID: SCR_015872) accessing 5OMV.[55,56]

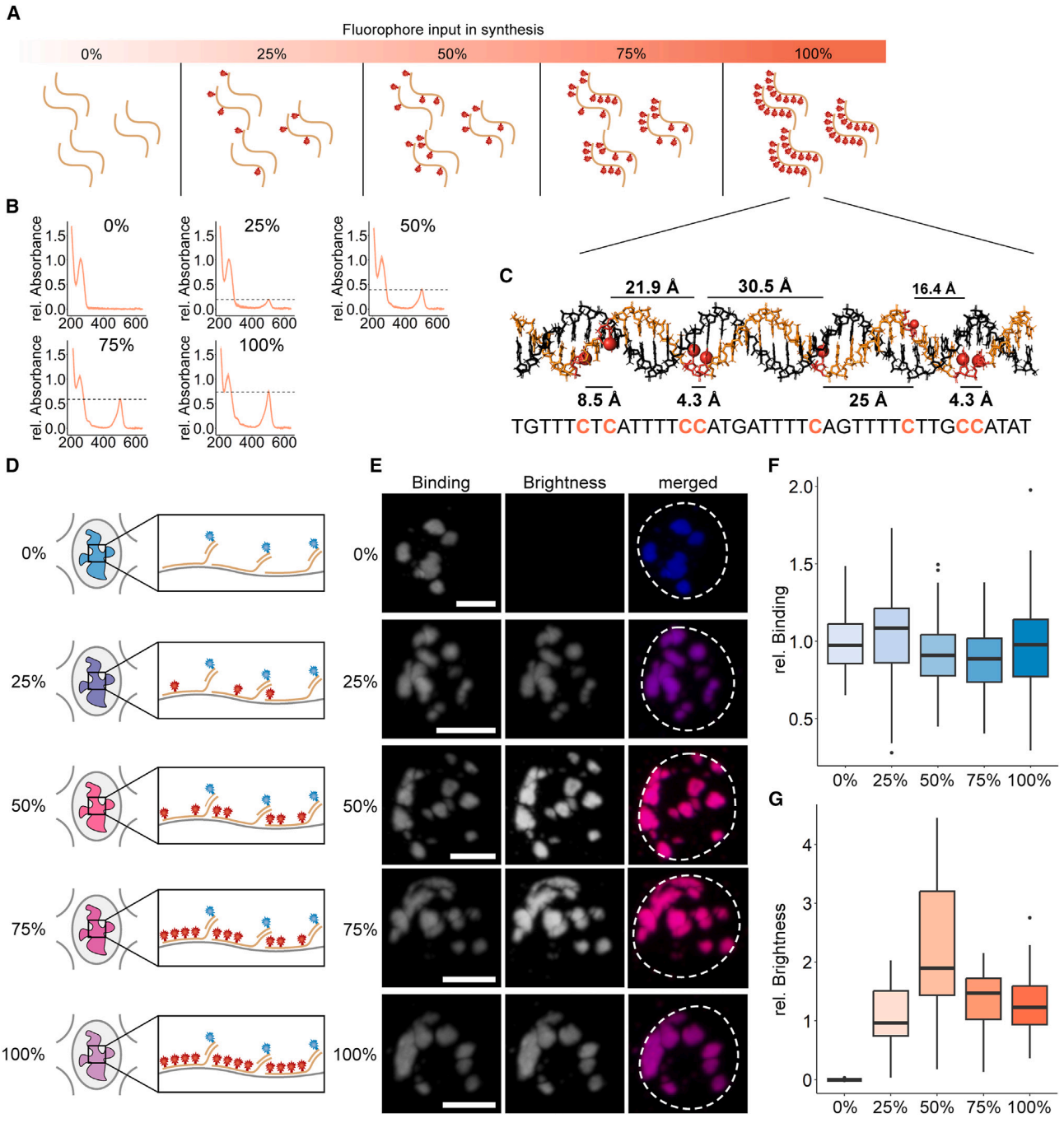

Figure 2. Binding efficiency and brightness of densely labeled probes

(A) Modulating labeling densities during NOVA probe synthesis. The labeling density is controlled through the ratio of labeled to unlabeled nucleotide (0%, 25%, 50%, 75%, 100%) in the synthesis reaction.

(B) Absorption spectra of probes with increasing labeling density. The absorbance was normalized by the absorption peak at 260 nm. The dotted lines indicate the absorption maximum of the fluorophore.

(C) Modeling fluorophore spacing in NOVA-FISH probes bound to major satellites. The B-form duplex formed by a NOVA-FISH probe (beige) and the genomic target (black) is shown. Red nucleotides indicate the locations of modified cytosines, and fluorophores are depicted as red knobs. The normal distance between neighboring fluorophores in the helix is depicted. The figure was created in Pymol v.2.5.5 (RRID: SCR_000305).[66]

(D) Assay to determine the impact of fluorophore number in the probe on hybridization efficiency. NOVA-FISH probes carrying increasing numbers of fluorophores (red) are hybridized with a locus of interest, and dye-labeled secondary strands (blue) are used as a reference.

(legend continued on next page)

Therminator DNA polymerase is a DNA polymerase that has been derived from the euryarchaeon *Thermococcus* sp. 9°N and carries mutations in its exonuclease domain (D141A, E143A) and finger domain (A485L)[57] (Figure 1H). As a result of these modifications, Therminator DNA polymerase exhibits decreased discrimination for modified nucleotides and has been used to synthesize a variety of unnatural nucleic acids.[58–61] To investigate the molecular basis for the observed variations in incorporation efficiencies among our candidates, we modeled dye-labeled nucleotides in different conformations in conjunction with finger domains of family A and B polymerases (Figure S2). We noted possible steric clashes between dye-labeled nucleotides and finger domains of family A members, whereas no such clashes were observed with family B polymerases. Using Therminator DNA polymerase, we determined that probes are robustly generated within an hour (Figure S1D). In addition, our approach allows free choice of fluorophore and flexible adjustment of labeling density (Figure S1E).

FISH probes require a high degree of purity since complementary or unlabeled strands will compete with the labeled probe during hybridization and, thus, reduce signal intensity. To remove unbound primers, free nucleotides, and enzymes, we adapted the buffer conditions to selectively yield double-stranded oligonucleotides after extension (Figures S3A–S3C). Also, unlabeled template DNA might block the synthesized probes and thereby prevent their hybridization with the locus of interest. Therefore, we have introduced phosphate groups at the 5′ ends of template strands to mark them for lambda-exonuclease-mediated degradation (Figure S3D). Using this approach, template DNA was effectively degraded within 30 min (Figure S3E). We then used ethanol-based purification to obtain the single-stranded probe (Figures S3A and S3C). This simple purification strategy yielded all NOVA probes used for microscopic measurements in this work.

After establishing a robust workflow, we assessed the number of incorporated fluorophores in NOVA probes. High-performance liquid chromatography (HPLC) analysis revealed that using a low ratio of modified to unmodified nucleotides (25%) in the synthesis reaction yields distinct elution peaks corresponding to the incorporation of increasing numbers of fluorophores (Figures S3F and S3G).

Visualizing telomere clustering below the diffraction limit

Next, we sought to utilize the brightness of NOVA probes to visualize telomeres below the diffraction limit. We tagged telomeres with telomere-specific NOVA probes and acquired images using confocal or stimulated emission depletion (STED) microscopy (Figure S1F). We observed clustered telomeres using STED microscopy, which appear as single entities in confocal images. We then applied 3D STED microscopy to gain further insights into the degree of telomere clustering (Figure S1G). Telomeres in the same cells exhibited considerable heterogeneity in their size, and clusters containing multiple telomeres were observed, consistent with previous works.[62–65] Next, we analyzed the number of detectable telomeres using confocal or STED microscopy (Figure S1G). In comparison to confocal images, STED microscopy detected, on average, 1.31 times more telomeres (±SD = 0.21), corresponding to clustered telomeres that are only resolved with super-resolution microscopy. Hence, the brightness of NOVA probes supports demanding super-resolution microscopy to visualize nuanced details of genomic loci with high optical resolution.

Dense labeling does not affect hybridization efficiency but reduces signal strength

As our workflow yields densely labeled probes, we next tested how the presence of multiple dyes in the probe affects hybridization efficiency. To address this, we generated barcoded probes with increasing labeling densities (Figures 2A–2C and S1E). These probes contain dye-labeled sequences that bind to the genome and unlabeled barcodes that hybridize with secondary probes carrying another dye. Using this approach, we can evaluate the brightness of the NOVA probe signal (green) and the relative number of probes localized at the target region (red) (Figures 2D and 2E). We found that increasing the number of dye-labeled nucleotides in the probe did not affect the number of bound probes at the locus of interest, as no notable drop in red signal was observed (Figure 2F). However, the brightness of our probes decreases at high labeling densities (Figure 2G). Consequently, densely labeled probes still bind to the region of interest, but short intermolecular distances between fluorophores impede signal strength (Figure 2C).

We next characterized the impact of dye-dye distances on probe fluorescence. We incorporated two dye molecules into overhangs of probes and increased the distances in between (1, 3, 5, 7, or 10 bases) (Figure 3A). Then, we measured the intensity of probes carrying two ATTO488 or ATTO647N molecules at the FISH spot (Figure 3B). The fluorescence of ATTO488- and ATTO647N-labeled probes increases with greater dye-dye distances (Figure 3C). Therefore, we hypothesize that distance-dependent fluorescence quenching impacts the brightness of densely labeled probes.

Establishing densely labeled probes with regularly spaced fluorophores

Our previous strategy yields labeled oligonucleotides in an efficient and cost-effective manner but depends on the occurrence of cytosines in the synthesized sequence. Therefore, we modified our workflow to generate extended probes (xNOVA probes) that carry fluorophores in a protruding sequence that does not bind to the genome (Figure 3D).[44,67] In this design, fluorophores are regularly spaced in the invariable sequence to avoid distance-dependent fluorescence quenching that might diminish

(E) Representative images of major satellites in mouse embryonic stem cells detected with NOVA-FISH probes containing increasing numbers of fluorophores. Scale bars, 5 μm.

(F) Binding efficiency is unaffected by dense labeling. The normalized intensity of dye-labeled secondary strands (blue) is depicted.

(G) Densely labeled probes exhibit a decrease in fluorescence. Related to (F). The normalized intensity of NOVA-FISH probes (red) is depicted. Number of cells analyzed: 0% (n = 149), 25% (n = 146), 50% (n = 172), 75% (n = 147), and 100% (n = 165).

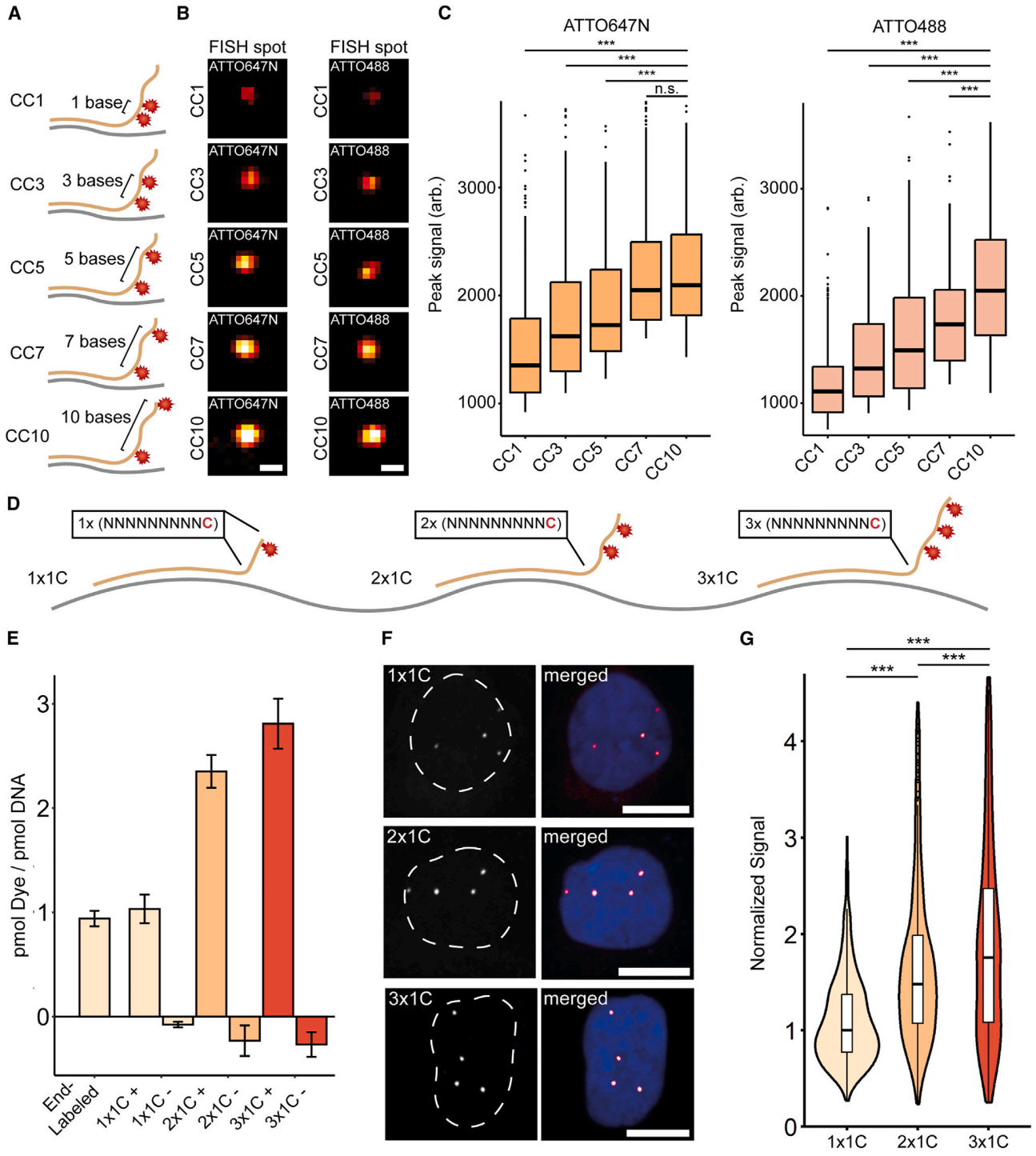

Figure 3. Designing xNOVA probes

(A) Design of probes to determine distance-dependent fluorescence quenching. NOVA probes are synthesized to carry two fluorophores with increasing distance in between (1, 3, 5, 7, or 10 bases).

(B) Representative images of chr13 (q34) targeted in IMR-90 cells. NOVA probes contain two ATTO488 or ATTO647N molecules. Scale bars, 500 nm.

(C) Dye-dye distances impact probe fluorescence. Datasets were tested for significance using the Wilcoxon rank-sum test with Bonferroni's correction for multiple testing (***$p < 0.001$).

(D) Design of extended NOVA-FISH (xNOVA) probes. xNOVA probes are extended by labeled 10-mers (NNNNNNNNNC) at their 3′ ends.

(legend continued on next page)

the specific brightness. We synthesized probes that either carried one (1 × 1C), two (2 × 1C), or three (3 × 1C) fluorophores and measured their fluorescence signals at the locus of interest (Figures 3E, 3F, and S4A). The addition of longer sequences (2 × 1C, 3 × 1C) resulted in stronger signals (Figure 3G). With this approach, we observed a steady increase in signal strength at higher labeling densities, arguing against substantial distance-dependent quenching in 3 × 1C sequences (Figures S4B and S4C).

NOVA-FISH detects non-repetitive genomic loci with kilobase resolution

Finally, we tested the limits of NOVA-FISH by detecting small non-repetitive genomic loci with nanoscale precision using STED microscopy (Figure 4A). We designed probe sets to detect non-repetitive neighboring regions on chr11 termed "A" and "B" that have been established in past works.[24] Probe sets against "A" contained 60, 50, 40, 30, 20, or 10 individual oligonucleotides, while "B" was targeted with 60 probes. The probe sets span 6.1, 4.8, 3.7, 1.7, or 0.5 kb for "A" and 4.8 kb for "B" and yield two adjacent spots (Figure 4B). A characteristic of the NOVA technology is the complete flexibility in probe synthesis, as probes can be selectively amplified from a large pool by adding appropriate primer combinations (Figure 4C). This allows the cost-effective repeated use of one oligonucleotide pool to generate probes against different target regions. Then, we targeted "A" with decreasing numbers of individual probes, maintaining the same set of probes for "B" (Figure 4D). Despite observing a decline in detection frequency with the reduced number of probes detecting "A," we were still able to detect genomic loci as small as 0.5 kb. The ratio of co-localizing spots to total number of spots is in the range of 38%–63% for A and 29%–54% for B. Furthermore, we used STED microscopy to robustly measure distances in all "A" and "B" probe pairs (Figures 4E and 4F). Thus, NOVA-FISH is a reliable tool to detect non-repetitive regions below the kilobase level.

DISCUSSION

Over the past decade, it became clear that the 3D genome organization contributes to the establishment, maintenance, and change of gene activity.[68,69] Chromatin capture assays have identified genome-wide interactions of regulatory elements and have delineated topologically associating domains (TADs).[20,70] These findings have traditionally been complemented by FISH-based imaging methods detecting entire genomes and individual chromosomes down to single genomic loci.[28,47,71] However, the optical detection of small genetic elements and the resolution of their spatial relationships at the nanoscale level remains challenging. Here, we developed a simple, rapid, flexible, and cost-effective protocol for the generation of FISH probe sets that are suited for nanoscopic measurements with kilobase resolution. In a recent study, we applied this technique to probe enhancer hijacking events upon tumorigenic translocations.[72]

Small genetic elements are ideally detected with multiple synthetic oligonucleotides that may either be directly labeled or hybridized with secondary, labeled probes. Whereas end-labeled commercial probes are expensive if large and diverse probe pools are used, enzyme-based synthesis is cost effective and flexible but requires the subsequent removal of template strands. While previously, RNA templates were reverse transcribed and subsequently degraded by RNases, we simply removed 5′ phosphorylated DNA templates using lambda exonuclease.[73] This enzymatic synthesis, including two purification steps, takes under 4 h and yields sets with hundreds of probes for less than 10 €. A detailed cost estimate of oligoFISH, end-labeled, and NOVA probes can be found in Tables S2–S4.

For enzymatic incorporation of dye-labeled nucleotides, we tested commonly available DNA polymerases. We found that B-family DNA polymerases incorporate all used modified nucleotides more effectively than A-family DNA polymerases, such as the Klenow fragment or Taq DNA polymerase. This is consistent with previous structural data of B-family polymerases, attributing their ability to incorporate dye-labeled nucleotides to a larger channel volume, the presence of B-form DNA, and phosphate backbone-mediated protein-DNA interactions.[55,74–76] Among the tested B-family polymerases, Therminator DNA polymerase, having mutations in its exonuclease domain (D141A, E143A) and finger domain (A485L), was best suited for the incorporation of dye-labeled nucleotides.[57]

As even minor FISH projects involve dozens of probes with different dye labels, we used inexpensive, commercially synthesized template pools in combination with plates of bioinformatically optimized, target-specific primers. This approach allows the flexible generation of small to large probe sets coupled with variable dyes. We demonstrate that regions as small as 500 base pairs can be detected and genomic distances of a few kilobases can be measured.

We found that the brightness of probes can be easily adjusted with the ratio of labeled to unlabeled nucleotides in the synthesis reaction. However, the brightness did not linearly increase, due to distance-dependent effects at high labeling densities. To become independent of probe-specific sequences and ensure incorporation of the same numbers of fluorescent nucleotides, we generated extended probes with overhanging, identical sequences (xNOVA). We successfully incorporated fluorophores with a spacing of ten nucleotides but note that distances down to seven nucleotides might be permissible. Our systematic analysis of distance-dependent dye-dye quenching is consistent with a previous study that measured dye-dye interactions in DNA origami.[77]

While current FISH techniques can sequentially label multiple targets, the use of end-labeled probes for secondary hybridization steps reduces signal strength. To enhance signal strength,

(E) Synthesizing xNOVA probes with specific fluorophore numbers (1 × 1C, 2 × 1C, 3 × 1C). xNOVA probes were synthesized with a 0% (−ATTO488) or 100% (+ATTO488) ratio of labeled to unlabeled nucleotides. Data are represented as mean ± SD. See also Figure S4A.
(F) Representative images of xNOVA probes detecting chr13 (q34) in U2OS cells. Scale bars, 10 μm.
(G) Quantification of xNOVA probe signals. Related to (F). The plot depicts the two brightest signals for each cell. Number of foci analyzed: 1C ($n = 513$), 2 × 1C ($n = 634$), and 3 × 1C ($n = 566$). Datasets were tested for significance using the Wilcoxon rank-sum test with Bonferroni's correction for multiple testing (***$p < 0.001$).

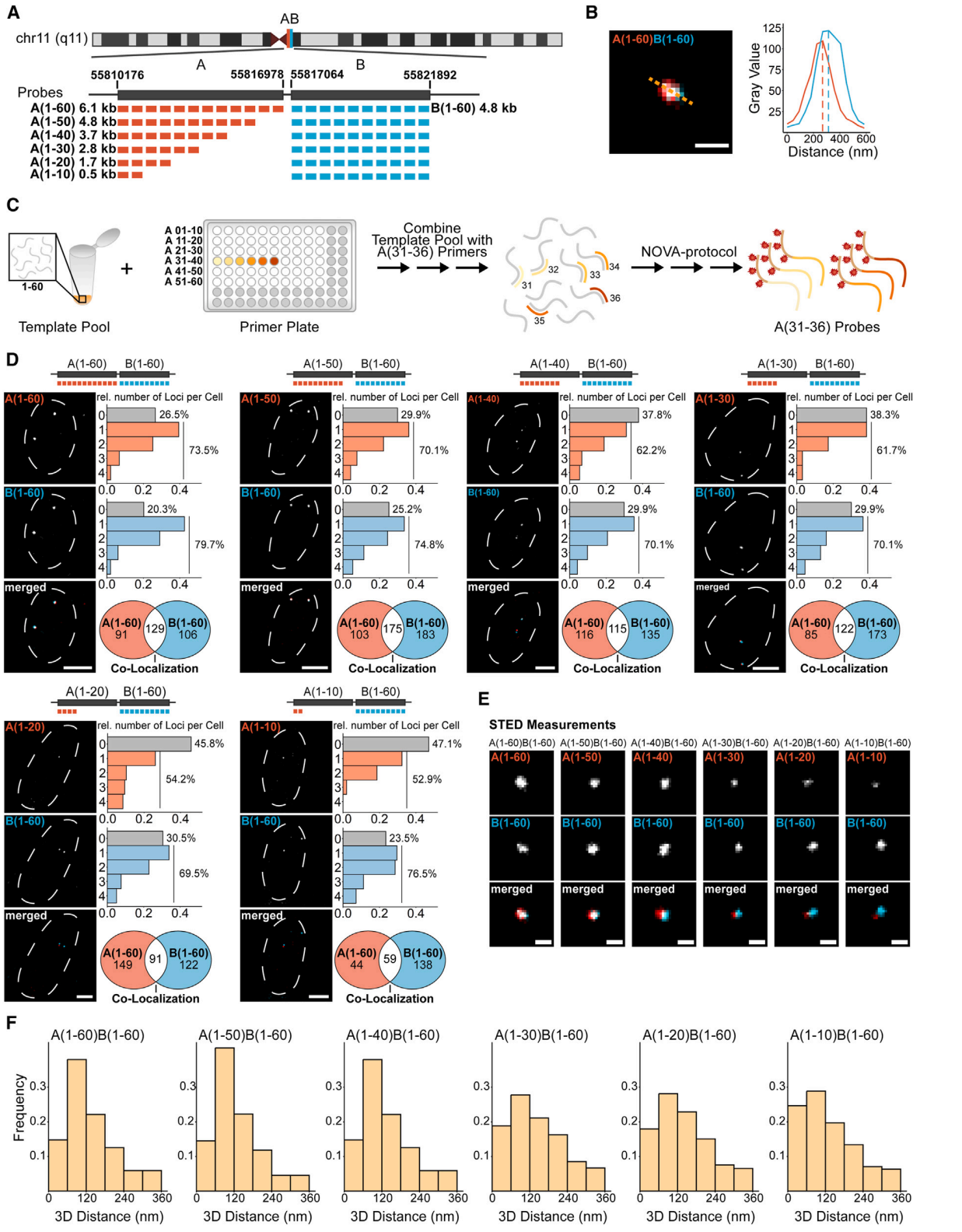

(legend on next page)

NOVA probes carrying multiple fluorophores could be employed for secondary hybridization. Moreover, we hypothesize that our workflow is suitable for applications beyond the detection of small genomic loci. Given that oligonucleotides carrying any number of desired fluorophores can be generated, opportunities in the fields of DNA-PAINT, DNA origami, or immunostainings emerge.[78,79] In summary, we present a simple, quick, and inexpensive approach to explore the spatial relationships of genetic elements governing the activity of clusters of genes.

Limitations of study

While NOVA probes enable the detection of sub-kilobase genomic loci, the number of detectable targets is currently limited by the number of distinguishable colors in the microscopy setup. Barcoded probes circumvent this limitation by sequentially binding and releasing labeled readout probes, which, however, leads to a reduction in sensitivity. NOVA probes are not compatible with multiplexed imaging techniques, as they carry fluorophores in their primary sequence. Probing the spatial relationships of a larger number of regulatory elements requires barcoded probes, which could use NOVA probes for readout.

Furthermore, NOVA probes are used for FISH experiments and therefore subject to the same general limitations of hybridization-based methods.[36,80] In particular, the same basic trade-offs between the preservation of fine structural details and hybridization penetrance apply.

STAR★METHODS

Detailed methods are provided in the online version of this paper and include the following:

SUPPLEMENTAL INFORMATION

Supplemental information can be found online at https://doi.org/10.1016/j.crmeth.2024.100840.

ACKNOWLEDGMENTS

We thank Cristina Cardoso and Irina Solovei for helpful discussions and input. This work was supported by grants from the Deutsche Forschungsgemeinschaft (SFB1064/project number 213249687 to H.L. and Priority Program SPP 2202/project number 422857584 to H.H. and H.L.) and by the BMBF in the framework of the Cluster4Future program (Cluster for Nucleic Acid Therapeutics Munich, CNATM) (project ID 03ZU1201AA to T.C. and H.L.). Microscopic images were acquired at microscopes of the Center for Advanced Light Microscopy (CALM) at LMU Munich.

AUTHOR CONTRIBUTIONS

C.S., H.L., and H.H. conceptualized the study and wrote the manuscript. C.S. synthesized NOVA probes, conducted FISH experiments, acquired microscopy images, and prepared the figures. D.H. acquired 3D STED images of telomeres and automated STED acquisition. M.G.O., G.S., and D.H. analyzed the data. A.J.T. performed HPLC purifications. H.L. and H.H. supervised the study, and H.L., H.H., and T.C. secured funding. All authors reviewed the manuscript and agreed to the published version.

DECLARATION OF INTERESTS

The authors declare no competing interests.

Received: March 12, 2024
Revised: June 16, 2024
Accepted: July 22, 2024
Published: August 12, 2024

REFERENCES

1. Cremer, T., and Cremer, M. (2010). Chromosome territories. Cold Spring Harb. Perspect. Biol. *2*, a003889. https://doi.org/10.1101/cshperspect.a003889.
2. Rao, S.S.P., Huntley, M.H., Durand, N.C., Stamenova, E.K., Bochkov, I.D., Robinson, J.T., Sanborn, A.L., Machol, I., Omer, A.D., Lander, E.S., and Aiden, E.L. (2014). A 3D map of the human genome at kilobase resolution reveals principles of chromatin looping. Cell *159*, 1665–1680. https://doi.org/10.1016/j.cell.2014.11.021.
3. Nora, E.P., Lajoie, B.R., Schulz, E.G., Giorgetti, L., Okamoto, I., Servant, N., Piolot, T., Van Berkum, N.L., Meisig, J., Sedat, J., et al. (2012). Spatial

Figure 4. Using xNOVA probes to detect non-repetitive loci at kilobase scale

(A) Depiction of the target regions. Two adjacent non-repetitive genomic regions on chr11 (hg19, chr11: 55,810,176–55,816,978, hg19, chr11: 55,817,064–55,821,892) were targeted with 60 xNOVA probes spanning 6.1 or 4.8 kb. In successive experiments, the number of xNOVA probes targeting A was gradually reduced from 60 to 10 probes. 60 xNOVA probes targeting B were used as a reference.

(B) Representative STED images of regions "A" and "B" in two colors. A(1–60) was tagged with ATTO594, and B(1–60) harbored ATTO647N. Scale bar, 500 nm.

(C) Schematic of selective xNOVA probe synthesis. Probe sets are selectively synthesized through the combination of region-specific primers with common template pools.

(D) Detecting kilobase genomic loci using confocal microscopy. 60 probes detecting B were paired with probe sets comprising 60 to 10 individual probes for A. Histograms depict the relative number of detected loci per cell. Venn diagrams depict the number of detected single and co-localizing signals. Scale bars, 5 μm. Number of cells analyzed: A(1–60)B(1–60): n = 151; A(1–50)B(1–60): n = 153; A(1–40)B(1–60): n = 172; A(1–30)B(1–60): n = 168; A(1–20)B(1–60): n = 124; A(1–10)B(1–60): n = 101.

(E) Representative z projections of A paired with B in K562 cells. Scale bars, 200 nm.

(F) 3D distance of A and B. Number of analyzed spot pairs: 1–60: n = 550; 1–50: n = 388; 1–40: n = 317; 1–30: n = 329; 1–20: n = 445; 1–10: n = 226.

partitioning of the regulatory landscape of the X-inactivation centre. Nature *485*, 381–385. https://doi.org/10.1038/nature11049.

4. Jeong, Y., El-Jaick, K., Roessler, E., Muenke, M., and Epstein, D.J. (2006). A functional screen for sonic hedgehog regulatory elements across a 1 Mb interval identifies long-range ventral forebrain enhancers. Development *133*, 761–772. https://doi.org/10.1242/dev.02239.
5. Pombo, A., and Dillon, N. (2015). Three-dimensional genome architecture: players and mechanisms. Nat. Rev. Mol. Cell Biol. *16*, 245–257. https://doi.org/10.1038/nrm3965.
6. Medrano-Fernandez, A., and Barco, A. (2016). Nuclear organization and 3D chromatin architecture in cognition and neuropsychiatric disorders. Mol. Brain *9*, 83. https://doi.org/10.1186/s13041-016-0263-x.
7. Lupiáñez, D.G., Kraft, K., Heinrich, V., Krawitz, P., Brancati, F., Klopocki, E., Horn, D., Kayserili, H., Opitz, J.M., Laxova, R., et al. (2015). Disruptions of topological chromatin domains cause pathogenic rewiring of gene-enhancer interactions. Cell *161*, 1012–1025. https://doi.org/10.1016/j.cell.2015.04.004.
8. Hnisz, D., Weintraub, A.S., Day, D.S., Valton, A.L., Bak, R.O., Li, C.H., Goldmann, J., Lajoie, B.R., Fan, Z.P., Sigova, A.A., et al. (2016). Activation of proto-oncogenes by disruption of chromosome neighborhoods. Science *351*, 1454–1458. https://doi.org/10.1126/science.aad9024.
9. Schuijers, J., Manteiga, J.C., Weintraub, A.S., Day, D.S., Zamudio, A.V., Hnisz, D., Lee, T.I., and Young, R.A. (2018). Transcriptional Dysregulation of MYC Reveals Common Enhancer-Docking Mechanism. Cell Rep. *23*, 349–360. https://doi.org/10.1016/j.celrep.2018.03.056.
10. Dixon, J.R., Jung, I., Selvaraj, S., Shen, Y., Antosiewicz-Bourget, J.E., Lee, A.Y., Ye, Z., Kim, A., Rajagopal, N., Xie, W., et al. (2015). Chromatin architecture reorganization during stem cell differentiation. Nature *518*, 331–336. https://doi.org/10.1038/nature14222.
11. Mateo, L.J., Murphy, S.E., Hafner, A., Cinquini, I.S., Walker, C.A., and Boettiger, A.N. (2019). Visualizing DNA folding and RNA in embryos at single-cell resolution. Nature *568*, 49–54. https://doi.org/10.1038/s41586-019-1035-4.
12. Gizzi, A.M.C., Cattoni, D.I., Fiche, J.-B., Espinola, S.M., Gurgo, J., Messina, O., Houbron, C., Ogiyama, Y., Papadopoulos, G.L., and Cavalli, G. (2019). Microscopy-based chromosome conformation capture enables simultaneous visualization of genome organization and transcription in intact organisms. Mol. Cell *74*, 212–222. https://doi.org/10.1016/j.molcel.2019.01.011.
13. Simonis, M., Klous, P., Splinter, E., Moshkin, Y., Willemsen, R., de Wit, E., van Steensel, B., and de Laat, W. (2006). Nuclear organization of active and inactive chromatin domains uncovered by chromosome conformation capture-on-chip (4C). Nat. Genet. *38*, 1348–1354. https://doi.org/10.1038/ng1896.
14. Dekker, J., Rippe, K., Dekker, M., and Kleckner, N. (2002). Capturing chromosome conformation. Science *295*, 1306–1311. https://doi.org/10.1126/science.1067799.
15. Lieberman-Aiden, E., van Berkum, N.L., Williams, L., Imakaev, M., Ragoczy, T., Telling, A., Amit, I., Lajoie, B.R., Sabo, P.J., Dorschner, M.O., et al. (2009). Comprehensive mapping of long-range interactions reveals folding principles of the human genome. Science *326*, 289–293. https://doi.org/10.1126/science.1181369.
16. Krietenstein, N., Abraham, S., Venev, S.V., Abdennur, N., Gibcus, J., Hsieh, T.H.S., Parsi, K.M., Yang, L., Maehr, R., Mirny, L.A., et al. (2020). Ultrastructural Details of Mammalian Chromosome Architecture. Mol. Cell *78*, 554–565.e7. https://doi.org/10.1016/j.molcel.2020.03.003.
17. Dixon, J.R., Selvaraj, S., Yue, F., Kim, A., Li, Y., Shen, Y., Hu, M., Liu, J.S., and Ren, B. (2012). Topological domains in mammalian genomes identified by analysis of chromatin interactions. Nature *485*, 376–380. https://doi.org/10.1038/nature11082.
18. Jerkovic, I., and Cavalli, G. (2021). Understanding 3D genome organization by multidisciplinary methods. Nat. Rev. Mol. Cell Biol. *22*, 511–528. https://doi.org/10.1038/s41580-021-00362-w.
19. Goel, V.Y., and Hansen, A.S. (2021). The macro and micro of chromosome conformation capture. Wiley Interdiscip. Rev. Dev. Biol. *10*, e395. https://doi.org/10.1002/wdev.395.
20. McCord, R.P., Kaplan, N., and Giorgetti, L. (2020). Chromosome Conformation Capture and Beyond: Toward an Integrative View of Chromosome Structure and Function. Mol. Cell *77*, 688–708. https://doi.org/10.1016/j.molcel.2019.12.021.
21. Nagano, T., Lubling, Y., Stevens, T.J., Schoenfelder, S., Yaffe, E., Dean, W., Laue, E.D., Tanay, A., and Fraser, P. (2013). Single-cell Hi-C reveals cell-to-cell variability in chromosome structure. Nature *502*, 59–64. https://doi.org/10.1038/nature12593.
22. Flyamer, I.M., Gassler, J., Imakaev, M., Brandão, H.B., Ulianov, S.V., Abdennur, N., Razin, S.V., Mirny, L.A., and Tachibana-Konwalski, K. (2017). Single-nucleus Hi-C reveals unique chromatin reorganization at oocyte-to-zygote transition. Nature *544*, 110–114. https://doi.org/10.1038/nature21711.
23. Stevens, T.J., Lando, D., Basu, S., Atkinson, L.P., Cao, Y., Lee, S.F., Leeb, M., Wohlfahrt, K.J., Boucher, W., O'Shaughnessy-Kirwan, A., et al. (2017). 3D structures of individual mammalian genomes studied by single-cell Hi-C. Nature *544*, 59–64. https://doi.org/10.1038/nature21429.
24. Brandstetter, K., Zülske, T., Ragoczy, T., Hörl, D., Guirao-Ortiz, M., Steinek, C., Barnes, T., Stumberger, G., Schwach, J., Haugen, E., et al. (2022). Differences in nanoscale organization of regulatory active and inactive human chromatin. Biophys. J. *121*, 977–990. https://doi.org/10.1016/j.bpj.2022.02.009.
25. Levi, V., Ruan, Q., Plutz, M., Belmont, A.S., and Gratton, E. (2005). Chromatin dynamics in interphase cells revealed by tracking in a two-photon excitation microscope. Biophys. J. *89*, 4275–4285. https://doi.org/10.1529/biophysj.105.066670.
26. Gabriele, M., Brandão, H.B., Grosse-Holz, S., Jha, A., Dailey, G.M., Cattoglio, C., Hsieh, T.-H.S., Mirny, L., Zechner, C., and Hansen, A.S. (2022). Dynamics of CTCF-and cohesin-mediated chromatin looping revealed by live-cell imaging. Science *376*, 496–501. https://doi.org/10.1126/science.abn6583.
27. Giorgetti, L., Galupa, R., Nora, E.P., Piolot, T., Lam, F., Dekker, J., Tiana, G., and Heard, E. (2014). Predictive polymer modeling reveals coupled fluctuations in chromosome conformation and transcription. Cell *157*, 950–963. https://doi.org/10.1016/j.cell.2014.03.025.
28. Bintu, B., Mateo, L.J., Su, J.H., Sinnott-Armstrong, N.A., Parker, M., Kinrot, S., Yamaya, K., Boettiger, A.N., and Zhuang, X. (2018). Super-resolution chromatin tracing reveals domains and cooperative interactions in single cells. Science *362*, eaau1783. https://doi.org/10.1126/science.aau1783.
29. Finn, E.H., Pegoraro, G., Brandao, H.B., Valton, A.L., Oomen, M.E., Dekker, J., Mirny, L., and Misteli, T. (2019). Extensive Heterogeneity and Intrinsic Variation in Spatial Genome Organization. Cell *176*, 1502–1515. https://doi.org/10.1016/j.cell.2019.01.020.
30. Cattoni, D.I., Cardozo Gizzi, A.M., Georgieva, M., Di Stefano, M., Valeri, A., Chamousset, D., Houbron, C., Déjardin, S., Fiche, J.B., González, I., et al. (2017). Single-cell absolute contact probability detection reveals chromosomes are organized by multiple low-frequency yet specific interactions. Nat. Commun. *8*, 1753. https://doi.org/10.1038/s41467-017-01962-x.
31. Bolzer, A., Kreth, G., Solovei, I., Koehler, D., Saracoglu, K., Fauth, C., Müller, S., Eils, R., Cremer, C., Speicher, M.R., and Cremer, T. (2005). Three-dimensional maps of all chromosomes in human male fibroblast nuclei and prometaphase rosettes. PLoS Biol. *3*, e157. https://doi.org/10.1371/journal.pbio.0030157.
32. Kallioniemi, O.P., Kallioniemi, A., Kurisu, W., Thor, A., Chen, L.C., Smith, H.S., Waldman, F.M., Pinkel, D., and Gray, J.W. (1992). ERBB2 amplification in breast cancer analyzed by fluorescence in situ hybridization. Proc. Natl. Acad. Sci. USA *89*, 5321–5325. https://doi.org/10.1073/pnas.89.12.5321.

33. Cui, C., Shu, W., and Li, P. (2016). Fluorescence In situ Hybridization: Cell-Based Genetic Diagnostic and Research Applications. Front. Cell Dev. Biol. *4*, 89. https://doi.org/10.3389/fcell.2016.00089.

34. Chrzanowska, N.M., Kowalewski, J., and Lewandowska, M.A. (2020). Use of Fluorescence In Situ Hybridization (FISH) in Diagnosis and Tailored Therapies in Solid Tumors. Molecules *25*, 1864. https://doi.org/10.3390/molecules25081864.

35. Pardue, M.L., and Gall, J.G. (1969). Molecular hybridization of radioactive DNA to the DNA of cytological preparations. Proc. Natl. Acad. Sci. USA *64*, 600–604. https://doi.org/10.1073/pnas.64.2.600.

36. Markaki, Y., Smeets, D., Fiedler, S., Schmid, V.J., Schermelleh, L., Cremer, T., and Cremer, M. (2012). The potential of 3D-FISH and super-resolution structured illumination microscopy for studies of 3D nuclear architecture: 3D structured illumination microscopy of defined chromosomal structures visualized by 3D (immuno)-FISH opens new perspectives for studies of nuclear architecture. Bioessays *34*, 412–426. https://doi.org/10.1002/bies.201100176.

37. Wiegant, J., Ried, T., Nederlof, P.M., van der Ploeg, M., Tanke, H.J., and Raap, A.K. (1991). In situ hybridization with fluoresceinated DNA. Nucleic Acids Res. *19*, 3237–3241. https://doi.org/10.1093/nar/19.12.3237.

38. Itzkovitz, S., and van Oudenaarden, A. (2011). Validating transcripts with probes and imaging technology. Nat. Methods *8*, S12–S19. https://doi.org/10.1038/nmeth.1573.

39. Shizuya, H., Birren, B., Kim, U.J., Mancino, V., Slepak, T., Tachiiri, Y., and Simon, M. (1992). Cloning and stable maintenance of 300-kilobase-pair fragments of human DNA in Escherichia coli using an F-factor-based vector. Proc. Natl. Acad. Sci. USA *89*, 8794–8797. https://doi.org/10.1073/pnas.89.18.8794.

40. Burke, D.T., Carle, G.F., and Olson, M.V. (1987). Cloning of large segments of exogenous DNA into yeast by means of artificial chromosome vectors. Science *236*, 806–812. https://doi.org/10.1126/science.3033825.

41. Boettiger, A., and Murphy, S. (2020). Advances in chromatin imaging at kilobase-scale resolution. TiG *36*, 273–287. https://doi.org/10.1016/j.tig.2019.12.010.

42. Huber, D., Voith von Voithenberg, L., and Kaigala, G. (2018). Fluorescence in situ hybridization (FISH): history, limitations and what to expect from micro-scale FISH? Micro Nano Eng. *1*, 15–24. https://doi.org/10.1016/j.mne.2018.10.006.

43. Raj, A., van den Bogaard, P., Rifkin, S.A., van Oudenaarden, A., and Tyagi, S. (2008). Imaging individual mRNA molecules using multiple singly labeled probes. Nat. Methods *5*, 877–879. https://doi.org/10.1038/nmeth.1253.

44. Beliveau, B.J., Joyce, E.F., Apostolopoulos, N., Yilmaz, F., Fonseka, C.Y., McCole, R.B., Chang, Y., Li, J.B., Senaratne, T.N., Williams, B.R., et al. (2012). Versatile design and synthesis platform for visualizing genomes with Oligopaint FISH probes. Proc. Natl. Acad. Sci. USA *109*, 21301–21306. https://doi.org/10.1073/pnas.1213818110.

45. Su, J.H., Zheng, P., Kinrot, S.S., Bintu, B., and Zhuang, X. (2020). Genome-Scale Imaging of the 3D Organization and Transcriptional Activity of Chromatin. Cell *182*, 1641–1659.e26. https://doi.org/10.1016/j.cell.2020.07.032.

46. Takei, Y., Zheng, S., Yun, J., Shah, S., Pierson, N., White, J., Schindler, S., Tischbirek, C.H., Yuan, G.C., and Cai, L. (2021). Single-cell nuclear architecture across cell types in the mouse brain. Science *374*, 586–594. https://doi.org/10.1126/science.abj1966.

47. Szabo, Q., Donjon, A., Jerković, I., Papadopoulos, G.L., Cheutin, T., Bonev, B., Nora, E.P., Bruneau, B.G., Bantignies, F., and Cavalli, G. (2020). Regulation of single-cell genome organization into TADs and chromatin nanodomains. Nat. Genet. *52*, 1151–1157. https://doi.org/10.1038/s41588-020-00716-8.

48. Lizardi, P.M., Huang, X., Zhu, Z., Bray-Ward, P., Thomas, D.C., and Ward, D.C. (1998). Mutation detection and single-molecule counting using isothermal rolling-circle amplification. Nat. Genet. *19*, 225–232. https://doi.org/10.1038/898.

49. Dirks, R.M., and Pierce, N.A. (2004). Triggered amplification by hybridization chain reaction. Proc. Natl. Acad. Sci. USA *101*, 15275–15278. https://doi.org/10.1073/pnas.0407024101.

50. Choi, H.M.T., Beck, V.A., and Pierce, N.A. (2014). Next-generation in situ hybridization chain reaction: higher gain, lower cost, greater durability. ACS Nano *8*, 4284–4294. https://doi.org/10.1021/nn405717p.

51. Rouhanifard, S.H., Mellis, I.A., Dunagin, M., Bayatpour, S., Jiang, C.L., Dardani, I., Symmons, O., Emert, B., Torre, E., Cote, A., et al. (2019). Amendments: Author Correction: ClampFISH detects individual nucleic acid molecules using click chemistry-based amplification. Nat. Biotechnol. *37*, 102. https://doi.org/10.1038/nbt0119-102b.

52. Dardani, I., Emert, B.L., Goyal, Y., Jiang, C.L., Kaur, A., Lee, J., Rouhanifard, S.H., Alicea, G.M., Fane, M.E., Xiao, M., et al. (2022). ClampFISH 2.0 enables rapid, scalable amplified RNA detection in situ. Nat. Methods *19*, 1403–1410. https://doi.org/10.1038/s41592-022-01653-6.

53. Xie, F., Timme, K.A., and Wood, J.R. (2018). Using Single Molecule mRNA Fluorescent in Situ Hybridization (RNA-FISH) to Quantify mRNAs in Individual Murine Oocytes and Embryos. Sci. Rep. *8*, 7930. https://doi.org/10.1038/s41598-018-26345-0.

54. Kishi, J.Y., Lapan, S.W., Beliveau, B.J., West, E.R., Zhu, A., Sasaki, H.M., Saka, S.K., Wang, Y., Cepko, C.L., and Yin, P. (2019). SABER amplifies FISH: enhanced multiplexed imaging of RNA and DNA in cells and tissues. Nat. Methods *16*, 533–544. https://doi.org/10.1038/s41592-019-0404-0.

55. Kropp, H.M., Betz, K., Wirth, J., Diederichs, K., and Marx, A. (2017). Crystal structures of ternary complexes of archaeal B-family DNA polymerases. PLoS One *12*, e0188005. https://doi.org/10.1371/journal.pone.0188005.

56. Pettersen, E.F., Goddard, T.D., Huang, C.C., Couch, G.S., Greenblatt, D.M., Meng, E.C., and Ferrin, T.E. (2004). UCSF Chimera–a visualization system for exploratory research and analysis. J. Comput. Chem. *25*, 1605–1612. https://doi.org/10.1002/jcc.20084.

57. Gardner, A.F., Jackson, K.M., Boyle, M.M., Buss, J.A., Potapov, V., Gehring, A.M., Zatopek, K.M., Corrêa, I.R., Jr., Ong, J.L., and Jack, W.E. (2019). Therminator DNA Polymerase: Modified Nucleotides and Unnatural Substrates. Front. Mol. Biosci. *6*, 28. https://doi.org/10.3389/fmolb.2019.00028.

58. Ichida, J.K., Horhota, A., Zou, K., McLaughlin, L.W., and Szostak, J.W. (2005). High fidelity TNA synthesis by Therminator polymerase. Nucleic Acids Res. *33*, 5219–5225. https://doi.org/10.1093/nar/gki840.

59. Renders, M., Emmerechts, G., Rozenski, J., Krecmerová, M., Holý, A., and Herdewijn, P. (2007). Enzymatic synthesis of phosphonomethyl oligonucleotides by therminator polymerase. Angew. Chem., Int. Ed. Engl. *46*, 2501–2504. https://doi.org/10.1002/anie.200603435.

60. Mohsen, M.G., Ji, D., and Kool, E.T. (2019). Polymerase synthesis of four-base DNA from two stable dimeric nucleotides. Nucleic Acids Res. *47*, 9495–9501. https://doi.org/10.1093/nar/gkz741.

61. Gardner, A.F., and Jack, W.E. (2002). Acyclic and dideoxy terminator preferences denote divergent sugar recognition by archaeon and Taq DNA polymerases. Nucleic Acids Res. *30*, 605–613. https://doi.org/10.1093/nar/30.2.605.

62. Jegou, T., Chung, I., Heuvelman, G., Wachsmuth, M., Görisch, S.M., Greulich-Bode, K.M., Boukamp, P., Lichter, P., and Rippe, K. (2009). Dynamics of telomeres and promyelocytic leukemia nuclear bodies in a telomerase-negative human cell line. Mol. Biol. Cell *20*, 2070–2082. https://doi.org/10.1091/mbc.e08-02-0108.

63. Crabbe, L., Cesare, A.J., Kasuboski, J.M., Fitzpatrick, J.A.J., and Karlseder, J. (2012). Human telomeres are tethered to the nuclear envelope during postmitotic nuclear assembly. Cell Rep. *2*, 1521–1529. https://doi.org/10.1016/j.celrep.2012.11.019.

64. Chuang, T.C.Y., Moshir, S., Garini, Y., Chuang, A.Y.C., Young, I.T., Vermolen, B., van den Doel, R., Mougey, V., Perrin, M., Braun, M., et al.

(2004). The three-dimensional organization of telomeres in the nucleus of mammalian cells. BMC Biol. *2*, 12. https://doi.org/10.1186/1741-7007-2-12.

65. Adam, N., Degelman, E., Briggs, S., Wazen, R.M., Colarusso, P., Riabowol, K., and Beattie, T. (2019). Telomere analysis using 3D fluorescence microscopy suggests mammalian telomere clustering in hTERT-immortalized Hs68 fibroblasts. Commun. Biol. *2*, 451. https://doi.org/10.1038/s42003-019-0692-z.
66. DeLano, W.L. (2002). Pymol: an open-source molecular graphics tool. CCP4 Newsletter Pro. Crystallogr. *40*, 82–92.
67. Beliveau, B.J., Boettiger, A.N., Avendaño, M.S., Jungmann, R., McCole, R.B., Joyce, E.F., Kim-Kiselak, C., Bantignies, F., Fonseka, C.Y., Erceg, J., et al. (2015). Single-molecule super-resolution imaging of chromosomes and in situ haplotype visualization using Oligopaint FISH probes. Nat. Commun. *6*, 7147. https://doi.org/10.1038/ncomms8147.
68. Willemin, A., Szabó, D., and Pombo, A. (2024). Epigenetic regulatory layers in the 3D nucleus. Mol. Cell *84*, 415–428. https://doi.org/10.1016/j.molcel.2023.12.032.
69. Zheng, H., and Xie, W. (2019). The role of 3D genome organization in development and cell differentiation. Nat. Rev. Mol. Cell Biol. *20*, 535–550. https://doi.org/10.1038/s41580-019-0132-4.
70. Sati, S., and Cavalli, G. (2017). Chromosome conformation capture technologies and their impact in understanding genome function. Chromosoma *126*, 33–44. https://doi.org/10.1007/s00412-016-0593-6.
71. Peng, T., Hou, Y., Meng, H., Cao, Y., Wang, X., Jia, L., Chen, Q., Zheng, Y., Sun, Y., Chen, H., et al. (2023). Mapping nucleolus-associated chromatin interactions using nucleolus Hi-C reveals pattern of heterochromatin interactions. Nat. Commun. *14*, 350. https://doi.org/10.1038/s41467-023-36021-1.
72. Weichenhan, D., Riedel, A., Sollier, E., Toprak, U.H., Hey, J., Breuer, K., Wierzbinska, J.A., Touzart, A., Lutsik, P., Bähr, M., et al. (2023). Altered enhancer-promoter interaction leads to MNX1 expression in pediatric acute myeloid leukemia with t (7; 12)(q36; p13). Preprint at bioRxiv. https://doi.org/10.1101/2023.09.13.557546.
73. Beliveau, B.J., Boettiger, A.N., Nir, G., Bintu, B., Yin, P., Zhuang, X., and Wu, C.T. (2017). In Situ Super-Resolution Imaging of Genomic DNA with OligoSTORM and OligoDNA-PAINT. Methods Mol. Biol. *1663*, 231–252. https://doi.org/10.1007/978-1-4939-7265-4_19.
74. Hottin, A., and Marx, A. (2016). Structural insights into the processing of nucleobase-modified nucleotides by DNA polymerases. Acc. Chem. Res. *49*, 418–427. https://doi.org/10.1021/acs.accounts.5b00544.
75. Tasara, T., Angerer, B., Damond, M., Winter, H., Dörhöfer, S., Hübscher, U., and Amacker, M. (2003). Incorporation of reporter molecule-labeled nucleotides by DNA polymerases. II. High-density labeling of natural DNA. Nucleic Acids Res. *31*, 2636–2646. https://doi.org/10.1093/nar/gkg371.
76. Kropp, H.M., Diederichs, K., and Marx, A. (2019). The Structure of an archaeal B-family DNA polymerase in complex with a chemically modified nucleotide. Angew. Chem., Int. Ed. Engl. *58*, 5457–5461. https://doi.org/10.1002/anie.201900315.
77. Schröder, T., Scheible, M.B., Steiner, F., Vogelsang, J., and Tinnefeld, P. (2019). Interchromophoric Interactions Determine the Maximum Brightness Density in DNA Origami Structures. Nano Lett. *19*, 1275–1281. https://doi.org/10.1021/acs.nanolett.8b04845.
78. Jungmann, R., Avendaño, M.S., Woehrstein, J.B., Dai, M., Shih, W.M., and Yin, P. (2014). Multiplexed 3D cellular super-resolution imaging with DNA-PAINT and Exchange-PAINT. Nat. Methods *11*, 313–318. https://doi.org/10.1038/nmeth.2835.
79. Schnitzbauer, J., Strauss, M.T., Schlichthaerle, T., Schueder, F., and Jungmann, R. (2017). Super-resolution microscopy with DNA-PAINT. Nat. Protoc. *12*, 1198–1228. https://doi.org/10.1038/nprot.2017.024.
80. Solovei, I., Cavallo, A., Schermelleh, L., Jaunin, F., Scasselati, C., Cmarko, D., Cremer, C., Fakan, S., and Cremer, T. (2002). Spatial preservation of nuclear chromatin architecture during three-dimensional fluorescence in situ hybridization (3D-FISH). Exp. Cell Res. *276*, 10–23. https://doi.org/10.1006/excr.2002.5513.
81. Anton, T., Bultmann, S., Leonhardt, H., and Markaki, Y. (2014). Visualization of specific DNA sequences in living mouse embryonic stem cells with a programmable fluorescent CRISPR/Cas system. Nucleus *5*, 163–172. https://doi.org/10.4161/nucl.28488.
82. Ma, H., Naseri, A., Reyes-Gutierrez, P., Wolfe, S.A., Zhang, S., and Pederson, T. (2015). Multicolor CRISPR labeling of chromosomal loci in human cells. Proc. Natl. Acad. Sci. USA *112*, 3002–3007. https://doi.org/10.1073/pnas.1420024112.
83. Xu, Q., Schlabach, M.R., Hannon, G.J., and Elledge, S.J. (2009). Design of 240,000 orthogonal 25mer DNA barcode probes. Proc. Natl. Acad. Sci. USA *106*, 2289–2294. https://doi.org/10.1073/pnas.0812506106.
84. Green, M.R., and Sambrook, J. (2019). Isolation of DNA Fragments from Polyacrylamide Gels by the Crush and Soak Method. Cold Spring Harb. Protoc. *2019*, prot100479. https://doi.org/10.1101/pdb.prot100479.
85. Heine, J., Reuss, M., Harke, B., D'Este, E., Sahl, S.J., and Hell, S.W. (2017). Adaptive-illumination STED nanoscopy. Proc. Natl. Acad. Sci. USA *114*, 9797–9802. https://doi.org/10.1073/pnas.1708304114.
86. Schindelin, J., Arganda-Carreras, I., Frise, E., Kaynig, V., Longair, M., Pietzsch, T., Preibisch, S., Rueden, C., Saalfeld, S., Schmid, B., et al. (2012). Fiji: an open-source platform for biological-image analysis. Nat. Methods *9*, 676–682. https://doi.org/10.1038/nmeth.2019.
87. Bahry, E., Breimann, L., Zouinkhi, M., Epstein, L., Kolyvanov, K., Mamrak, N., King, B., Long, X., Harrington, K.I.S., Lionnet, T., and Preibisch, S. (2022). RS-FISH: precise, interactive, fast, and scalable FISH spot detection. Nat. Methods *19*, 1563–1567. https://doi.org/10.1038/s41592-022-01669-y.

STAR★METHODS

KEY RESOURCES TABLE

REAGENT or RESOURCE	SOURCE	IDENTIFIER
Chemicals, peptides, and recombinant proteins		
5-Propargylamino-dCTP-ATTO-488 (1 mM)	Jena Bioscience	Cat# NU-809-488
5-Propargylamino-dCTP-ATTO-594 (1 mM)	Jena Bioscience	Cat# NU-809-594
5-Propargylamino-dCTP-ATTO-647N (1 mM)	Jena Bioscience	Cat# NU-809-647N-S/L
5-Propargylamino-dCTP-Cy3	Jena Bioscience	Cat# NU-809-CY3-S/L
Diamond™ Nucleic Acid Dye	Promega	Cat# H1181
DiYO-1	AAT Bioquest	Cat# 17580
dNTP Set (100 mM)	Thermo Fisher Scientific	Cat# R0181
Formaldehyde (16%)	Polysciences	Cat# 18814-10
Formamide ≥99.5%	Sigma Aldrich	Cat# F9037
Klenow Fragment (exo-)	Thermo Fisher Scientific	Cat# EP0421
Lambda exonuclease	Thermo Fisher Scientific	Cat# EN0561
Phusion® High-Fidelity DNA Polymerase (Phusion)	New England BioLabs	Cat# M0530 S/L
Q5® High-Fidelity DNA Polymerase (Q5)	New England BioLabs	Cat# M0491 S/L
RNase A	Thermo Fisher Scientific	Cat# EN0531
Taq DNA Polymerase (Taq)	Thermo Fisher Scientific	Cat# EP0401
Therminator™ DNA Polymeras	New England BioLabs	Cat# M0261 S/L
Critical commercial assays		
Monarch® PCR & DNA Cleanup Kit	New England BioLabs	Cat# T1030 S/L
NucleoSpin Gel and PCR Clean-up Kit	Macherey-Nagel	Cat# 740609
Deposited data		
Uncropped polyacrylamide gels	This paper	https://doi.org/10.17632/nskmtr4h9y.1
Experimental models: Cell lines		
IMR-90	Coriell Biorepository	I90-79
J1	ATCC	SCRC-1010
K562	ATCC	CCL-243
U2OS	ATCC	HTB-96
Oligonucleotides		
See Table S1		
Software and algorithms		
Fiji RRID:SCR_002285	Open Source	https://fiji.sc/
Illustrator CC 2023 RRID:SCR_010279	Adobe	www.adobe.com
ImageJ2 (v.1.54h) RRID:SCR_003070	NIH	www.ImageJ.net/
Microsoft Excel	Microsoft	N/A
Pymol (v.2.5.5) RRID:SCR_000305	Schrödinger	https://pymol.org/2/
UCSF ChimeraX (v.1.17.3) RRID:SCR_015872	UCSF	www.rbvi.ucsf.edu/chimera/

RESOURCE AVAILABILITY

Lead contact

Further information and resource requests can be directed to and will be fulfilled by the lead contact Heinrich Leonhardt (h.leonhardt@lmu.de).

Materials availability

NOVA probes were generated using commercially available reagents and services. Sequences and detailed synthesis instructions for generating the probes reported in this study are listed in Table S1 and the Method Details.

Data and code availability

- The uncropped polyacrylamide gels have been deposited at Mendeley Data and are publicly available as of the date of publication. An accession number is listed in the Key Resources Table.
- This paper does not report original code.
- Any additional information required to reanalyze the data reported in this paper is available from the lead contact upon request.

METHOD DETAILS

Cell culture

K562 cells were cultivated in Dulbecco's modified Eagle's medium (DMEM), 10% fetal bovine serum (FBS), 100 U/mL penicillin and 100 μg/mL streptomycin. U2OS cells were maintained in McCoy's 5A medium supplemented with 10% FBS, 100 U/ml penicillin, and 100 μg/mL streptomycin at 37 °C in 5% CO_2. IMR-90 cells were cultured in DMEM, 20% FBS, 1× MEM Non-essential amino acids, and 100 U/mL penicillin, 100 μg/mL streptomycin.

Mouse embryonic stem cells (ESCs) were maintained on culture dishes treated with 0.2% gelatin in DMEM containing 16% FBS, 0.1 mM β-mercaptoethanol, 2 mM L-glutamine, 1× MEM Non-essential amino acids, 100 U/mL penicillin, 100 μg/mL streptomycin, homemade recombinant LIF, and 2i (1 μM PD032591 and 3 μM CHIR99021). For imaging, ESCs were seeded on plates that have been pre-treated with Geltrex diluted 1:100 in DMEM/F12 overnight at 37 °C in 5% CO_2. Cells were passaged every 2–4 days. All cell lines were regularly tested for Mycoplasma contamination by PCR.

Probe design

All generated probe sets are listed in Table S1. NOVA-probes labeling murine major satellites and human repetitive regions (chrX (p11.1) or chr13 (q34), telomeres) were adapted from previously published sequences.[81,82] Target regions ("A": chr11:55810891-55816978 "B": chr11:55817064-55821430) were chosen in hg38 and 60 unique oligonucleotides were selected and filtered, respectively.[24] Barcodes of xNOVA-probes containing repetitive sequences (10-mers) were obtained from previous published data.[28] To generate non-repetitive barcodes, pairs of orthogonal sequences from[83] were merged. Then, the barcodes were filtered for those containing cytosines every 10 bases and trimmed to the required length.

NOVA-FISH Probe synthesis

5′-phosphorylated templates and unlabeled primers were ordered from IDT or Eurofins. Equimolar amounts of 5′-phosphorylated templates and primers (0.10–0.17 nmol each) were combined to a final concentration of 1 μg DNA/μL in 1x ThermoPol Reaction Buffer.

The annealing temperatures were adjusted to the length of the primers. For NOVA-probes (40 nt long templates, 20 nt long primers), the sample was heated up to 95°C for 5 min followed by a stepwise cool-down (1°C/minute) to room temperature. For xNOVA-probes or xNOVA-pools (50–70 nt long templates, 40 nt long primers) the sample was heated up to 95°C for 5 min followed by a stepwise cool-down (1°C/2 min) to 60°C. Complex xNOVA-probe sets were synthesized by adding 2-fold excess of primer sets (e.g., primer 31–40 against "A") to the template pool.

NOVA- and xNOVA-probes were synthesized by adding 2–4 μg annealed DNA (2–4 μL of the solution) to a reaction mixture containing 0.25 mM dATP/dGTP/dTTP each, 0–0.25 mM dCTP, 0–0.25 mM dye-labeled dCTP and 3 U Therminator DNA polymerase in 1x ThermoPol Reaction Buffer (10 μL total volume). The ratios of dye-labeled dCTP to unlabeled dCTP varied depending on the desired labeling density. The reaction was carried out for 60 min at 72°C.

To remove single-stranded DNA, NucleoSpin Gel and PCR Clean-up Kit (Macherey-Nagel) was used according to the manufacturer's instructions. 9 volumes of buffer NTI (provided by the manufacturer) were added to one volume of sample before binding. After washing, the DNA was eluted twice in 22 μL ddH_2O (44 μL final volume). In the next step, 5′-phosphorylated strands were removed by adding 1 μL Lambda exonuclease (10 U/μL) and 5 μL Lambda exonuclease reaction buffer (10x) to a final volume of 50 μL and incubating for 30 min at 37°C. The synthesized probes were then purified using the Monarch PCR & DNA Cleanup Kit (New England BioLabs) according to the manufacturer's instructions and the quality was verified on denaturing 12–16% polyacrylamide gels.

Quality control and purification

The absorbance of samples was measured at 260 nm and 488 nm, 596 nm, or 647 nm depending on the incorporated fluorophore using a Nanodrop 2000 spectrophotometer (Thermo Fisher Scientific). To assess the quality of generated probes, samples were denatured in 90% formamide, 0.5% EDTA, 0.1% Xylene cyanol, 0.1% bromophenol blue and loaded onto a 12% polyacrylamide gel containing 6 M urea. The gel was incubated in 1x TBE buffer containing 1x Diamond Nucleic Acid Dye for 30 min at room temperature to visualize single-stranded DNA.

Complex probe sets labeling target region "A" or "B" were further purified following the "crush and soak" method with adaptations.[84] Briefly, segments of the polyacrylamide gel containing the band of interest were cut out and 2 volumes of a buffer containing 10 mM magnesium acetate tetrahydrate, 0.5 M ammonium acetate, 1 mM EDTA (pH 8.0) and 0.1% (w/v) SDS was added followed by incubation at 37°C for 16–24 h. The samples were then centrifuged at 13000 x g for 1 min and the supernatant was once more purified

using the Monarch PCR & DNA Cleanup Kit (New England BioLabs). We expect the "crush and soak" method to improve signal strength if low labeling densities are used during extension.

Polymerase Screens

Polymerases were tested for their ability to incorporate dCTP-ATTO488, dCTP-ATTO594, or dCTP-ATTO647N into oligonucleotides. The maximum number of incorporated dCTP-dye in the probe was eight (CATCCTGAAGGAATGGTCCATG**C**TTA**CC**TGGG **CCC**AT**CC**T).

For detailed information about the reaction conditions see Table S2. 0.1 nmol annealed DNA was added to the recommended reaction mixtures (10 μL final volume) and 5 U of the respective polymerase was added. The following temperatures were used during synthesis: Klenow exo-at 30°C, Taq at 64°C, Q5 at 64°C, Phusion at 64°C, Therminator DNA polymerase at 72°C. All reactions were carried out for 60 min and the reactions were stopped by adding 1 μL 0.5 M EDTA. We did not observe notable differences in incorporation efficiency between the reported results and reactions carried out at higher temperatures (Klenow exo-at 37°C, Taq at 72°C, Q5 at 72°C, Phusion at 72°C, Therminator DNA Polymerase at 75°C) (figure not shown). The absorbance of synthesized products was measured at 200–700 nm on Nanoquant plates using a Tecan Spark microplate reader (Tecan) and choosing the following dye-correction factors: CF_{260}(ATTO488): 0.22, CF_{260}(ATTO594): 0.22, CF_{260}(ATTO647N): 0.04. The depicted data contained at least two measurements per biological replicate.

HPLC

HPLC was used to characterize the number of incorporated fluorophores in NOVA probes with low fluorophore input in synthesis (Figures S3G and S3H). ATTO594-labeled and ATTO647N-labeled probes (0.31 nmol or 0.34 nmol) were analyzed and purified by reverse-phase HPLC using an Agilent Technologies 1260 Infinity II System with a G7165A detector equipped with an EC 250/4 Nucleodur 100-3 C18ec column from Macherey Nagel. A gradient of 0–80% of buffer B in 45 min at 60°C with a flow rate of 1 mL/min was applied. The following buffer system was used: buffer A: 100 mM NEt_3/HOAc, pH 7.0 in H_2O and buffer B: 100 mM NEt_3/HOAc, pH 7.0 in H_2O/MeCN 20/80. The fractions of each signal peak were combined, and the solvents were concentrated by vacuum centrifugation.

Sample preparation and fluorescence *in situ* hybridization

Fluorescence *in situ* hybridization was performed as previously described.[24] Adherent cells were grown overnight on glass coverslips (1.5, 18 × 18 mm, Marienfeld), washed twice with 1x Dulbecco's Phosphate Buffered Saline (PBS), and fixed using osmotically balanced and methanol-free 4% formaldehyde for 10 min at room temperature. Alternatively, PBS-washed suspension cells were resuspended in a small volume of PBS at a density of 1 million cells per mL and applied to poly-L-lysine coated glass coverslips followed by the addition of methanol-free 4% formaldehyde for 10 min at room temperature. The slides were washed twice in 1x PBS for 5 min and the cells were permeabilized in 1X PBS containing 0.5% Triton X-100 for 15 min. After two successive washing steps in 1x PBS, 0.1 M HCl was added to the slides for 5 min. The slides were washed twice with 2 x SSC and were placed onto a solution containing 1 μg/mL RNase for 30 min at 37°C in a wet chamber. Then, adherent or suspension cells were pre-equilibrated in 2x SSC containing 50% formamide for 60 min or overnight, respectively, inverted onto 8 μL of hybridization solution, and sealed with rubber cement (Marabu). The slides were placed on a heat block set to 81°C for 3 min and incubated at 37°C overnight (16–20 h).

On the second day, slides were washed twice with 2x SSC for 15 min followed by two successive 7-min washes in 0.2x SSC containing 0.2% Tween 20 at 56°C. Then, slides were washed with 4x SSC containing 0.2% Tween 20 and with 2x SSC for 5 min, respectively.

For oligoFISH probes, a second hybridization step was performed for 30 min at room temperature. The slides were then washed once with 2x SSC containing 30% formamide for 7 min at 37°C, twice with 2 x SSC for 5 min, once with 0.2X SSC containing 0.2% Tween 20 at 56°C, once with 4x SSC containing 0.2% Tween 20 for 7 min at room temperature and once with 2x SSC for 5 min.

DNA was counterstained with DAPI (1 μg/mL in 2x SSC) for 10 min and washed twice with 2x SSC. For STED microscopy, nuclei were counterstained with or DiYO-1 (12.5 nM in 2x SSC) for 30 min and washed twice with 2x SSC for 5 min, respectively. Coverslips were mounted on microscopic slides with MOWIOL (2.5% DABCO, pH 7.0), dried for 30 min, and sealed with nail polish.

Image acquisition

Confocal images were acquired using a Nikon TiE microscope equipped with a Yokogawa CSU-W1 spinning-disk confocal unit (50 μm pinhole size), an Andor Borealis illumination unit, Andor ALC600 laser beam combiner (405 nm/488 nm/561 nm/640 nm), Andor IXON 888 Ultra EMCCD camera, and a Nikon 100×/1.45 NA oil immersion objective. The microscope was controlled by software from Nikon (NIS Elements, ver. 5.02.00).

Super-resolution was carried out on a 2C STED 775 QUAD Scan microscope (Abberior Instruments) equipped with a 100x 1.4 NA UPlanSApo oil immersion objective lens (Olympus), 3 pulsed excitation lasers (485 nm, 594 nm, 640 nm) and a pulsed depletion laser of 775 nm.

3D STED microscopy of telomers using adaptive illumination

To avoid photobleaching NOVA-FISH stained telomers of IMR90 cells in 3D, stacks were acquired using adaptive illumination STED microscopy.[85] Cells were recorded using a pixel size of 30 nm, z-steps of 80 nm, a 10 μs dwell time, and a pinhole size of 50 μm.

Automated STED microscopy for two-color NOVA-FISH

Automated STED microscopy was performed according to Brandstetter et al..[24] The acquisition of 3D confocal stacks was automated using home-written Python scripts to control the microscope. Spots within confocal scans were detected using a Laplacian-of-Gaussian blob detector for both channels. Detected spots no further apart than 5 pixels from another spot in the other channel were imaged using 3D STED settings. This process was repeated for each detected spot pair within a confocal scan. Following a spiral pattern, the stage was moved to the next overview to repeat the confocal scan and the subsequent detailed STED acquisition until a specified amount of time elapsed.

Image analysis

For the analysis of the effects of labeling density (Figures 2E–2G), cells in confocal z-stacks of major satellites were segmented first via automatic thresholding in a z-maximum projection of the DAPI channel followed by a second round of thresholding in the 640nm (rel. binding) channel to segment major satellites. In the segmented areas, intensities of both the 488nm (rel. brightness) and the 640nm (rel. binding) channels were measured, background, determined by a manually selected ROI outside the cells, was subtracted, and measurements were averaged (median) per cell. For the plots, measurements were normalized to the intensity at 100% for the binding channel and at 25% for the brightness channel. Analysis was carried out using Fiji.[86]

For analysis of image data of repetitive and non-repetitive loci (in Figures 1D–1F; Figures 3B and 3C, Figures 3F and 3G; Figures 4D; S4C), nuclear segmentation maps of confocal images stained with DAPI or DiYO-1 were obtained using Otsu thresholding. FISH spots within segmentation maps were detected using a Laplacian-of-Gaussian blob detector (Figure 3F and 3G; Figure S4C). Alternatively, FISH spots were detected in each channel using RSFISH[87] and detection threshold parameters were adjusted if necessary (in Figures 1D–1F; Figures 3B and 3C; Figure 4D). Segmentation maps were used to calculate the total number of spots per cell, to obtain the mean background signal within single nuclei to calculate the spot signal over the nucleus background, and the signal-to-noise ratio of single spots. For Figure 4D, distances <500 nm between A and B were considered co-localizing.

Analysis of automated STED measurements of FISH spot pairs was performed as previously described.[24] Automated image acquisition generated large quantities of data requiring an additional quality control step. To filter out low-quality images, we used a machine learning-based classifier (Random Forest) to label images as "good" or "bad". The classifier was trained with a ground truth dataset created by an experienced scientist who manually sorted images.

Detailed spot analysis was performed on images passing this QC step. Subpixel localization of FISH spots in both channels was performed by fitting a multidimensional Gaussian function plus a constant background using the Levenberg-Marquardt algorithm. The peak height of the fitted Gaussians was used to determine spot intensity.

QUANTIFICATION AND STATISTICAL ANALYSIS

The experiments shown in this study were performed as three biologically independent experiments ($n = 3$) and the figures contain pooled data. No statistical methods were used to predetermine the sample size. Images depicted are representative images from the experiments and dotted lines indicate the outlines of the cells. Data plotted as boxplots indicate the 25th and 75th percentiles, with the whiskers showing the minima and maxima (5th and 95th percentiles), black circles indicating the outliers, and the horizontal line showing the median. Some data are plotted in bar graphs as the mean ± SD. Data was normalized by the median of the first depicted condition in the replicates, if not stated otherwise. Significance levels were tested by non-parametric two-sided Wilcoxon tests or pairwise comparisons using the Wilcoxon rank-sum test with Bonferroni's correction for multiple testing (* = $p < 0.05$, ** = $p < 0.01$, *** = $p < 0.001$). Sample sizes for all of the graphs are indicated in the figures or figure legends.

Cell Reports Methods, Volume *4*

Supplemental information

Generation of densely labeled oligonucleotides for the detection of small genomic elements

Clemens Steinek, Miguel Guirao-Ortiz, Gabriela Stumberger, Annika J. Tölke, David Hörl, Thomas Carell, Hartmann Harz, and Heinrich Leonhardt

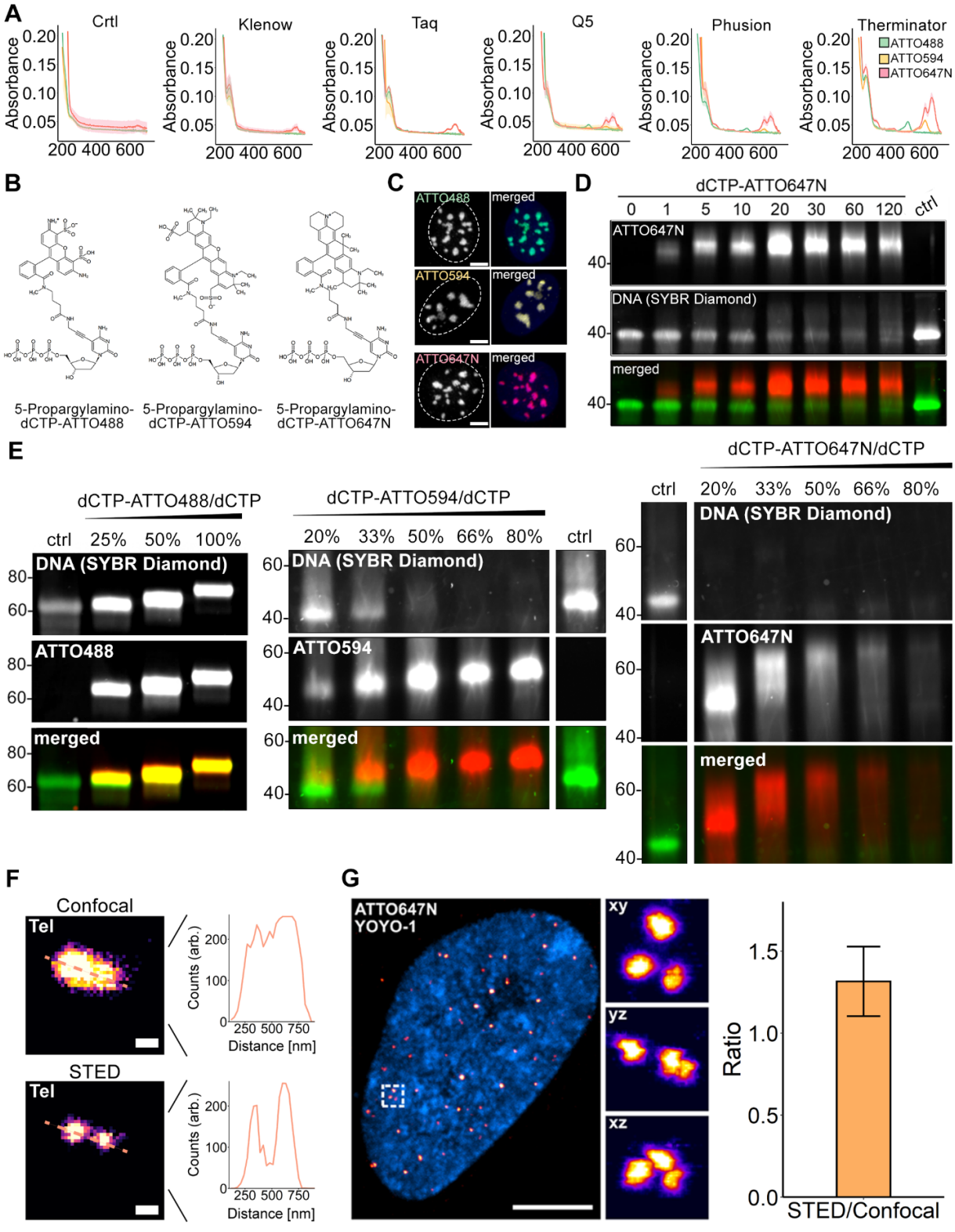
A
Crtl
Klenow
Taq
Q5
Phusion
Therminator
Absorbance
0.20
0.15
0.10
0.05
200 400 600
ATTO488
ATTO594
ATTO647N
B
5-Propargylamino-dCTP-ATTO488
5-Propargylamino-dCTP-ATTO594
5-Propargylamino-dCTP-ATTO647N
C
ATTO488
ATTO594
ATTO647N
merged
D
dCTP-ATTO647N
0 1 5 10 20 30 60 120 ctrl
ATTO647N
DNA (SYBR Diamond)
merged
40
E
dCTP-ATTO488/dCTP
ctrl 25% 50% 100%
dCTP-ATTO594/dCTP
20% 33% 50% 66% 80% ctrl
dCTP-ATTO647N/dCTP
ctrl 20% 33% 50% 66% 80%
DNA (SYBR Diamond)
ATTO488
ATTO594
ATTO647N
merged
60
80
40
F
Confocal
STED
Tel
Counts (arb.)
200
100
0
250 500 750
Distance [nm]
G
ATTO647N
YOYO-1
xy
yz
xz
Ratio
1.5
1.0
0.5
0.0
STED/Confocal

Supplementary Figure 1 Synthesizing NOVA-probes harboring different fluorophores. Related to Figure 1. (A) Absorption spectra of synthesized probes. The line depicts the mean absorption and the area indicates the standard deviation of three experiments with at least two separate measurements (n = 3). The incorporated nucleotides are indicated as follows: ATTO488 = green, ATTO594 = yellow, ATTO647N = red. (B) Structural formulas of used modified nucleotides. Dyes (ATTO488, ATTO594, ATTO647N) are linked to 5C positions of cytosines. The structures were provided by the manufacturer (Jena Bioscience). (C) Labeling major satellites in J1 cells with NOVA-FISH using three different fluorophores. All probes (maj. Sat.-ATTO488, maj. Sat.-ATTO594, maj. Sat.-ATTO647N) were generated using a one to four molar ratio of dye-labeled to unlabeled nucleotides. Scale bars, 5 µm (D) Therminator DNA polymerase effectively generates dye-labeled probes. The synthesis was carried out between 0-120 minutes using 0.15 nmol DNA and 3 U Therminator polymerase. Fluorescent DNA (ATO647N) and DNA (SYBR-Diamond) are shown in red and green, respectively. (E) Generating probes with different labeling densities. Left: Synthesis of ATTO488-labeled probes detecting major satellites. Middle: Synthesis of ATTO594-labeled probes targeting a subtelomeric region in chromosome 13. Right: Synthesis of ATTO647N-labeled probes detecting a subtelomeric region in chromosome 13. Different dye-labeled dCTP to dCTP ratios were used (25%, 50%, 100% or 20%, 33%, 50%, 66% 80%). Unlabeled probes were used as a control. Fluorophores and stained DNA (SYBR Diamond) are shown in red and green, respectively. (F) Super-resolution microscopy uncovers clustered telomeres. Representative image of two clustered telomeres using confocal microscopy or STED microscopy. Scale bars, 200 nm. (G) Telomere clustering is a common phenomenon in mitotic cells. Representative image of telomeres in IMR-90 cells using 3D-STED microscopy. Detailed view (white box) in three dimensions. Scale bar, 5 µm. Ratio of telomeres detected with STED or confocal microscopy in the same cells is depicted. Telomeres were counted in 10 individual cells from three experiments (n = 3). The black lines depict the mean.

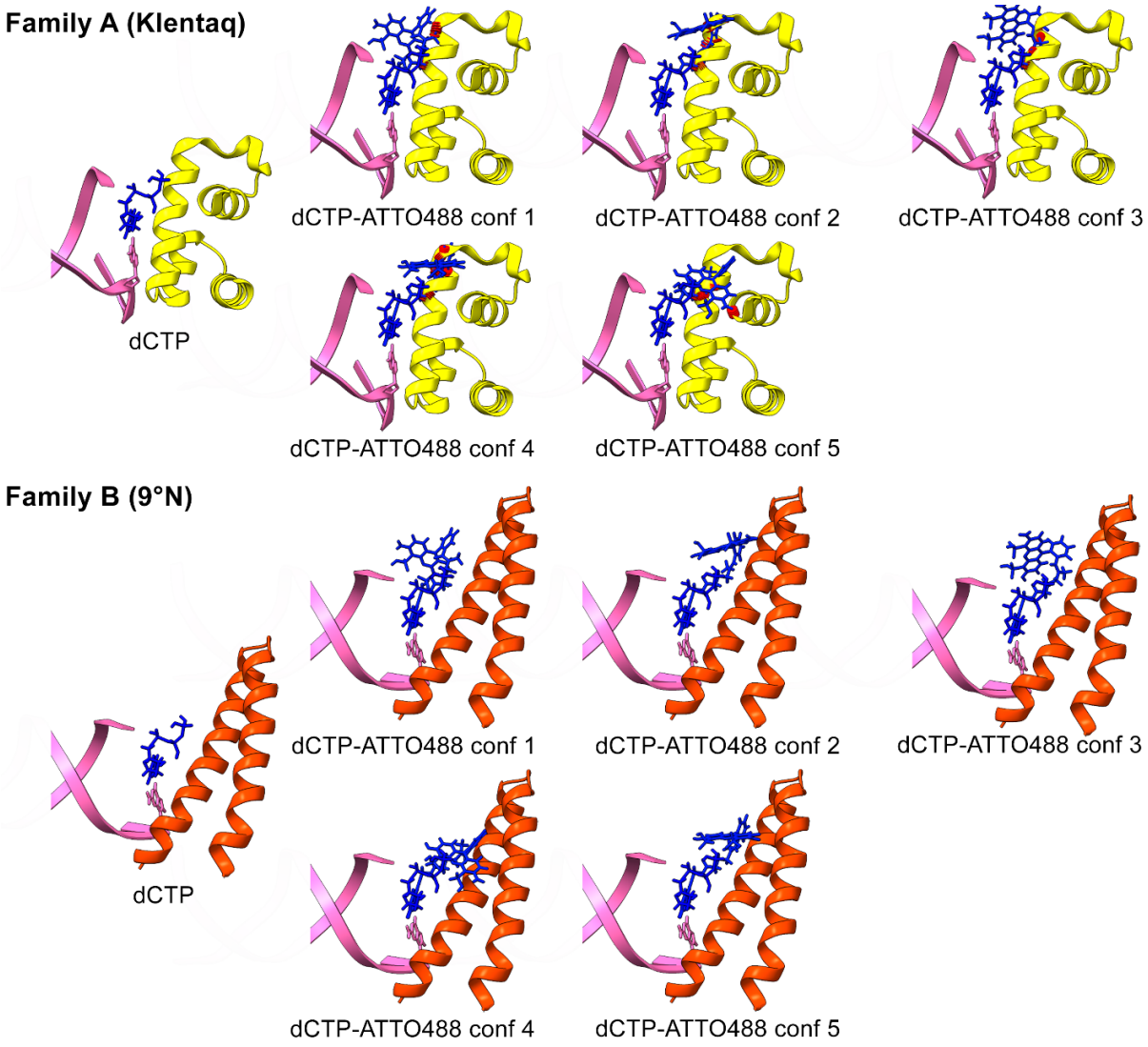

Supplementary Figure 2 Modeling the proximity of dCTP-ATTO488 to family A or family B finger domains. Related to Figure 1. Finger domains are shown in yellow (Klentaq) and orange (9°N DNA polymerase) with DNA in pink and the substrate in blue. Five different conformations of dCTP-ATTO488 (conf1-5) were superimposed on cytosine. Distances between the finger domain and dCTP-ATTO488 < 1 Å are depicted as red knobs. The finger domains are shown in the closed state. The figure was generated with UCSF Chimera (v.1.17.3, RRID:SCR_015872) by using the structures 3RTV and 5OMV [S1-S3].

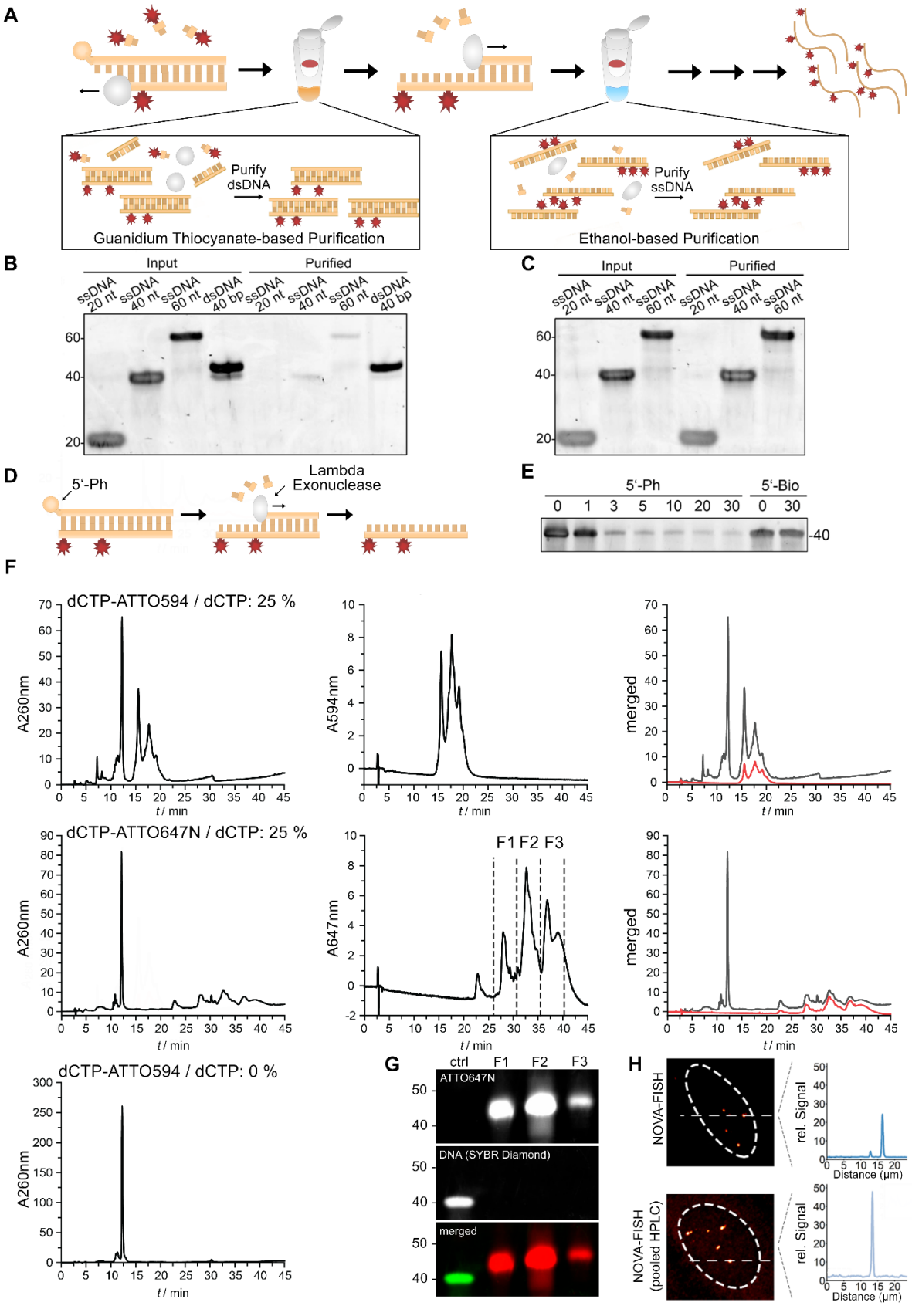
A
Purify dsDNA
Guanidium Thiocyanate-based Purification
Purify ssDNA
Ethanol-based Purification
B
Input
Purified
ssDNA 20 nt
ssDNA 40 nt
ssDNA 60 nt
dsDNA 40 bp
C
D
5'-Ph
Lambda Exonuclease
E
5'-Ph
5'-Bio
0 1 3 5 10 20 30 0 30
-40
F
dCTP-ATTO594 / dCTP: 25 %
A260nm
A594nm
merged
t / min
dCTP-ATTO647N / dCTP: 25 %
A647nm
F1 F2 F3
dCTP-ATTO594 / dCTP: 0 %
G
ctrl F1 F2 F3
ATTO647N
DNA (SYBR Diamond)
merged
H
NOVA-FISH
NOVA-FISH (pooled HPLC)
rel. Signal
Distance (µm)

Supplementary Figure 3 Optimization of probe purification. Related to STAR Methods. (A) Schematic highlighting two purification steps in the protocol. While guanidium thiocyanate-based purification enriches double-stranded DNA, ethanol-based purification purifies single-stranded oligonucleotides. (B) Guanidium thiocyanate-based purification yields double-stranded DNA. ssDNA (20 nt, 40 nt, 60 nt) and dsDNA (40 bp) were loaded before (input) and after (purified) purification. (C) Ethanol-based purification yields single-stranded DNA. ssDNA (20 nt, 40 nt, 60 nt) was loaded before (input) and after (purified) purification. (D) Schematic of lambda exonuclease-mediated degradation. Lambda exonuclease selectively removes 5'-phosphorylated (5'-Ph) strands. (E) Removal of the 5'-phosphoryated template. Templates were incubated with 10 U lambda exonuclease. 5-biotinylated oligonucleotides were used as a control. (F) HPLC of NOVA-FISH probes. Probes were synthesized with Therminator DNA Polymerase using a one to four molar ratio of dye-labeled to unlabeled nucleotides (highest possible number of incorporated fluorophores: 8). The absorptions of ATTO594-labeled and ATTO647N-labeled probes were measured at 260 nm / 594 nm and 260 nm / 647 nm, respectively. Local peaks indicate probes with varying numbers of fluorophores. Probes synthesized without modified nucleotides were used as a control (left). (G) Polyacrylamide gel reveals a visible shift between populations with different fluorophore numbers. Three fractions (F1, F2, F3) were isolated from (F) through preparative HPLC. The precise mechanism of SYBR-Diamond-ssDNA interactions has yet to be elucidated but we observed that the presence of fluorophores in the probe impacts staining efficiency. Unlabeled DNA was used as a control (ctrl). (H) Side-by-side comparison of unpurified and purified NOVA-probes. To evaluate the benefits of HPLC purification, we conducted FISH in U2OS cells using NOVA-probes before and after HPLC purification. The relative signal intensity along the dotted line is depicted. Images were acquired at the same conditions.

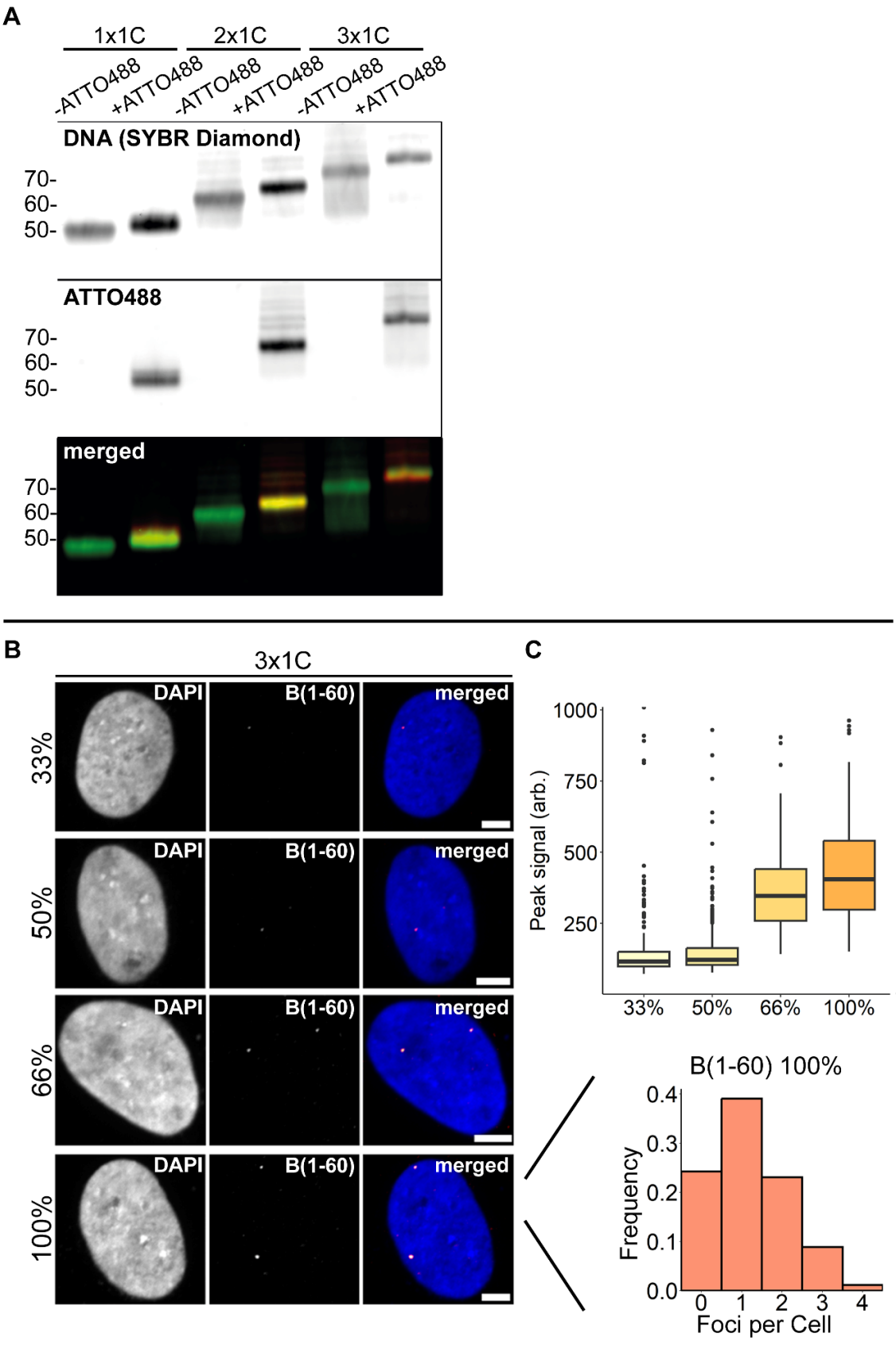
A
1x1C
2x1C
3x1C
-ATTO488
+ATTO488
-ATTO488
+ATTO488
-ATTO488
+ATTO488
DNA (SYBR Diamond)
70-
60-
50-
ATTO488
70-
60-
50-
merged
70-
60-
50-
B
3x1C
DAPI
B(1-60)
merged
33%
50%
66%
100%
C
Peak signal (arb.)
1000
750
500
250
33%
50%
66%
100%
B(1-60) 100%
Frequency
0.4
0.3
0.2
0.1
0.0
0
1
2
3
4
Foci per Cell

Supplementary Figure 4 Characterization of xNOVA-probes. Related to Figure 3. (A) Synthesis of 1C, 2x1C, or 3x1C probes carrying ATTO488 dyes. Stained DNA (SYBR Diamond) and fluorophores (ATTO488) are shown in green and red, respectively. (B) Representative confocal image of a non-repetitive region (“B”, see Figure 4A) in U2OS cells. “B” was labeled with 60 xNOVA-probes (3x1C) containing increasing labeling densities (33%, 50%, 66%, 100%). Scale bars, 5 µm. (C) xNOVA-FISH signals increase with higher labeling densities. Detected FISH intensities are displayed as boxplots. The signal was normalized by the background. Histogram of the number of foci detected in U2OS cells (n = 169). The values were normalized by the total number of cells.

	Manufacturer	Input	Costs
NOVA-FISH			
1. Consumables (0.25 nmol, 100 FISH slides)			
dNTP Mix (10 mM each)	ThermoFisher Scientific	2,5 µl	0,10 €
5-Propargylamino-dCTP-ATTO-647N (1mM)	Jena Bioscience	0,25-1,25 µl*	2,95-14,675 €*
Therminator™ DNA Polymerase	New England Biolabs	3 U	1,815 €
Monarch® PCR & DNA Cleanup Kit (250x)	New England Biolabs	1 Column	1,5 €
NucleoSpin Gel and PCR Clean-up Kit (250x)	Macherey-Nagel	1 Column	0,97 €
Thermo Scientific Lambda Exonuclease (1000 U)	ThermoFisher Scientific	10 U	1,02 €
Consumables Costs:			**8,4-20,08 €**
2. DNA strands (for 100 Reactions)			
For 1 Probe:			
Template Strand (25 nmol)	IDT	3 µg	21,66 €
Primer Strand (25 nmol)	IDT	1,5 µg	2,33 €
Total Costs:			**32.35-44.07 €**
For 50 Probes:			
Template Pool (50 pmol / oligo)	IDT	3 µg	106,00 €
Primer Pool (50 pmol / oligo)	IDT	1,5 µg	106,00 €
Total Costs:			**220,36-232,082 €**
For 5 x 10 Probes:			
Template Pool (50 pmol / oligo)	IDT	3 µg	106,00€
Primer Plate (25 nmol / oligo)	Merck	1,5 µg	220 €
Total Costs:			**367,79-426,41 €**

Supplementary Table 2 Calculated costs of NOVA-probe synthesis. Related to STAR Methods.

*depending on the desired labeling density (20%, 100% fluorophore input in synthesis shown).

	Manufacturer	Yield	Costs
oligoFISH (one-time purchase)			
End-Labeled Secondary Probe (ATTO647N)	IDT	100 nmol***	204,97 €
For 1 Probe:			
Primary Probe	IDT	25 nmol	7,00 €
Total Costs:			**7,00 € (211,97 €)***
For 50 Probes:			
Primary Probe Pool	IDT	50 pmol/oligo	106,00 €
Total Costs:			**106,00 € (310,97 €)***
For 5 x 10 Probes:			
Primary Probe Plate	Merck	(25 nmol / oligo in plate)	330 €
Total Costs:			**330,00 € (534,97 €)***

Supplementary Table 3 Calculated costs of OligoFISH probes. Related to STAR Methods. *211,97 €, 310,97 €, or 534,97 € if a 3'-labeled readout probe has to be ordered.

	Manufacturer	Yield	Costs
End-Labeled Probes (one-time purchase)			
For 1 Probe:			
End-labeled Primary Probe (ATTO647N)	IDT	100 nmol*	**204,97 €**
For 50 Probes:			
End-labeled Primary Probe Plate (ATTO647N)	Eurofins Genomics	10 nmol / oligo	**4845 €**
For 5 x 10 Probes:			
End-labeled Primary Probe Plate (ATTO647N)	Eurofins Genomics	10 nmol / oligo	**4845 €**

Supplementary Table 4 Calculated costs of end-labeled probes. Related to STAR Methods.

*minimum synthesis scale

REFERENCES

S1. Pettersen, E.F., Goddard, T.D., Huang, C.C., Couch, G.S., Greenblatt, D.M., Meng, E.C., and Ferrin, T.E. (2004). UCSF Chimera--a visualization system for exploratory research and analysis. J Comput Chem *25*, 1605-1612. https://doi.org/10.1002/jcc.20084.

S2. Betz, K., Malyshev, D.A., Lavergne, T., Welte, W., Diederichs, K., Dwyer, T.J., Ordoukhanian, P., Romesberg, F.E., and Marx, A. (2012). KlenTaq polymerase replicates unnatural base pairs by inducing a Watson-Crick geometry. Nat Chem Biol *8*, 612-614. https://doi.org/10.1038/nchembio.966.

S3. Kropp, H.M., Betz, K., Wirth, J., Diederichs, K., and Marx, A. (2017). Crystal structures of ternary complexes of archaeal B-family DNA polymerases. PLoS One *12*, e0188005. https://doi.org/10.1371/journal.pone.0188005.

2.2 Nanoscale Dynamics of Enhancer-Promoter Interactions during Exit from Pluripotency

Stumberger, G., Hörl, D., Tsouraki, D., Steinek, C., Oudelaar, A. M., Leonhardt, H. and Harz, H. (2025) *Nucleic Acids Research*, 53, gkaf1255.

DOI: 10.1093/nar/gkaf1255

Nucleic Acids Research, 2025, **53**, gkaf1255
https://doi.org/10.1093/nar/gkaf1255
Gene regulation, Chromatin and Epigenetics

Nanoscale dynamics of enhancer–promoter interactions during exit from pluripotency

Gabriela Stumberger[1], David Hörl[1], Dimitra Tsouraki[2], Clemens Steinek[1], A. Marieke Oudelaar[2], Heinrich Leonhardt[1,*], Hartmann Harz[1,*]

[1]Human Biology & Bioimaging, Faculty of Biology, Ludwig-Maximilians-Universität München, Munich 81377, Germany
[2]Genome Organization and Regulation, Max Planck Institute for Multidisciplinary Sciences, Göttingen 37077, Germany

*To whom correspondence should be addressed Email: harz@biologie.uni-muenchen.de
Correspondence may also be addressed to Heinrich Leonhardt. Email: h.leonhardt@biologie.uni-muenchen.de

Abstract

While compelling genetic evidence supports the role of enhancers in regulating promoter activity even over large genomic distances, it remains unclear to what extent physical proximity to promoters is required. To address this, we combined fluorescence *in situ* hybridization (FISH) with super-resolution microscopy and Tri-C to examine enhancer–promoter (E–P) distances and regulatory element clustering at regulated loci (*Nanog*, *Dppa3*, *Dnmt3a*, *Sox2*, *Prdm14*) during the transition from naive to primed pluripotency in mouse embryonic stem cells. Despite transcriptional changes of several orders of magnitude, most genes show no major alterations in median E–P distances or in the probability of multiway contacts across states. However, Tri-C reveals a weak enrichment of multiway contacts at *Nanog* in naive cells, where it is highly expressed. Because transcription often occurs in transient bursts within a subset of cells, we combined RNA and DNA FISH to identify active alleles. For *Nanog* and *Dppa3*, reduced E–P distances correlate with transcriptional activity. Together, these findings support models in which transcription is associated with transient E–P proximity and suggest that multiway contact formation among regulatory elements may contribute to gene regulation.

Graphical abstract

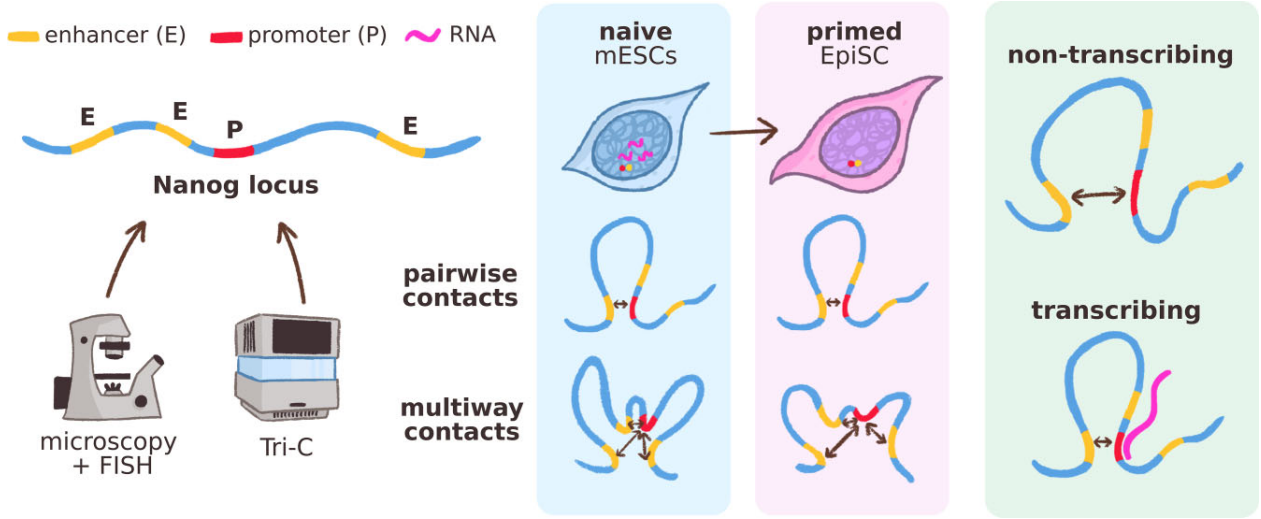

Introduction

In recent years, it has become clear that in addition to genetic elements such as enhancers and transcription factors, physical aspects such as the spatial and temporal proximity of these elements also regulate transcription, which is important for disease [1] and development [2]. While it is commonly accepted that enhancer–promoter (E–P) interactions can drive gene expression through the recruitment of transcription factors and RNA Pol II, several conflicting models describe how regulatory elements communicate (reviewed in [3]).

On the one hand, action-at-a-distance models propose that direct physical contact between enhancers and promoters is not required for a functional interaction. This view is supported by imaging studies, which report average E–P distances of ~200–350 nm [4–11] at transcriptional activation, and by observations showing no [4, 6, 12, 13] or even inverse correla-

Received: January 20, 2025. **Accepted:** October 15, 2025

tion between E–P proximity and transcription at the respective locus [11, 14]. Some variants of these models suggest that E–P communication occurs via phase-separated compartments enriched in transcription factors, coactivators, and RNA polymerase II, ranging several hundred nanometers in diameter [6, 15–19]. Alternatively, the transcription factor activity gradient model posits that enhancer-bound coactivators (e.g. p300) modify nearby transcription factors (e.g. acetylation), creating a gradient of active TFs diffusing from the enhancer [20]. On the other hand, structural studies of various components involved in transcription (eg. Mediator–Pol II pre-initiation complex) [21–24] and measurements showing reduced E–P distances upon transcriptional activation [9, 10, 25–28], support a direct-contact model, in which enhancers physically interact with promoters over short spatial distances. This discussion is further complicated by the fact that eukaryotic genes, especially those encoding developmental regulators, are typically regulated by multiple enhancers. Recent studies have suggested the existence of multi-enhancer hubs or nested microcompartments, where several (genomically distant) *cis* regulatory elements cluster in close spatial proximity to each other, activating transcription [29–31]. However, it is still unknown how frequent these multiway hubs are in single cells and whether they play any role in regulating gene expression. Another subject of discussion is the duration of communication between the respective elements. While classical studies assume stable loops, live cell studies show that the interactions of chromatin elements are dynamic, with contact durations in the range of 10–30 min, possibly even significantly shorter in the case of E–P interactions (reviewed in [3]).

Both sequencing-based and microscopic methods for studying genome architecture have undergone significant advances in recent years [27, 32–42] and have led to a deeper understanding of genome organization. These two methodological approaches are complementary: while microscopy can provide single-cell data, sequence-based methods enable the detection of rare events within large populations.

Here, we utilize oligo-based DNA fluorescence *in situ* hybridization (FISH) combined with super-resolution microscopy and Tri-C, to investigate E–P 3D distances of five differentially expressed genes (*Nanog*, *Dppa3*, *Dnmt3a*, *Sox2*, *Prdm14*) during the naive to primed transition in mouse embryonic stem cells (mESCs). This developmental transition is known to involve extensive epigenetic reprogramming and conformational changes at regulatory elements [43–46]. We observe that for most, but not all measured genes, both pairwise and multiway E–P conformations undergo only minor changes in distance and contact frequency between naive and primed states. Tri-C data reveal a modest enrichment of multiway contacts at the *Nanog* locus in naive cells, where this protein is highly expressed. Furthermore, we could show that at the *Nanog* and *Dppa3* loci, actively transcribed alleles display significantly shorter E–P distances, supporting the notion that spatial interactions between enhancers and promoters are transient.

Materials and methods

Cell culture

Naive J1 mESCs were cultured in serum-free media consisting of: N2B27 [50% neurobasal medium (Life Technologies), 50% Dulbecco's modified Eagle's medium (DMEM)/F12 (Life Technologies)], 2i [1 μM PD032591 and 3 μM CHIR99021 (Axon Medchem)], 1000 U/ml recombinant leukemia inhibitory factor (LIF; Millipore), and 0.3% bovine serum albumin (BSA; Gibco), 2 mM L-glutamine (Life Technologies), 0.1 mM B-mercaptoethanol (Life Technologies), N2 supplement (Life Technologies), and B27 serum-free supplement (Life Technologies). Naive mESCs were cultured on 0.2% gelatin-coated flasks.

To derive primed mSCs, naive mESC were plated on Geltrex (Gibco) diluted 1:100 in DMEM/F12 medium (Gibco) and transferred to the same serum-free media used for naive mESCs, without 2i, LIF, and BSA and supplemented with 10 ng/ml Fgf2 (R&D Systems), 20 ng/ml Activin A (R&D Systems), and 0.1× Knockout Serum Replacement (Life Technologies). Cells were differentiated for 7 days, splitting every 2–3 days. All cells were tested negative for Mycoplasma contamination by polymerase chain reaction (PCR).

Quantitative real-time PCR

To validate the identities of naive and primed cell types and confirm the transcription levels of selected pluripotency genes, quantitative real-time PCR (qRT-PCR) was performed (Supplementary Fig. S1C). Total RNA was isolated using NucleoSpin RNA, Mini kit for RNA purification (Marchery-Nagel) according to the manufacturer's instructions. cDNA was synthesized using the High-Capacity complementary DNA (cDNA) Reverse Transcription Kit (Applied Biosystems) with 500 ng RNA as input. qRT-PCR with primers (Supplementary Table S1) was performed in 10 μl reactions with 5 ng cDNA as input. Luna® Universal qPCR Master Mix (New England Biolabs) was used for detection. The reactions were run on a LightCycler480 (Roche).

Immunofluorescence for validation of cell identity

To further validate the identities of naive and primed cell types at a single-cell level, immunofluorescence of four key marker genes was performed (Supplementary Fig. S1A and B). NANOG and ESRRB were used as naive markers, together with OTX2 and OCT6 as primed markers [47–52]. Cells were seeded on Geltrex (Gibco) coated coverslips (12 × 12 mm) at a density of 10^5 cells per cm^2 on the previous evening. The following steps were performed at room temperature. Next morning, cells were washed 2× with 1× Dulbecco's Phosphate buffered saline (PBS) and fixed with methanol-free 4% formaldehyde (Polysciences, 18814-20) in 1× PBS for 10 min. Cells were rinsed with 1× PBS and washed with 1× PBS for 5 min. Cells were permeabilized with 0.5% Triton X-100 (Sigma–Aldrich) in 1× PBS for 15 min, rinsed with 1× PBS and then washed with 1× PBS. Cells were blocked in 2.5% BSA for 1 h and incubated with primary antibodies for 1 h. The samples were washed 3× for 5 min with 1× PBST and incubated for another 1 h with secondary antibodies. Samples were washed 3× for 5 min with 1× PBS with 0.2% Tween 20 (Carl Roth) (PBST). DNA was counterstained with DAPI (4′,6-diamidino-2-phenylindole) (1 μg/ml in 1× PBS) for 5 min and washed 2× with 1× PBS. Slides were mounted in Mowiol (2.5% DABCO (1,4-diazabicyclo [2.2.2]octane), pH 8.5), dried for 30 min and sealed with nail polish. For a list of used antibodies, see Supplementary Table S2.

Processing published raw sequencing data for putative enhancer calling model input

To obtain the .bam files required for the activity-by-contact (ABC) -model input, the data needed to be reprocessed. For ATAC-seq (GEO: GSE131556) and H3K27ac data (GEO: GSE156261) [48] the raw sequences were downloaded from GEO [53, 54] using SRA-Toolkit [55] For ATAC-seq, sequences were quality trimmed using TrimGalore (zenodo.org/records/7598955), discarding reads shorter than 15 bp. Reads were aligned to mm9 using bowtie2 [56] with parameters '–very-sensitive –trim3 1 -X 2000'. Mitochondrial reads and PCR duplicates were removed using Piccard tools (broadinstitute.github.io/picard/). Peaks were called using Genrich (github.com/jsh58/Genrich) in ATAC-seq mode, with otherwise default parameters. Bigwig files for visualization were created using deepTools [57] bamCoverage with '–binSize 10 –normalizeUsing RPKM'.

Raw H3K27ac ChIP-seq sequences were quality controlled with FastQC v0.12.1(www.bioinformatics.babraham.ac.uk/projects/fastqc/) and the output was summarized with MultiQC [58] Reads were aligned to the mm9 genome using bwa mem 0.7.10-r789 [59] using default parameters. Mitochondrial reads, Y chromosome, and nonchromosome scaffolds were removed. Bigwig files for visualization were created using deepTools bamCoverage with '–binSize 30 –normalizeUsing RPKM'.

Putative E–P pair calling

Putative E–P pairs in naive and primed cells were called using the ABC model [60] with default parameters. The epigenetic signal was normalized to the K562 data provided in the model. As input, already published ATAC-seq (GEO: GSE131556), H3K27ac ChIP-seq (GEO: GSE156261), RNA-seq (GEO: GSE131556) [48], and Hi-C (GEO: GSE124342) [61] data from naive and primed mESCs was used. Genes and transcription start sites were annotated as described in [60]. mm9 blacklisted regions from [62] were used. The generated datasets and interactions were visualized using CoolBox [63]. A complete list of all called enhancers in the genome will be provided on request.

Target selection

Genes were first filtered for developmental genes which show significant changes in gene expression during the differentiation from naive to primed mouse stem cells. Genes with at least three putative enhancers over both states were then selected. It is important to note that the selected enhancers are putative and do not represent a comprehensive list of all enhancers of a gene. For chosen E–P pairs see Supplementary Tables S2 and S3 and Supplementary Fig. S2. For target coordinates (mm9) see Supplementary Table S4. For information on which of the chosen enhancers have previously been functionally validated see Supplementary Table S2.

Probe design

For oligoDNA FISH probes, a 20 kb region around each target was tiled into nonoverlapping 40 bp oligonucleotides. These were filtered for uniqueness against the mm9 genome using BLAT [64] (default settings), retaining those with <5 matches and excluding repetitive sequences. Melting temperatures were constrained to 30–60°C in 50% formamide. This approach was tailored to a higher probe density [65], compared to other published design tools, optimized for whole-genome coverage or chromosome walking [66–68]. A 20 bp barcode was appended to the 3′ ends for visualization via fluorescently labeled readout oligos. RNA SABER FISH probes against introns were designed with PaintSHOP [69]. A complete list of probe sequences can be found in Supplementary Table S5 and S6.

Probe synthesis

DNA FISH probes were synthesized as described previously [67, 70] with adaptations. Briefly, the target oligos were amplified from the template oligopool (GenScript) via PCR using 20 nt primers (obtained from PaintSHOP, ordered from Merck), according to the manufacturer's instructions (BIO-21110, Bioline). The PCR product was purified using columns (#740609, Macherey-Nagel).

The purified DNA was converted to RNA via a high yield *in vitro* transcription (IVT) according to the manufacturer's instructions (#E2050S, New England Biolabs). Each 30 µl reaction consisted of ∼1 µg template DNA, 6.66 µM of each NTP, 20 U/µl RNaseOUT (Thermo Fisher) and 2 µl T7 polymerase mix. To maximize yield, the reaction was incubated at 37°C for 16 h.

DNA was removed by incubating the product from the IVT reaction with 2 µl DNase I (2 U/µl, M0303S, New England Biolabs) and 20 µl RNAse-free water at 37°C for 15 min. The RNA was purified using columns (#T2010, New England Biolabs) and converted to DNA via a reverse transcription (RT) reaction. Each 30 µl RT reaction contained 1/5 of the purified RNA from IVT, 2 µM of 41 nt froward RT primer with readout barcode, 1.5 mM each dNTP, 300 U Maxima H Minus Reverse Transcriptase (#EP0751, Thermo Fisher), and 1× RT buffer. The reaction was incubated at 50°C for 1 h and inactivated at 85°C for 15 min.

The template RNA was removed by incubating the product from the RT reaction with 20 µl of each 0.5 M ethylenediaminetetraacetic acid (EDTA) and 1 M NaOH at 95°C for 15 min. The DNA product was purified using columns (#T1030L, New England Biolabs) and eluted in 15 µl ultrapure H_2O and stored at −20°C. The quality of the probes was assessed using NanoDrop and poly-acrylamide gel electrophoresis.

SABER RNA FISH probes were synthesized as described in [71]. NOVA FISH probes were synthesized as described in [41].

Fluorescently labeled readout oligonucleotides were ordered from Eurofins/Ella Biotech. DNA FISH readout oligos were labeled with either Atto565 (spinning disk confocal microscopy) or Atto594 [stimulated emission depletion (STED) microscopy] for promoters and STAR635P for enhancers. Readout oligos for RNA FISH were labeled with Atto594.

Fluorescence *in situ* hybridization

FISH was performed as described previously [65, 72], with minor modifications. Cells were seeded on Geltrex (Gibco) coated coverslips (12 × 12 mm) at a density of 10^5 cells per cm^2 on the previous evening. Next morning, cells were washed 2× with 1× Dulbecco's PBS and fixed with methanol-free 4% formaldehyde (Polysciences, 18814-20) in 1× PBS for 10 min. Cells were rinsed with 1× PBS and washed with 1× PBS

for 5 min. Cells were permeabilized with 0.5% Triton X-100 (Sigma–Aldrich) in 1× PBS for 15 min, rinsed with 1× PBS and then washed with 1× PBS.

For oligoDNA FISH only, cells were treated with 0.1 M HCl for 5 min and washed 2× with 2× saline-sodium citrate (SSC) buffer for 5 min. RNA was digested by incubating cells with 100 µg/ml RNase A (ThermoScientific) in 2× SSC for 30 min at 37°C. After washing 2× with 2× SSC, cells were pre-equilibrated in 50% formamide (Merck) in 2× SSC for 60 min. The coverslip was placed cell-side down onto 4.5 µl of hybridization solution [0.05–0.2 nM probe, 50% formamide, 10% dextran sulfate (Sigma–Aldrich), 0.125% Tween 20 (Carl Roth), 2× SSC] and sealed with rubber cement (Marabu). Slides were placed on a heat block at 81°C for 3 min and incubated at 37°C overnight (16–20 h). After incubation, coverslips were washed 2× with 2× SSC for 15 min, followed by two washes with 0.2× SSC at 56°C, 2 washes with 4× SSC and one wash with 2× SSC. The second hybridization was performed in 20 µl of secondary hybridization solution (250 nM fluorescently labeled barcode, 10% dextran sulfate, 35% formamide, 2× SSC) for 30–120 min at room temperature. Cells were then washed 1× with 30% formamide in 2× SSC for 7 min at 37°C, 2× with 2× SSC for 5 min, 1× with 0.2× SSC at 56°C, 1× with 4× SSC for 5 min, and 1× with 2× SSC for 5 min. Sample were post-fixed with 4% PFA in 2× SSC for 10 min and washed 2× with 2× SSC for 5 min. DNA was counterstained with DAPI (1 µg/ml in 2× SSC) for 5 min and washed 2× with 2× SSC. Slides were mounted in MOWIOL (2.5% DABCO, pH 8.5), dried for 30 min and sealed with nail polish. The same procedure was applied for NOVA FISH, omitting the secondary probe hybridization.

For sequential SABER RNA and oligoDNA/NOVA FISH, cells were seeded into Geltrex-coated channel slides (#80161, Ibidi) and pre-treated as described above, omitting RNA digestion and using RNase-free reagents. After permeabilization, cells were washed with 2× SSC. The slide was filled with 200 µl hybridization solution (same as for DNA FISH with 1–2 nM probe) and incubated at 42°C for 2 days. Cells were then washed 2× with 2× SSC at 37°C for 10 min, 2× with 0.2× SSC at 60°C for 5 min, 1× with 2× SSC and transferred into 1× PBS. Cells were incubated with 100 nM readout probe in 1× PBS and 1 µg/ml DAPI for 1 h at 37°C. The cells were washed with 1× PBS at 37°C for 5 min and rinsed 2× with 1× PBS. Cells were post-fixed with 4% formaldehyde and washed with 1× PBS for 5 min. To enable later alignment of RNA and DNA images, the sample was incubated with FluoSpheres (505/515 nm, #P7220, Thermo Fisher) diluted 1:50 in 1× PBS for 15 min. Nonattached beads were washed away by rinsing 3× with 1× PBS. The sample was imaged in 1× PBS with 2.5% DABCO. After imaging the RNA, the slide was rinsed with 1× PBS and treated as described in the DNA FISH protocol above. Imaging was again performed in 1× PBS with 2.5% DABCO.

Microscopy

Images of pairwise contacts relating to Fig. 1 were acquired using spinning disk confocal microscopy on a Nikon TiE, equipped with a Yokogawa CSU-W1 spinning-disk confocal unit (50 µm pinhole size), an Andor Borealis illumination unit, Andor ALC600 laser beam combiner (405/488/561/640 nm), Andor IXON 888 Ultra EMCCD camera, and a Nikon 100×/1.45 numerical aperture (NA) oil immersion objective, as also described in [65, 73]. The microscope was controlled via NIS Elements (Nikon, ver. 5.02.00). To ensure an unbiased selection of cells, most images were taken automatically, using NIS-Elements JOBS (Nikon). Images were acquired at 405, 561, and 640 nm using 10%, 75%, and 75% laser powers, with corresponding exposure times of 50, 100, and 50 ms.

Imaging of experiments related to Fig. 2 was performed using STED super-resolution microscopy on a 3D STED microscope (Abberior Instruments), equipped with three pulsed excitation lasers (485, 594, and 640 nm), one pulsed depletion laser (775 nm), and Avalanche photodiodes for detection. All acquisitions were performed using a 100× UPlanSApo 1.4 NA oil immersion objective (Olympus). Imaging of Fig. 3 was performed using the same microscope in confocal mode.

To enable measurement of many E–P configurations in individual cells, we automated STED imaging using Python (version 3.7 or later) via the SpecPy (v.1.2.3) (github.com/certified-spec/specPy) interface to the Imspector microscope control software (v.16.3) [65, 74]. In short, we had our system acquire confocal overview stacks (50 × 50 × 5 µm FOV in xyz, 150 × 150 × 250 nm pixel sizes) in a regular grid or spiral. After each overview, we detected co-localizing promoter and enhancer signals and proceeded to acquire small STED stacks (2.5 × 2.5 × 2.5 µm, 30 × 30 × 150 nm pixel size) around each detection before moving on to the next overview. For samples with sequential RNA and DNA FISH, green FluoSpheres (505/515 nm, #P7220, Thermo Fisher) were imaged in all overview stacks.

Chromatic aberration correction

Correction of chromatic aberrations for spinning disk images was done based on calibration samples of cells covered with Tetraspeck four-color fluorescent microspheres (100 nm diameter). To estimate the chromatic shift between two channels, we detected beads in both channels as local maxima above a user-defined threshold after applying a DoG filter. We then estimated subpixel coordinates of the detections by fitting a 3D Gaussian function in the local environment of the bead. As shifts were generally small, we matched bead coordinates in one channel to the closest coordinate in the other (using linear assignment to prevent matching one bead with multiple partners and discarding matches with a distance above 1 µm). The matched coordinate pairs from multiple images were pooled and affine transformation parameters between them were estimated using least-squares fitting with RANSAC outlier removal. The resulting parameter matrices (for coordinates in physical units) were saved to a JSON text file.

To correct tables of FISH spot locations in new images, we loaded the transformation matrix of each channel to a reference channel and applied it to the coordinates of that channel (detections in the reference channel were left as-is). Notably, as our microscope allows for both top-to-bottom and bottom-to-top recording of z-stacks we also saved the direction to the parameter file. If a new image did not match the z-direction of calibration images, z-coordinates were flipped around the z-center of the image before correction and flipped back afterwards.

As we did not observe strong chromatic aberrations in STED images, and they are drastically reduced due to use of a single depletion laser for both excitation channels [75], we

did not apply any coordinate corrections (except to align sequential DNA- and RNA-FISH) to STED data.

Characterization of chromatic aberrations

Using the RANSAC-inlier coordinate pairs of the 561 and 640 nm channels of the calibration images, we constructed a linearly interpolated map of the shifts (Supplementary Fig. S3A). We observe a lateral (xy) zoom aberration across the field-of-view with shifts increasing radially from approximately the center, while axial (z) shifts remain relatively constant but nonzero across the field.

Our calibration dataset consists of 11 images, allowing us to quantify the chromatic aberration correction performance via cross-validation. We proceed in a leave-one-out fashion, estimating chromatic shift from 10 of the images and using it to correct the 11th, repeating until we have corrected all coordinates. The broad distributions of lateral shifts are drastically reduced and centered around zero after correction (Supplementary Fig. S3B). The z shifts still have a broad distribution (likely due to lower localization accuracy), but the systematic shift is corrected well.

Image analysis

FISH spots were detected in each channel with sub-pixel accuracy using RS-FISH and Gaussian fitting [76]. Parameters 'Thershold' and 'intensityThreshold' were adjusted as necessary.

For spinning disk confocal images, the spot coordinates were corrected for chromatic aberrations (see above). Nuclear segmentation masks were generated from images of DAPI-stained nuclei, using a Cellpose [77] model, trained on naive- and primed- cell nuclei. FISH spots outside the nuclei or in nuclei with >2 spots were discarded. Spots in the promoter channel were matched to their nearest neighbor in the enhancer channel using Scipy linear sum assignment [78] and the Euclidean 3D distance between the 2 channels for each pair was calculated.

For STED images, the STED detail images were filtered for images containing 1 spot in the promoter channel, and the number of targeted enhancers in the enhancer channel. The Euclidean 3D distance between the promoter and all its enhancers was calculated. The expected inaccuracy of pairwise distance measurements is below 10nm [65].

To align sequential RNA and DNA FISH data, we detected fluorescent beads in the 488nm channel in the overview stacks of both rounds and converted their pixel coordinates to global coordinates by combining them with the stage position of the image. To match beads between rounds, we assigned each bead a descriptor based on the vectors to its nearest neighbors expressed in a local coordinate system via QR-factorization, similar to [79]. After matching beads based on descriptor distance, a similarity transform between the images was estimated using RANSAC. Finally, we applied this transform estimated from beads to the (global) coordinates of detected FISH spots to enable measurement of distances between RNA and DNA FISH signals. The mean alignment error per image was ~460 nm.

Code for image analysis is available at github.com/CALM-LMU/enhancer-promoter.git or Zenodo: doi.org/10.5281/zenodo.14698025.

Quantification of localization precision

To quantify localization precision in spinning disk measurements, we recorded 29 stacks of FISH samples of mESCs with a 20 kb region overlaping the *Nanog* promoter alternatingly stained with both ATTO565 and STAR635P (Supplementary Fig. S4A). Spots were detected in both channels using our standard pipeline of RS-FISH followed by Gaussian fitting. Affine chromatic aberration correction matrices were applied to the coordinates of the STAR635P channel. After correction, the x, y, and z components of vectors between matched spots (nearest neighbors were matched using linear assignment) are symmetrically distributed around zero with standard deviations of around 40 nm in z and 30 nm in x and y (Supplementary Fig. S4B). This inaccuracy estimation combines localization inaccuracies in both channels and remaining chromatic aberrations and due to the symmetric distribution around zero it should not introduce systematic bias, as it applies equally to all distance measurements. We quantified localization precision of STED measurements as part of a previous study [65] and found the expected inaccuracy of pairwise distance measurements to be below 10nm.

Simulations of statistical power

To assess the effects of localization imprecision on statistical power, we performed simplified simulations in which we sampled two sets of vectors with random orientations and lengths drawn from a Maxwell–Boltzmann distribution (with scale parameter a picked so mean lengths match average distances observed in data). These vectors would correspond to the position of one of two FISH signals with the other one placed at the origin. We then simulated localization uncertainty by adding random "noise" vectors from a multivariate Normal distribution to each vector. The magnitudes of all resulting vectors were calculated, and the two distance distributions were checked for significant differences via a two-sided Wilcoxon rank-sum test. By repeating this procedure 1000 times and counting the fraction of significant tests, we get a measure of the statistical power (Supplementary Fig. S4C).

Using sample sizes and localization uncertainties approximately matching experimental data, we performed a grid search of various mean distances and differences in mean. To match spinning disk experiments, we use two equal samples of size 1500 and noise standard deviation of 40 nm. We estimate high statistical power at points in the parameter space corresponding to observed significant naive-primed differences. It should be noted that even when we sampled our noise vectors from a Normal distribution with nonzero mean (simulating uncorrected chromatic aberrations) or higher levels of inaccuracy, statistical power remained high, as both simulated distance distributions would be affected in the same way.

In conclusion, while remaining inaccuracies in the spot localization may skew the measured values, statistical significance of differences between two conditions/targets can still be determined with high power.

Statistical analyses

Statistical analysis was performed using R (www.R-project.org/). Two-sided Wilcoxon rank sum tests were calculated for all comparisons. When comparing multiple groups, Benjamini–Hochberg (BH) false discovery rate correction was applied.

Tri-C

For the Tri-C experiments, three independent biological replicates were performed as previously described [80, 81]. Briefly, 5 million cells per replicate were fixed in 5 ml culture medium using 2% formaldehyde (Thermo Fisher Scientific, 28908) at room temperature for 10 min while rotating. Formaldehyde was quenched with 125 mM ice-cold glycine, the cells were centrifuged at 4°C and 500 × *g* for 10 min and washed with cold PBS. The cell pellet was then resuspended in fresh lysis buffer (10 mM Tris, 10 mM NaCl, 0.2% Igepal CA-630, 1× cOmplete Protease Inhibitor cocktail), incubated at 4°C for 30 min and washed once with cold PBS. Restriction enzyme digestion was performed with 750 U DpnII (NEB, R0543S) at 37°C for 24 h. DpnII was subsequently inactivated at 65°C for 20 min and proximity ligation took place in 1× ligation buffer and 240 U T4 DNA ligase (Thermo Fisher Scientific, EL0013) at 16°C for 18 h. Ligation reactions were centrifuged at room temperature and 500 × *g* for 15 min, the pellets were resuspended in 300 µl of Tris–EDTA buffer (TE buffer; Sigma–Aldrich, 93283) and incubated with 3 U proteinase K at 65°C for 16 h, followed by an incubation with 7.5 mU of RNase (Roche, 11119915001) at 37°C for 30 min. DNA was subsequently extracted from the samples by mixing with equal volume phenol-chloroform-isoamyl alcohol mixture (Sigma–Aldrich, 77617) and centrifugation at room temperature and 12 600 × *g* for 10 min in prespun 5Prime light Phase Lock gel tubes (VWR, 733-2477). The upper aqueous layer was then mixed with 30 µl sodium acetate 3M, 1 µl GlycoBlue Coprecipitant (Thermo Fisher Scientific, AM9515) and ethanol 75% v/v at −20°C for 2 h. DNA was pelleted by centrifugation at 4°C and 21 000 × *g* for 30 min, washed with cold 70% ethanol, resuspended in TE buffer and concentration was determined with Qubit™ 1× double-stranded DNA (dsDNA) Broad Range assay (Thermo Fisher Scientific, Q33266), according to the manufacturer's instructions.

A total of 6.5 µg of DNA in 130 µl TE buffer were sonicated to fragments of 450 bp using a Covaris S220 Ultrasonicator (55 s; 10% duty factor; 140 W peak incident power; 200 cycles per burst) and fragments larger than 300 bp were size selected with 0.7× volume Mag-Bind TotalPure NGS beads (Omega Bio-tek, M1378-01). Four micrograms of each sample were indexed in duplicates (2 µg each) using the NEBNext Ultra II Library Prep kit for Illumina (NEB, E7645S). Briefly, samples were first incubated with 3 µl End Prep enzyme in 7 µl 10× End Prep buffer at 20°C for 45 min and 30 min at 65°C, followed by an incubation in 30 µl Ultra II Ligation Master Mix with 7 µl of NEBNext Adaptor and 1 µl Ligation Enhancer at 20°C for 30 min and a final incubation with 3 µl of the USER enzyme at 37°C for 30 min. Samples were then subjected to size selection with 1.8× volume Mag-Bind TotalPure NGS beads. Each sample was subsequently split in two indexing PCR reaction, performed with the Herculase II Fusion DNA polymerase kit (Agilent Technologies, 600677) by incubating 28.5 µl adaptor-ligated library, 5 µl NEB Universal primer, 5 µl NEB index primer, 10 µl Herculase II 5× buffer, 0.5 µl dNTPs and 1 µl Herculase II polymerase in a thermocycler at initial 98°C for 30 s, followed by 98°C for 10 s, 65°C for 30 s, 72°C for 30 s for 7 cycles and 72°C for 5 min. Samples were then subjected to clean-up with 1.8× volume Mag-Bind TotalPure NGS beads.

For the enrichment of fragments containing the viewpoints of interest, two subsequent hybridization reactions were performed using the KAPA HyperCapture Reagent kit (Roche, 9075828001) with biotinylated single-stranded DNA (ssDNA) probes complementary to the regions of interest. The ssDNA probes used for the Capture reactions were 100 nt long (Supplementary Table S7), designed using the oligo 0.2.0 python package (oligo.readthedocs.io/en/latest/) and ordered from Integrated DNA Technologies as two xGen™ MRD Hybridization panels. Probes targeting positions found at a short distance on the genome were not included in the same panel. For the first hybridization reaction, 2 µg of each uniquely indexed library were combined in 1:1 mass ratio with 5 µl per library mouse Cot-1 DNA (Thermo Fisher Scientific, 18440016) and desiccated at 45°C in a vacuum centrifuge. The DNA pellet was then resuspended in 6.7 µl per library Universal Enhancing Oligonucleotides, 14 µl per library of Hybridization buffer, 6 µl per library Hybridization Component H and 4.5 µl per library diluted biotinylated oligonucleotides (2.9 nM per probe) and incubated at 95°C for 5 min and at 47°C for 72 h.

Pulldown of the viewpoint-containing fragments was performed with 51 µl of M-270 streptavidin Dynabeads (Thermo Fisher Scientific, 65306) per library and using the KAPA HyperCapture Reagent kit (Roche, 9075828001). Briefly, the beads were washed three times with 1× Bead Wash buffer at 47°C and incubated with the entire hybridization reaction at 47° and 600 rpm for 45 min, for the probes to bind to the beads. The bead-bound DNA was washed twice with 100 µl 1× Stringent Wash buffer per library at 47°C and 600 rpm for 5 min and consecutively with 100 µl 1× Wash buffer I, II, and III per library at room temperature for 1 min each time, resuspended in 40 µl per library PCR-grade water and subjected to clean-up with 90 µl per library Mag-Bind TotalPure NGS beads. Bead-bound DNA was PCR-amplified with 25 µl per library of 2× KAPA HiFi HotStart ReadyMix and 5 µl per library Post-Capture PCR Oligos as follows: initial 98°C for 45 s, followed by 98°C for 15 s, 60°C for 30 s, 72°C for 30 s for 14 cycles, and 72°C for 60 s. DNA was then subjected to cleanup with 90 µl per library Mag-Bind TotalPure NGS beads. All the captured DNA was used for a second capture reaction performed as described above but using the volumes for a single library and hybridization was performed for 24 h. Quality control was performed using D1000 TapeStation (Agilent Technologies, 5067-5583 and 5067-5582), Qubit™ 1× dsDNA Broad Range assay (Thermo Fisher Scientific, Q33266) and fragment analyzer according to the manufacturers' instructions. The libraries were sequenced with 300 cycles of paired-end reads on the Illumina NextSeq 2000 platform. Data analysis was performed using the CapCruncher pipeline [82] (github.com/sims-lab/CapCruncher) in capture mode against the mm10 genome assembly. Custom python scripts were used for the extraction of the reads with two or more *cis* reporter fragments, for the calculation of multiway interaction counts and the interaction matrix plotting [83].

Results

Changes in pairwise E–P distances during naive to primed transition

To investigate whether E–P distances change when genes are upregulated/downregulated during differentiation, we utilized an *in vitro* model of the transition from naive to primed pluripotency in mESCs [84] (Fig. 1A and B). This transition is

characterized by large gene expression changes and extensive rewiring of E–P contacts [43–46]. Cell state identities were validated via qRT-PCR and immunostaining of key marker genes (Supplementary Fig. S1A and B). We identified putative enhancers across both naive and primed states using the "Activity-by-contact model" [60]. From this set, we selected genes with at least three distinct enhancers, either functionally validated or predicted using the ABC model (Supplementary Table S3, Fig. 1C, and Supplementary Fig. S2).

Target regions were visualized via oligonucleotide-based FISH (DNA oligoFISH) and imaged using two-color spinning disk confocal microscopy (Fig. 1D). For pairwise measurements of the *Nanog* –5 enhancer, the enhancer and promoter were visualized using nanoscopy-compatible oligonucleotides with dyes in variable arrays (NOVA FISH) [41] and imaged using automated STED super-resolution microscopy. Spots were detected with subpixel-localization accuracy using RS-FISH [76]. The subpixel localization in confocal images was refined using Gaussian fit (see the 'Materials and methods' section; Supplementary Fig. S4). To confirm that we have sufficient power to detect differences between naive and primed states, we performed simulations of statistical power (see the 'Materials and methods' section; Supplementary Fig. S4).

An ∼8.5× decrease in *Nanog* transcription (from 11% to 1.3% GAPDH transcription, Fig. 1B) was accompanied by nonsignificant differences ($P > .05$, two-sided Wilcoxon rank sum test with BH correction) in median 3D E–P distance (Fig. 1E). A similar trend was observed for E–P pairs of some measured genes (*Dppa3*, *Prdm14*). Notably, the largest, highly significant changes in E–P distance were observed between the *Sox2* promoter and the *Sox2* control region (SCR) ($\Delta_{n\rightarrow p} = 110$ nm) as well as the *Sox2* promoter and a putative enhancer ∼1280 kb downstream ($\Delta_{n\rightarrow p} = 110$ nm) (Supplementary Fig. S7A). Interestingly, for *Dnmt3a*, enhancer and promoter move significantly further apart, despite the gene being upregulated in the primed state (Supplementary Fig. S7A). We verified that these differences in E–P distance are not a result of a difference in nucleus size between the two cell types (Supplementary Fig. S5). Additionally, comparison of the selected targets with published live-cell measurements in mESCs [4, 85] confirmed that our DNA FISH procedure does not introduce major artifacts (Supplementary Fig. S6). Additionally, spatial distances for most E–P pairs seemed to be largely influenced by genomic distance (Supplementary Fig. S7B). These findings indicate that transcriptional changes during the naive to primed transition are gene specific and suggest that regulation does not universally require major alterations in 3D genome architecture.

Changes in multiway E–P contacts during naive to primed transition

We then asked whether more complex 3D chromatin structures that may encompass some or all enhancers of one promoter (Fig. 2D) are enriched in naive and/or primed mESCs. Conventional chromosome conformation capture methods, such as Hi-C or Micro-Capture-C, are based on the detection of pairwise interactions and thus unable to detect such complex structures. We therefore performed Tri-C to capture *cis*-regulatory interactions at the *Nanog/Dppa3* locus (Fig. 2C and Supplementary Fig. S8). Tri-C interactions are depicted using viewpoint-specific contact matrices, which display the frequencies at which two chromatin fragments simultaneously interact with the viewpoint (Fig. 2B). Note that the regions across the diagonals from the viewpoints are in close genomic proximity to the viewpoint and are therefore expected to form strong interactions. Therefore, those regions have been grayed out from the contact matrixes [83].

At the *Nanog* locus in naive cells, we observe a weak enrichment of three-way contacts between the promoter and the −45 and −5 enhancers, as well as the −45, −5, and +60 enhancers (Fig. 2C). Interestingly, in primed cells where *Nanog* is downregulated, this enrichment of three-way contacts is lost.

To further investigate multiway interactions at a single-cell level, we focused on the example of *Nanog*, where we observed changes in multiway interactions via Tri-C. We imaged the promoter (labeled with one barcode) and its cognate enhancers (labeled with a second barcode) using STED super-resolution microscopy (Fig. 2E). The plots display a percentage of alleles, in which a certain number of enhancers are in proximity to the promoter simultaneously. Since it is unknown over which distances promoters and enhancers can exchange information, this information is shown for a range of different distance thresholds (Fig. 2F). For a visualization with an adjustable distance threshold see our data viewer: py.cafe/app/hoerldavid/promoter-enhancer-interactive-fig2. To avoid artifacts that might be caused by the different sensitivity of the hybridization procedure for the different enhancers, only images with all enhancers labeled were analyzed for Fig. 2F.

We observe that multiway E–P contacts, compared to pairwise contacts, are rare. For example, at the *Nanog* locus (−45 E, −5 E, promoter, +60 E; Fig. 2E) in naive cells, for an arbitrary distance threshold of 200 nm [86], pairwise E–P contacts occur in 55% of all alleles, while three-way contacts (P–E–E) occur in 25%, and four-way contacts (P–E–E–E) in only 3% of alleles (Fig. 2F and G). Interestingly, in the primed state where *Nanog* is downregulated, pairwise as well as multiway contact frequencies decrease by a few % for E–P distances below 300 nm. To a smaller extent, a reduction in three-way, but not four-way E–P contacts upon differentiation can also be observed for *Dppa3* (Supplementary fig. S9B and C). Together with Tri-C, these data show that downregulation of *Nanog* expression during the naive to primed transition is accompanied by a small reduction in multiway contact frequency.

Effect of transcription on E–P distance

Since many genes are transcribed in bursts, we reasoned that transient changes in E–P distances associated with transcription could be hidden at a population level (Fig. 3A). To address this, we designed probes targeting introns of *Nanog* (Fig. 3B) and performed a sequential protocol starting with RNA SABER FISH against the intron, followed by DNA FISH against the –5, –45, and + 60 enhancers (Fig. 3C; see the 'Materials and methods' section). We assumed that the distance between the nascent RNA and the promoter can serve as a proxy for transcriptional timing, with shorter distances indicating a more recent transcription event.

For *Nanog*, alleles which were transcribed more recently show significantly decreased E–P distances (Fig. 3E). For example, when a nascent RNA is located within 0.25 μm of the promoter, the median E–P distance is about 50 nm shorter than when the RNA is within 0.5 μm, and about 90 nm shorter than when it is within 1 μm ($P < .05$, two-sided Wilcoxon rank sum test). A similar effect was also observed for *Dppa3* (Supplementary Fig. S10C). When the three labeled

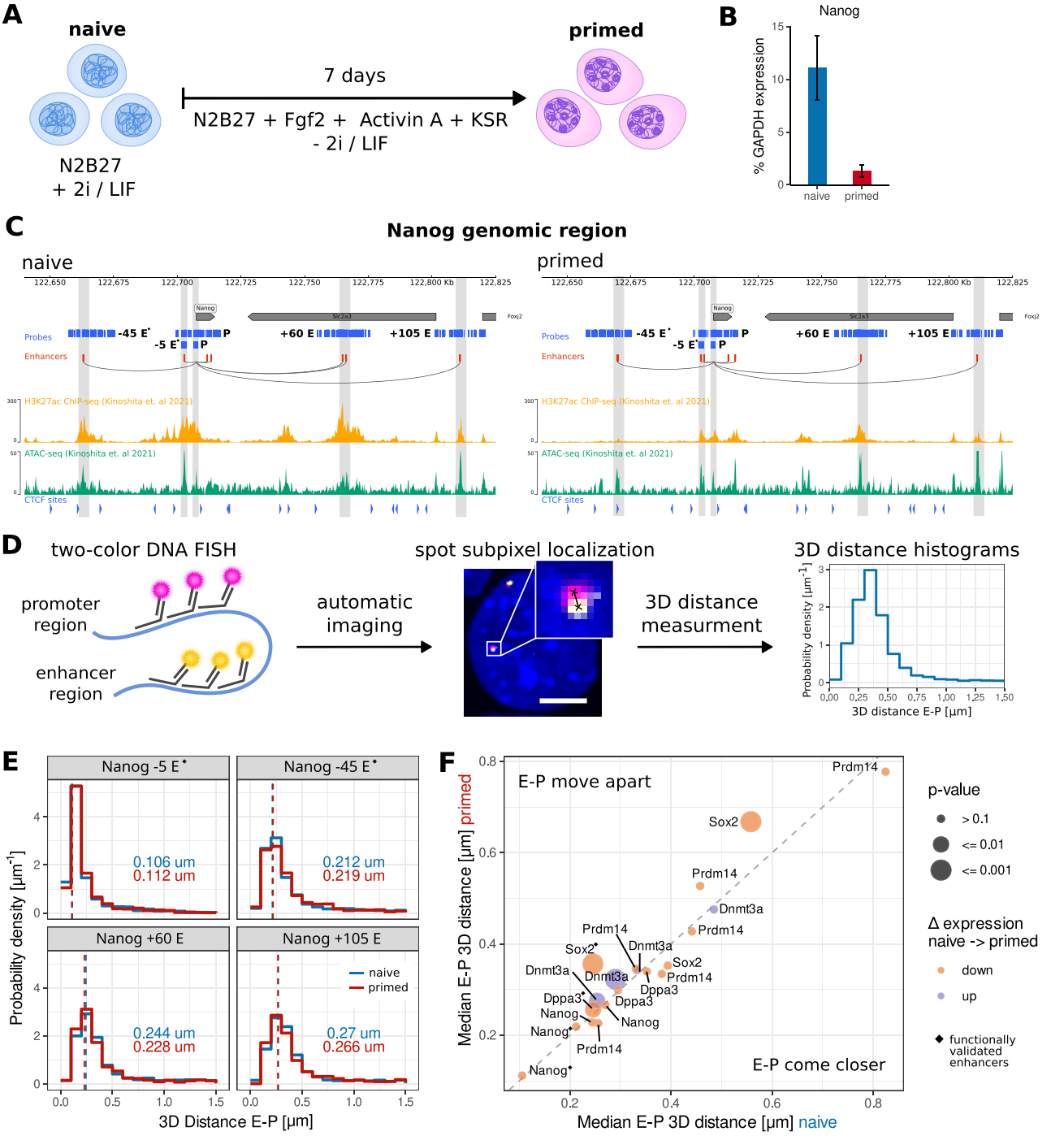

Figure 1. E–P distances of selected differentially expressed genes show small changes during differentiation from naive to primed mESCs. **(A)** Cell culture model of naive to primed transition in mESCs. **(B)** Changes in *Nanog* transcription levels (% GAPDH transcription) in naive and primed cells measured by qRT-PCR. The graph depicts median ± standard error of the mean ($n = 5$ biological replicates). **(C)** *Nanog* genomic region for naive and primed cells, showing from top to bottom: DNA oligoFISH and NOVA FISH probes against promoter and selected enhancers, all predicted enhancers, connection of *Nanog* promoter to its enhancers, H3K27ac ChiP signal (from [48]), ATAC-seq signal (from [48]), CTCF binding motifs, and targeted enhancer regions (vertical gray stripes). Functionally validated enhancers are marked by ♦. **(D)** Experimental workflow: regions of interest are marked with two-color DNA oligoFISH, the samples are imaged automatically with spinning disk confocal microscopy, FISH spots are detected automatically with subpixel localization accuracy and 3D distances between matched E–P spots are calculated to produce a E–P distance distribution of the population. Scale bar represents 1 µm. **(E)** 3D distance [µm] distributions between *Nanog* promoter and its −5, −45, +60, and +105 (putative) enhancers in naive and primed cells. Dashed line and number next to the histogram represent the median distance. The changes between naive and primed cells are not significant ($P > 0.05$, two-sided Wilcoxon rank sum test, BH correction). From closest to furthest enhancer: $n_{naive} = 916, 1718, 837, 1220$; $n_{primed} = 1037, 1038, 1362, 701$; three biological replicates each. **(F)** Change in median 3D E–P distance [µm] of genes down- and up-regulated during the naive to primed transition. E–P pairs above the diagonal show increased distances during differentiation, while distance in pairs below the diagonal decreases. Each circle refers to a different enhancer. The test of statistical significance is the same as in panel (E). Functionally validated enhancers are marked by ♦.

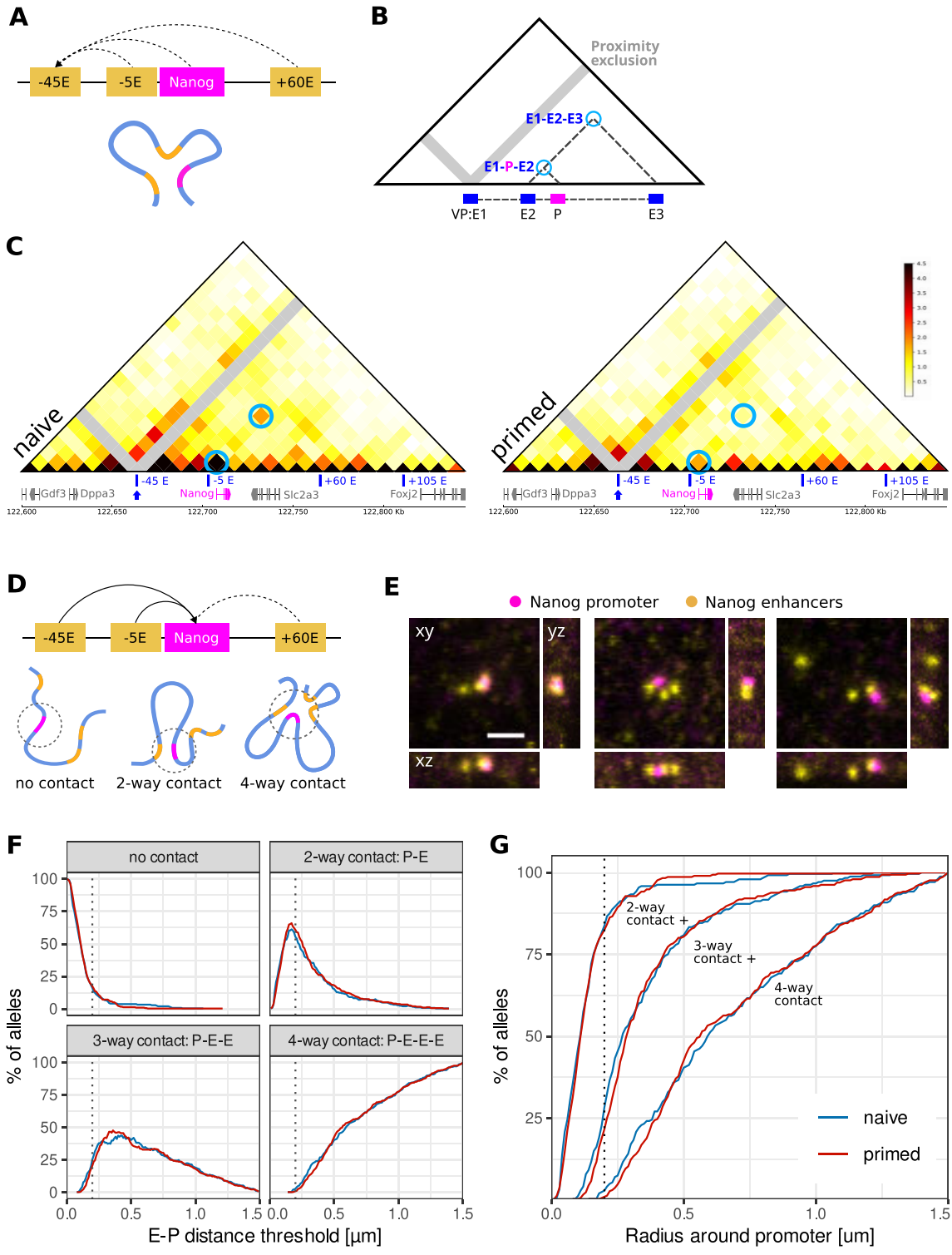

Figure 2. Changes in multiway E–P contacts at the *Nanog* locus during the naive to primed differentiation. **(A)** Schematic representation of Tri-C viewpoint (VP) and possible interactions at the *Nanog* locus. **(B)** Schematic representation of Tri-C data visualization. VP-specific contact matrices show the interaction frequencies at which the viewpoint interacts with two genomic regions simultaneously. Proximity signals around the viewpoint are excluded (gray stripes). **(C)** Tri-C contact matrices of the *Nanog* locus (chr6: 122,600,000–122,845,000; 10 kb resolution; mm10) in naive and primed cells. The data is shown from the viewpoint of the –45 enhancer. Contacts between 45E–P–5E, as well as between 45E–P–60E are highlighted with blue circles. **(D)** Schematic representations of possible E–P constellations: promoter does not contact enhancers; promoter contacts one enhancer at a time; promoter contacts several enhancers at the same time. **(E)** STED microscopy images (maximum intensity projections) of enhancer and promoter constellations for *Nanog* and enhancers shown in panel (D). Scale bar represents 1 μm. **(F)** Interaction frequencies between a promoter (P) and different numbers of enhancers for a range of contact thresholds [μm]. Naive cells are plotted in blue, primed in red. $n_{naive} = 240$, $n_{primed} = 291$ over three biological replicates. **(G)** Cumulative plot of data shown in panel (F). The curves represent interaction frequencies between a promoter and at least 1, 2, or 3 enhancers (two-way+, three-way+, or four-way contact) over a range of contact thresholds [μm].

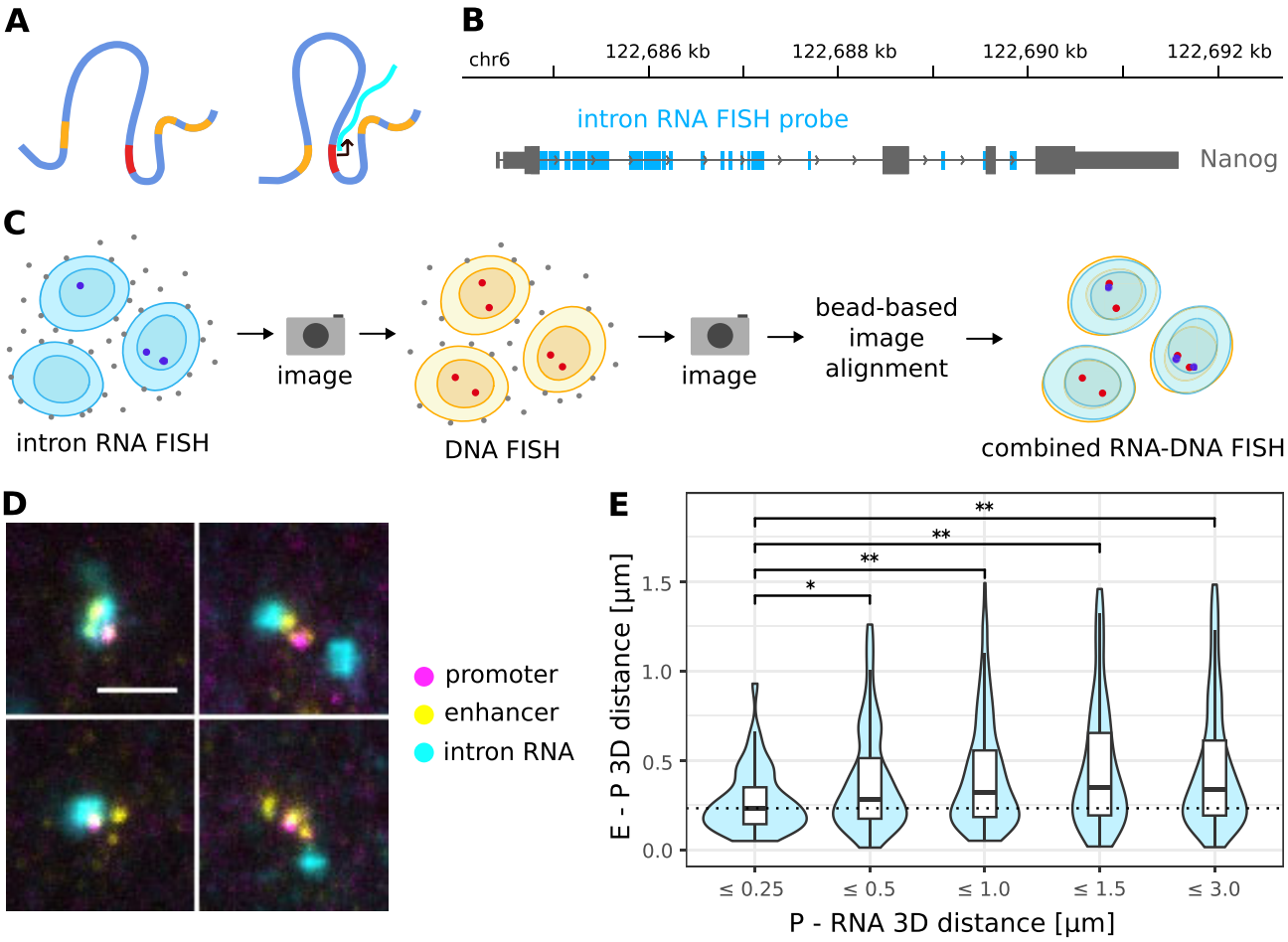

Figure 3. Shorter E–P distances correlate with active transcription. **(A)** Schematic representation: do enhancer and promoter come closer when the gene is actively transcribed? **(B)** Genomic location of *Nanog* intron RNA FISH probes. **(C)** Experimental workflow: intron RNA is marked by RNA FISH, imaged, promoters and enhancers are marked by DNA FISH, imaged, then RNA and DNA images are aligned using fiducial markers. **(D)** STED microscopy images (maximum intensity projections) of promoter (magenta), enhancers (yellow), and intron RNA (cyan) for *Nanog*. Scale bar represents 1 µm. **(E)** E–P 3D distance [µm] changes significantly based on distance of nascent RNA to P ($P < 0.05$: $*$, $P < 0.005$: $**$, two-sided Wilcoxon rank sum test). $n_{\leq 0.25} = 46$, $n_{\leq 0.5} = 156$, $n_{\leq 1} = 272$, $n_{\leq 1.5} = 172$, $n_{\leq 3} = 259$ over three biological replicates.

Nanog enhancers were ordered by proximity to the promoter, a similar trend was observed, although not significant, likely due to the limited sample size (Supplementary fig. S10D). Together, these data indicate that for *Nanog* and *Dppa3*, E–P distances change based on the transcriptional state of the alleles.

Discussion

Enhancers play a key role in gene regulation during development, but the spatiotemporal interaction with their promoters is still under investigation. Here, we use oligoFISH, NOVA FISH, and SABER FISH, combined with various super-resolution microscopy techniques and Tri-C to investigate selected differentially expressed genes of mESCs in different states: during the transition from naive to primed pluripotency and after onset of transcription.

Our data suggest that changes in pairwise E–P distances during the naive to primed transition are gene- and enhancer-specific. For example, although *Nanog* E–P distances do not significantly change between states, the SCR moves significantly further away from its promoter ($\Delta \approx 110$ nm) when downregulated. Our findings at the investigated *Nanog* loci are consistent with Ohishi *et al.* (2025).

Furthermore, our Tri-C data suggest the presence of weak multiway E–P hubs at the *Nanog* locus, which disappear when *Nanog* is downregulated in the primed state. Formation of stronger hubs has previously been reported at the globin loci [87, 88] and for primed specific genes [43]. Such differences may reflect cell type and locus-specific effects. In line with the Tri-C data, our microscopy data show only minor differences between the naive and the primed state. A central limitation in the interpretation of microscopic E–P contact data is that measured contact frequencies do not account for spontaneously occurring interactions, necessitating appropriate normalization [85, 89]. By contrast, Tri-C and related proximity ligation assays provide data on the enrichment of contacts over background in a population of cells.

A key unresolved question in assessing E–P contacts is what counts as a functional contact. Different distance thresholds have been reported, with some models suggesting that sequential "contacts" may be required to trigger transcription [90, 91]. Moreover, the duration of a "contact" necessary to trigger an event is unknown. Therefore, further assumptions or

even complex models are necessary to interpret absolute contact frequencies [85, 89]. At an arbitrary threshold of 200 nm, absolute pairwise contacts (P–E) at the *Nanog* locus occur in 55% of alleles, three-way contacts (P–E–E) in 25%, while four-way contacts (P–E–E–E) occur in only ∼3% of alleles. Interestingly, our data differ markedly from results of a recent preprint [86], reporting much lower multiway contact frequencies at the *Nanog* locus. The most likely explanations for this discrepancy are methodological and/or underlying biological differences.

Interpretation of FISH measurements requires careful consideration, since these measurements are prone to artifacts due to fixation and harsh sample preparation. To assess the robustness of our FISH procedure and subsequent data acquisition and—analysis steps, we compared our pairwise FISH data at the Fbn2 TAD and Sox2—SCR region with state of the art live-cell measurements in mESCs [4, 85] and found good concordance (Supplementary Fig. S6).

Our RNA-DNA FISH data show that E–P distances change with the transcriptional state, suggesting that such contacts are likely transient. *Nanog* and *Dppa3* regions in which transcription occurred recently, as determined by a nascent RNA closer to the promoter, display significantly shorter E–P distances (Fig. 3E). This is in agreement with a recent study by Ohishi et al 2024, which found that *Nanog* enhancers spend longer times in the proximity of actively transcribed promoters. However, a limitation of fixed-cell studies is that each cell captures only a single moment, “a snapshot”, within a continuous process. Since our measurements detect the mRNA but not the regulatory initiation event, it is unclear to what extent the observed 3D conformation reflects the state at transcriptional onset. Live-cell measurements at TAD boundaries have demonstrated the dynamic and transient nature of loop structures, a property that may also extend to E–P looping interactions [85]. For this reason, small or even absent changes in E–P distances of genes which are differentially expressed should not be over interpreted as in a population of cells only a fraction of alleles is transcribed. Here we show for the *Nanog* and *Dppa3* locus a short-lived E–P distance reduction correlated with transcription which is not detected in measurements of the whole population. This seems to be gene- and cell type-specific, as live-cell imaging studies have reported both correlations and lack of correlations between E–P distance and transcription, depending on the system examined [92].

In summary, our data show that during the naive to primed transition, most of the studied genes show no major changes in average E–P distances, even though expression levels change by several orders of magnitude. This suggests that regulation of many genes may not always depend on change in the underlying 3D genome architecture. At the *Nanog* locus, Tri-C data show a weak enrichment of multiway contacts in the naive state where the gene is highly expressed. This supports models proposing that multiway contacts play a role in transcriptional regulation. Since the required duration of pairwise or multiway contacts and the necessary spatial proximity remain elusive, our microscopy data can help parameterize quantitative models. Finally, we observe a correlation between the presence of a nascent transcript and a shortening of the corresponding E–P distances. This is in line with models where short E–P distances are stabilized transiently during transcription, possibly within a multiprotein complex or transcriptional condensate.

Acknowledgements

We thank Dr Irina Solovei and Dr Simon Ulrich for assistance with RNA FISH and valuable scientific discussions. We thank Lara Carola Seppi for performing the qRT-PCR. We thank Yi Zhu for assistance with bioinformatic analysis of Tri-C data. We thank Dr Enes Ugur and Dr Weihua Qin for assistance with stem cell differentiation, and Jeannette Koch, Andreas Maiser, Ruzica Barisic, and Natasa Boskovski for technical assistance. G.S. gratefully acknowledges the integrated research training group 1064 (IRTG 1064) for training and support. D.T. is supported by the MSc/PhD program "Molecular Biology"—International Max Planck Research School at the Georg August University Göttingen.

Author contributions: G.S. and H.H. designed the study. H.H. and H.L. supervised the study. G.S. performed all FISH experiments and analyzed the data. C.S. synthesized the DNA FISH probes. D.H. and G.S. wrote the scripts for analysis of imaging data. D.H. automated the STED microscope. D.T. performed the Tri-C experiments. G.S. and D.T. analyzed the Tri-C data. G.S., D.T., A.M.O., and H.H. interpreted the data. All authors wrote the manuscript and prepared the figures. All authors discussed the results, read, and approved the manuscript.

Supplementary data

Supplementary data is available at NAR online.

Conflict of interest

None declared.

Funding

This work was supported by grants from the Deutsche Forschungsgemeinschaft: SFB1064 (project number 213249687) to H.L., Priority Program SPP 2202 (project number 422857584) to H.H. and H.L. and a research grant (project number HO 7333/1-1) to D.H. Funding to pay the Open Access publication charges for this article was provided by the Priority Program SPP 2202.

Data availability

The FISH spot coordinates generated in this study have been deposited at doi.org/10.5281/zenodo.17115347. Imaging data is available upon reasonable request. The Tri-C data generated in this study have been deposited at GEO: GSE308397.

The reanalyzed data used for enhancer calling can be found at GEO: GSE131556 (ATAC-seq), GEO: GSE156261 (H3K27ac ChIP-seq), GEO: GSE131556 (RNA-seq) [48] and GEO: GSE124342 (Hi-C) [61].

The code used for analyzing and processing the images can be found at: doi.org/10.5281/zenodo.17123359. The STED automation code can be found at: doi.org/10.5281/zenodo.14627119.

References

1. Weischenfeldt J, Ibrahim DM. When 3D genome changes cause disease: the impact of structural variations in congenital disease and cancer. *Curr Opin Genet Dev* 2023;80:102048. https://doi.org/10.1016/j.gde.2023.102048

2. Furlong EEM, Levine M. Developmental enhancers and chromosome topology. *Science* 2018;361:1341–5. https://doi.org/10.1126/science.aau0320
3. Yang JH, Hansen AS. Enhancer selectivity in space and time: from enhancer–promoter interactions to promoter activation. *Nat Rev Mol Cell Biol* 2024;25:574–91. https://doi.org/10.1038/s41580-024-00710-6
4. Alexander JM, Guan J, Li B *et al.* Live-cell imaging reveals enhancer-dependent Sox2 transcription in the absence of enhancer proximity. *eLife* 2019;8:e41769. https://doi.org/10.7554/eLife.41769
5. Heist T, Fukaya T, Levine M. Large distances separate coregulated genes in living Drosophila embryos. *Proc Natl Acad Sci USA* 2019;116:15062–7. https://doi.org/10.1073/pnas.1908962116
6. Du M, Stitzinger SH, Spille JH *et al.* Direct observation of a condensate effect on super-enhancer controlled gene bursting. *Cell* 2024;187:331–44. https://doi.org/10.1016/j.cell.2023.12.005
7. Chen H, Levo M, Barinov L *et al.* Dynamic interplay between enhancer–promoter topology and gene activity. *Nat Genet* 2018;50:1296–303. https://doi.org/10.1038/s41588-018-0175-z
8. Levo M, Raimundo J, Bing XY *et al.* Transcriptional coupling of distant regulatory genes in living embryos. *Nature* 2022;605:754–60. https://doi.org/10.1038/s41586-022-04680-7
9. Chen Z, Snetkova V, Bower G *et al.* Increased enhancer–promoter interactions during developmental enhancer activation in mammals. *Nat Genet* 2024;56:675–85. https://doi.org/10.1038/s41588-024-01681-2
10. Li J, Hsu A, Hua Y *et al.* Single-gene imaging links genome topology, promoter-enhancer communication and transcription control. *Nat Struct Mol Biol* 2020;27:1032–40. https://doi.org/10.1038/s41594-020-0493-6
11. Benabdallah NS, Williamson I, Illingworth RS *et al.* Decreased enhancer–promoter proximity accompanying enhancer activation. *Mol Cell* 2019;76:473–84. https://doi.org/10.1016/j.molcel.2019.07.038
12. Espinola SM, Gotz M, Bellec M *et al.* Cis-regulatory chromatin loops arise before TADs and gene activation, and are independent of cell fate during early Drosophila development. *Nat Genet* 2021;53:477–86. https://doi.org/10.1038/s41588-021-00816-z
13. Platania A, Erb C, Barbieri M *et al.* Transcription processes compete with loop extrusion to homogenize promoter and enhancer dynamics. *Sci Adv* 2024;10:eadq0987. https://doi.org/10.1126/sciadv.adq0987
14. Kane L, Williamson I, Flyamer IM *et al.* Cohesin is required for long-range enhancer action at the Shh locus. *Nat Struct Mol Biol* 2022;29:891–7. https://doi.org/10.1038/s41594-022-00821-8
15. Cho WK, Spille JH, Hecht M *et al.* Mediator and RNA polymerase II clusters associate in transcription-dependent condensates. *Science* 2018;361:412–5. https://doi.org/10.1126/science.aar4199
16. Shrinivas K, Sabari BR, Coffey EL *et al.* Enhancer features that drive formation of transcriptional condensates. *Mol Cell* 2019;75:549–61. https://doi.org/10.1016/j.molcel.2019.07.009
17. Sabari BR, Dall'Agnese A, Boija A *et al.* Coactivator condensation at super-enhancers links phase separation and gene control. *Science* 2018;361:eaar3958. https://doi.org/10.1126/science.aar3958
18. Boija A, Klein IA, Sabari BR *et al.* Transcription factors activate genes through the phase-separation capacity of their activation domains. *Cell* 2018;175:1842–55. https://doi.org/10.1016/j.cell.2018.10.042
19. Li J, Dong A, Saydaminova K *et al.* Single-molecule nanoscopy elucidates RNA polymerase II transcription at single genes in live cells. *Cell* 2019;178:491–506. https://doi.org/10.1016/j.cell.2019.05.029
20. Karr JP, Ferrie JJ, Tjian R *et al.* The transcription factor activity gradient (TAG) model: contemplating a contact-independent mechanism for enhancer–promoter communication. *Genes Dev* 2022;36:7–16. https://doi.org/10.1101/gad.349160.121
21. Deng W, Rupon JW, Krivega I *et al.* Reactivation of developmentally silenced globin genes by forced chromatin looping. *Cell* 2014;158:849–60. https://doi.org/10.1016/j.cell.2014.05.050
22. Vazquez J, Muller M, Pirrotta V *et al.* The Mcp element mediates stable long-range chromosome-chromosome interactions in Drosophila. *Mol Biol Cell* 2006;17:2158–65. https://doi.org/10.1091/mbc.e06-01-0049
23. Chen X, Yin X, Li J *et al.* Structures of the human Mediator and Mediator-bound preinitiation complex. *Science* 2021;372: eabg0635. https://doi.org/10.1126/science.abg0635
24. Richter WF, Nayak S, Iwasa J *et al.* The Mediator complex as a master regulator of transcription by RNA polymerase II. *Nat Rev Mol Cell Biol* 2022;23:732–49. https://doi.org/10.1038/s41580-022-00498-3
25. Bartman CR, Hsu SC, Hsiung CC *et al.* Enhancer regulation of transcriptional bursting parameters revealed by forced chromatin looping. *Mol Cell* 2016;62:237–47. https://doi.org/10.1016/j.molcel.2016.03.007
26. Williamson I, Lettice LA, Hill RE *et al.* Shh and ZRS enhancer colocalisation is specific to the zone of polarising activity. *Development* 2016;143:2994–3001. https://doi.org/10.1242/dev.139188
27. Mateo LJ, Murphy SE, Hafner A *et al.* Visualizing DNA folding and RNA in embryos at single-cell resolution. *Nature* 2019;568:49–54. https://doi.org/10.1038/s41586-019-1035-4
28. Amano T, Sagai T, Tanabe H *et al.* Chromosomal dynamics at the Shh locus: limb bud-specific differential regulation of competence and active transcription. *Dev Cell* 2009;16:47–57. https://doi.org/10.1016/j.devcel.2008.11.011
29. Lim B, Levine MS. Enhancer–promoter communication: hubs or loops? *Curr Opin Genet Dev* 2021;67:5–9. https://doi.org/10.1016/j.gde.2020.10.001
30. Nollmann M, Bennabi I, Gotz M *et al.* The impact of space and time on the functional output of the genome. *Cold Spring Harb Perspect Biol* 2022;14:a040378. https://10.1101/cshperspect.a040378
31. Goel VY, Huseyin MK, Hansen AS. Region capture Micro-C reveals coalescence of enhancers and promoters into nested microcompartments. *Nat Genet* 2023;55:1048–56. https://doi.org/10.1038/s41588-023-01391-1
32. Dekker J, Rippe K, Dekker M *et al.* Capturing chromosome conformation. *Science* 2002;295:1306–11. https://doi.org/10.1126/science.1067799
33. Lieberman-Aiden E, van Berkum NL, Williams L *et al.* Comprehensive mapping of long-range interactions reveals folding principles of the human genome. *Science* 2009;326:289–93. https://doi.org/10.1126/science.1181369
34. Quinodoz SA, Bhat P, Chovanec P *et al.* SPRITE: a genome-wide method for mapping higher-order 3D interactions in the nucleus using combinatorial split-and-pool barcoding. *Nat Protoc* 2022;17:36–75. https://doi.org/10.1038/s41596-021-00633-y
35. Vermeulen C, Allahyar A, Bouwman BAM *et al.* Multi-contact 4C: long-molecule sequencing of complex proximity ligation products to uncover local cooperative and competitive chromatin topologies. *Nat Protoc* 2020;15:364–97. https://doi.org/10.1038/s41596-019-0242-7
36. Oudelaar AM, Davies JOJ, Hanssen LLP *et al.* Single-allele chromatin interactions identify regulatory hubs in dynamic compartmentalized domains. *Nat Genet* 2018;50:1744–51. https://doi.org/10.1038/s41588-018-0253-2
37. Beagrie RA, Scialdone A, Schueler M *et al.* Complex multi-enhancer contacts captured by genome architecture mapping. *Nature* 2017;543:519–24. https://doi.org/10.1038/nature21411
38. Tjalsma SJ, de Laat W. Novel orthogonal methods to uncover the complexity and diversity of nuclear architecture. *Curr Opin Genet Dev* 2021;67:10–7. https://doi.org/10.1016/j.gde.2020.10.002

39. Bouwman BAM, Crosetto N, Bienko M. The era of 3D and spatial genomics. *Trends Genet* 2022;38:1062–75. https://doi.org/10.1016/j.tig.2022.05.010
40. Takei Y, Yun J, Zheng S *et al.* Integrated spatial genomics reveals global architecture of single nuclei. *Nature* 2021;590:344–50. https://doi.org/10.1038/s41586-020-03126-2
41. Steinek C, Guirao-Ortiz M, Stumberger G *et al.* Generation of densely labeled oligonucleotides for the detection of small genomic elements. *Cell Rep Methods* 2024;4:100840. https://doi.org/10.1016/j.crmeth.2024.100840
42. Devos X, Fiche JB, Bardou M *et al.* pyHiM: a new open-source, multi-platform software package for spatial genomics based on multiplexed DNA-FISH imaging. *Genome Biol* 2024;25:47. https://doi.org/10.1186/s13059-024-03178-x
43. Lando D, Ma X, Cao Y *et al.* Enhancer–promoter interactions are reconfigured through the formation of long-range multiway hubs as mouse ES cells exit pluripotency. *Mol Cell* 2024;84:1406–1421.e8. https://doi.org/10.1016/j.molcel.2024.02.015
44. Atlasi Y, Megchelenbrink W, Peng T *et al.* Epigenetic modulation of a hardwired 3D chromatin landscape in two naive states of pluripotency. *Nat Cell Biol* 2019;21:568–78. https://doi.org/10.1038/s41556-019-0310-9
45. Buecker C, Srinivasan R, Wu Z *et al.* Reorganization of enhancer patterns in transition from naive to primed pluripotency. *Cell Stem Cell* 2014;14:838–53. https://doi.org/10.1016/j.stem.2014.04.003
46. Novo CL, Javierre BM, Cairns J *et al.* Long-range enhancer interactions are prevalent in mouse embryonic stem cells and are reorganized upon pluripotent state transition. *Cell Rep* 2018;22:2615–27. https://doi.org/10.1016/j.celrep.2018.02.040
47. Endoh M, Niwa H. Stepwise pluripotency transitions in mouse stem cells. *EMBO Rep* 2022;23:e55010. https://doi.org/10.15252/embr.202255010
48. Kinoshita M, Barber M, Mansfield W *et al.* Capture of mouse and human stem cells with features of formative pluripotency. *Cell Stem Cell* 2021;28:453–471. https://doi.org/10.1016/j.stem.2020.11.005
49. Kalkan T, Olova N, Roode M *et al.* Tracking the embryonic stem cell transition from ground state pluripotency. *Development* 2017;144:1221–34. https://doi.org/10.1242/dev.142711
50. Neagu A, van Genderen E, Escudero I *et al. In vitro* capture and characterization of embryonic rosette-stage pluripotency between naive and primed states. *Nat Cell Biol* 2020;22:534–45. https://doi.org/10.1038/s41556-020-0508-x
51. Carbognin E, Carlini V, Panariello F *et al.* Esrrb guides naive pluripotent cells through the formative transcriptional programme. *Nat Cell Biol* 2023;25:643–57. https://doi.org/10.1038/s41556-023-01131-x
52. Langkabel J, Horne A, Bonaguro L *et al.* Induction of Rosette-to-Lumen stage embryoids using reprogramming paradigms in ESCs. *Nat Commun* 2021;12:7322. https://doi.org/10.1038/s41467-021-27586-w
53. Barrett T, Wilhite SE, Ledoux P *et al.* NCBI GEO: archive for functional genomics data sets–update. *Nucleic Acids Res* 2013;41:D991–5. https://doi.org/10.1093/nar/gks1193
54. Edgar R, Domrachev M, Lash AE. Gene Expression Omnibus: NCBI gene expression and hybridization array data repository. *Nucleic Acids Res* 2002;30:207–10. https://doi.org/10.1093/nar/30.1.207
55. Leinonen R, Sugawara H, Shumway M *et al.* The sequence read archive. *Nucleic Acids Res* 2011;39:D19–21. https://doi.org/10.1093/nar/gkq1019
56. Langmead B, Salzberg SL. Fast gapped-read alignment with Bowtie 2. *Nat Methods* 2012;9:357–9. https://doi.org/10.1038/nmeth.1923
57. Ramirez F, Dundar F, Diehl S *et al.* deepTools: a flexible platform for exploring deep-sequencing data. *Nucleic Acids Res* 2014;42:W187–91. https://doi.org/10.1093/nar/gku365
58. Ewels P, Magnusson M, Lundin S *et al.* MultiQC: summarize analysis results for multiple tools and samples in a single report. *Bioinformatics* 2016;32:3047–8. https://doi.org/10.1093/bioinformatics/btw354
59. Li H. Aligning sequence reads, clone sequences and assembly contigs with BWA-MEM. 2013; *arXiv:1303.3997*.
60. Fulco CP, Nasser J, Jones TR *et al.* Activity-by-contact model of enhancer–promoter regulation from thousands of CRISPR perturbations. *Nat Genet* 2019;51:1664–9. https://doi.org/10.1038/s41588-019-0538-0
61. McLaughlin K, Flyamer IM, Thomson JP *et al.* DNA methylation directs polycomb-dependent 3D genome re-organization in naive pluripotency. *Cell Rep* 2019;29:1974–85. https://doi.org/10.1016/j.celrep.2019.10.031
62. Amemiya HM, Kundaje A, Boyle AP. The ENCODE blacklist: identification of problematic regions of the genome. *Sci Rep* 2019;9:9354. https://doi.org/10.1038/s41598-019-45839-z
63. Xu W, Zhong Q, Lin D *et al.* CoolBox: a flexible toolkit for visual analysis of genomics data. *BMC Bioinformatics* 2021;22:489. https://doi.org/10.1186/s12859-021-04408-w
64. Kent WJ. BLAT–the BLAST-like alignment tool. *Genome Res* 2002;12:656–64.
65. Brandstetter K, Zulske T, Ragoczy T *et al.* Differences in nanoscale organization of regulatory active and inactive human chromatin. *Biophys J* 2022;121:977–90. https://doi.org/10.1016/j.bpj.2022.02.009
66. Beliveau BJ, Kishi JY, Nir G *et al.* OligoMiner provides a rapid, flexible environment for the design of genome-scale oligonucleotide in situ hybridization probes. *Proc Natl Acad Sci USA* 2018;115:E2183–92. https://doi.org/10.1073/pnas.1714530115
67. Gelali E, Girelli G, Matsumoto M *et al.* iFISH is a publically available resource enabling versatile DNA FISH to study genome architecture. *Nat Commun* 2019;10:1636. https://doi.org/10.1038/s41467-019-09616-w
68. Beliveau BJ, Joyce EF, Apostolopoulos N *et al.* Versatile design and synthesis platform for visualizing genomes with Oligopaint FISH probes. *Proc Natl Acad Sci USA* 2012;109:21301–6. https://doi.org/10.1073/pnas.1213818110
69. Hershberg EA, Camplisson CK, Close JL *et al.* PaintSHOP enables the interactive design of transcriptome- and genome-scale oligonucleotide FISH experiments. *Nat Methods* 2021;18:937–44. https://doi.org/10.1038/s41592-021-01187-3
70. Boettiger AN, Bintu B, Moffitt JR *et al.* Super-resolution imaging reveals distinct chromatin folding for different epigenetic states. *Nature* 2016;529:418–22. https://doi.org/10.1038/nature16496
71. Kishi JY, Lapan SW, Beliveau BJ *et al.* SABER amplifies FISH: enhanced multiplexed imaging of RNA and DNA in cells and tissues. *Nat Methods* 2019;16:533–44. https://doi.org/10.1038/s41592-019-0404-0
72. Bintu B, Mateo LJ, Su JH *et al.* Super-resolution chromatin tracing reveals domains and cooperative interactions in single cells. *Science* 2018;362.
73. Weichenhan D, Riedel A, Sollier E *et al.* Altered enhancer–promoter interaction leads to MNX1 expression in pediatric acute myeloid leukemia with t(7;12)(q36;p13). *Blood Adv* 2024;8:5100–11. https://doi.org/10.1182/bloodadvances.2023012161
74. Hörl D. A flexible framework for automated STED super-resolution microscopy. 2025. *bioRxiv*. https://doi.org/10.1101/2025.05.05.652196
75. Göttfert F, Wurm CA, Mueller V *et al.* Coaligned dual-channel STED nanoscopy and molecular diffusion analysis at 20 nm resolution. *Biophys J* 2013;105:L01–3. https://doi.org/10.1016/j.bpj.2013.05.029
76. Bahry E, Breimann L, Zouinkhi M *et al.* RS-FISH: precise, interactive, fast, and scalable FISH spot detection. *Nat Methods* 2022;19:1563–7. https://doi.org/10.1038/s41592-022-01669-y

77. Stringer C, Wang T, Michaelos M *et al.* Cellpose: a generalist algorithm for cellular segmentation. *Nat Methods* 2021;18:100–6. https://doi.org/10.1038/s41592-020-01018-x
78. Virtanen P, Gommers R, Oliphant TE *et al.* SciPy 1.0: fundamental algorithms for scientific computing in Python. *Nat Methods* 2020;17:261–72. https://doi.org/10.1038/s41592-019-0686-2
79. Preibisch S, Saalfeld S, Schindelin J *et al.* Software for bead-based registration of selective plane illumination microscopy data. *Nat Methods* 2010;7:418–9. https://doi.org/10.1038/nmeth0610-418
80. Hamley JC, Li H, Denny N *et al.* Determining chromatin architecture with micro Capture-C. *Nat Protoc* 2023;18:1687–711. https://doi.org/10.1038/s41596-023-00817-8
81. Oudelaar AM, Downes DJ, Hughes JR. Assessment of multiway interactions with Tri-C. *Methods Mol Biol* 2022;2532:95–112.
82. Downes DJ, Smith AL, Karpinska MA *et al.* Capture-C: a modular and flexible approach for high-resolution chromosome conformation capture. *Nat Protoc* 2022;17:445–75. https://doi.org/10.1038/s41596-021-00651-w
83. Karpinska MA, Zhu Y, Fakhraei Ghazvini Z *et al.* CTCF depletion decouples enhancer-mediated gene activation from chromatin hub formation. *Nat Struct Mol Biol* 2025;32:1268–81. https://doi.org/10.1038/s41594-025-01555-z
84. Hayashi K, Ohta H, Kurimoto K *et al.* Reconstitution of the mouse germ cell specification pathway in culture by pluripotent stem cells. *Cell* 2011;146:519–32. https://doi.org/10.1016/j.cell.2011.06.052
85. Gabriele M, Brandao HB, Grosse-Holz S *et al.* Dynamics of CTCF- and cohesin-mediated chromatin looping revealed by live-cell imaging. *Science* 2022;376:496–501.
86. Le DJ, Hafner A, Gaddam S *et al.* Super-enhancer interactomes from single cells link clustering and transcription. *bioRxiv* 2024. https://doi.org/10.1101/2024.05.08.593251
87. Allahyar A, Vermeulen C, Bouwman BAM *et al.* Enhancer hubs and loop collisions identified from single-allele topologies. *Nat Genet* 2018;50:1151–60. https://doi.org/10.1038/s41588-018-0161-5
88. Oudelaar AM, Harrold CL, Hanssen LLP *et al.* A revised model for promoter competition based on multi-way chromatin interactions at the alpha-globin locus. *Nat Commun* 2019;10:5412. https://doi.org/10.1038/s41467-019-13404-x
89. Jusuf JM, Grosse-Holz S, Gabriele M *et al.* Genome-wide absolute quantification of chromatin looping. *Biorxiv* 2025. https://doi.org/10.1101/2025.01.13.632736
90. Xiao JY, Hafner A, Boettiger AN. How subtle changes in 3D structure can create large changes in transcription. *eLife* 2021;10:e64320. https://doi.org/10.7554/eLife.64320
91. Zuin J, Roth G, Zhan Y *et al.* Nonlinear control of transcription through enhancer–promoter interactions. *Nature* 2022;604:571–7. https://doi.org/10.1038/s41586-022-04570-y
92. Nazarova M, Sexton T. The dance of promoters and enhancers in gene regulation: fast or slow, entwined or distant? *J Mol Biol* 2025;169223. https://doi.org/10.1016/j.jmb.2025.169223

Received: January 20, 2025. **Accepted:** October 15, 2025

SUPPLEMENTARY FIGURES for

Nanoscale Dynamics of Enhancer-Promoter Interactions during Exit from Pluripotency

Authors:
Gabriela Stumberger, David Hörl, Dimitra Tsouraki, Clemens Steinek, A. Marieke Oudelaar, Heinrich Leonhardt, Hartmann Harz

Correspondence:
harz@biologie.uni-muenchen.de, h.leonhardt@biologie.uni-muenchen.de

This PDF includes:

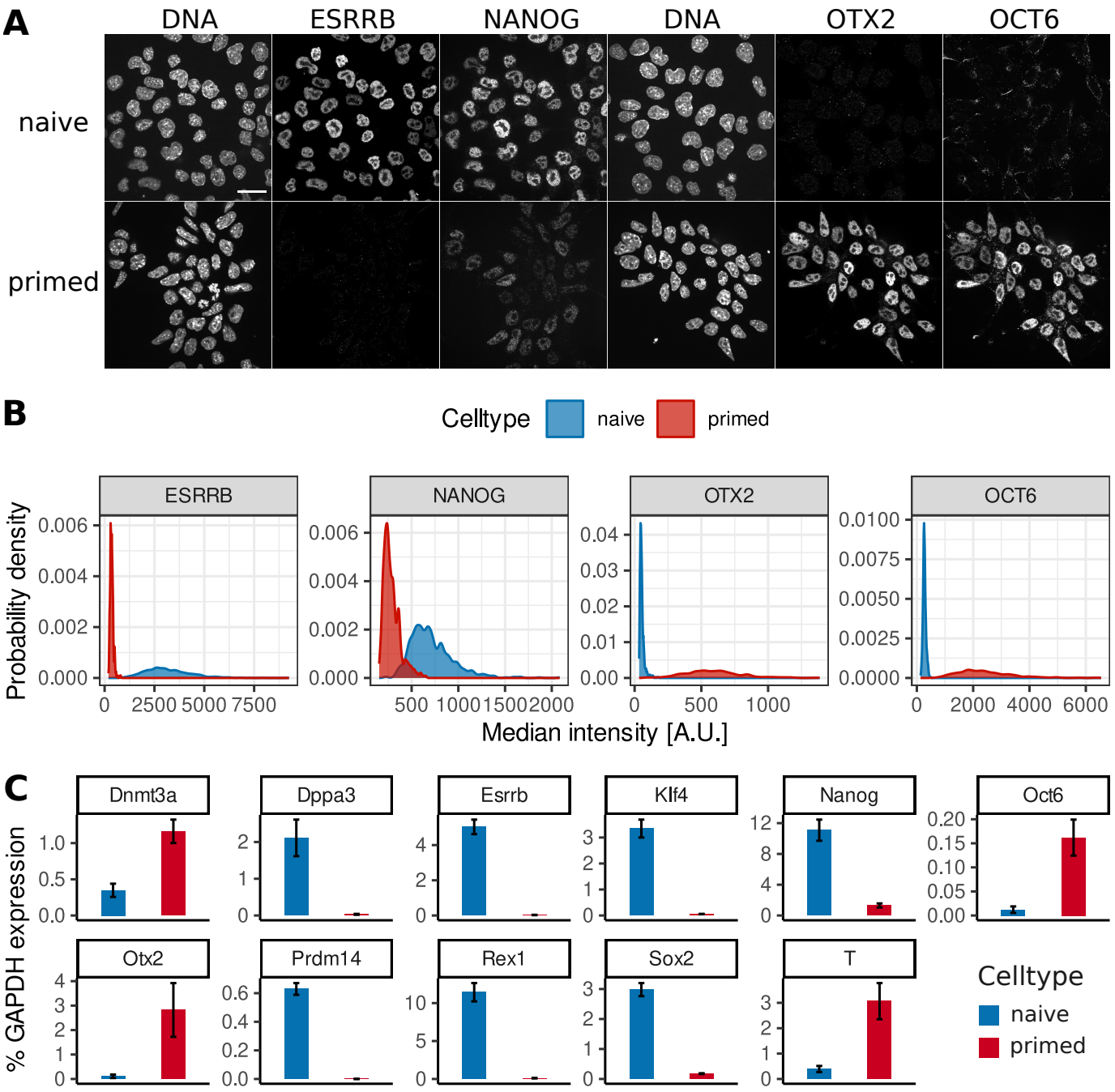

Supplementary Figure S1: Verification of naive -> primed system.
(A) Immunofluorescence of naive (ESRRB, NANOG) and primed (OTX2, OCT6) differentiation markers. Scale bar represents 20 µm. (B) Distribution of marker gene expression in naive (blue) and primed (red) cell nuclei. There is a clear decrease in ESRRB and NANOG expression and an increase in OTX2 and OCT6 expression as cells transition from naive to primed. ESRRB, NANOG: n_{naive}=665, n_{primed}=455; OTX2, OCT6: n_{naive}=680, n_{primed}=591. (C) mRNA expression levels of target makrer genes in naive (blue) and primed (red) mouse embryonic stem cells were measured via quantitative real-time PCR at 0 h (naive) and after 7 days (primed) of differentiation. Expression is represented as % GAPDH expression (median ± SEM, n=5 biological replicates).

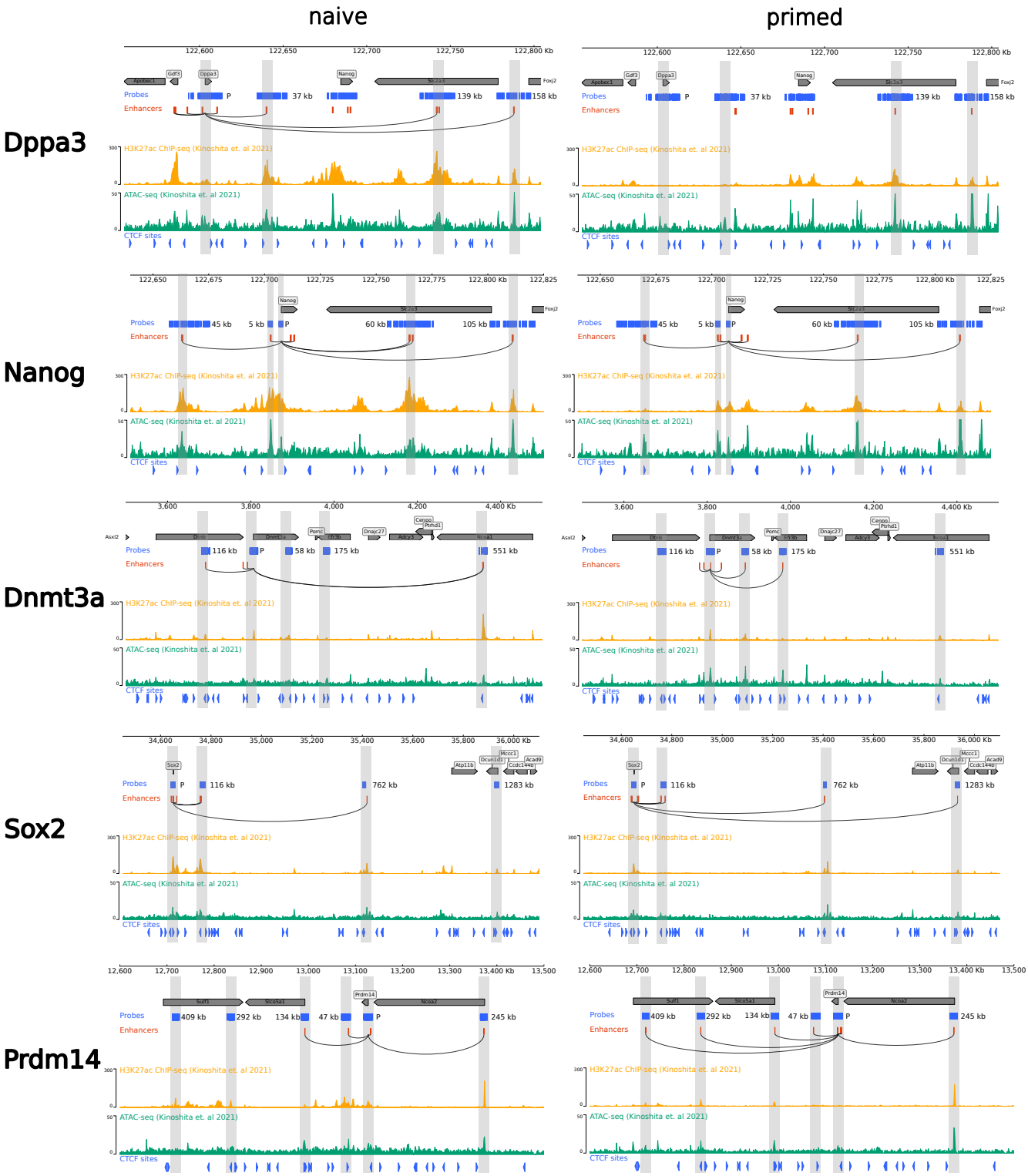

Supplementary Figure S2: Genomic data for target regions in naive and primed cells. For each gene and cell state, from top to bottom: DNA oligoFISH probes against promoter and selected enhancers (blue), all predicted enhancers (red), connection between promoter and its predicted enhancers (black arcs), H3K27ac ChIP signal (yellow, from Kinoshita et al. 2021), ATAC-seq signal (green, from Kinoshita et al. 2021), CTCF binding motifs (blue arrows) and targeted enhancer regions (vertical gray stripes).

A: Chromatic aberrations across field-of-view (561nm - 640nm)

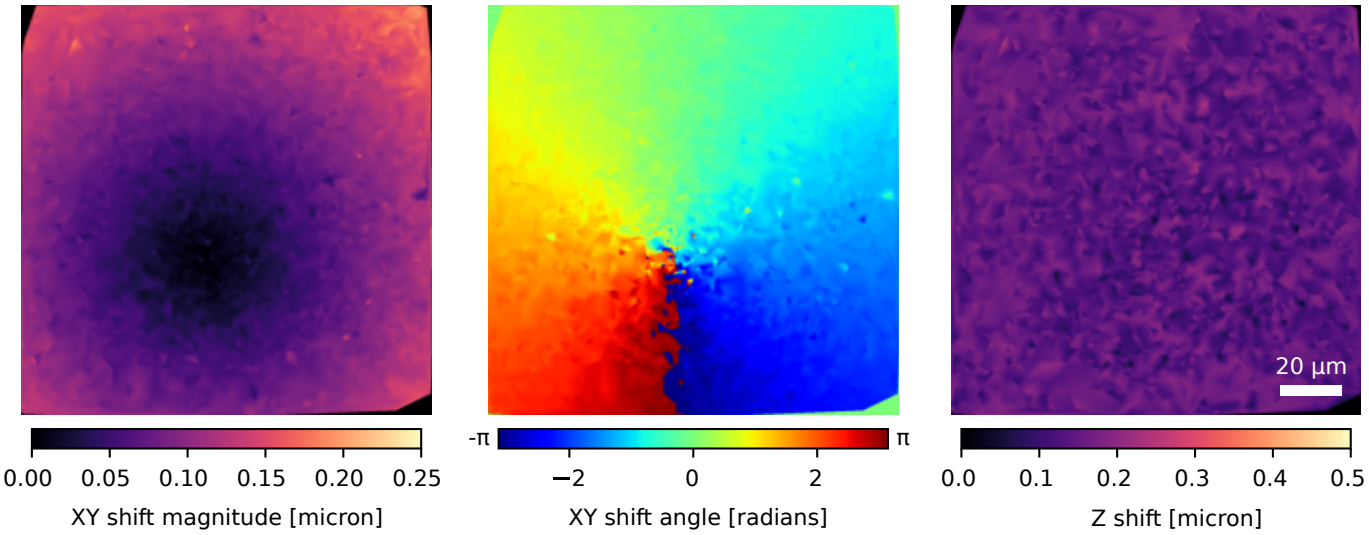

B: Chromatic aberrations per dimension (561nm - 640nm)

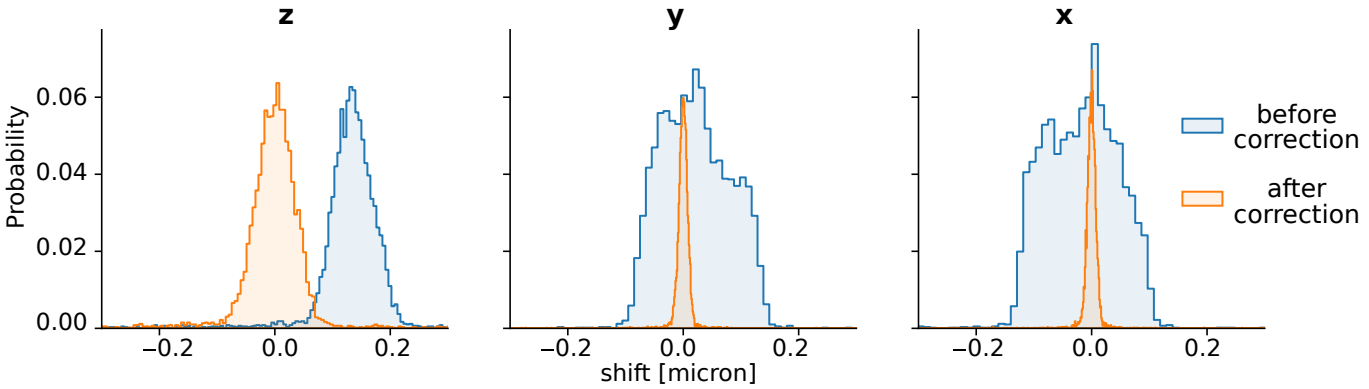

Supplementary Figure S3: Characterization of chromatic aberrations between the 561nm and 640nm channels of our spinning disk microscope. (A) Shifts across the field-of-view interpolated from matched Tetraspeck beads. (B) Histograms of shifts (difference of coordinates of matched beads) per dimension of the same dataset. Corrected coordinates were calculated using a leave-one-out cross validation scheme on the 11-image calibration dataset.

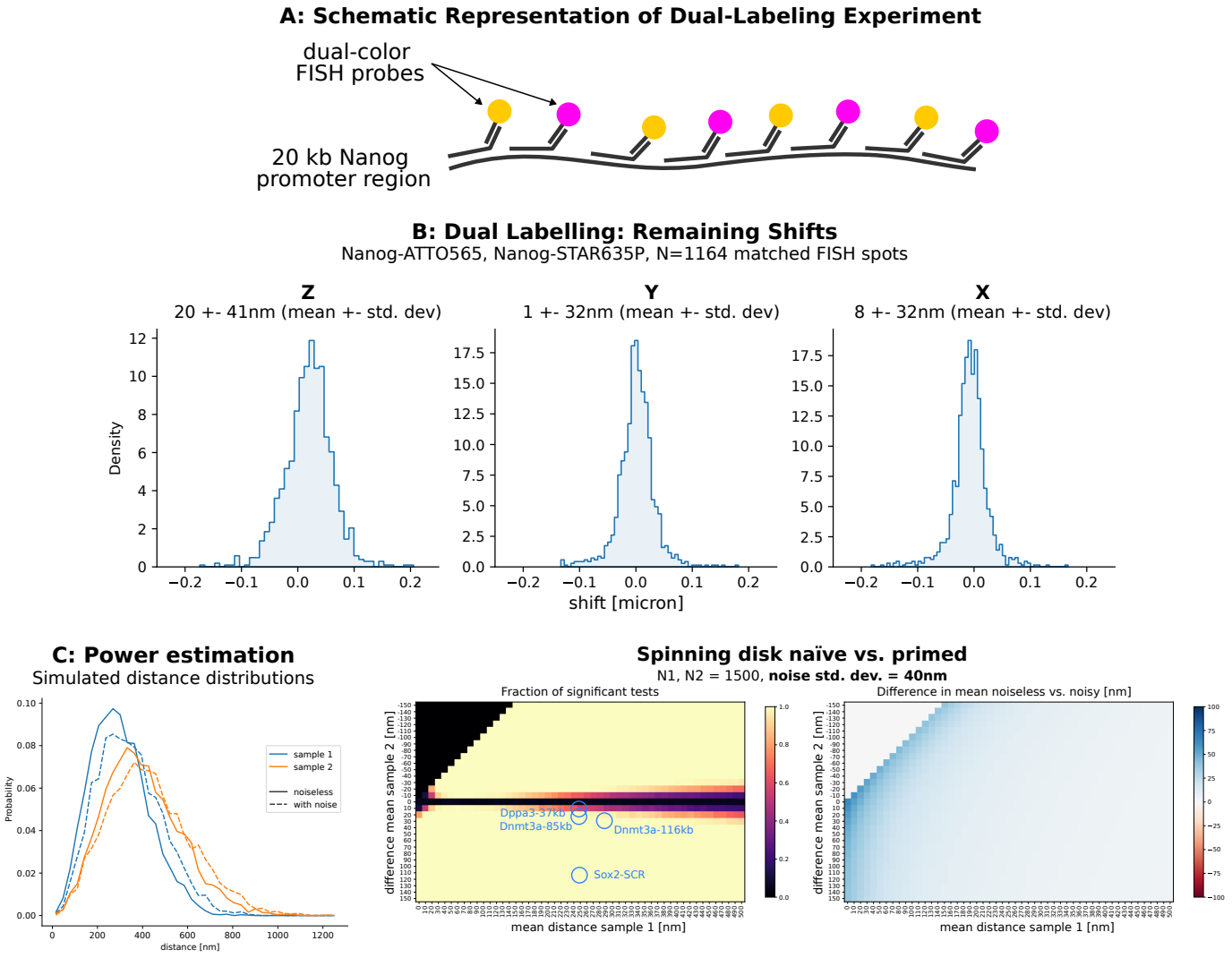

Supplementary Figure S4: (A) Schematic representation of dual-labeling experiment: a 20 kb region overlapping the Nanog promoter was labelled with alternating ATTO565 and STAR635P FISH probes. (B) Distance distributions of matched FISH spots in two channels in a dual-labelling experiment per dimension. (C) Statistical power estimation via repeated simulations of pairs of distance distributions. Middle: Fraction of 1000 repetitions that resulted in significant differences for various combinations of mean distances in sample 1 and difference in mean in sample 2. Combinations that would result in negative distances are skipped. Combinations of average distances that show significant differences in observed data are highlighted in blue. Right: Mean differences in distance between simulated vectors with and without noise.

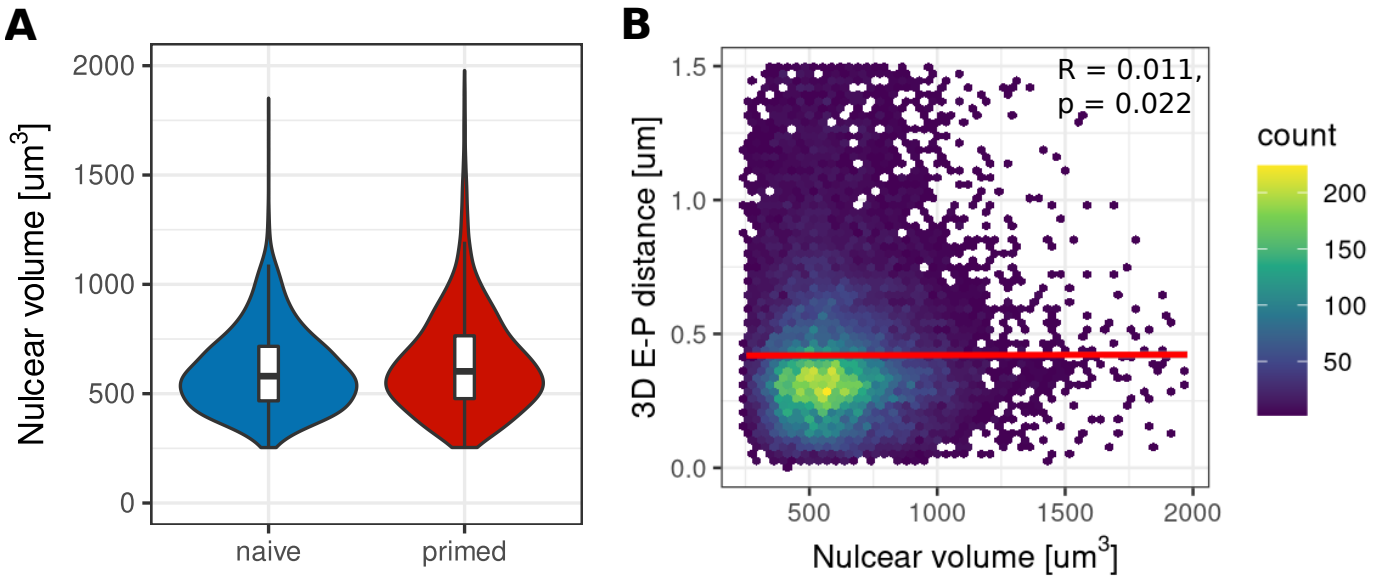

Suppplementary Figure S5: Relationship between nuclear volume and enhancer-promoter (E-P) distance. (A) Nuclear volume [µm³] distributions in naive (blue) and primed (red) cells (n_{naive}=27167, n_{primed}=23970, from all nuclei in Fig 1 F, measured with spinning disk confocal micorscope). (B) There is no notable correlation between nuclear volume and E-P distances (Spearman's Rank Correlation, R=0.011, p=0.022; n= 51137, over 2 celltypes and 3 biological replicates).

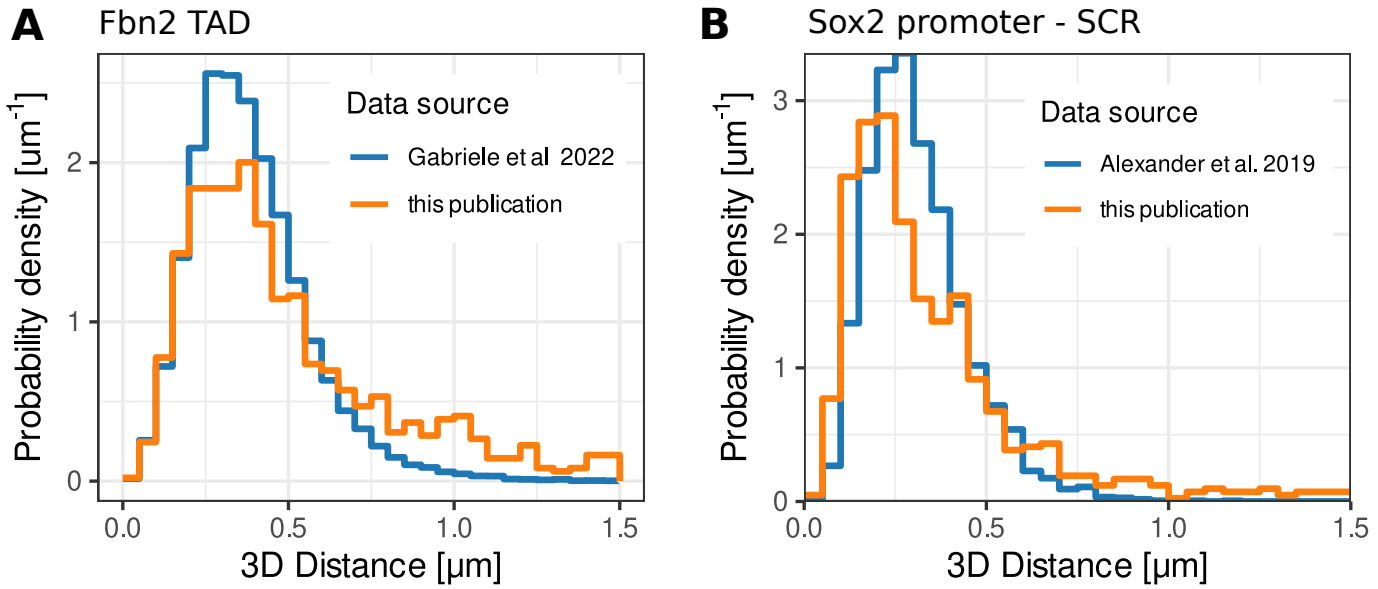

Supplementary Figure S6: Comparison of FISH and live cell measurments at sleected loci. (A) 3D distances at the Fbn2 locus for our DNA FISH (orange) and live cell measurements from Gabriele et al. 2022 (blue). $n_{this\ publication}$=979, $n_{Gabriele\ et\ al.\ 2022}$=46163. (B) 3D distances between the Sox2 promoter and the SCR enhancer region for our DNA FISH (orange) and live cell measurements from Alexander et al. 2019 (blue). $n_{this\ publication}$=831, $n_{Alexander\ et\ al.\ 2019}$=4380.

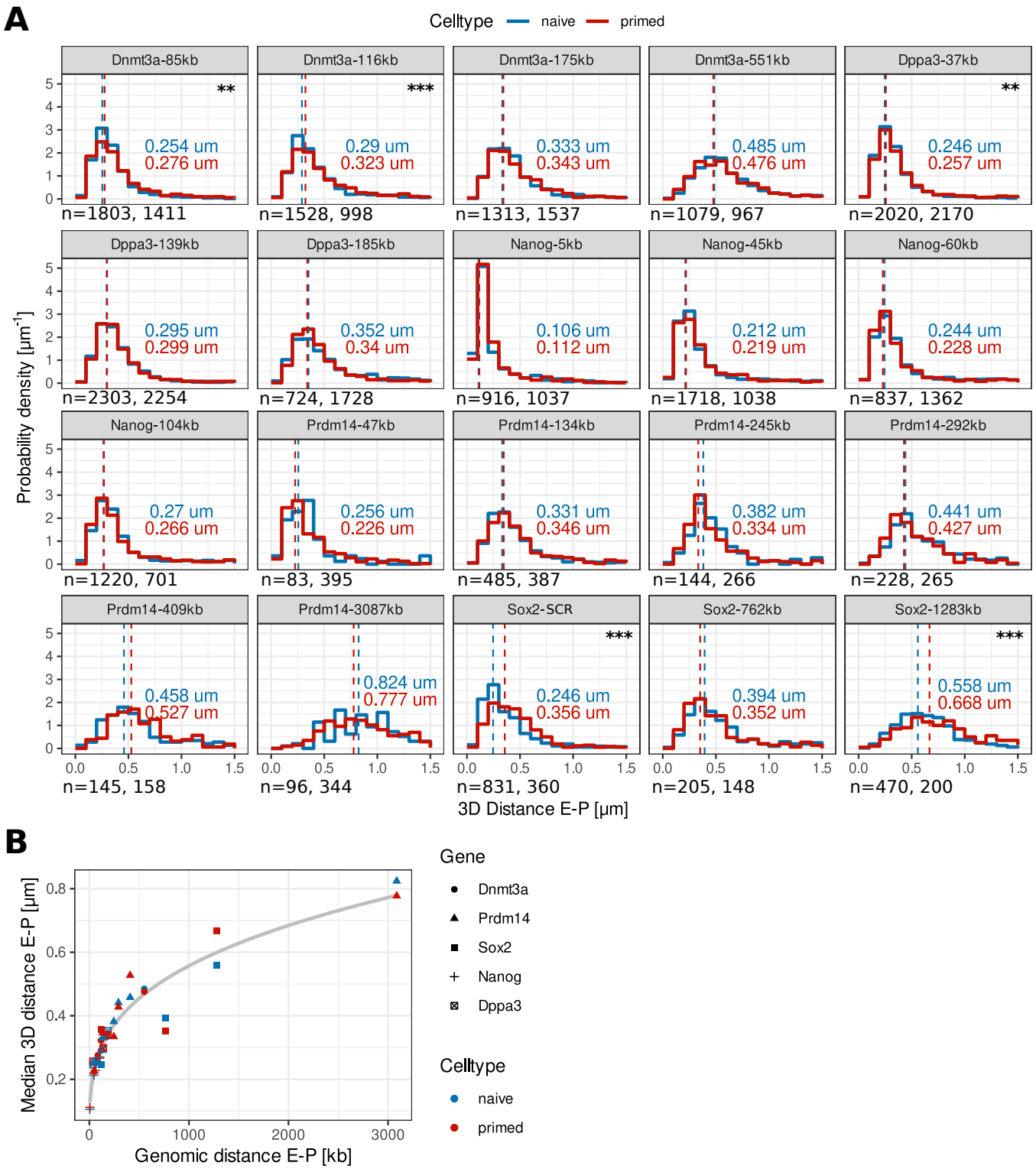

Supplementary Figure S7: Summary of enhancer-promoter (E-P) distances in developmental enhancers in naive and primed cells. (A) 3D distance [µm] distributions of promoters and their corresponding enhancers in naive (blue) and primed (red) cells. Dashed line and number next to histogram represent the median distance. Significant differences between naive and primed indicated by: * $p \leq 0.05$, ** $p \leq 0.01$, *** $p \leq 0.001$ (Wilcoxon rank sum test, Benjamini-Hochberg FDR correction). (B) Median 3D E-P distance [µm] as function of genomic distance [kb] for 5 genes. 3D distance for most E-P pairs is largely influenced by genomic distance. The curve was fitted to the data using a power law model: $y = a*x^b+c$, with estimated coeficients: a=0.63, b=0.31,c=0.024.

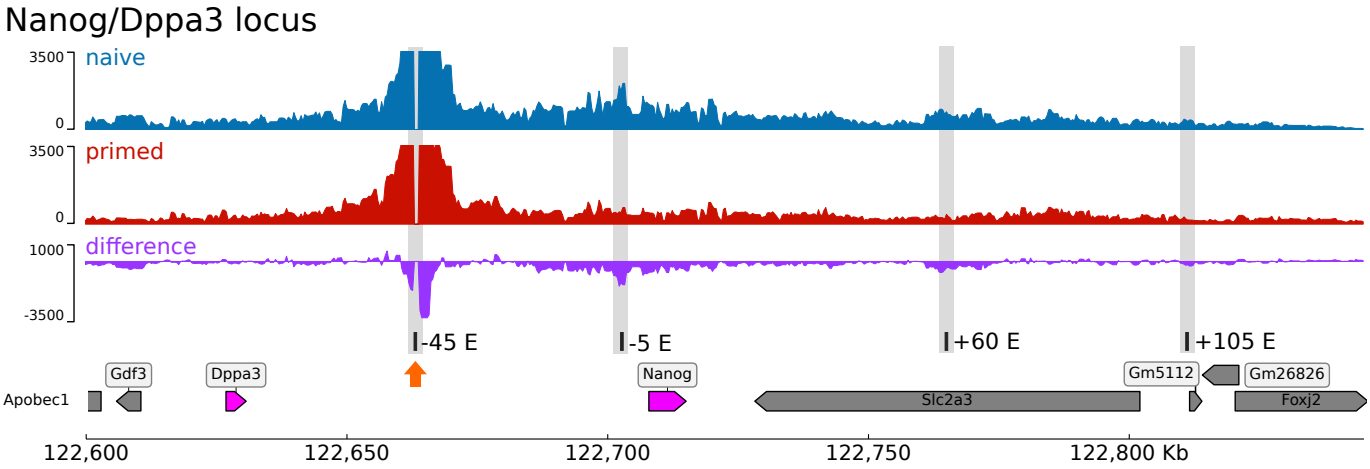

Supplementary Figure S8: Tri-C Pairwise interactions at the Nanog/Dppa3 locus. Naive cells are shown in blue, primed cells in red and the difference between the two (naive - primed) in purple. The viewpoint (Nanog -45 E) is indicated with an orange arrow.

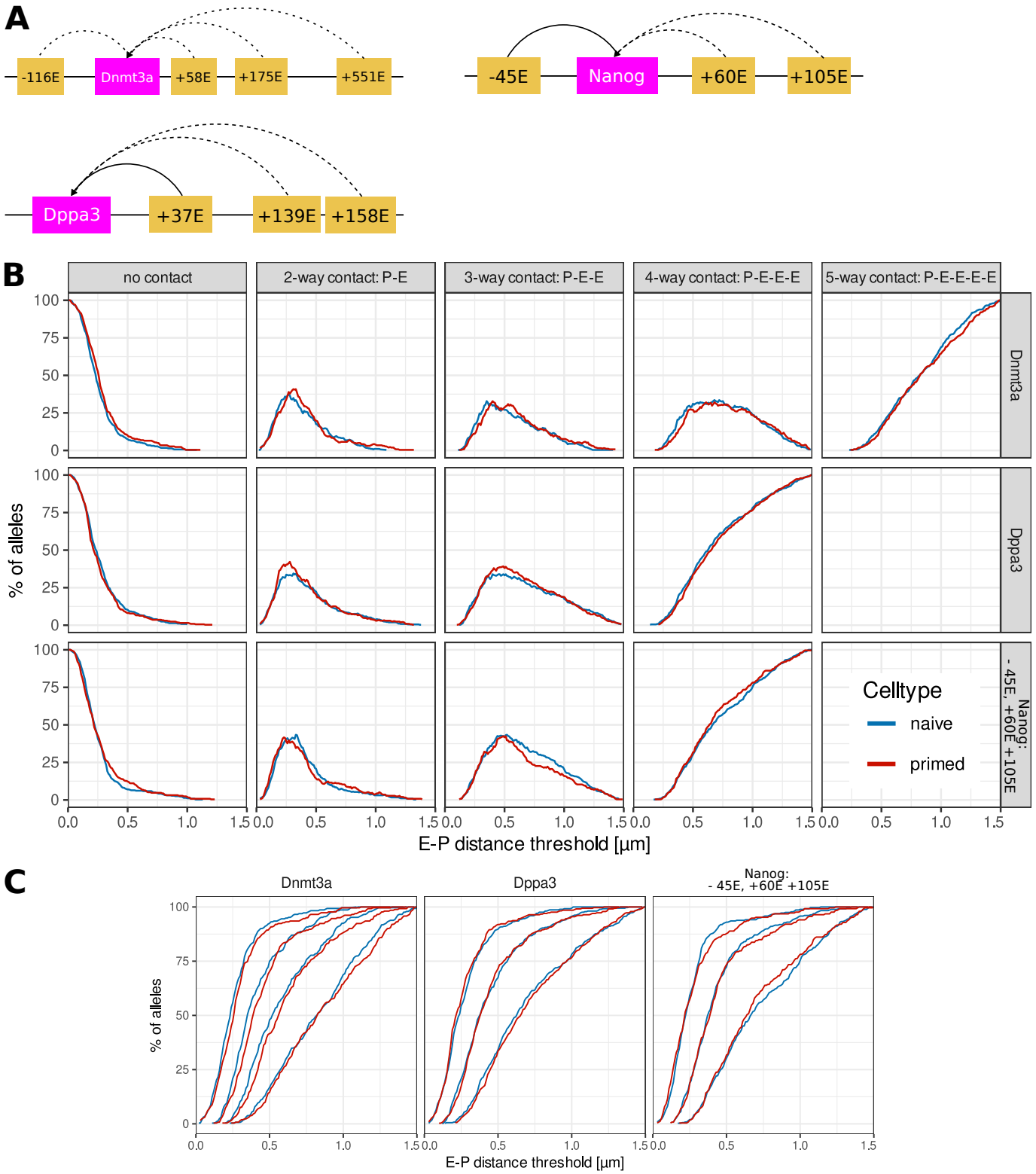

Supplementary Figure S9: Multiway E-P contacts during the naive to primed differentiation. (A) Schematic representation of measured interactions at Dnmt3a, Dppa3 and Nanog loci. (B) Interaction frequencies between a promoter (P) and different numbers of enhancers for a range of contact thresholds [µm]. Naive cells are plotted in blue, primed in red. Dnmt3a: n_n=292, n_p=262; Dppa3: n_n = 371, n_p =334; Nanog (-45,+60E,+105E): n_n=357, n_p=252 over 3 replicates. (C) % of detected alleles with at least 1, 2, 3 or 4 enhancers for a range of contact thresholds [µm]. For n see (B).

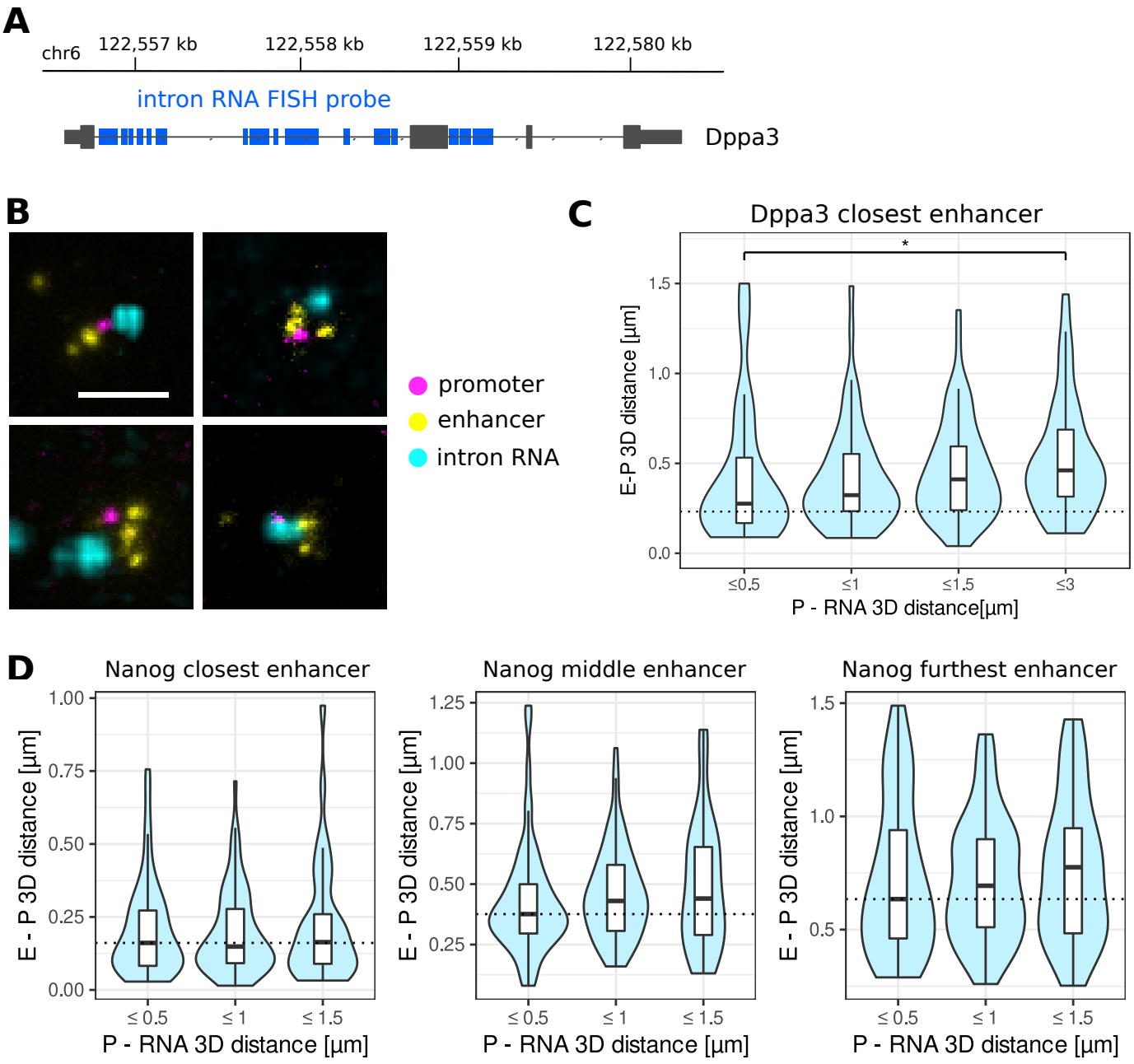

Supplementary Figure S10: (A) Shorter enhancer - promoter (E - P) distances correlate with active transcription. (A) Genomic location of Nanog intron RNA FISH probes. (B) STED microscopy images (maximum intensity projections) of promoter (magenta), enhancers (yellow) and intron RNA (cyan) for Dppa3. Scale bar represents 1 µm. (C) Dppa3 E-P 3D distance, based on distance of promoter to closest nascent RNA. ($p < 0.05$: *, two-sided Wilcoxon rank sum test). $n \leq 0.5 = 21$, $n \leq 1 = 59$, $n \leq 1.5 = 60$, $n \leq 3 = 109$ over 3 biological replicates. (D) E - P 3D distances of Nanog's closest middle and furthest enhancer, based on the distance of the promoter to the closest nascent RNA. $n \leq 0.5 = 57$, $n \leq 1 = 72$, $n \leq 1.5 = 35$ over 3 biological replicates.

Discussion

3.1 Visualizing small genomic elements with FISH

Over the past decade, enhancers have emerged as one of the key players in regulating gene expression. However, mapping of enhancer-promoter (E-P) contacts at high resolution remains challenging. While 3C-based assays have enabled mapping of genome-wide interactions at kb resolution [11, 127, 252], both fluorescence in situ hybridization (FISH) and single-cell Hi-C have revealed that features from population-averaged contact maps can be highly variable at the single-cell level [54–57]. Single-cell high-throughput chromosome conformation capture (Hi-C) methods suffer from limited resolution and sampling due to the low amount of input material [10, 54], making FISH-based approaches particularly valuable for studying spatial organization in individual cells. Early FISH probes were synthesized from bacterial artificial chromosomes (BACs) and yeast artificial chromosomes (YACs), which limits their resolution to tens of kb [374]. The development of chemically synthesized oligonucleotides, like Oligopaint-based probes, significantly improved resolution to a few kb [377]. However, this is still insufficient when trying to visualize small genomic elements separated by only a few kb with high resolution and sensitivity. Although signal amplification methods provide stronger signals through multiple rounds of hybridization, nonspecific background signals from the high density of fluorophores can make the visualization of sub-kilobase genomic loci difficult [364, 398, 399]. We developed a time and cost-effective protocol - nanoscopy-compatible oligonucleotides with dyes in variable arrays (NOVA) - for the generation of FISH probes that enable the visualization of small genomic regions at sub-kilobase resolution, without the need for multiple hybridization steps.

3.1.1 A novel method for visualizing sub-kilobase chromatin

In general, FISH probes can be labeled either directly, or hybridized with secondary fluorescently-labeled oligos. While many other FISH approaches use secondary oligos for cost-effectiveness and to enable multiplexing [371, 378–380], our results demonstrate that using directly labeled oligos significantly improves signal strength, likely in part by avoiding fluorophore loss during secondary hybridization [378]. NOVA-FISH improves signal of directly labeled probes by incorporating multiple fluorophores per probe. This is similar to other FISH amplification strategies that increase signal intensity by allowing multiple secondary probes, and thus additional fluorophores, to bind to each target [364, 398, 399]. The enhanced brightness of NOVA probes enables visualization of sub-kilobase regions as small as 0.5 kb using only 10 probes. However, probe sets below 30 probes (2.8 kb region) display significantly lower detection sensitivity, requiring users to balance the need for high spatial resolution against detection efficiency.

In addition to offering sub-kilobase resolution, NOVA-FISH is also time- and cost-effective. A typical Oligopaint-based approach for generating probes from an oligopool involves selective probe amplification via polymerase chain reaction (PCR), production of single-stranded DNA through methods like *in vitro* transcription, and subsequent barcoding by reverse transcription. This multistep process can be time-consuming, requiring 2–3 days [371, 378–380]. Ordering directly labeled commercial probes offers a simpler alternative, but costs increase substantially for large pools. The NOVA approach speeds up the template removal process by using 5'-phosphorylated templates that are degraded with lambda exonuclease, reducing the total probe synthesis time to approximately 4 hours. Moreover, the consumable cost for generating probes sufficient for about 100 FISH samples remains below 10 EUR, compared to just over 25 EUR when employing Oligopaint-based synthesis.

3.1.2 NOVA-FISH protocol optimization

To identify the most efficient way of enzymatically incorporating fluorescently labeled nucleotides into our probes, we compared several commonly available family A (Klenow exo-, Taq) and family B (Q5, Phusion, Therminator) DNA polymerases. We found that family B polymerases exhibit higher efficiency in incorporating labeled dNTPs compared to family A polymerases. This is consistent with studies examining the crystal structures of different polymerases, which attribute the B family's ability to process bulky, modified nucleotides to larger channel volume, fewer steric hindrances,

and B-form DNA conformation [416–418]. Therminator DNA polymerase showed the highest incorporation efficiency, possibly due to the D141A and E143A mutations which inactivate its 3'-5' exonuclease proofreading activity, and the A485L mutation on its finger domain, which reduces its substrate selectivity [419]. We were able to successfully incorporate ATTO647N, ATTO594 and ATTO488, but depending on fluorophore size, charge, linker chemistry and enzyme compatibility, we expect other fluorophores may also be incorporated [416–418, 420].

To control the maximum number of incorporated fluorophores independently of the target sequence, we designed short overhangs at the 3' end of each probe. Fluorophores were then incorporated specifically at cytosine residues within these overhangs. We found that cytosines had to be spaced sufficiently apart to prevent a reduction in fluorescence intensity. This can be explained by self-quenching. When two identical fluorophores are in close proximity or physical contact, they form a dimer that dissipates energy non-radiatively as heat rather than fluorescence emission [421]. For ATTO647N, a minimum spacing of 7 nucleotides between fluorophores was required to avoid a reduction in signal, consistent with the findings of Schröder et al. [422], who reported that dyes must be separated by at least 7 nucleotides to prevent contact-mediated quenching. At this distance, the quenching mechanism shifts from contact-mediated quenching toward Förster resonance energy transfer (FRET), which has minimal effect on fluorescence emission between identical dyes at low excitation intensities [422]. Interestingly, for ATTO488, reduction in signal was observed even when fluorophores were separated by 10 nucleotides, which is in agreement with previous reports that optimal fluorophore spacing varies depending on the dye's chemical structure [421, 423].

The number of simultaneously detectable targets with NOVA is limited by the available fluorescence channels in the microscopy setup. Unlike methods that rely on secondary oligo hybridization, such as signal amplification by exchange reaction (SABER)-FISH [364], directly labeled NOVA probes are not inherently compatible with sequential imaging strategies that achieve multiplexing through cycles of oligo stripping and rehybridization. However, given they carry multiple fluorophores per molecule, NOVA probes could in principle serve as brighter alternatives to conventional secondary oligos. Whether this approach would offer advantages over established signal amplification methods like SABER remains to be determined, and would require systematic comparison. As with any fixed-cell approach, NOVA provides snapshots rather than dynamic information. Investigating temporal aspects of E-P interactions will therefore require complementary live-cell imaging methods. Additionally, like conventional

FISH, the use of formamide and heat denaturation may alter native chromatin structure, potentially affecting the observed spatial relationships between genomic loci [391, 393]. Future integration of NOVA with gentler FISH protocols, such as resolution after single-strand exonuclease resection (RASER)-FISH [397] or genome oligopaint via local denaturation (GOLD)-FISH [396] would help address these limitations.

3.1.3 Current and future applications of NOVA-FISH

Nonetheless, NOVA's ability to detect sub-kilobase chromatin is useful in many applications. First, NOVA can be used to investigate chromatin interactions when high resolution is required or when regulatory elements are positioned close together on the linear genome. For instance, we applied NOVA to investigate interactions between the *Nanog* promoter and its 5 kb enhancer, as discussed in detail in Section 3.2. NOVA could also be useful for investigating multiway contacts between individual domains of super-enhancers clusters. Although bulk assays have revealed increased contact frequencies between these domains, their close genomic proximity has made it challenging to resolve precise 3D spatial dynamics and to correlate these interactions to transcription at the single-cell level [168, 255, 280, 424]. In addition, we have already applied NOVA-FISH to detect small genomic loci near breakpoints in acute myeloid leukemia (AML) models [284]. Second, NOVA could be used to label clusters of transcription factor (TF) binding motifs in combination with immunostaining of the corresponding TFs. Previous studies have visualized condensates by labeling TFs directly [147, 425], and it is known that regulatory DNA sequences harboring TF binding sites contribute to establishing high local TF concentrations [426, 427]. NOVA could reveal the spatial organization of these regulatory sequences within condensates. This would be particularly interesting during early embryonic development, for example, when the genome becomes transcriptionally active during zygotic genome activation (ZGA) [179, 180], or during developmental transitions such as the naive-to-primed transition, when enhancer clusters are thought to drive cell type-specific changes in gene expression [169, 255]. Finally, as NOVA represents a cost-effective method to generate oligonucleotides carrying custom numbers of fluorophores, we anticipate future applications in DNA-PAINT, DNA origami, and immunostaining where brighter probes are required [428, 429].

In summary, NOVA-FISH provides a simple, quick, and cost-effective approach for high-resolution imaging of sub-kilobase chromatin, which has already proven valuable in investigating enhancer hijacking in AML, and visualizing E-P interactions during pluripotency transitions.

3.2 Investigating changes in enhancer - promoter distances during pluripotency transition

Even though enhancers and promoters are known to play an important role in regulating gene expression, how they interact to exchange regulatory information is still debated. Specifically, it is unclear whether close spatial proximity between regulatory elements is required for transcription. While some studies report that enhancers and promoters are brought into close spatial proximity during active transcription [117, 125, 140–142], others have shown that transcription can occur even when these elements are several hundred nanometers apart [115, 116, 144]. Adding another layer of complexity, recent studies have revealed multiway E-P interactions that appear to drive cell type-specific gene expression patterns [168, 169]. However, the frequency of these multiway interactions in single cells remains under-explored. To address these questions, we combined FISH, super-resolution microscopy and Tri-C to investigate E-P contacts of five differentially expressed genes (i) during the transition from naive to primed pluripotency in mouse embryonic stem cells (mESCs) and (ii) immediately after transcription.

3.2.1 Stable vs. transient models of enhancer - promoter interaction

While classical models stemming from studies in prokaryotes [174, 175] propose that enhancers and promoters form stable contacts over longer periods of time, imaging studies in animals have generally found chromatin interactions to be dynamic [40, 61, 114, 117, 118, 430]. Our combined RNA-DNA FISH data recapitulate these observations, showing that E-P distances change with transcriptional state and that E-P contacts are likely transient. At the *Nanog* and *Dppa3* loci, alleles with more recent transcriptional activity (as measured by nascent RNA proximity to the promoter) exhibited significantly shorter E-P distances than those transcribed longer ago. This observation is consistent with data from Ohishi et al. [141], who reported that *Nanog* enhancers spent more time in proximity of actively transcribed promoters. However, nascent RNA FISH can only provide information about E-P distances after transcription has already been initiated and the RNA (partially) synthesized. Moreover, like all fixed-cell methods, FISH captures only "snapshots" of continuous processes such as transcription, making it unclear whether the chromatin structures measured here correspond to those present at transcriptional initiation. Nonetheless, our observations are supported by live cell imaging data and simulations [40, 61, 117, 118, 430, 431].

Gabriele et al. [40] demonstrated using live-cell imaging in mESCs that TAD loops persist for only 10–30 minutes and Brückner et al. [430] found similar lifetimes between enhancers and promoters in *Drosophila* embryos. Mathematical models and polymer simulations based on live-cell imaging data estimated that the vast majority of E-P contacts in mESCs are even more transient, lasting only a few seconds [118, 431]. In agreement with others, our data argue against models of stable, sustained E-P contact in mESCs.

3.2.2 Direct contact vs. action-at-a-distance models of enhancer - promoter interaction

Models of direct contact propose that enhancers must come into direct physical proximity with promoters to enable transcription. However, we rarely observed E-P distances below 50 nm in any of our measurements. While shorter distances were also observed, the median of actively transcribing alleles in our combined RNA-DNA FISH data at the *Nanog* locus was ∼230 nm. Beyond technical limitations (see Section 3.2.5), two non-mutually exclusive explanations could account for this observation. First, as discussed above, close E-P contacts are highly transient and may therefore represent only a small fraction of the population at any given time. This would make them difficult to detect with the sample sizes of hundreds to thousands of alleles measured here. Second, "direct" contact may not equate to zero distance, as TFs, co-factors, and transcriptional machinery occupy physical space between enhancers and promoters [114]. For example, structural studies of the Mediator-bound pre-initiation complex (PIC) have shown that the Mediator complex bridges transcriptional activators at enhancers with the core transcription machinery at promoters, facilitating assembly of the PIC. Given that the assembled Mediator-PIC alone spans roughly 35-40 nm [432–436], enhancers and promoters may be able to functionally interact without direct physical contact. E-P contact should therefore be considered as a threshold, rather than zero distance [120]. Defining such a threshold for functional E-P contact remains challenging (which will be discussed in Section 3.2.3) and blurs the line between direct contact and action-at-a-distance models.

Examining distances of 20 different E-P pairs, we find that changes in E-P distances during the naive-to-primed transition are highly locus specific and do not always follow predicted patterns. Consistent with Ohishi et al. [141], distances between *Nanog* and any of its enhancers remained largely unchanged as *Nanog* was downregulated during the pluripotency transition. In contrast, the *Sox2* control region (SCR) moved significantly further away (∼110 nm) from is promoter as *Sox2* was downregulated. In

agreement with others [118, 128, 437], we also observed that median E-P distance is largely influenced by genomic distance, regardless of cell state. The difference between changed and unchanged E–P distances could therefore, in part, be explained by the notion that genomically proximal enhancers (typically $\leq$ 50 kb) are close enough to make sufficiently frequent stochastic contacts with the promoter, whereas long-range enhancers (typically $>$ 100 kb) require additional mechanisms to bring them into close spatial proximity [430, 438]. These mechanisms often include architectural proteins such as cohesin and CCCTC-binding factor (CTCF) which drive loop formation [131, 173, 438–441]. It is conceivable that the more distal *Sox2* enhancer (∼110 kb) shows a stronger overall increase in promoter proximity in the upregulated state because it requires greater spatial rearrangement, whereas the more proximal *Nanog* enhancers (5 kb, 45 kb, 60 kb) are already relatively close to their promoter. As both *Sox2* and *Nanog* are cohesin dependent (but not CTCF dependent) [131, 442], this change in proximity could be driven by cohesin-mediated loop extrusion.

Furthermore, although live-cell imaging studies by Alexander et al. [115] and Du et al. [144] have shown that *Sox2* transcription does not require E-P contact in mESCs, it is important to distinguish between dynamics observed during developmental transitions versus those within a stable cell state. In their mESCs (corresponding to our naive state), the SCR might have already been brought into sufficient spatial proximity for stochastic E-P contacts to enable transcription. With those stochastic contacts, a direct correlation between E-P contact and transcription might not necessarily be expected [118, 119, 160, 298, 443] (see Section 3.2.4). The lack of changes at other measured loci (eg., *Dppa3, Prdm14*) may also reflect the fact that several enhancers included here are putative and not functionally validated, though the *Nanog* and *Sox2* enhancers are well established.

Our data suggest that a certain degree of E-P proximity is likely required for transcriptional activation. Specifically, at the *Nanog* locus, E-P distances decrease transiently during transcription, and at *Sox2* locus, the SCR moves closer to the promoter during the naive-to-primed transition. The median E–P distances observed in the active *Nanog* state and in the upregulated *Sox2* state (∼230–250 nm) are not compatible with strict direct contact models that assume zero separation between regulatory elements. At these distances, E–P communication could instead be mediated through phase-separated transcriptional condensates containing Mediator and RNA polymerase II (RNAPII) [147, 159]. Alternatively, because E–P contacts are transient and we cannot directly capture chromatin organization at the precise moment of transcriptional initiation (when E-P distance may be even closer) our observations also align with

contact models that permit a less stringent distance threshold. Notably, these models are not mutually exclusive [114]. Overall, our findings support models of dynamic contact in which shorter E-P distances are transiently stabilized during transcriptional initiation.

3.2.3 Multiway enhancer - promoter contacts during developmental transitions

Examining multiway E-P interactions at the *Nanog* locus using Tri-C, we found that these interactions are enriched in the naive state and diminish upon downregulation of *Nanog* in the primed state. Although the globin- [168] and primed-specific [169] hubs observed by others were considerably stronger than those detected here, this may reflect cell type-specific differences in chromatin organization. mESCs are characterized by more open chromatin [235, 444], and stronger hubs may therefore be a feature of further differentiated cell types. Consistent with our Tri-C data, our microscopy measurements revealed a small trend toward increased multiway contact frequency in naive cells. While the difference in effect size may seem contradicting at first, it is important to note that Tri-C data, like other 3C-based methods, displays enrichment over background, whereas FISH quantifies absolute contact frequencies. Extracting signal enrichment from FISH would require accurate background estimation, which is non-trivial given that background contact frequencies are locus-specific. An interesting approach was recently presented by Jusuf et al. [445], who quantified absolute looping frequencies in Micro-C maps by calibrating them against live-cell measurements using Bayesian inference of looping dynamics (BILD). Such locus-specific estimates could, in principle, be used to calibrate background in FISH-based analyses. Overall, our data supports models proposing that multiway chromatin hubs could contribute to regulating cell type–specific gene expression during differentiation, however, to what extent remains unknown [168, 169].

We therefore further explored the frequency of pairwise and multiway E-P contacts in single cells. As expected, pairwise (P-E) contacts occurred more frequently than three-way (P-E-E) contacts, which in turn were more frequent than four-way (P-E-E-E) contacts. However, estimating absolute contact frequencies is challenging, as the distance for a functional E-P contact is unknown [114]. A contact can be considered functional if it leads to transcription, but enhancers can activate transcription through multiple mechanisms: (i) direct transfer of proteins such as RNAPII, TFs, co-activators, or chromatin remodelers from the enhancer to the promoter [151, 446, 447]; (ii) recruitment of these proteins to the promoter [448–450]; (iii) establishment of a

high local concentration of proteins at the promoter [147, 149, 159]; and (iv) enhancer-mediated post-translational modification (PTM) of promoter-associated proteins [114, 247]. Any of these mechanisms may contribute to transcriptional activation with a delay [114, 118, 119, 298], making it difficult to distinguish functional contacts from background interactions without knowing the exact mode of enhancer action.

In our study, we therefore provided contact frequencies across a range of distance thresholds. One approach to estimating an appropriate threshold could be to calibrate our FISH measurements against the same live-cell data (*Fbn2* TAD) [40] used by Jusuf et al. [445]. Specifically, using the looping frequency reported by Jusuf et al. (∼6.5%) we identified the 3D distance threshold below which 6.5% of all alleles in our data fall, yielding a threshold of 138 nm. Applying this threshold, the contact frequency between the *Sox2* promoter and the SCR was ∼20%, consistent with estimates from Jusuf et al. At the *Nanog* - 60 kb enhancer, however, our contact frequency was considerably higher: 17% vs 5% in Jusuf et al. This discrepancy could, at least in part, arise from FISH capturing background chromosomal interactions that are filtered out in their analysis. Since the genomic distance between *Nanog* and its enhancer is substantially smaller (∼60 kb) than between *Sox2* and the SCR (∼110 kb), a higher rate of spurious proximity-based contacts at the *Nanog* locus would be expected. Alternatively, one can apply an arbitrary threshold: 200 nm lies within the range of observed E-P distances [115–117, 125, 143, 144, 158]. At this threshold, pairwise contacts at the *Nanog* locus occurred in 55% of alleles, three-way contacts in 25%, and four-way contacts in only ∼3% of alleles. Comparing our contact frequencies at the *Nanog* locus to other recent FISH measurements [451], our data show markedly higher contact frequencies. These differences are likely due to methodological and / or underlying biological differences.

Nevertheless, our data, together with that of others [451], clearly show that in mESCs, higher-order multiway contacts (e.g., four-way interactions) are far less frequent than pairwise contacts. However, if such multiway contacts occur in only a small fraction of cells, it remains unclear to what extent these rare events can influence cell type–specific gene expression. A recent study by Karpinska and Zhu et al. [452] demonstrated that CTCF depletion severely disrupts multiway contact hubs during macrophage differentiation, yet gene expression remains largely unaffected. This suggests that multiway contact formation during differentiation may not be primarily involved in enhancer-mediated gene activation. Further studies will be required to determine whether, and to what extent, multiway interactions can drive cell type–specific gene expression, or whether multiple redundant enhancers instead function mainly to confer phenotypic

robustness during differentiation [172, 453]

3.2.4 Towards more complex models of enhancer - promoter interaction

As multiple studies have observed little to no correlation between E-P proximity and transcription, it is becoming increasingly clear that models where an E-P contact (or contact-at-a-distance) immediately triggers transcription may be overly simplistic [114, 116, 128, 143]. This is also visible in our combined RNA-DNA FISH data. Although the E-P distances were, on median, shorter when transcription was more recent, shorter E-P distances were still observed in the absence of transcription, and transcription was still detected when enhancer and promoter were far apart. While the reasons for this are at least partly methodological, they may also be biological. Methodologically, as discussed above, E-P distances were measured after the nascent RNA was already synthesized and might not reflect the chromatin structure at transcriptional initiation. Additionally, noise was introduced by performing RNA and DNA FISH separately, and subsequently having to align the two sets of images.

Biologically, others have suggested that little to no correlation between E-P distance and transcription should be expected, as the regulatory influence of enhancers (e.g., recruitment of TFs, co-factors, chromatin remodellers and histone PTMs) can persist from a few seconds up to a few hours, providing "transcription memory" [118, 119, 160, 298, 443]. Introducing a temporal delay between E-P contact and transcription would result in no detectable correlation in fixed-cell studies [114, 116, 128, 143]. Similarly, it has been proposed that individual contacts may not be sufficient to initiate a transcriptional burst [118, 119, 298]. Zuin et al. [118] and Tünnermann et al [298] have, for example, proposed a model in which the promoter can either be in a low- or high-burst-frequency regime. The role of the enhancer is to modulate the rate at which the promoter switches between those two regimes. Each E-P interaction initiates one or more reversible regulatory steps, which correspond to stochastic regulatory processes, such as the assembly of the Mediator complex. If the E-P interactions are either long enough or frequent enough to allow for the completion of n regulatory steps, the promoter switches to the high-frequency regime, resulting in a transient increase in promoter activity. This could explain why live cell imaging studies, such as those at the *Sox2* locus [115, 144], have observed no direct correlation between E-P proximity and transcription. Future live-cell imaging studies, taking into account multiple enhancers (sequentially or simultaneously), coupled with mathematical models will therefore be necessary to disentangle the complex spatiotemporal dynamics of E-P

interactions.

3.2.5 Technical limitations

FISH measurements must be interpreted carefully, as fixation and harsh sample preparation can introduce artifacts, particularly for structures smaller than 200 nm [391, 393]. Due to possible distortions, making claims about absolute contact frequencies is difficult, however, relative comparisons between conditions within the same experiment are still informative. To assess the robustness of our sample preparation, image acquisition, and data analysis, we compared our pairwise distance measurements at the *Fbn2* TAD and *Sox2* - SCR in mESCs with previously published state-of-the-art live cell measurements [40, 115]. We observed good agreement, with some false positives at longer distances above 0.5 µm, indicating that our method does not introduce major artifacts at the loci and spatial scales examined here. It is also worth noting that while heat denaturation-based FISH is often criticized for poor structural preservation, denaturation-free methods present their own challenges and might not necessarily yield superior results at the examined loci. GOLD-FISH, for example, currently requires denaturing fixation with methanol and acetic acid, which may lack the stabilization provided by covalent crosslinking, leading to altered 3D genome structure [396, 397]. Additionally, the Cas9/Rep-X-based denaturation adds technical complexity and requires optimizing parameters for individual targets. RASER-FISH non-specifically digests DNA throughout the genome and requires overnight bromodeoxyuridine (BrdU) treatment in live cells prior to cell fixation [396, 397]. This restricts analysis to S-phase cells and may alter DNA stability, transcription levels, and cell cycle duration [454]. Moreover, a recent study has shown that while RASER-FISH did offer better structural preservation, it also reduced the sensitivity by 15% [393], which is a significant drawback when visualizing multiple simultaneous loci as in our study. Given these considerations, heat denaturation-based Oligopaint was best suited for our application.

Beyond sample preparation, microscopy-based methods introduce technical limitations such as localization error and chromatic aberrations, which can cause measured 3D distances to overestimate actual E-P distances [114, 176]. To minimize these effects, we applied bead-based chromatic shift correction to all spinning disk (SD) images prior to analysis, and performed regular calibrations for chromatic shift correction in stimulated emission depletion (STED) microscopy data. After correction, the localization precision was 30 nm laterally (x,y), and 40 nm axially (z) for SD measurements, and 10 nm for STED measurements. Power simulations demonstrated that despite these

measurement uncertainties in SD data, our sample sizes of thousands of alleles provided sufficient statistical power to reliably detect the observed differences between naive and primed populations. However, the localization precision of 30-40 nm likely impacts absolute E-P distance measurements, which could explain why distances below 50 nm were rarely observed for SD measurements [114].

In summary, our data show that during the naive-to-primed transition, despite expression changes of several orders of magnitude, changes in pairwise E-P distances are highly locus-dependent. This suggests that gene regulation is not necessarily dictated by chromatin proximity. Tri-C data at the *Nanog* locus reveal that multiway contacts are weakly enriched in the naive state, when *Nanog* is highly expressed, but not in the primed state, when *Nanog* is downregulated. These observations are consistent with models proposing that multiway hubs contribute to regulating cell-type-specific gene expression. Finally, we observe a correlation between median E-P distance and transcription at the *Nanog* and *Dppa3* loci. Overall, our data is compatible with models of dynamic contact, in which shorter E-P distances are transiently stabilized during transcriptional initiation.

3.3 Outlook

Our understanding of enhancers is rapidly expanding thanks to advancements in sample preparation, imaging, and computational analysis, which provide continuously improving resolution, throughput, and spatiotemporal precision. Our work has contributed a new method, NOVA-FISH, which improves upon the previously available resolution for visualizing small genomic elements in fixed cells. Moreover, we have contributed to the growing body of studies that combine E-P distance measurements with transcriptional readouts and were among the first to quantify multiway E-P interactions in single cells.

However, many questions in the field remain unanswered. We have seen that multiway E-P interactions are relatively rare, but to what extent do these interactions increase transcriptional output? Do the enhancers act cooperatively or competitively when engaging with the same promoter? Is E-P proximity required for transcription and what is a functional interaction threshold? What are the molecular mechanisms behind E-P interaction? Addressing these questions will require methods with higher sensitivity and precision, greater throughput, and the ability to detect interactions in real time. As E-P contacts are highly dynamic and transient, moving beyond fixed-cell approaches toward live-cell imaging will be essential to fully capture their dynamics and functional

relevance. Ultimately, understanding the mechanisms behind E-P interactions during homeostasis and development will require identifying the key molecular players and integrating this data into quantitative models capable of predicting gene regulatory outcomes.

References

1. Fraser, J., Williamson, I., Bickmore, W. A. & Dostie, J. An Overview of Genome Organization and How We Got There: from FISH to Hi-C. *Microbiology and Molecular Biology Reviews : MMBR* **79,** 347–372. doi:10.1128/MMBR.00006-15 (2015).

2. Bonev, B. & Cavalli, G. Organization and function of the 3D genome. *Nature Reviews Genetics* **17,** 661–678. doi:10.1038/nrg.2016.112 (2016).

3. Zheng, H. & Xie, W. The role of 3D genome organization in development and cell differentiation. *Nature Reviews Molecular Cell Biology* **20,** 535–550. doi:10.1038/s41580-019-0132-4 (2019).

4. Cremer, T. & Cremer, M. Chromosome territories. *Cold Spring Harbor Perspectives in Biology* **2,** a003889. doi:10.1101/cshperspect.a003889 (2010).

5. Misteli, T. The Self-Organizing Genome: Principles of Genome Architecture and Function. *Cell* **183,** 28–45. doi:10.1016/j.cell.2020.09.014 (2020).

6. Branco, M. R. & Pombo, A. Intermingling of Chromosome Territories in Interphase Suggests Role in Translocations and Transcription-Dependent Associations. *PLOS Biology* **4,** e138. doi:10.1371/journal.pbio.0040138 (2006).

7. Fritz, A. J., Sehgal, N., Pliss, A., Xu, J. & Berezney, R. Chromosome territories and the global regulation of the genome. *Genes, chromosomes & cancer* **58,** 407–426. doi:10.1002/gcc.22732 (2019).

8. Su, J.-H., Zheng, P., Kinrot, S. S., Bintu, B. & Zhuang, X. Genome-Scale Imaging of the 3D Organization and Transcriptional Activity of Chromatin. *Cell* **182,** 1641–1659.e26. doi:10.1016/j.cell.2020.07.032 (2020).

9. Lieberman-Aiden, E. *et al.* Comprehensive mapping of long range interactions reveals folding principles of the human genome. *Science (New York, N.Y.)* **326,** 289–293. doi:10.1126/science.1181369 (2009).

10. Stevens, T. J. *et al.* 3D structures of individual mammalian genomes studied by single-cell Hi-C. *Nature* **544,** 59–64. doi:10.1038/nature21429 (2017).

11. Rao, S. S. P. *et al.* A 3D map of the human genome at kilobase resolution reveals principles of chromatin looping. *Cell* **159,** 1665–1680. doi:10.1016/j.cell.2014.11.021 (2014).

12. Hildebrand, E. & Dekker, J. Mechanisms and functions of chromosome compartmentalization. *Trends in biochemical sciences* **45,** 385–396. doi:10.1016/j.tibs.2020.01.002 (2020).

13. Chen, Y. *et al.* Mapping 3D genome organization relative to nuclear compartments using TSA-Seq as a cytological ruler. *Journal of Cell Biology* **217,** 4025–4048. doi:10.1083/jcb.201807108 (2018).

14. Nora, E. P. *et al.* Spatial partitioning of the regulatory landscape of the X-inactivation centre. *Nature* **485,** 381–385. doi:10.1038/nature11049 (2012).

15. Dixon, J. R. *et al.* Topological domains in mammalian genomes identified by analysis of chromatin interactions. *Nature* **485,** 376–380. doi:10.1038/nature11082 (2012).

16. Dekker, J. & Mirny, L. The 3D Genome as Moderator of Chromosomal Communication. *Cell* **164,** 1110–1121. doi:10.1016/j.cell.2016.02.007 (2016).

17. Zufferey, M., Tavernari, D., Oricchio, E. & Ciriello, G. Comparison of computational methods for the identification of topologically associating domains. *Genome Biology* **19,** 217. doi:10.1186/s13059-018-1596-9 (2018).

18. Dixon, J. R. *et al.* Chromatin architecture reorganization during stem cell differentiation. *Nature* **518,** 331–336. doi:10.1038/nature14222 (2015).

19. Krefting, J., Andrade-Navarro, M. A. & Ibn-Salem, J. Evolutionary stability of topologically associating domains is associated with conserved gene regulation. *BMC Biology* **16,** 87. doi:10.1186/s12915-018-0556-x (2018).

20. Okhovat, M. *et al.* TAD evolutionary and functional characterization reveals diversity in mammalian TAD boundary properties and function. *Nature Communications* **14,** 8111. doi:10.1038/s41467-023-43841-8 (2023).

21. Gómez-Marín, C. *et al.* Evolutionary comparison reveals that diverging CTCF sites are signatures of ancestral topological associating domains borders. *Proceedings of the National Academy of Sciences* **112,** 7542–7547. doi:10.1073/pnas.1505463112 (2015).

22. Crane, E. *et al.* Condensin-driven remodelling of X chromosome topology during dosage compensation. *Nature* **523,** 240–244. doi:10.1038/nature14450 (2015).

23. Hsieh, T.-H. S. *et al.* Mapping nucleosome resolution chromosome folding in yeast by Micro-C. *Cell* **162,** 108–119. doi:10.1016/j.cell.2015.05.048 (2015).

24. Mizuguchi, T. *et al.* Cohesin-dependent globules and heterochromatin shape 3D genome architecture in S. pombe. *Nature* **516,** 432–435. doi:10.1038/nature13833 (2014).

25. Van Steensel, B. & Furlong, E. E. M. The role of transcription in shaping the spatial organization of the genome. *Nature Reviews Molecular Cell Biology* **20,** 327–337. doi:10.1038/s41580-019-0114-6 (2019).

26. Lupiáñez, D. G. *et al.* Disruptions of topological chromatin domains cause pathogenic rewiring of gene-enhancer interactions. *Cell* **161,** 1012–1025. doi:10.1016/j.cell.2015.04.004 (2015).

27. Guo, Y. *et al.* CRISPR Inversion of CTCF Sites Alters Genome Topology and Enhancer/Promoter Function. *Cell* **162,** 900–910. doi:10.1016/j.cell.2015.07.038 (2015).

28. Franke, M. *et al.* Formation of new chromatin domains determines pathogenicity of genomic duplications. *Nature* **538,** 265–269. doi:10.1038/nature19800 (2016).

29. Rajderkar, S. *et al.* Topologically associating domain boundaries are required for normal genome function. *Communications Biology* **6,** 1–10. doi:10.1038/s42003-023-04819-w (2023).

30. Symmons, O. *et al.* The Shh Topological Domain Facilitates the Action of Remote Enhancers by Reducing the Effects of Genomic Distances. *Developmental Cell* **39,** 529–543. doi:10.1016/j.devcel.2016.10.015 (2016).

31. Narendra, V. *et al.* CTCF establishes discrete functional chromatin domains at the Hox clusters during differentiation. *Science* **347,** 1017–1021. doi:10.1126/science.1262088 (2015).

32. Dixon, J. R., Gorkin, D. U. & Ren, B. Chromatin Domains: The Unit of Chromosome Organization. *Molecular Cell* **62,** 668–680. doi:10.1016/j.molcel.2016.05.018 (2016).

33. Jordan Rowley, M. & Corces, V. G. Organizational Principles of 3D Genome Architecture. *Nature reviews. Genetics* **19,** 789–800. doi:10.1038/s41576-018-0060-8 (2018).

34. Sanborn, A. L. *et al.* Chromatin extrusion explains key features of loop and domain formation in wild-type and engineered genomes. *Proceedings of the National Academy of Sciences* **112,** E6456–E6465. doi:10.1073/pnas.1518552112 (2015).

35. Fudenberg, G. *et al.* Formation of Chromosomal Domains by Loop Extrusion. *Cell Reports* **15,** 2038–2049. doi:10.1016/j.celrep.2016.04.085 (2016).

36. Nora, E. P. *et al.* Targeted Degradation of CTCF Decouples Local Insulation of Chromosome Domains from Genomic Compartmentalization. *Cell* **169,** 930–944.e22. doi:10.1016/j.cell.2017.05.004 (2017).

37. Rao, S. S. P. *et al.* Cohesin Loss Eliminates All Loop Domains. *Cell* **171,** 305–320.e24. doi:10.1016/j.cell.2017.09.026 (2017).

38. Wutz, G. *et al.* Topologically associating domains and chromatin loops depend on cohesin and are regulated by CTCF, WAPL, and PDS5 proteins. *The EMBO Journal* **36,** 3573–3599. doi:10.15252/embj.201798004 (2017).

39. Kim, Y., Shi, Z., Zhang, H., Finkelstein, I. J. & Yu, H. Human cohesin compacts DNA by loop extrusion. *Science (New York, N.Y.)* **366,** 1345–1349. doi:10.1126/science.aaz4475 (2019).

40. Gabriele, M. *et al.* Dynamics of CTCF- and cohesin-mediated chromatin looping revealed by live-cell imaging. *Science* **376,** 496–501. doi:10.1126/science.abn6583 (2022).

41. Ghirlando, R. & Felsenfeld, G. CTCF: making the right connections. *Genes & Development* **30,** 881–891. doi:10.1101/gad.277863.116 (2016).

42. Davidson, I. F. & Peters, J.-M. Genome folding through loop extrusion by SMC complexes. *Nature Reviews Molecular Cell Biology* **22,** 445–464. doi:10.1038/s41580-021-00349-7 (2021).

43. Strunnikov, A. V., Larionov, V. L. & Koshland, D. SMC1: an essential yeast gene encoding a putative head-rod-tail protein is required for nuclear division and defines a new ubiquitous protein family. *The Journal of Cell Biology* **123,** 1635–1648. doi:10.1083/jcb.123.6.1635 (1993).

44. Guacci, V., Koshland, D. & Strunnikov, A. A Direct Link between Sister Chromatid Cohesion and Chromosome Condensation Revealed through the Analysis of *MCD1* in S. cerevisiae. *Cell* **91,** 47–57. doi:10.1016/S0092-8674(01)80008-8 (1997).

45. Michaelis, C., Ciosk, R. & Nasmyth, K. Cohesins: Chromosomal Proteins that Prevent Premature Separation of Sister Chromatids. *Cell* **91,** 35–45. doi:10.1016/S0092-8674(01)80007-6 (1997).

46. Ciosk, R. *et al.* Cohesin's binding to chromosomes depends on a separate complex consisting of Scc2 and Scc4 proteins. *Molecular Cell* **5,** 243–254. doi:10.1016/s1097-2765(00)80420-7 (2000).

47. Nichols, M. H. & Corces, V. G. A CTCF Code for 3D Genome Architecture. *Cell* **162,** 703–705. doi:10.1016/j.cell.2015.07.053 (2015).

48. De Wit, E. *et al.* CTCF Binding Polarity Determines Chromatin Looping. *Molecular Cell* **60,** 676–684. doi:10.1016/j.molcel.2015.09.023 (2015).

49. Tedeschi, A. *et al.* Wapl is an essential regulator of chromatin structure and chromosome segregation. *Nature* **501,** 564–568. doi:10.1038/nature12471 (2013).

50. Gassler, J. *et al.* A mechanism of cohesin-dependent loop extrusion organizes zygotic genome architecture. *The EMBO Journal* **36,** 3600–3618. doi:10.15252/embj.201798083 (2017).

51. Haarhuis, J. H. I. *et al.* The Cohesin Release Factor WAPL Restricts Chromatin Loop Extension. *Cell* **169,** 693–707.e14. doi:10.1016/j.cell.2017.04.013 (2017).

52. Schwarzer, W. *et al.* Two independent modes of chromatin organization revealed by cohesin removal. *Nature* **551,** 51–56. doi:10.1038/nature24281 (2017).

53. Beagan, J. A. & Phillips-Cremins, J. E. On the existence and functionality of topologically associating domains. *Nature Genetics* **52,** 8–16. doi:10.1038/s41588-019-0561-1 (2020).

54. Nagano, T. *et al.* Single cell Hi-C reveals cell-to-cell variability in chromosome structure. *Nature* **502,** 10.1038/nature12593. doi:10.1038/nature12593 (2013).

55. Flyamer, I. M. *et al.* Single-nucleus Hi-C reveals unique chromatin reorganization at oocyte-to-zygote transition. *Nature* **544,** 110–114. doi:10.1038/nature21711 (2017).

56. Bintu, B. *et al.* Super-resolution chromatin tracing reveals domains and cooperative interactions in single cells. *Science* **362,** eaau1783. doi:10.1126/science.aau1783 (2018).

57. Szabo, Q. *et al.* Regulation of single-cell genome organization into TADs and chromatin nanodomains. *Nature genetics* **52,** 1151–1157. doi:10.1038/s41588-020-00716-8 (2020).

58. Hafner, A. & Boettiger, A. The spatial organization of transcriptional control. *Nature Reviews Genetics* **24,** 53–68. doi:10.1038/s41576-022-00526-0 (2023).

59. De Wit, E. TADs as the Caller Calls Them. *Journal of Molecular Biology. Perspectives on Chromosome Folding* **432,** 638–642. doi:10.1016/j.jmb.2019.09.026 (2020).

60. Da Costa-Nunes, J. A. & Noordermeer, D. TADs: Dynamic structures to create stable regulatory functions. *Current Opinion in Structural Biology* **81,** 102622. doi:10.1016/j.sbi.2023.102622 (2023).

61. Mach, P. *et al.* Cohesin and CTCF control the dynamics of chromosome folding. *Nature Genetics* **54,** 1907–1918. doi:10.1038/s41588-022-01232-7 (2022).

62. Cutter, A. & Hayes, J. J. A Brief Review of Nucleosome Structure. *FEBS letters* **589,** 2914–2922. doi:10.1016/j.febslet.2015.05.016 (2015).

63. Schalch, T., Duda, S., Sargent, D. F. & Richmond, T. J. X-ray structure of a tetranucleosome and its implications for the chromatin fibre. *Nature* **436,** 138–141. doi:10.1038/nature03686 (2005).

64. Tremethick, D. J. Higher-Order Structures of Chromatin: The Elusive 30 nm Fiber. *Cell* **128,** 651–654. doi:10.1016/j.cell.2007.02.008 (2007).

65. Fussner, E. *et al.* Open and closed domains in the mouse genome are configured as 10-nm chromatin fibres. *EMBO Reports* **13,** 992–996. doi:10.1038/embor.2012.139 (2012).

66. Ricci, M. A., Manzo, C., García-Parajo, M. F., Lakadamyali, M. & Cosma, M. P. Chromatin fibers are formed by heterogeneous groups of nucleosomes in vivo. *Cell* **160,** 1145–1158. doi:10.1016/j.cell.2015.01.054 (2015).

67. Ou, H. D. *et al.* ChromEMT: Visualizing 3D chromatin structure and compaction in interphase and mitotic cells. *Science* **357,** eaag0025. doi:10.1126/science.aag0025 (2017).

68. Long, H. K., Prescott, S. L. & Wysocka, J. Ever-Changing Landscapes: Transcriptional Enhancers in Development and Evolution. *Cell* **167,** 1170–1187. doi:10.1016/j.cell.2016.09.018 (2016).

69. Pachano, T., Haro, E. & Rada-Iglesias, A. Enhancer-gene specificity in development and disease. *Development* **149,** dev186536. doi:10.1242/dev.186536 (2022).

70. Thomas, H. F. & Buecker, C. What is an enhancer? *BioEssays* **45,** 2300044. doi:10.1002/bies.202300044 (2023).

71. Andersson, R. & Sandelin, A. Determinants of enhancer and promoter activities of regulatory elements. *Nature Reviews Genetics* **21,** 71–87. doi:10.1038/s41576-019-0173-8 (2020).

72. Banerji, J., Rusconi, S. & Schaffner, W. Expression of a beta-globin gene is enhanced by remote SV40 DNA sequences. *Cell* **27,** 299–308. doi:10.1016/0092-8674(81)90413-x (1981).

73. Gillies, S. D., Morrison, S. L., Oi, V. T. & Tonegawa, S. A tissue-specific transcription enhancer element is located in the major intron of a rearranged immunoglobulin heavy chain gene. *Cell* **33,** 717–728. doi:10.1016/0092-8674(83)90014-4 (1983).

74. Mercola, M., Wang, X. F., Olsen, J. & Calame, K. Transcriptional enhancer elements in the mouse immunoglobulin heavy chain locus. *Science (New York, N.Y.)* **221,** 663–665. doi:10.1126/science.6306772 (1983).

75. Moreau, P. *et al.* The SV40 72 base repair repeat has a striking effect on gene expression both in SV40 and other chimeric recombinants. *Nucleic Acids Research* **9,** 6047–6068. doi:10.1093/nar/9.22.6047 (1981).

76. Banerji, J., Olson, L. & Schaffner, W. A lymphocyte-specific cellular enhancer is located downstream of the joining region in immunoglobulin heavy chain genes. *Cell* **33,** 729–740. doi:10.1016/0092-8674(83)90015-6 (1983).

77. Dynan, W. S. & Tjian, R. The promoter-specific transcription factor Sp1 binds to upstream sequences in the SV40 early promoter. *Cell* **35,** 79–87. doi:10.1016/0092-8674(83)90210-6 (1983).

78. Piette, J., Kryszke, M. & Yaniv, M. Specific interaction of cellular factors with the B enhancer of polyoma virus. *The EMBO Journal* **4,** 2675–2685. doi:10.1002/j.1460-2075.1985.tb03987.x (1985).

79. Nair, S. J. *et al.* Transcriptional Enhancers at 40: Evolution of a viral DNA element to nuclear architectural structures. *Trends in genetics : TIG* **38,** 1019–1047. doi:10.1016/j.tig.2022.05.015 (2022).

80. Garabedian, M. J., Shepherd, B. M. & Wensink, P. C. A tissue-specific transcription enhancer from the Drosophila yolk protein 1 gene. *Cell* **45,** 859–867. doi:10.1016/0092-8674(86)90560-X (1986).

81. Goto, T., Macdonald, P. & Maniatis, T. Early and late periodic patterns of *even skipped* expression are controlled by distinct regulatory elements that respond to different spatial cues. *Cell* **57,** 413–422. doi:10.1016/0092-8674(89)90916-1 (1989).

82. Harding, K., Hoey, T., Warrior, R. & Levine, M. Autoregulatory and gap gene response elements of the even-skipped promoter of Drosophila. *The EMBO Journal* **8,** 1205–1212. doi:10.1002/j.1460-2075.1989.tb03493.x (1989).

83. Vesque, C. *et al.* Hoxb-2 transcriptional activation in rhombomeres 3 and 5 requires an evolutionarily conserved cis-acting element in addition to the Krox-20 binding site. *The EMBO Journal* **15,** 5383–5396. doi:10.1002/j.1460-2075.1996.tb00922.x (1996).

84. DiMattia, G. E. *et al.* The PIT-1 Gene Is Regulated by Distinct Early and Late Pituitary-Specific Enhancers. *Developmental Biology* **182,** 180–190. doi:10.1006/dbio.1996.8472 (1997).

85. Pertea, M. & Salzberg, S. L. Between a chicken and a grape: estimating the number of human genes. *Genome Biology* **11,** 206. doi:10.1186/gb-2010-11-5-206 (2010).

86. Halfon, M. S. Studying transcriptional enhancers: the founder fallacy, validation creep, and other biases. *Trends in genetics : TIG* **35,** 93–103. doi:10.1016/j.tig.2018.11.004 (2019).

87. Koch, F. *et al.* Transcription initiation platforms and GTF recruitment at tissue-specific enhancers and promoters. *Nature Structural & Molecular Biology* **18,** 956–963. doi:10.1038/nsmb.2085 (2011).

88. Core, L. J. *et al.* Analysis of nascent RNA identifies a unified architecture of initiation regions at mammalian promoters and enhancers. *Nature genetics* **46,** 1311–1320. doi:10.1038/ng.3142 (2014).

89. Andersson, R. *et al.* Nuclear stability and transcriptional directionality separate functionally distinct RNA species. *Nature Communications* **5,** 5336. doi:10.1038/ncomms6336 (2014).

90. Scruggs, B. S. *et al.* Bidirectional Transcription Arises from Two Distinct Hubs of Transcription Factor Binding and Active Chromatin. *Molecular Cell* **58,** 1101–1112. doi:10.1016/j.molcel.2015.04.006 (2015).

91. Andersson, R. *et al.* Human Gene Promoters Are Intrinsically Bidirectional. *Molecular Cell* **60,** 346–347. doi:10.1016/j.molcel.2015.10.015 (2015).

92. Chen, Y. *et al.* Principles for RNA metabolism and alternative transcription initiation within closely spaced promoters. *Nature Genetics* **48,** 984–994. doi:10.1038/ng.3616 (2016).

93. Rajagopal, N. *et al.* High-throughput mapping of regulatory DNA. *Nature Biotechnology* **34,** 167–174. doi:10.1038/nbt.3468 (2016).

94. Engreitz, J. M. *et al.* Local regulation of gene expression by lncRNA promoters, transcription and splicing. *Nature* **539,** 452–455. doi:10.1038/nature20149 (2016).

95. Diao, Y. *et al.* A tiling-deletion-based genetic screen for cis-regulatory element identification in mammalian cells. *Nature Methods* **14,** 629–635. doi:10.1038/nmeth.4264 (2017).

96. Dao, L. T. M. *et al.* Genome-wide characterization of mammalian promoters with distal enhancer functions. *Nature Genetics* **49,** 1073–1081. doi:10.1038/ng.3884 (2017).

97. Andersson, R. *et al.* An atlas of active enhancers across human cell types and tissues. *Nature* **507,** 455–461. doi:10.1038/nature12787 (2014).

98. De Santa, F. *et al.* A large fraction of extragenic RNA pol II transcription sites overlap enhancers. *PLoS biology* **8,** e1000384. doi:10.1371/journal.pbio.1000384 (2010).

99. Kim, T.-K. *et al.* Widespread transcription at neuronal activity-regulated enhancers. *Nature* **465,** 182–187. doi:10.1038/nature09033 (2010).

100. Pei, G., Lyons, H., Li, P. & Sabari, B. R. Transcription regulation by biomolecular condensates. *Nature Reviews Molecular Cell Biology* **26,** 213–236. doi:10.1038/s41580-024-00789-x (2025).

101. Cramer, P. Organization and regulation of gene transcription. *Nature* **573,** 45–54. doi:10.1038/s41586-019-1517-4 (2019).

102. Harlen, K. M. & Churchman, L. S. The code and beyond: transcription regulation by the RNA polymerase II carboxy-terminal domain. *Nature Reviews Molecular Cell Biology* **18,** 263–273. doi:10.1038/nrm.2017.10 (2017).

103. Hahn, S. & Young, E. T. Transcriptional regulation in Saccharomyces cerevisiae: transcription factor regulation and function, mechanisms of initiation, and roles of activators and coactivators. *Genetics* **189,** 705–736. doi:10.1534/genetics.111.127019 (2011).

104. Robinson, P. J. *et al.* Structure of a Complete Mediator-RNA Polymerase II Pre-Initiation Complex. *Cell* **166,** 1411–1422.e16. doi:10.1016/j.cell.2016.08.050 (2016).

105. Adelman, K. & Lis, J. T. Promoter-proximal pausing of RNA polymerase II: emerging roles in metazoans. *Nature reviews. Genetics* **13,** 720–731. doi:10.1038/nrg3293 (2012).

106. Peterlin, B. M. & Price, D. H. Controlling the elongation phase of transcription with P-TEFb. *Molecular Cell* **23,** 297–305. doi:10.1016/j.molcel.2006.06.014 (2006).

107. Shandilya, J. & Roberts, S. G. E. The transcription cycle in eukaryotes: From productive initiation to RNA polymerase II recycling. *Biochimica et Biophysica Acta (BBA) - Gene Regulatory Mechanisms* **1819,** 391–400. doi:10.1016/j.bbagrm.2012.01.010 (2012).

108. Jonkers, I. & Lis, J. T. Getting up to speed with transcription elongation by RNA polymerase II. *Nature reviews. Molecular cell biology* **16,** 167–177. doi:10.1038/nrm3953 (2015).

109. Chen, F. X., Smith, E. R. & Shilatifard, A. Born to run: control of transcription elongation by RNA polymerase II. *Nature Reviews Molecular Cell Biology* **19,** 464–478. doi:10.1038/s41580-018-0010-5 (2018).

110. Sawado, T., Halow, J., Bender, M. & Groudine, M. The β-globin locus control region (LCR) functions primarily by enhancing the transition from transcription initiation to elongation. *Genes & Development* **17,** 1009–1018. doi:10.1101/gad.1072303 (2003).

111. Bender, M. A. *et al.* The hypersensitive sites of the murine β-globin locus control region act independently to affect nuclear localization and transcriptional elongation. *Blood* **119,** 3820–3827. doi:10.1182/blood-2011-09-380485 (2012).

112. Hay, D. *et al.* Genetic dissection of the α-globin super-enhancer in vivo. *Nature genetics* **48,** 895–903. doi:10.1038/ng.3605 (2016).

113. Larke, M. S. C. *et al.* Enhancers predominantly regulate gene expression during differentiation via transcription initiation. *Molecular cell* **81,** 983–997.e7. doi:10.1016/j.molcel.2021.01.002 (2021).

114. Yang, J. H. & Hansen, A. S. Enhancer selectivity in space and time: from enhancer–promoter interactions to promoter activation. *Nature Reviews Molecular Cell Biology,* 1–18. doi:10.1038/s41580-024-00710-6 (2024).

115. Alexander, J. M. *et al.* Live-cell imaging reveals enhancer-dependent Sox2 transcription in the absence of enhancer proximity. *eLife* **8** (eds Singer, R. H., Struhl, K. & Liu, Z.) e41769. doi:10.7554/eLife.41769 (2019).

116. Benabdallah, N. S. *et al.* Decreased Enhancer-Promoter Proximity Accompanying Enhancer Activation. *Molecular Cell* **76,** 473–484.e7. doi:10.1016/j.molcel.2019.07.038 (2019).

117. Chen, H. *et al.* Dynamic interplay between enhancer–promoter topology and gene activity. *Nature Genetics* **50,** 1296–1303. doi:10.1038/s41588-018-0175-z (2018).

118. Zuin, J. *et al.* Nonlinear control of transcription through enhancer–promoter interactions. *Nature* **604,** 571–577. doi:10.1038/s41586-022-04570-y (2022).

119. Xiao, J. Y., Hafner, A. & Boettiger, A. N. How subtle changes in 3D structure can create large changes in transcription. *eLife* **10,** e64320. doi:10.7554/eLife.64320 (2021).

120. Nollmann, M., Bennabi, I., Götz, M. & Gregor, T. The Impact of Space and Time on the Functional Output of the Genome. *Cold Spring Harbor Perspectives in Biology* **14,** a040378. doi:10.1101/cshperspect.a040378 (2022).

121. Furlong, E. E. M. & Levine, M. Developmental enhancers and chromosome topology. *Science* **361,** 1341–1345. doi:10.1126/science.aau0320 (2018).

122. Kong, S., Bohl, D., Li, C. & Tuan, D. Transcription of the HS2 Enhancer toward a *cis* -Linked Gene Is Independent of the Orientation, Position, and Distance of the Enhancer Relative to the Gene. *Molecular and Cellular Biology* **17,** 3955–3965. doi:10.1128/MCB.17.7.3955 (1997).

123. Travers, A. Chromatin modification by DNA tracking. *Proceedings of the National Academy of Sciences of the United States of America* **96,** 13634–13637 (1999).

124. Bulger, M. & Groudine, M. Looping versus linking: toward a model for long-distance gene activation. *Genes & Development* **13,** 2465–2477 (1999).

125. Chen, Z. *et al.* Increased enhancer–promoter interactions during developmental enhancer activation in mammals. *Nature Genetics* **56,** 675–685. doi:10.1038/s41588-024-01681-2 (2024).

126. Sanyal, A., Lajoie, B., Jain, G. & Dekker, J. The long-range interaction landscape of gene promoters. *Nature* **489,** 109–113. doi:10.1038/nature11279 (2012).

127. Goel, V. Y., Huseyin, M. K. & Hansen, A. S. Region Capture Micro-C reveals coalescence of enhancers and promoters into nested microcompartments. *Nature Genetics* **55,** 1048–1056. doi:10.1038/s41588-023-01391-1 (2023).

128. Mateo, L. J. *et al.* Visualizing DNA folding and RNA in embryos at single-cell resolution. *Nature* **568,** 49–54. doi:10.1038/s41586-019-1035-4 (2019).

129. Deng, W. *et al.* Reactivation of developmentally silenced globin genes by forced chromatin looping. *Cell* **158,** 849–860. doi:10.1016/j.cell.2014.05.050 (2014).

130. Deng, W. *et al.* Controlling long-range genomic interactions at a native locus by targeted tethering of a looping factor. *Cell* **149,** 1233–1244. doi:10.1016/j.cell.2012.03.051 (2012).

131. Aljahani, A. *et al.* Analysis of sub-kilobase chromatin topology reveals nano-scale regulatory interactions with variable dependence on cohesin and CTCF. *Nature Communications* **13,** 2139. doi:10.1038/s41467-022-29696-5 (2022).

132. Dunn, T. M. & Schleif, R. Deletion analysis of the *Escherichia coli ara* PC and PBAD promoters. *Journal of Molecular Biology* **180,** 201–204. doi:10.1016/0022-2836(84)90437-6 (1984).

133. Takahashi, K. *et al.* Requirement of stereospecific alignments for initiation from the simian virus 40 early promoter. *Nature* **319,** 121–126. doi:10.1038/319121a0 (1986).

134. Popay, T. M. & Dixon, J. R. Coming full circle: On the origin and evolution of the looping model for enhancer–promoter communication. *Journal of Biological Chemistry* **298.** doi:10.1016/j.jbc.2022.102117 (2022).

135. Sankaran, V. G. & Orkin, S. H. The Switch from Fetal to Adult Hemoglobin. *Cold Spring Harbor Perspectives in Medicine* **3,** a011643. doi:10.1101/cshperspect.a011643 (2013).

136. Grosveld, F., Assendelft, G. B. v., Greaves, D. R. & Kollias, G. Position-independent, high-level expression of the human β-globin gene in transgenic mice. *Cell* **51,** 975–985. doi:10.1016/0092-8674(87)90584-8 (1987).

137. Forrester, W. C., Takegawa, S., Papayannopoulou, T., Stamatoyannopoulos, G. & Groudine, M. Evidence for a locus activation region: the formation of developmentally stable hypersensitive sites in globin-expressing hybrids. *Nucleic Acids Research* **15,** 10159–10177. doi:10.1093/nar/15.24.10159 (1987).

138. Rupon, J. W. *et al.* Using Forced Chromatin Looping To Overcome Developmental Silencing Of Embryonic and Fetal β-Type Globin Genes In Adult Erythroid Cells. *Blood* **122,** 433. doi:10.1182/blood.V122.21.433.433 (2013).

139. Bartman, C. R., Hsu, S. C., Hsiung, C. C.-S., Raj, A. & Blobel, G. A. Enhancer Regulation of Transcriptional Bursting Parameters Revealed by Forced Chromatin Looping. *Molecular Cell* **62,** 237–247. doi:10.1016/j.molcel.2016.03.007 (2016).

140. Williamson, I., Lettice, L. A., Hill, R. E. & Bickmore, W. A. Shh and ZRS enhancer colocalisation is specific to the zone of polarising activity. *Development* **143,** 2994–3001. doi:10.1242/dev.139188 (2016).

141. Ohishi, H. *et al.* Transcription-coupled changes in genomic region proximities during transcriptional bursting. *Science Advances* **10,** eadn0020. doi:10.1126/sciadv.adn0020 (2024).

142. Li, J. *et al.* Single-gene imaging links genome topology, promoter–enhancer communication and transcription control. *Nature Structural & Molecular Biology* **27,** 1032–1040. doi:10.1038/s41594-020-0493-6 (2020).

143. Heist, T., Fukaya, T. & Levine, M. Large distances separate coregulated genes in living Drosophila embryos. *Proceedings of the National Academy of Sciences of the United States of America* **116,** 15062–15067. doi:10.1073/pnas.1908962116 (2019).

144. Du, M. *et al.* Direct observation of a condensate effect on super-enhancer controlled gene bursting. *Cell* **187,** 331–344.e17. doi:10.1016/j.cell.2023.12.005 (2024).

145. Wang, X., Cairns, M. J. & Yan, J. Super-enhancers in transcriptional regulation and genome organization. *Nucleic Acids Research* **47,** 11481–11496. doi:10.1093/nar/gkz1038 (2019).

146. Boija, A. *et al.* Transcription Factors Activate Genes through the Phase-Separation Capacity of Their Activation Domains. *Cell* **175,** 1842–1855.e16. doi:10.1016/j.cell.2018.10.042 (2018).

147. Sabari, B. R. *et al.* Coactivator condensation at super-enhancers links phase separation and gene control. *Science (New York, N.Y.)* **361,** eaar3958. doi:10.1126/science.aar3958 (2018).

148. Chong, S. *et al.* Imaging dynamic and selective low-complexity domain interactions that control gene transcription. *Science* **361,** eaar2555. doi:10.1126/science.aar2555 (2018).

149. Hnisz, D., Shrinivas, K., Young, R. A., Chakraborty, A. K. & Sharp, P. A. A Phase Separation Model for Transcriptional Control. *Cell* **169,** 13–23. doi:10.1016/j.cell.2017.02.007 (2017).

150. Shrinivas, K. *et al.* Enhancer Features that Drive Formation of Transcriptional Condensates. *Molecular Cell* **75,** 549–561.e7. doi:10.1016/j.molcel.2019.07.009 (2019).

151. Li, J. *et al.* Single-Molecule Nanoscopy Elucidates RNA Polymerase II Transcription at Single Genes in Live Cells. *Cell* **178,** 491–506.e28. doi:10.1016/j.cell.2019.05.029 (2019).

152. Lu, H. *et al.* Phase-separation mechanism for C-terminal hyperphosphorylation of RNA polymerase II. *Nature* **558,** 318–323. doi:10.1038/s41586-018-0174-3 (2018).

153. Wu, Y. *et al.* Disrupting the phase separation of KAT8-IRF1 diminishes PD-L1 expression and promotes antitumor immunity. *Nature Cancer* **4,** 382–400. doi:10.1038/s43018-023-00522-1 (2023).

154. He, Y. *et al.* MSL1 Promotes Liver Regeneration by Driving Phase Separation of STAT3 and Histone H4 and Enhancing Their Acetylation. *Advanced Science* **10,** 2301094. doi:10.1002/advs.202301094 (2023).

155. Quinodoz, S. A. *et al. RNA promotes the formation of spatial compartments in the nucleus* tech. rep. (2020), 2020.08.25.267435. doi:10.1101/2020.08.25.267435.

156. Henninger, J. E. *et al.* RNA-Mediated Feedback Control of Transcriptional Condensates. *Cell* **184,** 207–225.e24. doi:10.1016/j.cell.2020.11.030 (2021).

157. Kawasaki, K. & Fukaya, T. Functional coordination between transcription factor clustering and gene activity. *Molecular Cell* **83,** 1605–1622.e9. doi:10.1016/j.molcel.2023.04.018 (2023).

158. Levo, M. *et al.* Transcriptional coupling of distant regulatory genes in living embryos. *Nature* **605,** 754–760. doi:10.1038/s41586-022-04680-7 (2022).

159. Cho, W.-K. *et al.* Mediator and RNA polymerase II clusters associate in transcription-dependent condensates. *Science* **361,** 412–415. doi:10.1126/science.aar4199 (2018).

160. Karr, J. P., Ferrie, J. J., Tjian, R. & Darzacq, X. The transcription factor activity gradient (TAG) model: contemplating a contact-independent mechanism for enhancer–promoter communication. *Genes & Development* **36,** 7–16. doi:10.1101/gad.349160.121 (2022).

161. Biggar, K. K. & Li, S. S.-C. Non-histone protein methylation as a regulator of cellular signalling and function. *Nature Reviews Molecular Cell Biology* **16,** 5–17. doi:10.1038/nrm3915 (2015).

162. Narita, T. *et al.* Enhancers are activated by p300/CBP activity-dependent PIC assembly, RNAPII recruitment, and pause release. *Molecular Cell* **81,** 2166–2182.e6. doi:10.1016/j.molcel.2021.03.008 (2021).

163. Raisner, R. *et al.* Enhancer Activity Requires CBP/P300 Bromodomain-Dependent Histone H3K27 Acetylation. *Cell Reports* **24,** 1722–1729. doi:10.1016/j.celrep.2018.07.041 (2018).

164. De Laat, W. & Duboule, D. Topology of mammalian developmental enhancers and their regulatory landscapes. *Nature* **502,** 499–506. doi:10.1038/nature12753 (2013).

165. Fulco, C. P. *et al.* Activity-by-contact model of enhancer–promoter regulation from thousands of CRISPR perturbations. *Nature Genetics* **51,** 1664–1669. doi:10.1038/s41588-019-0538-0 (2019).

166. Oudelaar, A. M. & Higgs, D. R. The relationship between genome structure and function. *Nature Reviews Genetics* **22,** 154–168. doi:10.1038/s41576-020-00303-x (2021).

167. Beagrie, R. A. *et al.* Complex multi-enhancer contacts captured by Genome Architecture Mapping (GAM). *Nature* **543,** 519–524. doi:10.1038/nature21411 (2017).

168. Oudelaar, A. M. *et al.* Single-allele chromatin interactions identify regulatory hubs in dynamic compartmentalized domains. *Nature Genetics* **50,** 1744–1751. doi:10.1038/s41588-018-0253-2 (2018).

169. Lando, D. *et al.* Enhancer-promoter interactions are reconfigured through the formation of long-range multiway hubs as mouse ES cells exit pluripotency. *Molecular Cell* **84,** 1406–1421.e8. doi:10.1016/j.molcel.2024.02.015 (2024).

170. Schoenfelder, S. *et al.* The pluripotent regulatory circuitry connecting promoters to their long-range interacting elements. *Genome Research* **25,** 582–597. doi:10.1101/gr.185272.114 (2015).

171. Mifsud, B. *et al.* Mapping long-range promoter contacts in human cells with high-resolution capture Hi-C. *Nature Genetics* **47,** 598–606. doi:10.1038/ng.3286 (2015).

172. Osterwalder, M. *et al.* Enhancer redundancy provides phenotypic robustness in mammalian development. *Nature* **554,** 239–243. doi:10.1038/nature25461 (2018).

173. Schoenfelder, S. & Fraser, P. Long-range enhancer–promoter contacts in gene expression control. *Nature Reviews Genetics* **20,** 437–455. doi:10.1038/s41576-019-0128-0 (2019).

174. Krämer, H., Amouyal, M., Nordheim, A. & Müller-Hill, B. DNA supercoiling changes the spacing requirement of two lac operators for DNA loop formation with lac repressor. *The EMBO Journal* **7,** 547–556. doi:10.1002/j.1460-2075.1988.tb02844.x (1988).

175. Bellomy, G. R. & Record, M. T. Stable DNA loops in vivo and in vitro: roles in gene regulation at a distance and in biophysical characterization of DNA. *Progress in Nucleic Acid Research and Molecular Biology* **39,** 81–128. doi:10.1016/s0079-6603(08)60624-8 (1990).

176. Brandão, H. B., Gabriele, M. & Hansen, A. S. Tracking and interpreting long-range chromatin interactions with super-resolution live-cell imaging. *Current Opinion in Cell Biology. Cell Nucleus* **70,** 18–26. doi:10.1016/j.ceb.2020.11.002 (2021).

177. Smith, A. Formative pluripotency: the executive phase in a developmental continuum. *Development* **144,** 365–373. doi:10.1242/dev.142679 (2017).

178. Endoh, M. & Niwa, H. Stepwise pluripotency transitions in mouse stem cells. *EMBO Reports* **23,** e55010. doi:10.15252/embr.202255010 (2022).

179. Kojima, M. L., Hoppe, C. & Giraldez, A. J. The maternal-to-zygotic transition: reprogramming of the cytoplasm and nucleus. *Nature Reviews Genetics* **26,** 245–267. doi:10.1038/s41576-024-00792-0 (2025).

180. Burton, A. & Torres-Padilla, M.-E. Epigenome dynamics in early mammalian embryogenesis. *Nature Reviews Genetics* **26,** 587–603. doi:10.1038/s41576-025-00831-4 (2025).

181. Schulz, K. N. & Harrison, M. M. Mechanisms regulating zygotic genome activation. *Nature Reviews Genetics* **20,** 221–234. doi:10.1038/s41576-018-0087-x (2019).

182. Paranjpe, S. S. & Veenstra, G. J. C. Establishing pluripotency in early development. *Biochimica et Biophysica Acta (BBA) - Gene Regulatory Mechanisms* **1849,** 626–636. doi:10.1016/j.bbagrm.2015.03.006 (2015).

183. Fiorentino, J., Torres-Padilla, M.-E. & Scialdone, A. Measuring and Modeling Single-Cell Heterogeneity and Fate Decision in Mouse Embryos. *Annual Review of Genetics* **54,** 167–187. doi:10.1146/annurev-genet-021920-110200 (2020).

184. Niwa, H. How is pluripotency determined and maintained? *Development* **134,** 635–646. doi:10.1242/dev.02787 (2007).

185. De Los Angeles, A. *et al.* Hallmarks of pluripotency. *Nature* **525,** 469–478. doi:10.1038/nature15515 (2015).

186. Wu, J., Yamauchi, T. & Izpisua Belmonte, J. C. An overview of mammalian pluripotency. *Development* **143,** 1644–1648. doi:10.1242/dev.132928 (2016).

187. Takahashi, S., Kobayashi, S. & Hiratani, I. Epigenetic differences between naïve and primed pluripotent stem cells. *Cellular and Molecular Life Sciences: CMLS* **75,** 1191–1203. doi:10.1007/s00018-017-2703-x (2017).

188. Evans, M. J. & Kaufman, M. H. Establishment in culture of pluripotential cells from mouse embryos. *Nature* **292,** 154–156. doi:10.1038/292154a0 (1981).

189. Martin, G. R. Isolation of a pluripotent cell line from early mouse embryos cultured in medium conditioned by teratocarcinoma stem cells. *Proceedings of the National Academy of Sciences* **78,** 7634–7638. doi:10.1073/pnas.78.12.7634 (1981).

190. Thomson, J. A. *et al.* Embryonic Stem Cell Lines Derived from Human Blastocysts. *Science* **282,** 1145–1147. doi:10.1126/science.282.5391.1145 (1998).

191. Smith, A. G. *et al.* Inhibition of pluripotential embryonic stem cell differentiation by purified polypeptides. *Nature* **336,** 688–690. doi:10.1038/336688a0 (1988).

192. Williams, R. L. *et al.* Myeloid leukaemia inhibitory factor maintains the developmental potential of embryonic stem cells. *Nature* **336,** 684–687. doi:10.1038/336684a0 (1988).

193. Hayashi, K., de Sousa Lopes, S. M. C., Tang, F., Lao, K. & Surani, M. A. Dynamic equilibrium and heterogeneity of mouse pluripotent stem cells with distinct functional and epigenetic states. *Cell Stem Cell* **3,** 391–401. doi:10.1016/j.stem.2008.07.027 (2008).

194. Toyooka, Y., Shimosato, D., Murakami, K., Takahashi, K. & Niwa, H. Identification and characterization of subpopulations in undifferentiated ES cell culture. *Development (Cambridge, England)* **135,** 909–918. doi:10.1242/dev.017400 (2008).

195. Boroviak, T., Loos, R., Bertone, P., Smith, A. & Nichols, J. The ability of inner-cell-mass cells to self-renew as embryonic stem cells is acquired following epiblast specification. *Nature Cell Biology* **16,** 516–528. doi:10.1038/ncb2965 (2014).

196. Ying, Q.-L. *et al.* The ground state of embryonic stem cell self-renewal. *Nature* **453,** 519–523. doi:10.1038/nature06968 (2008).

197. Guo, G. *et al.* Klf4 reverts developmentally programmed restriction of ground state pluripotency. *Development (Cambridge, England)* **136,** 1063–1069. doi:10.1242/dev.030957 (2009).

198. Bao, S. *et al.* Epigenetic reversion of post-implantation epiblast to pluripotent embryonic stem cells. *Nature* **461,** 1292–1295. doi:10.1038/nature08534 (2009).

199. Han, D. W. *et al.* Epiblast stem cell subpopulations represent mouse embryos of distinct pregastrulation stages. *Cell* **143,** 617–627. doi:10.1016/j.cell.2010.10.015 (2010).

200. Ohinata, Y. *et al.* A signaling principle for the specification of the germ cell lineage in mice. *Cell* **137,** 571–584. doi:10.1016/j.cell.2009.03.014 (2009).

201. Hayashi, K., Ohta, H., Kurimoto, K., Aramaki, S. & Saitou, M. Reconstitution of the mouse germ cell specification pathway in culture by pluripotent stem cells. *Cell* **146,** 519–532. doi:10.1016/j.cell.2011.06.052 (2011).

202. Nakaki, F. *et al.* Induction of mouse germ-cell fate by transcription factors in vitro. *Nature* **501,** 222–226. doi:10.1038/nature12417 (2013).

203. Aasen, T. *et al.* Efficient and rapid generation of induced pluripotent stem cells from human keratinocytes. *Nature Biotechnology* **26,** 1276–1284. doi:10.1038/nbt.1503 (2008).

204. Park, I.-H. *et al.* Reprogramming of human somatic cells to pluripotency with defined factors. *Nature* **451,** 141–146. doi:10.1038/nature06534 (2008).

205. Takahashi, K. *et al.* Induction of Pluripotent Stem Cells from Adult Human Fibroblasts by Defined Factors. *Cell* **131,** 861–872. doi:10.1016/j.cell.2007.11.019 (2007).

206. Takahashi, K. & Yamanaka, S. Induction of Pluripotent Stem Cells from Mouse Embryonic and Adult Fibroblast Cultures by Defined Factors. *Cell* **126,** 663–676. doi:10.1016/j.cell.2006.07.024 (2006).

207. Wernig, M. *et al.* In vitro reprogramming of fibroblasts into a pluripotent ES-cell-like state. *Nature* **448,** 318–324. doi:10.1038/nature05944 (2007).

208. Han, D. W. *et al.* Direct reprogramming of fibroblasts into epiblast stem cells. *Nature Cell Biology* **13,** 66–71. doi:10.1038/ncb2136 (2011).

209. Hochedlinger, K. & Jaenisch, R. Induced Pluripotency and Epigenetic Reprogramming. *Cold Spring Harbor Perspectives in Biology* **7,** a019448. doi:10.1101/cshperspect.a019448 (2015).

210. Cowan, C. A., Atienza, J., Melton, D. A. & Eggan, K. Nuclear Reprogramming of Somatic Cells After Fusion with Human Embryonic Stem Cells. *Science* **309,** 1369–1373. doi:10.1126/science.1116447 (2005).

211. Tada, M., Takahama, Y., Abe, K., Nakatsuji, N. & Tada, T. Nuclear reprogramming of somatic cells by in vitro hybridization with ES cells. *Current Biology* **11,** 1553–1558. doi:10.1016/S0960-9822(01)00459-6 (2001).

212. Tachibana, M. *et al.* Human Embryonic Stem Cells Derived by Somatic Cell Nuclear Transfer. *Cell* **153,** 1228–1238. doi:10.1016/j.cell.2013.05.006 (2013).

213. Hou, P. *et al.* Pluripotent Stem Cells Induced from Mouse Somatic Cells by Small-Molecule Compounds. *Science* **341,** 651–654. doi:10.1126/science.1239278 (2013).

214. Nichols, J. *et al.* Formation of pluripotent stem cells in the mammalian embryo depends on the POU transcription factor Oct4. *Cell* **95,** 379–391. doi:10.1016/s0092-8674(00)81769-9 (1998).

215. Schöler, H. R., Hatzopoulos, A. K., Balling, R., Suzuki, N. & Gruss, P. A family of octamer-specific proteins present during mouse embryogenesis: evidence for germline-specific expression of an Oct factor. *The EMBO journal* **8,** 2543–2550. doi:10.1002/j.1460-2075.1989.tb08392.x (1989).

216. Niwa, H., Miyazaki, J.-i. & Smith, A. G. Quantitative expression of Oct-3/4 defines differentiation, dedifferentiation or self-renewal of ES cells. *Nature Genetics* **24,** 372–376. doi:10.1038/74199 (2000).

217. Thomson, M. *et al.* Pluripotency circuit members mediate germ layer fate choice of embryonic stem cells. *Cell* **145,** 875–889. doi:10.1016/j.cell.2011.05.017 (2011).

218. Ivanova, N. *et al.* Dissecting self-renewal in stem cells with RNA interference. *Nature* **442,** 533–538. doi:10.1038/nature04915 (2006).

219. Ying, Q. L., Nichols, J., Chambers, I. & Smith, A. BMP induction of Id proteins suppresses differentiation and sustains embryonic stem cell self-renewal in collaboration with STAT3. *Cell* **115,** 281–292. doi:10.1016/s0092-8674(03)00847-x (2003).

220. Suzuki, A. *et al.* Maintenance of embryonic stem cell pluripotency by Nanog-mediated reversal of mesoderm specification. *Nature Clinical Practice. Cardiovascular Medicine* **3 Suppl 1,** S114–122. doi:10.1038/ncpcardio0442 (2006).

221. Chambers, I. *et al.* Functional expression cloning of Nanog, a pluripotency sustaining factor in embryonic stem cells. *Cell* **113,** 643–655. doi:10.1016/s0092-8674(03)00392-1 (2003).

222. Mitsui, K. *et al.* The homeoprotein Nanog is required for maintenance of pluripotency in mouse epiblast and ES cells. *Cell* **113,** 631–642. doi:10.1016/s0092-8674(03)00393-3 (2003).

223. Sinha, K. K., Bilokapic, S., Du, Y., Malik, D. & Halic, M. Histone modifications regulate pioneer transcription factor cooperativity. *Nature* **619,** 378–384. doi:10.1038/s41586-023-06112-6 (2023).

224. Gadea, F. C. M. & Nikolova, E. N. Structural plasticity of pioneer factor Sox2 and DNA bendability modulate nucleosome engagement and Sox2-Oct4 synergism. *Journal of molecular biology* **435,** 167916. doi:10.1016/j.jmb.2022.167916 (2023).

225. Whyte, W. A. *et al.* Master Transcription Factors and Mediator Establish Super-Enhancers at Key Cell Identity Genes. *Cell* **153,** 307–319. doi:10.1016/j.cell.2013.03.035 (2013).

226. Jaenisch, R. & Young, R. Stem Cells, the Molecular Circuitry of Pluripotency and Nuclear Reprogramming. *Cell* **132,** 567–582. doi:10.1016/j.cell.2008.01.015 (2008).

227. Lee, K. C., Wong, W. K. & Feng, B. Decoding the Pluripotency Network: The Emergence of New Transcription Factors. *Biomedicines* **1,** 49–78. doi:10.3390/biomedicines1010049 (2013).

228. Wang, X. *et al.* Formative pluripotent stem cells show features of epiblast cells poised for gastrulation. *Cell Research* **31,** 526–541. doi:10.1038/s41422-021-00477-x (2021).

229. Kinoshita, M. *et al.* Capture of Mouse and Human Stem Cells with Features of Formative Pluripotency. *Cell Stem Cell* **28,** 453–471.e8. doi:10.1016/j.stem.2020.11.005 (2021).

230. Burdon, T., Stracey, C., Chambers, I., Nichols, J. & Smith, A. Suppression of SHP-2 and ERK Signalling Promotes Self-Renewal of Mouse Embryonic Stem Cells. *Developmental Biology* **210,** 30–43. doi:10.1006/dbio.1999.9265 (1999).

231. Wray, J. *et al.* Inhibition of glycogen synthase kinase-3 alleviates Tcf3 repression of the pluripotency network and increases embryonic stem cell resistance to differentiation. *Nature Cell Biology* **13,** 838–845. doi:10.1038/ncb2267 (2011).

232. Kunath, T. *et al.* FGF stimulation of the Erk1/2 signalling cascade triggers transition of pluripotent embryonic stem cells from self-renewal to lineage commitment. *Development (Cambridge, England)* **134,** 2895–2902. doi:10.1242/dev.02880 (2007).

233. Thisse, B. & Thisse, C. Functions and regulations of fibroblast growth factor signaling during embryonic development. *Developmental Biology* **287,** 390–402. doi:10.1016/j.ydbio.2005.09.011 (2005).

234. Camus, A., Perea-Gomez, A., Moreau, A. & Collignon, J. Absence of Nodal signaling promotes precocious neural differentiation in the mouse embryo. *Developmental Biology* **295,** 743–755. doi:10.1016/j.ydbio.2006.03.047 (2006).

235. Buecker, C. *et al.* Reorganization of enhancer patterns in transition from naive to primed pluripotency. *Cell Stem Cell* **14,** 838–853. doi:10.1016/j.stem.2014.04.003 (2014).

236. Yang, S.-H. *et al.* Otx2 and Oct4 Drive Early Enhancer Activation during Embryonic Stem Cell Transition from Naive Pluripotency. *Cell Reports* **7,** 1968–1981. doi:10.1016/j.celrep.2014.05.037 (2014).

237. Kalkan, T. & Smith, A. Mapping the route from naive pluripotency to lineage specification. *Philosophical Transactions of the Royal Society B: Biological Sciences* **369,** 20130540. doi:10.1098/rstb.2013.0540 (2014).

238. Auclair, G., Guibert, S., Bender, A. & Weber, M. Ontogeny of CpG island methylation and specificity of DNMT3 methyltransferases during embryonic development in the mouse. *Genome Biology* **15,** 545. doi:10.1186/s13059-014-0545-5 (2014).

239. Seisenberger, S. *et al.* The dynamics of genome-wide DNA methylation reprogramming in mouse primordial germ cells. *Molecular Cell* **48,** 849–862. doi:10.1016/j.molcel.2012.11.001 (2012).

240. Marks, H. *et al.* The Transcriptional and Epigenomic Foundations of Ground State Pluripotency. *Cell* **149,** 590–604. doi:10.1016/j.cell.2012.03.026 (2012).

241. Turner, D. A., Trott, J., Hayward, P., Rué, P. & Martinez Arias, A. An interplay between extracellular signalling and the dynamics of the exit from pluripotency drives cell fate decisions in mouse ES cells. *Biology Open* **3,** 614–626. doi:10.1242/bio.20148409 (2014).

242. Zhang, K. *et al.* Distinct functions of BMP4 during different stages of mouse ES cell neural commitment. *Development* **137,** 2095–2105. doi:10.1242/dev.049494 (2010).

243. Mulas, C., Kalkan, T. & Smith, A. NODAL Secures Pluripotency upon Embryonic Stem Cell Progression from the Ground State. *Stem Cell Reports* **9,** 77–91. doi:10.1016/j.stemcr.2017.05.033 (2017).

244. Hariprakash, J. M. & Ferrari, F. Computational Biology Solutions to Identify Enhancers-target Gene Pairs. *Computational and Structural Biotechnology Journal* **17,** 821–831. doi:10.1016/j.csbj.2019.06.012 (2019).

245. Kvon, E. Z. Using transgenic reporter assays to functionally characterize enhancers in animals. *Genomics. Recent advances in functional assays of transcriptional enhancers* **106,** 185–192. doi:10.1016/j.ygeno.2015.06.007 (2015).

246. Wurmser, A. & Basu, S. Enhancer-Promoter Communication: It's Not Just About Contact. *Frontiers in Molecular Biosciences* **9,** 867303. doi:10.3389/fmolb.2022.867303 (2022).

247. Panigrahi, A. & O'Malley, B. W. Mechanisms of enhancer action: the known and the unknown. *Genome Biology* **22,** 108. doi:10.1186/s13059-021-02322-1 (2021).

248. Simonis, M. *et al.* Nuclear organization of active and inactive chromatin domains uncovered by chromosome conformation capture–on-chip (4C). *Nature Genetics* **38,** 1348–1354. doi:10.1038/ng1896 (2006).

249. Zhao, Z. *et al.* Circular chromosome conformation capture (4C) uncovers extensive networks of epigenetically regulated intra- and interchromosomal interactions. *Nature Genetics* **38,** 1341–1347. doi:10.1038/ng1891 (2006).

250. Dekker, J., Rippe, K., Dekker, M. & Kleckner, N. Capturing chromosome conformation. *Science (New York, N.Y.)* **295,** 1306–1311. doi:10.1126/science.1067799 (2002).

251. Fullwood, M. J. *et al.* An oestrogen-receptor-alpha-bound human chromatin interactome. *Nature* **462,** 58–64. doi:10.1038/nature08497 (2009).

252. Bonev, B. *et al.* Multiscale 3D Genome Rewiring during Mouse Neural Development. *Cell* **171,** 557–572.e24. doi:10.1016/j.cell.2017.09.043 (2017).

253. Hsieh, T.-H. S. *et al.* Resolving the 3D Landscape of Transcription-Linked Mammalian Chromatin Folding. *Molecular Cell* **78,** 539–553.e8. doi:10.1016/j.molcel.2020.03.002 (2020).

254. Williams, R. M. *et al.* Reconstruction of the Global Neural Crest Gene Regulatory Network In Vivo. *Developmental Cell* **51,** 255–276.e7. doi:10.1016/j.devcel.2019.10.003 (2019).

255. Novo, C. L. *et al.* Long-Range Enhancer Interactions Are Prevalent in Mouse Embryonic Stem Cells and Are Reorganized upon Pluripotent State Transition. *Cell Reports* **22,** 2615–2627. doi:10.1016/j.celrep.2018.02.040 (2018).

256. Johnson, D. S., Mortazavi, A., Myers, R. M. & Wold, B. Genome-Wide Mapping of in Vivo Protein-DNA Interactions. *Science* **316,** 1497–1502. doi:10.1126/science.1141319 (2007).

257. Barski, A. *et al.* High-Resolution Profiling of Histone Methylations in the Human Genome. *Cell* **129,** 823–837. doi:10.1016/j.cell.2007.05.009 (2007).

258. Cotney, J. *et al.* Chromatin state signatures associated with tissue-specific gene expression and enhancer activity in the embryonic limb. *Genome Research* **22,** 1069–1080. doi:10.1101/gr.129817.111 (2012).

259. Visel, A. *et al.* ChIP-seq accurately predicts tissue-specific activity of enhancers. *Nature* **457,** 854–858. doi:10.1038/nature07730 (2009).

260. Arnold, C. D. *et al.* Genome-wide quantitative enhancer activity maps identified by STARR-seq. *Science (New York, N.Y.)* **339,** 1074–1077. doi:10.1126/science.1232542 (2013).

261. Bonn, S. *et al.* Tissue-specific analysis of chromatin state identifies temporal signatures of enhancer activity during embryonic development. *Nature Genetics* **44,** 148–156. doi:10.1038/ng.1064 (2012).

262. Rada-Iglesias, A. *et al.* A unique chromatin signature uncovers early developmental enhancers in humans. *Nature* **470,** 279–283. doi:10.1038/nature09692 (2011).

263. Heintzman, N. D. *et al.* Histone modifications at human enhancers reflect global cell-type-specific gene expression. *Nature* **459,** 108–112. doi:10.1038/nature07829 (2009).

264. Bernstein, B. E. *et al.* A bivalent chromatin structure marks key developmental genes in embryonic stem cells. *Cell* **125,** 315–326. doi:10.1016/j.cell.2006.02.041 (2006).

265. Vastenhouw, N. L. *et al.* Chromatin signature of embryonic pluripotency is established during genome activation. *Nature* **464,** 922–926. doi:10.1038/nature08866 (2010).

266. Creyghton, M. P. *et al.* Histone H3K27ac separates active from poised enhancers and predicts developmental state. *Proceedings of the National Academy of Sciences of the United States of America* **107,** 21931–21936. doi:10.1073/pnas.1016071107 (2010).

267. Kharchenko, P. V. *et al.* Comprehensive analysis of the chromatin landscape in Drosophila melanogaster. *Nature* **471,** 480–485. doi:10.1038/nature09725 (2011).

268. Shen, Y. *et al.* A map of the cis-regulatory sequences in the mouse genome. *Nature* **488,** 116–120. doi:10.1038/nature11243 (2012).

269. Wamstad, J. A. *et al.* Dynamic and coordinated epigenetic regulation of developmental transitions in the cardiac lineage. *Cell* **151,** 206–220. doi:10.1016/j.cell.2012.07.035 (2012).

270. Boyle, A. P. *et al.* High-resolution mapping and characterization of open chromatin across the genome. *Cell* **132,** 311–322. doi:10.1016/j.cell.2007.12.014 (2008).

271. Buenrostro, J. D., Chang, H. Y. & Greenleaf, W. J. ATAC-seq: A Method for Assaying Chromatin Accessibility Genome-Wide. *Current Protocols in Molecular Biology* **109,** 21.29.1–21.29.9. doi:10.1002/0471142727.mb2129s109 (2015).

272. Ryan, G. E. & Farley, E. K. Functional genomic approaches to elucidate the role of enhancers during development. *Wiley Interdisciplinary Reviews. Systems Biology and Medicine* **12,** e1467. doi:10.1002/wsbm.1467 (2020).

273. Karabacak Calviello, A., Hirsekorn, A., Wurmus, R., Yusuf, D. & Ohler, U. Reproducible inference of transcription factor footprints in ATAC-seq and DNase-seq datasets using protocol-specific bias modeling. *Genome Biology* **20,** 42. doi:10.1186/s13059-019-1654-y (2019).

274. Kempfer, R. & Pombo, A. Methods for mapping 3D chromosome architecture. *Nature Reviews Genetics* **21,** 207–226. doi:10.1038/s41576-019-0195-2 (2020).

275. Tolhuis, B., Palstra, R.-J., Splinter, E., Grosveld, F. & Laat, W. d. Looping and Interaction between Hypersensitive Sites in the Active β-globin Locus. *Molecular Cell* **10,** 1453–1465. doi:10.1016/S1097-2765(02)00781-5 (2002).

276. Palstra, R.-J. *et al.* The beta-globin nuclear compartment in development and erythroid differentiation. *Nature Genetics* **35,** 190–194. doi:10.1038/ng1244 (2003).

277. Würtele, H. & Chartrand, P. Genome-wide scanning of HoxB1-associated loci in mouse ES cells using an open-ended Chromosome Conformation Capture methodology. *Chromosome Research: An International Journal on the Molecular, Supramolecular and Evolutionary Aspects of Chromosome Biology* **14,** 477–495. doi:10.1007/s10577-006-1075-0 (2006).

278. Gao, F., Wei, Z., An, W., Wang, K. & Lu, W. The interactomes of POU5F1 and SOX2 enhancers in human embryonic stem cells. *Scientific Reports* **3,** 1588. doi:10.1038/srep01588 (2013).

279. Ghavi-Helm, Y. *et al.* Enhancer loops appear stable during development and are associated with paused polymerase. *Nature* **512,** 96–100. doi:10.1038/nature13417 (2014).

280. Jiang, T. *et al.* Identification of multi-loci hubs from 4C-seq demonstrates the functional importance of simultaneous interactions. *Nucleic Acids Research* **44,** 8714–8725. doi:10.1093/nar/gkw568 (2016).

281. Cai, M. *et al.* 4C-seq revealed long-range interactions of a functional enhancer at the 8q24 prostate cancer risk locus. *Scientific Reports* **6,** 22462. doi:10.1038/srep22462 (2016).

282. Weintraub, A. S. *et al.* YY1 Is a Structural Regulator of Enhancer-Promoter Loops. *Cell* **171,** 1573–1588.e28. doi:10.1016/j.cell.2017.11.008 (2017).

283. Moon, B.-S. *et al.* Long range inter-chromosomal interaction of Oct4 distal enhancer loci regulates ESCs pluripotency. *Cell Death Discovery* **9,** 61. doi:10.1038/s41420-023-01363-8 (2023).

284. Weichenhan, D. *et al.* Altered enhancer-promoter interaction leads to MNX1 expression in pediatric acute myeloid leukemia with t(7;12)(q36;p13). *Blood Advances* **8,** 5100–5111. doi:10.1182/bloodadvances.2023012161 (2024).

285. Tjalsma, S. J. D. *et al.* Long-range enhancer-controlled genes are hypersensitive to regulatory factor perturbations. *Cell Genomics* **5,** 100778. doi:10.1016/j.xgen.2025.100778 (2025).

286. Hsieh, T.-H. S., Fudenberg, G., Goloborodko, A. & Rando, O. J. Micro-C XL: assaying chromosome conformation from the nucleosome to the entire genome. *Nature Methods* **13,** 1009–1011. doi:10.1038/nmeth.4025 (2016).

287. Hughes, J. R. *et al.* Analysis of hundreds of cis-regulatory landscapes at high resolution in a single, high-throughput experiment. *Nature Genetics* **46,** 205–212. doi:10.1038/ng.2871 (2014).

288. Schoenfelder, S., Javierre, B.-M., Furlan-Magaril, M., Wingett, S. W. & Fraser, P. Promoter Capture Hi-C: High-resolution, Genome-wide Profiling of Promoter Interactions. *Journal of Visualized Experiments,* 57320. doi:10.3791/57320 (2018).

289. Downes, D. J. *et al.* Capture-C: A modular and flexible approach for high-resolution chromosome conformation capture. *Nature protocols* **17,** 445–475. doi:10.1038/s41596-021-00651-w (2022).

290. Mumbach, M. R. *et al.* HiChIP: efficient and sensitive analysis of protein-directed genome architecture. *Nature Methods* **13,** 919–922. doi:10.1038/nmeth.3999 (2016).

291. Yu, M., Juric, I., Abnousi, A., Hu, M. & Ren, B. Proximity Ligation-Assisted ChIP-Seq (PLAC-Seq). *Methods in Molecular Biology (Clifton, N.J.)* **2351,** 181–199. doi:10.1007/978-1-0716-1597-3_10 (2021).

292. Handoko, L. *et al.* CTCF-Mediated Functional Chromatin Interactome in Pluripotent Cells. *Nature genetics* **43,** 630–638. doi:10.1038/ng.857 (2011).

293. Sandhu, K. S. *et al.* Large-Scale Functional Organization of Long-Range Chromatin Interaction Networks. *Cell reports* **2,** 1207. doi:10.1016/j.celrep.2012.09.022 (2012).

294. Finn, E. H. & Misteli, T. Molecular basis and biological function of variability in spatial genome organization. *Science (New York, N.Y.)* **365,** eaaw9498. doi:10.1126/science.aaw9498 (2019).

295. Cattoni, D. I. *et al.* Single-cell absolute contact probability detection reveals chromosomes are organized by multiple low-frequency yet specific interactions. *Nature Communications* **8,** 1753. doi:10.1038/s41467-017-01962-x (2017).

296. Finn, E. H. *et al.* Extensive Heterogeneity and Intrinsic Variation in Spatial Genome Organization. *Cell* **176,** 1502–1515.e10. doi:10.1016/j.cell.2019.01.020 (2019).

297. Wang, S. *et al.* Spatial organization of chromatin domains and compartments in single chromosomes. *Science* **353,** 598–602. doi:10.1126/science.aaf8084 (2016).

298. Tünnermann, J., Roth, G., Cramard, J. & Giorgetti, L. *Enhancer control of promoter activity and variability via frequency modulation of clustered transcriptional bursts* 2025. doi:10.1101/2025.03.26.645410.

299. Ramani, V. *et al.* Massively multiplex single-cell Hi-C. *Nature Methods* **14,** 263–266. doi:10.1038/nmeth.4155 (2017).

300. Nagano, T. *et al.* Cell-cycle dynamics of chromosomal organization at single-cell resolution. *Nature* **547,** 61–67. doi:10.1038/nature23001 (2017).

301. Quinodoz, S. A. *et al.* Higher-Order Inter-chromosomal Hubs Shape 3D Genome Organization in the Nucleus. *Cell* **174,** 744–757.e24. doi:10.1016/j.cell.2018.05.024 (2018).

302. Gong, H. *et al.* Computational methods for identifying enhancer-promoter interactions. *Quantitative Biology* **11,** 122–142. doi:10.15302/J-QB-022-0322 (2023).

303. Thurman, R. E. *et al.* The accessible chromatin landscape of the human genome. *Nature* **489,** 75–82. doi:10.1038/nature11232 (2012).

304. Sheffield, N. C. *et al.* Patterns of regulatory activity across diverse human cell types predict tissue identity, transcription factor binding, and long-range interactions. *Genome Research* **23,** 777–788. doi:10.1101/gr.152140.112 (2013).

305. Corradin, O. *et al.* Combinatorial effects of multiple enhancer variants in linkage disequilibrium dictate levels of gene expression to confer susceptibility to common traits. *Genome Research* **24,** 1–13. doi:10.1101/gr.164079.113 (2014).

306. Yao, L., Shen, H., Laird, P. W., Farnham, P. J. & Berman, B. P. Inferring regulatory element landscapes and transcription factor networks from cancer methylomes. *Genome Biology* **16,** 105. doi:10.1186/s13059-015-0668-3 (2015).

307. Bo, X. & Wang, S. TargetFinder: a software for antisense oligonucleotide target site selection based on MAST and secondary structures of target mRNA. *Bioinformatics* **21,** 1401–1402. doi:10.1093/bioinformatics/bti211 (2005).

308. He, B., Chen, C., Teng, L. & Tan, K. Global view of enhancer–promoter interactome in human cells. *Proceedings of the National Academy of Sciences* **111,** E2191–E2199. doi:10.1073/pnas.1320308111 (2014).

309. Zhao, C., Li, X. & Hu, H. PETModule: a motif module based approach for enhancer target gene prediction. *Scientific Reports* **6,** 30043. doi:10.1038/srep30043 (2016).

310. Hafez, D. *et al.* McEnhancer: predicting gene expression via semi-supervised assignment of enhancers to target genes. *Genome Biology* **18,** 199. doi:10.1186/s13059-017-1316-x (2017).

311. Whalen, S., Truty, R. M. & Pollard, K. S. Enhancer–promoter interactions are encoded by complex genomic signatures on looping chromatin. *Nature Genetics* **48,** 488–496. doi:10.1038/ng.3539 (2016).

312. Wei, Z. *et al.* Klf4 Organizes Long-Range Chromosomal Interactions with the Oct4 Locus in Reprogramming and Pluripotency. *Cell Stem Cell* **13,** 36–47. doi:10.1016/j.stem.2013.05.010 (2013).

313. Apostolou, E. *et al.* Genome-wide Chromatin Interactions of the Nanog Locus in Pluripotency, Differentiation, and Reprogramming. *Cell Stem Cell* **12,** 699–712. doi:10.1016/j.stem.2013.04.013 (2013).

314. Stadhouders, R. *et al.* Transcription factors orchestrate dynamic interplay between genome topology and gene regulation during cell reprogramming. *Nature Genetics* **50,** 238–249. doi:10.1038/s41588-017-0030-7 (2018).

315. Gschwind, A. R. *et al.* An encyclopedia of enhancer-gene regulatory interactions in the human genome. *bioRxiv: The Preprint Server for Biology,* 2023.11.09.563812. doi:10.1101/2023.11.09.563812 (2023).

316. Fishilevich, S. *et al.* GeneHancer: genome-wide integration of enhancers and target genes in GeneCards. *Database* **2017,** bax028. doi:10.1093/database/bax028 (2017).

317. Lichtman, J. W. & Conchello, J.-A. Fluorescence microscopy. *Nature Methods* **2,** 910–919. doi:10.1038/nmeth817 (2005).

318. Grimm, J. B. & Lavis, L. D. Caveat fluorophore: an insiders' guide to small-molecule fluorescent labels. *Nature Methods* **19,** 149–158. doi:10.1038/s41592-021-01338-6 (2022).

319. Jabłoński, A. Über den Mechanismus der Photolumineszenz von Farbstoffphosphoren. *Zeitschrift für Physik* **94,** 38–46. doi:10.1007/BF01330795 (1935).

320. Zimmermann, T., Marrison, J., Hogg, K. & O'Toole, P. Clearing up the signal: spectral imaging and linear unmixing in fluorescence microscopy. *Methods in Molecular Biology (Clifton, N.J.)* **1075,** 129–148. doi:10.1007/978-1-60761-847-8_5 (2014).

321. Takei, Y. *et al.* Integrated spatial genomics reveals global architecture of single nuclei. *Nature* **590,** 344–350. doi:10.1038/s41586-020-03126-2 (2021).

322. Demchenko, A. P. Photobleaching of organic fluorophores: quantitative characterization, mechanisms, protection*. *Methods and Applications in Fluorescence* **8,** 022001. doi:10.1088/2050-6120/ab7365 (2020).

323. Wurm, C. A., Neumann, D., Schmidt, R., Egner, A. & Jakobs, S. Sample preparation for STED microscopy. *Methods in Molecular Biology (Clifton, N.J.)* **591,** 185–199. doi:10.1007/978-1-60761-404-3_11 (2010).

324. Poo, M. M. & Cone, R. A. Lateral diffusion of phodopsin in Necturus rods. *Experimental Eye Research* **17,** 503–510. doi:10.1016/0014-4835(73)90079-1 (1973).

325. Liebman, P. A. & Entine, G. Lateral diffusion of visual pigment in photorecptor disk membranes. *Science (New York, N.Y.)* **185,** 457–459. doi:10.1126/science.185.4149.457 (1974).

326. Alexiev, U. & Farrens, D. L. Fluorescence spectroscopy of rhodopsins: Insights and approaches. *Biochimica et Biophysica Acta (BBA) - Bioenergetics. Retinal Proteins* **1837,** 694–709. doi:10.1016/j.bbabio.2013.10.008 (2014).

327. Truong, K. & Ikura, M. The use of FRET imaging microscopy to detect protein–protein interactions and protein conformational changes *in vivo*. *Current Opinion in Structural Biology* **11,** 573–578. doi:10.1016/S0959-440X(00)00249-9 (2001).

328. Mota, A. *et al.* FRET-FISH probes chromatin compaction at individual genomic loci in single cells. *Nature Communications* **13,** 6680. doi:10.1038/s41467-022-34183-y (2022).

329. Miyawaki, A. *et al.* Fluorescent indicators for Ca2+ based on green fluorescent proteins and calmodulin. *Nature* **388,** 882–887. doi:10.1038/42264 (1997).

330. Truong, K. *et al.* FRET-based in vivo Ca2+ imaging by a new calmodulin-GFP fusion molecule. *Nature Structural Biology* **8,** 1069–1073. doi:10.1038/nsb728 (2001).

331. Huang, B., Bates, M. & Zhuang, X. Super resolution fluorescence microscopy. *Annual review of biochemistry* **78,** 993–1016. doi:10.1146/annurev.biochem.77.061906.092014 (2009).

332. Sigal, Y. M., Zhou, R. & Zhuang, X. Visualizing and discovering cellular structures with super-resolution microscopy. *Science* **361,** 880–887. doi:10.1126/science.aau1044 (2018).

333. Boettiger, A. N. *et al.* Super-resolution imaging reveals distinct chromatin folding for different epigenetic states. *Nature* **529,** 418–422. doi:10.1038/nature16496 (2016).

334. Nozaki, T. *et al.* Dynamic Organization of Chromatin Domains Revealed by Super-Resolution Live-Cell Imaging. *Molecular Cell* **67,** 282–293.e7. doi:10.1016/j.molcel.2017.06.018 (2017).

335. Reindl, J. *et al.* Chromatin organization revealed by nanostructure of irradiation induced γH2AX, 53BP1 and Rad51 foci. *Scientific Reports* **7,** 40616. doi:10.1038/srep40616 (2017).

336. Brandstetter, K. *et al.* Differences in nanoscale organization of regulatory active and inactive human chromatin. *Biophysical Journal* **121,** 977–990. doi:10.1016/j.bpj.2022.02.009 (2022).

337. Kanchanawong, P. *et al.* Nanoscale architecture of integrin-based cell adhesions. *Nature* **468,** 580–584. doi:10.1038/nature09621 (2010).

338. Van den Bogaart, G. *et al.* Membrane protein sequestering by ionic protein–lipid interactions. *Nature* **479,** 552–555. doi:10.1038/nature10545 (2011).

339. Chojnacki, J. *et al.* Maturation-Dependent HIV-1 Surface Protein Redistribution Revealed by Fluorescence Nanoscopy. *Science* **338,** 524–528. doi:10.1126/science.1226359 (2012).

340. Löschberger, A. *et al.* Super-resolution imaging visualizes the eightfold symmetry of gp210 proteins around the nuclear pore complex and resolves the central channel with nanometer resolution. *Journal of Cell Science* **125,** 570–575. doi:10.1242/jcs.098822 (2012).

341. Van Engelenburg, S. B. *et al.* Distribution of ESCRT machinery at HIV assembly sites reveals virus scaffolding of ESCRT subunits. *Science (New York, N.Y.)* **343,** 653–656. doi:10.1126/science.1247786 (2014).

342. Große, L. *et al.* Bax assembles into large ring-like structures remodeling the mitochondrial outer membrane in apoptosis. *The EMBO journal* **35,** 402–413. doi:10.15252/embj.201592789 (2016).

343. Eggeling, C. *et al.* Direct observation of the nanoscale dynamics of membrane lipids in a living cell. *Nature* **457,** 1159–1162. doi:10.1038/nature07596 (2009).

344. Giannone, G. *et al.* Dynamic superresolution imaging of endogenous proteins on living cells at ultra-high density. *Biophysical Journal* **99,** 1303–1310. doi:10.1016/j.bpj.2010.06.005 (2010).

345. Sahl, S. J., Leutenegger, M., Hilbert, M., Hell, S. W. & Eggeling, C. Fast molecular tracking maps nanoscale dynamics of plasma membrane lipids. *Proceedings of the National Academy of Sciences of the United States of America* **107,** 6829–6834. doi:10.1073/pnas.0912894107 (2010).

346. Shim, S.-H. *et al.* Super-resolution fluorescence imaging of organelles in live cells with photoswitchable membrane probes. *Proceedings of the National Academy of Sciences of the United States of America* **109,** 13978–13983. doi:10.1073/pnas.1201882109 (2012).

347. Nixon-Abell, J. *et al.* Increased spatiotemporal resolution reveals highly dynamic dense tubular matrices in the peripheral ER. *Science* **354,** aaf3928. doi:10.1126/science.aaf3928 (2016).

348. Tønnesen, J., Inavalli, V. V. G. K. & Nägerl, U. V. Super-Resolution Imaging of the Extracellular Space in Living Brain Tissue. *Cell* **172,** 1108–1121.e15. doi:10.1016/j.cell.2018.02.007 (2018).

349. Hell, S. W. & Wichmann, J. Breaking the diffraction resolution limit by stimulated emission: stimulated-emission-depletion fluorescence microscopy. *Optics Letters* **19,** 780–782. doi:10.1364/ol.19.000780 (1994).

350. Vicidomini, G., Bianchini, P. & Diaspro, A. STED super-resolved microscopy. *Nature Methods* **15,** 173–182. doi:10.1038/nmeth.4593 (2018).

351. Schermelleh, L. *et al.* Super-resolution microscopy demystified. *Nature Cell Biology* **21,** 72–84. doi:10.1038/s41556-018-0251-8 (2019).

352. Staudt, T. *et al.* Far-field optical nanoscopy with reduced number of state transition cycles. *Optics Express* **19,** 5644–5657. doi:10.1364/OE.19.005644 (2011).

353. Göttfert, F. *et al.* Strong signal increase in STED fluorescence microscopy by imaging regions of subdiffraction extent. *Proceedings of the National Academy of Sciences of the United States of America* **114,** 2125–2130. doi:10.1073/pnas.1621495114 (2017).

354. Heine, J. *et al.* Adaptive-illumination STED nanoscopy. *Proceedings of the National Academy of Sciences of the United States of America* **114,** 9797–9802. doi:10.1073/pnas.1708304114 (2017).

355. Betzig, E. *et al.* Imaging Intracellular Fluorescent Proteins at Nanometer Resolution. *Science* **313,** 1642–1645. doi:10.1126/science.1127344 (2006).

356. Hess, S. T., Girirajan, T. P. K. & Mason, M. D. Ultra-High Resolution Imaging by Fluorescence Photoactivation Localization Microscopy. *Biophysical Journal* **91,** 4258–4272. doi:10.1529/biophysj.106.091116 (2006).

357. Rust, M. J., Bates, M. & Zhuang, X. Sub-diffraction-limit imaging by stochastic optical reconstruction microscopy (STORM). *Nature Methods* **3,** 793–796. doi:10.1038/nmeth929 (2006).

358. Sharonov, A. & Hochstrasser, R. M. Wide-field subdiffraction imaging by accumulated binding of diffusing probes. *Proceedings of the National Academy of Sciences* **103,** 18911–18916. doi:10.1073/pnas.0609643104 (2006).

359. Jungmann, R. *et al.* Quantitative super-resolution imaging with qPAINT. *Nature Methods* **13,** 439–442. doi:10.1038/nmeth.3804 (2016).

360. Balzarotti, F. *et al.* Nanometer resolution imaging and tracking of fluorescent molecules with minimal photon fluxes. *Science* **355,** 606–612. doi:10.1126/science.aak9913 (2017).

361. Reinhardt, S. C. M. *et al.* Ångström-resolution fluorescence microscopy. *Nature* **617,** 711–716. doi:10.1038/s41586-023-05925-9 (2023).

362. Brown, J. M. *et al.* A tissue-specific self-interacting chromatin domain forms independently of enhancer-promoter interactions. *Nature Communications* **9,** 3849. doi:10.1038/s41467-018-06248-4 (2018).

363. Cardozo Gizzi, A. M. *et al.* Microscopy-Based Chromosome Conformation Capture Enables Simultaneous Visualization of Genome Organization and Transcription in Intact Organisms. *Molecular Cell* **74,** 212–222.e5. doi:10.1016/j.molcel.2019.01.011 (2019).

364. Kishi, J. Y. *et al.* SABER amplifies FISH: enhanced multiplexed imaging of RNA and DNA in cells and tissues. *Nature Methods* **16,** 533–544. doi:10.1038/s41592-019-0404-0 (2019).

365. Ried, T., Schröck, E., Ning, Y. & Wienberg, J. Chromosome painting: a useful art. *Human Molecular Genetics* **7,** 1619–1626. doi:10.1093/hmg/7.10.1619 (1998).

366. Cremer, M. *et al.* Multicolor 3D fluorescence in situ hybridization for imaging interphase chromosomes. *Methods in Molecular Biology (Clifton, N.J.)* **463,** 205–239. doi:10.1007/978-1-59745-406-3_15 (2008).

367. Minderman, H. *et al.* Image Cytometry Based Detection of Aneuploidy by Fluorescence In situ Hybridization in Suspension. *Cytometry. Part A : the journal of the International Society for Analytical Cytology* **81,** 776–784. doi:10.1002/cyto.a.22101 (2012).

368. Shakoori, A. R. Fluorescence In Situ Hybridization (FISH) and Its Applications. *Chromosome Structure and Aberrations,* 343–367. doi:10.1007/978-81-322-3673-3_16 (2017).

369. Perez, M. W., Camplisson, C. K. & Beliveau, B. J. Designing oligonucleotide-based FISH probe sets with PaintSHOP. *Methods in molecular biology (Clifton, N.J.)* **2784,** 177–189. doi:10.1007/978-1-0716-3766-1_12 (2024).

370. Beliveau, B. J. *et al.* OligoMiner provides a rapid, flexible environment for the design of genome-scale oligonucleotide in situ hybridization probes. *Proceedings of the National Academy of Sciences of the United States of America* **115,** E2183–E2192. doi:10.1073/pnas.1714530115 (2018).

371. Gelali, E. *et al.* iFISH is a publically available resource enabling versatile DNA FISH to study genome architecture. *Nature Communications* **10,** 1636. doi:10.1038/s41467-019-09616-w (2019).

372. Hu, M. *et al.* ProbeDealer is a convenient tool for designing probes for highly multiplexed fluorescence in situ hybridization. *Scientific Reports* **10,** 22031. doi:10.1038/s41598-020-76439-x (2020).

373. Zhang, T., Liu, G., Zhao, H., Braz, G. T. & Jiang, J. Chorus2: design of genome-scale oligonucleotide-based probes for fluorescence in situ hybridization. *Plant Biotechnology Journal* **19,** 1967–1978. doi:10.1111/pbi.13610 (2021).

374. Deaven, L. L. *et al.* Construction of human chromosome-specific DNA libraries from flow-sorted chromosomes. *Cold Spring Harbor Symposia on Quantitative Biology* **51 Pt 1,** 159–167. doi:10.1101/sqb.1986.051.01.019 (1986).

375. Green, M. R. & Sambrook, J. Labeling of DNA Probes by Nick Translation. *Cold Spring Harbor Protocols* **2020,** 100602. doi:10.1101/pdb.prot100602 (2020).

376. Green, M. R. & Sambrook, J. Random Priming: Labeling of Purified DNA Fragments by Extension of Random Oligonucleotides. *Cold Spring Harbor Protocols* **2019.** doi:10.1101/pdb.prot100586 (2019).

377. Beliveau, B. J. *et al.* Versatile design and synthesis platform for visualizing genomes with Oligopaint FISH probes. *Proceedings of the National Academy of Sciences* **109,** 21301–21306. doi:10.1073/pnas.1213818110 (2012).

378. Chen, K. H., Boettiger, A. N., Moffitt, J. R., Wang, S. & Zhuang, X. Spatially resolved, highly multiplexed RNA profiling in single cells. *Science* **348,** aaa6090. doi:10.1126/science.aaa6090 (2015).

379. Murgha, Y. *et al.* Combined in vitro transcription and reverse transcription to amplify and label complex synthetic oligonucleotide probe libraries. *BioTechniques* **58,** 301–307. doi:10.2144/000114298 (2015).

380. Beliveau, B. J. *et al.* In Situ Super-Resolution Imaging of Genomic DNA with OligoSTORM and OligoDNA-PAINT. *Methods in Molecular Biology (Clifton, N.J.)* **1663,** 231–252. doi:10.1007/978-1-4939-7265-4_19 (2017).

381. Nelson, P. S., Kent, M. & Muthini, S. Oligonucleotide labeling methods 3. Direct labeling of oligonucleotides employing a novel, non-nucleosidic, 2-aminobutyl-1,3-propanediol backbone. *Nucleic Acids Research* **20,** 6253–6259. doi:10.1093/nar/20.23.6253 (1992).

382. Raj, A., van den Bogaard, P., Rifkin, S. A., van Oudenaarden, A. & Tyagi, S. Imaging individual mRNA molecules using multiple singly labeled probes. *Nature Methods* **5,** 877–879. doi:10.1038/nmeth.1253 (2008).

383. Ishizuka, T., Liu, H. S., Ito, K. & Xu, Y. Fluorescence imaging of chromosomal DNA using click chemistry. *Scientific Reports* **6,** 33217. doi:10.1038/srep33217 (2016).

384. Hepperger, C., Otten, S., von Hase, J. & Dietzel, S. Preservation of large-scale chromatin structure in FISH experiments. *Chromosoma* **116,** 117–133. doi:10.1007/s00412-006-0084-2 (2007).

385. Chambeyron, S. & Bickmore, W. A. Chromatin decondensation and nuclear reorganization of the HoxB locus upon induction of transcription. *Genes & Development* **18,** 1119–1130. doi:10.1101/gad.292104 (2004).

386. Williams, R. R. E., Broad, S., Sheer, D. & Ragoussis, J. Subchromosomal positioning of the epidermal differentiation complex (EDC) in keratinocyte and lymphoblast interphase nuclei. *Experimental Cell Research* **272,** 163–175. doi:10.1006/excr.2001.5400 (2002).

387. Hoetelmans, R. W. M. *et al.* Effects of Acetone, Methanol, or Paraformaldehyde on Cellular Structure, Visualized by Reflection Contrast Microscopy and Transmission and Scanning Electron Microscopy. *Applied Immunohistochemistry & Molecular Morphology* **9,** 346 (2001).

388. Volpi, E. V. *et al.* Large-scale chromatin organization of the major histocompatibility complex and other regions of human chromosome 6 and its response to interferon in interphase nuclei. *Journal of Cell Science* **113 (Pt 9),** 1565–1576. doi:10.1242/jcs.113.9.1565 (2000).

389. Schnell, U., Dijk, F., Sjollema, K. A. & Giepmans, B. N. G. Immunolabeling artifacts and the need for live-cell imaging. *Nature Methods* **9,** 152–158. doi:10.1038/nmeth.1855 (2012).

390. Golczyk, H. A simple non-toxic ethylene carbonate fluorescence in situ hybridization (EC-FISH) for simultaneous detection of repetitive DNA sequences and fluorescent bands in plants. *Protoplasma* **256,** 873–880. doi:10.1007/s00709-019-01345-7 (2019).

391. Markaki, Y. *et al.* The potential of 3D-FISH and super-resolution structured illumination microscopy for studies of 3D nuclear architecture: 3D structured illumination microscopy of defined chromosomal structures visualized by 3D (immuno)-FISH opens new perspectives for studies of nuclear architecture. *BioEssays* **34,** 412–426. doi:10.1002/bies.201100176 (2012).

392. Szabo, Q. *et al.* TADs are 3D structural units of higher-order chromosome organization in Drosophila. *Science Advances* **4,** eaar8082. doi:10.1126/sciadv.aar8082 (2018).

393. Shim, A. R. *et al.* Formamide denaturation of double-stranded DNA for fluorescence in situ hybridization (FISH) distorts nanoscale chromatin structure. *PLOS ONE* **19,** e0301000. doi:10.1371/journal.pone.0301000 (2024).

394. Solovei, I. *et al.* Spatial Preservation of Nuclear Chromatin Architecture during Three-Dimensional Fluorescence *in Situ* Hybridization (3D-FISH). *Experimental Cell Research* **276,** 10–23. doi:10.1006/excr.2002.5513 (2002).

395. Hausmann, M. *et al.* COMBO-FISH: specific labeling of nondenatured chromatin targets by computer-selected DNA oligonucleotide probe combinations. *BioTechniques* **35,** 564–577. doi:10.2144/03353rr03 (2003).

396. Wang, Y. *et al.* Genome oligopaint via local denaturation fluorescence in situ hybridization. *Molecular Cell* **81,** 1566–1577.e8. doi:10.1016/j.molcel.2021.02.011 (2021).

397. Brown, J. M., De Ornellas, S., Parisi, E., Schermelleh, L. & Buckle, V. J. RASER-FISH: non-denaturing fluorescence in situ hybridization for preservation of three-dimensional interphase chromatin structure. *Nature Protocols* **17,** 1306–1331. doi:10.1038/s41596-022-00685-8 (2022).

398. Choi, H. M. T., Beck, V. A. & Pierce, N. A. Next-Generation in Situ Hybridization Chain Reaction: Higher Gain, Lower Cost, Greater Durability. *ACS Nano* **8,** 4284–4294. doi:10.1021/nn405717p (2014).

399. Choi, H. M. T. *et al.* Third-generation in situ hybridization chain reaction: multiplexed, quantitative, sensitive, versatile, robust. *Development* **145,** dev165753. doi:10.1242/dev.165753 (2018).

400. Huber, D., Voith von Voithenberg, L. & Kaigala, G. V. Fluorescence *in situ* hybridization (FISH): History, limitations and what to expect from micro-scale FISH? *Micro and Nano Engineering* **1,** 15–24. doi:10.1016/j.mne.2018.10.006 (2018).

401. Sullivan, K. E., Kapustina, M., Bristow, B. N. & Cembrowski, M. S. Quantification and analysis of multiplexed fluorescence insitu hybridization data using open-source tools. *STAR Protocols* **6,** 104127. doi:10.1016/j.xpro.2025.104127 (2025).

402. Stringer, C., Wang, T., Michaelos, M. & Pachitariu, M. Cellpose: a generalist algorithm for cellular segmentation. *Nature Methods* **18,** 100–106. doi:10.1038/s41592-020-01018-x (2021).

403. Lee, M. Y. *et al.* CellSeg: a robust, pre-trained nucleus segmentation and pixel quantification software for highly multiplexed fluorescence images. *BMC Bioinformatics* **23,** 46. doi:10.1186/s12859-022-04570-9 (2022).

404. Chen, J. *et al. The Allen Cell and Structure Segmenter: a new open source toolkit for segmenting 3D intracellular structures in fluorescence microscopy images* 2020. doi:10.1101/491035.

405. Bahry, E. *et al.* RS-FISH: precise, interactive, fast, and scalable FISH spot detection. *Nature Methods* **19,** 1563–1567. doi:10.1038/s41592-022-01669-y (2022).

406. Imbert, A. *et al.* FISH-quant v2: a scalable and modular tool for smFISH image analysis. *RNA (New York, N.Y.)* **28,** 786–795. doi:10.1261/rna.079073.121 (2022).

407. Eichenberger, B. T., Zhan, Y., Rempfler, M., Giorgetti, L. & Chao, J. A. deepBlink: threshold-independent detection and localization of diffraction-limited spots. *Nucleic Acids Research* **49,** 7292–7297. doi:10.1093/nar/gkab546 (2021).

408. Xu, W. *et al.* U-FISH: a fluorescent spot detector for imaging-based spatial-omics analysis and AI-assisted FISH diagnosis. *Genome Biology* **26,** 261. doi:10.1186/s13059-025-03736-x (2025).

409. Cisar, C., Keener, N., Ruffalo, M. & Paten, B. A unified pipeline for FISH spatial transcriptomics. *Cell Genomics* **3.** doi:10.1016/j.xgen.2023.100384 (2023).

410. Van Staalduinen, J., van Staveren, T., Grosveld, F. & Wendt, K. S. Live-cell imaging of chromatin contacts opens a new window into chromatin dynamics. *Epigenetics & Chromatin* **16,** 27. doi:10.1186/s13072-023-00503-9 (2023).

411. Robinett, C. C. *et al.* In vivo localization of DNA sequences and visualization of large-scale chromatin organization using lac operator/repressor recognition. *The Journal of Cell Biology* **135,** 1685–1700. doi:10.1083/jcb.135.6.1685 (1996).

412. Belmont, A. S. & Straight, A. F. In vivo visualization of chromosomes using lac operator-repressor binding. *Trends in Cell Biology* **8,** 121–124. doi:10.1016/s0962-8924(97)01211-7 (1998).

413. Lucas, J. S., Zhang, Y., Dudko, O. K. & Murre, C. 3D trajectories adopted by coding and regulatory DNA elements: first-passage times for genomic interactions. *Cell* **158,** 339–352. doi:10.1016/j.cell.2014.05.036 (2014).

414. Germier, T., Audibert, S., Kocanova, S., Lane, D. & Bystricky, K. Real-time imaging of specific genomic loci in eukaryotic cells using the ANCHOR DNA labelling system. *Methods (San Diego, Calif.)* **142,** 16–23. doi:10.1016/j.ymeth.2018.04.008 (2018).

415. Chen, B. *et al.* Dynamic imaging of genomic loci in living human cells by an optimized CRISPR/Cas system. *Cell* **155,** 1479–1491. doi:10.1016/j.cell.2013.12.001 (2013).

416. Hottin, A. & Marx, A. Structural Insights into the Processing of Nucleobase-Modified Nucleotides by DNA Polymerases. *Accounts of Chemical Research* **49,** 418–427. doi:10.1021/acs.accounts.5b00544 (2016).

417. Kropp, H. M., Betz, K., Wirth, J., Diederichs, K. & Marx, A. Crystal structures of ternary complexes of archaeal B-family DNA polymerases. *PLOS ONE* **12,** e0188005. doi:10.1371/journal.pone.0188005 (2017).

418. Kropp, H. M., Diederichs, K. & Marx, A. The Structure of an Archaeal B-Family DNA Polymerase in Complex with a Chemically Modified Nucleotide. *Angewandte Chemie International Edition* **58,** 5457–5461. doi:10.1002/anie.201900315 (2019).

419. Gardner, A. F. *et al.* Therminator DNA Polymerase: Modified Nucleotides and Unnatural Substrates. *Frontiers in Molecular Biosciences* **6.** doi:10.3389/fmolb.2019.00028 (2019).

420. Tasara, T. *et al.* Incorporation of reporter molecule-labeled nucleotides by DNA polymerases. II. High-density labeling of natural DNA. *Nucleic Acids Research* **31,** 2636–2646. doi:10.1093/nar/gkg371 (2003).

421. Kessler, L. F. *et al.* Self-Quenched Fluorophore-DNA Labels for Super-Resolution Fluorescence Microscopy. *The Journal of Physical Chemistry B* **128,** 6751–6759. doi:10.1021/acs.jpcb.4c02065 (2024).

422. Schröder, T., Scheible, M. B., Steiner, F., Vogelsang, J. & Tinnefeld, P. Interchromophoric Interactions Determine the Maximum Brightness Density in DNA Origami Structures. *Nano Letters* **19,** 1275–1281. doi:10.1021/acs.nanolett.8b04845 (2019).

423. Zimmers, Z. A., Adams, N. M., Gabella, W. E. & Haselton, F. R. Fluorophore-quencher interactions effect on hybridization characteristics of complementary oligonucleotides. *Analytical Methods* **11,** 2862–2867. doi:10.1039/C9AY00584F (2019).

424. Uyehara, C. M. & Apostolou, E. 3D enhancer-promoter interactions and multi-connected hubs: Organizational principles and functional roles. *Cell Reports* **42.** doi:10.1016/j.celrep.2023.112068 (2023).

425. Bothma, J. P., Norstad, M. R., Alamos, S. & Garcia, H. G. LlamaTags: A Versatile Tool to Image Transcription Factor Dynamics in Live Embryos. *Cell* **173,** 1810–1822.e16. doi:10.1016/j.cell.2018.03.069 (2018).

426. Kent, S. *et al.* Phase-Separated Transcriptional Condensates Accelerate Target-Search Process Revealed by Live-Cell Single-Molecule Imaging. *Cell Reports* **33.** doi:10.1016/j.celrep.2020.108248 (2020).

427. Bhat, P., Honson, D. & Guttman, M. Nuclear compartmentalization as a mechanism of quantitative control of gene expression. *Nature Reviews. Molecular Cell Biology* **22,** 653–670. doi:10.1038/s41580-021-00387-1 (2021).

428. Jungmann, R. *et al.* Multiplexed 3D cellular super-resolution imaging with DNA-PAINT and Exchange-PAINT. *Nature Methods* **11,** 313–318. doi:10.1038/nmeth.2835 (2014).

429. Schnitzbauer, J., Strauss, M. T., Schlichthaerle, T., Schueder, F. & Jungmann, R. Super-resolution microscopy with DNA-PAINT. *Nature Protocols* **12,** 1198–1228. doi:10.1038/nprot.2017.024 (2017).

430. Brückner, D. B., Chen, H., Barinov, L., Zoller, B. & Gregor, T. Stochastic motion and transcriptional dynamics of pairs of distal DNA loci on a compacted chromosome. *Science (New York, N.Y.)* **380,** 1357–1362. doi:10.1126/science.adf5568 (2023).

431. Ubertini, M. *et al. Loop extrusion creates rare, long-lived encounters underlying enhancer-promoter communication* 2025. doi:10.1101/2025.09.24.678119.

432. Petrenko, N., Jin, Y., Wong, K. H. & Struhl, K. Mediator Undergoes a Compositional Change during Transcriptional Activation. *Molecular Cell* **64,** 443–454. doi:10.1016/j.molcel.2016.09.015 (2016).

433. Chen, X. *et al.* Structures of the human Mediator and Mediator-bound preinitiation complex. *Science* **372,** eabg0635. doi:10.1126/science.abg0635 (2021).

434. Abdella, R. *et al.* Structure of the human Mediator-bound transcription preinitiation complex. *Science* **372,** 52–56. doi:10.1126/science.abg3074 (2021).

435. Rengachari, S., Schilbach, S., Aibara, S., Dienemann, C. & Cramer, P. Structure of the human Mediator–RNA polymerase II pre-initiation complex. *Nature* **594,** 129–133. doi:10.1038/s41586-021-03555-7 (2021).

436. Chen, L.-F. *et al.* Structural elements promote architectural stripe formation and facilitate ultra-long-range gene regulation at a human disease locus. *Molecular Cell* **83,** 1446–1461.e6. doi:10.1016/j.molcel.2023.03.009 (2023).

437. Cardozo Gizzi, A. M. *et al.* Direct and simultaneous observation of transcription and chromosome architecture in single cells with Hi-M. *Nature Protocols* **15,** 840–876. doi:10.1038/s41596-019-0269-9 (2020).

438. Kubo, N. *et al.* Promoter-proximal CTCF binding promotes distal enhancer-dependent gene activation. *Nature Structural & Molecular Biology* **28,** 152–161. doi:10.1038/s41594-020-00539-5 (2021).

439. Hsieh, T.-H. S. *et al.* Enhancer–promoter interactions and transcription are largely maintained upon acute loss of CTCF, cohesin, WAPL or YY1. *Nature Genetics* **54,** 1919–1932. doi:10.1038/s41588-022-01223-8 (2022).

440. Hafner, A. *et al.* Loop stacking organizes genome folding from TADs to chromosomes. *Molecular Cell* **83,** 1377–1392.e6. doi:10.1016/j.molcel.2023.04.008 (2023).

441. Karpinska, M. A. & Oudelaar, A. M. The role of loop extrusion in enhancer-mediated gene activation. *Current Opinion in Genetics & Development* **79,** 102022. doi:10.1016/j.gde.2023.102022 (2023).

442. Kagey, M. H. *et al.* Mediator and Cohesin Connect Gene Expression and Chromatin Architecture. *Nature* **467,** 430–435. doi:10.1038/nature09380 (2010).

443. Tsujimura, T. *et al.* Controlling gene activation by enhancers through a drug-inducible topological insulator. *eLife* **9,** e47980. doi:10.7554/eLife.47980 (2020).

444. Wu, J. *et al.* The landscape of accessible chromatin in mammalian preimplantation embryos. *Nature* **534,** 652–657. doi:10.1038/nature18606 (2016).

445. Jusuf, J. M. *et al.* Genome-wide absolute quantification of chromatin looping. *bioRxiv: The Preprint Server for Biology,* 2025.01.13.632736. doi:10.1101/2025.01.13.632736 (2025).

446. Baek, I., Friedman, L. J., Gelles, J. & Buratowski, S. Single-molecule studies reveal branched pathways for activator-dependent assembly of RNA polymerase II pre-initiation complexes. *Molecular Cell* **81,** 3576–3588.e6. doi:10.1016/j.molcel.2021.07.025 (2021).

447. Thomas, H. F. *et al.* Temporal dissection of an enhancer cluster reveals distinct temporal and functional contributions of individual elements. *Molecular Cell* **81,** 969–982.e13. doi:10.1016/j.molcel.2020.12.047 (2021).

448. Spitz, F. & Furlong, E. E. M. Transcription factors: from enhancer binding to developmental control. *Nature Reviews Genetics* **13,** 613–626. doi:10.1038/nrg3207 (2012).

449. Zabidi, M. A. & Stark, A. Regulatory Enhancer-Core-Promoter Communication via Transcription Factors and Cofactors. *Trends in genetics: TIG* **32,** 801–814. doi:10.1016/j.tig.2016.10.003 (2016).

450. Reiter, F., Wienerroither, S. & Stark, A. Combinatorial function of transcription factors and cofactors. *Current Opinion in Genetics & Development* **43,** 73–81. doi:10.1016/j.gde.2016.12.007 (2017).

451. Le, D. J., Hafner, A., Gaddam, S., Wang, K. C. & Boettiger, A. N. Super-enhancer interactomes from single cells link clustering and transcription. *bioRxiv,* 2024.05.08.593251. doi:10.1101/2024.05.08.593251 (2024).

452. Karpinska, M. A. *et al.* CTCF depletion decouples enhancer-mediated gene activation from chromatin hub formation. *Nature Structural & Molecular Biology* **32,** 1268–1281. doi:10.1038/s41594-025-01555-z (2025).

453. Frankel, N. *et al.* Phenotypic robustness conferred by apparently redundant transcriptional enhancers. *Nature* **466,** 490–493. doi:10.1038/nature09158 (2010).

454. Taupin, P. BrdU immunohistochemistry for studying adult neurogenesis: paradigms, pitfalls, limitations, and validation. *Brain Research Reviews* **53,** 198–214. doi:10.1016/j.brainresrev.2006.08.002 (2007).

Appendix

A Acknowledgments

Science does not happen in a vacuum, and I am grateful to have been supported by many wonderful people along this part of my scientific journey.

First I wish to express my gratitude to Heinrich Leonhardt. Thank you for giving me the freedom to explore my ideas and offering insightful advice when I needed direction.

Most of all, I would like to thank Hartmann Harz for the great mentorship. Thank you for all the stimulating scientific discussions, guidance and support of my scientific development throughout the project. I appreciate your constant encouragement, patience, trust in my ideas and showing that you care.

I would like to thank Clemens Steinek for being my FISH buddy. Thank you for the fun brainstormings, discussions and valuable advice. I know I can always count on you. I wish to thank Miguel Guirao Ortiz who was my first introduction to the lab during my bachelor's thesis and with whom I have shared at big part of my time in the Leonhardt lab. Thank you for all the fun times at the bench, your patience with me as a bachelor's student, always having time for me, and encouraging me to become more confident. Your support is deeply appreciated. My thanks also goes to Weihua Qin. Thank you for the fun scientific and personal discussions, your help, advice, and support. Science can be lonely, but with you it was a little less lonely.

I am grateful to my colleagues for creating a fun, creative, and welcoming working environment. Thank you David Hörl, for your continuous support and discussions about anything involving computation and microscopy. Thank you Simon Ullrich and Irina Solovei for your support with FISH and valuable scientific discussions. Thank you Mustafa Abdellatif, Jyotirmoy Rajurkar, Jonathan Schwach, Marlene Rauschmayer,

Enes Ugur, Deis Haxolli, Jeanette Koch, Susanne Breitsameter, Andrea Mathieu, Ruzica Barisic and everyone in the Leonhradt and Stengl labs for your continuous support throughout the years.

Many thanks to our collaborators Marieke Oudelaar and Dimitra Tsouraki for their valuable contribution to our publication, hosting me in their amazing lab and sharing their knowledge with me.

I also wish to thank the IRTG 1064 "Chromatin dynamcis" for connecting me with many friendly, brilliant PhD students and providing me with valuable training opportunities. I would especially like to thank Elizabeth Schroeder-Reiter for fostering such as welcoming and open environment.

Thank you to my amazing students Lara Carola Seppi and Valentin Hartsch for their excitement about our science and their hard work. I wish you both a great success in the future!

I would like to thank my friends who supported me throughout this journey, especially Thomas, Bart, Fiona and Boštjan. Thank you for all the nice conversations, rants, and wonderful bouldering and climbing sessions.

I would also like to express my gratitude to my parents, Gorazd and Nataša, and my sister Nina, who always encouraged me to follow my curiosity, question and explore. Thank you for continuously reminding me I can do (almost) anything I set my mind to.

Finally, I would like to thank Ralf Weidner for the incredible support, listening to my countless troubleshooting ideas for my failed experiments and celebrating the small victories with me. Your support is deeply appropriated.